Temporal Multiscale Methods for a Model of Atherosclerosis

Zeitliche Mehrskalenmethoden
für ein Modell von Atherosklerose

Der naturwissenschaftlichen Fakultät
Der Friedrich-Alexander-Universität
Erlangen-Nürnberg

zur

Erlangung des Doktorgrades Dr. rer. nat.

vorgelegt von

Florian Sonner
aus Hamburg

Als Dissertation genehmigt
von der naturwissenschaftlichen Fakultät
der Friedrich-Alexander-Universität Erlangen-Nürnberg

Tag der mündlichen Prüfung:

Vorsitzender des Promotionsorgans: Prof. Dr. Georg Kreimer

Gutachter:

Zusammenfassung. Atherosklerose ist eine Krankheit der Arterien in Folge derer der Blutfluss stark eingeschränkt oder gänzlich blockiert werden kann. Dadurch kann es zu Herzinfarkten oder Schlaganfällen kommen, zwei der häufigsten Todesursachen weltweit. Dies motiviert eine mathematische Modellierung und Simulation dieser Krankheit. Die Zeitskala des Krankheitsverlaufs, primär bestimmt durch das Anwachsen eines Plaques in der Arterien-Wand über Jahre, unterscheidet sich stark von der Zeitskala anderer als relevant vermuteter Phänomene, z.B. auf die Wand wirkende Scherkräfte durch den Blutfluss, oszillierend mit dem Herzschlag auf einer Sekundenskala. Dies verhindert eine direkte numerische Simulation dieser Modelle, da lange Zeiträume mit einer sehr feinen Diskretisierung aufgelöst werden müssten. Das Ziel dieser Arbeit ist die Konstruktion von einfacher zu lösenden Approximationen durch Mehrskalenmethoden mit einer rigorosen Fehleranalyse.

Motiviert durch einer Arbeit von Yang et. al. [Yan+15] werden zwei vereinfachte Teilmodelle von Atherosklerose betrachtet, deren Mehrskalenanalyse sich rigoros durchführen lässt. Das erste Modell behandelt das langsame Plaque-Wachstum gekoppelt an die schnell oszillierenden Scherkräfte der Blutströmung. Dies ist mathematisch realisiert durch eine langsame gewöhnliche Differentialgleichung gekoppelt an eine Strömungsgleichung mit schnell oszillierenden Randwerten und einem vom Wachstum abhängenden, nicht-zylindrischen Orts-Zeit-Gebiet. Das zweite Modell betrachtet schnell durch die Arterie advektierte Substanzen mit einer langsamen Diffusion durch die Arterienwand und besteht aus einem System von Advektions-Diffusions- und Diffusions-Reaktions-Gleichungen, gekoppelt über das permeable Interface.

Mit einem kleinen Parameter ε, welcher die Zeitskalenseparierung ausdrückt, wird das Verhalten der Lösungen dieser Modelle im Grenzwert $\varepsilon \to 0$ analysiert. Beide Modelle sind singulär gestört, d.h. der Grenzwert der Lösungen erfüllt eine Differentialgleichung eines anderen Typs. Für das erste Modell wird gezeigt, dass die Lösung mit der Ordnung $\mathcal{O}(\varepsilon)$ gegen die Lösung einer Grenzgleichung konvergiert, welche die Auswirkung einer zeitlich-periodischen Strömungsgleichung mittelt. Für das zweite Modell ergibt sich im Grenzwert ein gekoppeltes System aus Advektions- und Diffusions-Reaktions-Gleichungen. Die Konvergenzordnung hängt dabei von der Lösungsregularität und der Advektionsgeschwindigkeit ab, für z.B. das stationäre Problem mit der Poiseuille-Strömung ergeben sich die Ordnungen $\mathcal{O}(\varepsilon^{1/2})$ und $\mathcal{O}(\varepsilon^{1/6})$ für den örtlichen L^2- und H^1-Fehler im Strömungsgebiet und $\mathcal{O}(\varepsilon^{1/3})$ für den H^1-Fehler in der Wand. Verbunden werden hierfür Techniken für qualitative Konvergenzaussagen von Advektions-Diffusionsgleichungen im singulären Grenzwert von verschwindender Diffusion mit einer speziellen Spurabschätzung für die Kopplung über das permeable Interface.

Für beide Modelle werden numerische Beispielrechnungen durchgeführt. Für das Plaque-Wachstums-Modell liegt hierbei der Fokus auf der Lösung von zeit-periodischen Navier-Stokes-Gleichungen welche für das Grenzproblem benötigt werden werden, ein existierender Algorithmus wird dabei verbessert. Außerdem wird eine Fehleranalyse für die zeitdiskrete Grenzgleichung durchgeführt, welche verdeutlicht und quantifiziert, dass für die effiziente numerische Lösung eine Balance der verschiedenen Fehlerquellen notwendig ist. Für das zweite Modell wird eine discontinuous Galerkin Diskretisierung vorgestellt und die Übereinstimmung zwischen theoretischen und numerischen Ergebnissen gezeigt.

Der Aufbau der Arbeit ist wie folgt. Nach der Einleitung wird im 2.

Kapitel eine Übersicht über die Krankheit Atherosklerose und existierende mathematische Modelle gegeben, gefolgt von einer Präsentation und Entdimensionalisierung des Modells von Yang et. al. auf deren Grundlage die Skalierung der später betrachteten Modelle gewählt wird. Kapitel 3 bis 5 beschäftigen sich mit dem Plaque-Wachstums-Modell, im 3. Kapitel in abstrakter Form, um die Mehrskalen-Techniken zu präsentieren, und in Kapitel 4 für das konkrete Modell mit einer Stokes-Gleichung auf einem nicht-zylindrischen Gebiet welches von der Wachstums-Lösung abhängt. Kapitel 5 behandelt die Numerik dieses Modells. Im finalen Kapitel 6 wird die Mehrskalenanalyse und die numerischen Ergebnisse für das zweite Modell der permeablen Wand präsentiert.

Abstract. Atherosclerosis is a disease of the arteries which can cause a reduction or complete blockage of blood flow and may thus lead to heart attacks or strokes, two of the most common causes of death worldwide. This motivates mathematical modelling and simulation of the disease. The timescale of disease progression, driven by the growth of plaque in the artery wall over years, differs greatly from other processes which are assumed to be relevant, e.g. the shear stresses exerted by the blood flow on the artery wall, which oscillates with the heart beat every second. This prevents a direct numerical simulation of such models, since long timescales would have to be resolved with a very fine step size. The goal of this thesis is to construct approximations which are simpler to solve numerically, through the use of multiscale methods, and to prove quantitative convergence results.

Motivated by a model by Yang et. al. [Yan+15], we will investigate two simplified submodels of atherosclerosis for which a rigorous multiscale analysis is possible. The first model studies slow plaque growth coupled to fast oscillating shear stresses caused by the blood flow. Mathematically this is realized through a slow ordinary differential equation coupled to a fluid equation with rapidly oscillating boundary conditions and growth-dependent, non-cylindrical space-time domain. The second model investigates substances quickly advected through the artery but only slowly diffusing into the semi-permeable wall. It consists of a system of coupled advection-diffusion and diffusion-reaction equations.

With a small parameter ε, which expresses the timescale separation, the behavior of the solutions to these models in the limit $\varepsilon \to 0$ is investigated. Both models are singularly perturbed, meaning that their solutions converge to functions which solve a differential equation of different type. For the first model it will be shown that the solution converges with order $\mathcal{O}(\varepsilon)$ to the solution of a limit equation which averages the effect of a time-periodic fluid equation. The second model yields a limit consisting of a coupled advection and diffusion-reaction equation. The order of convergence depends on the solution regularity and the behavior of the advection field. For e.g. the stationary problem and Poiseuille flow it will be shown that the spatial L^2- and H^1-errors are of order $\mathcal{O}(\varepsilon^{1/2})$, respectively $\mathcal{O}(\varepsilon^{1/6})$, in the advection domain. Inside the wall the H^1-error will be of order $\mathcal{O}(\varepsilon^{1/3})$. The derivation of this result combines qualitative convergence theory for advection-diffusion equations in the vanishing diffusion limit with a specific trace estimate for the coupling through the permeable wall.

Numerical calculations are carried out for both models. For the plaque growth the focus lies on the solution of the time-periodic Navier–Stokes equation which will be required for the limit system, an existing

algorithm from the literature is improved here. Furthermore, the error of the time-discrete equation is analyzed, which quantifies and emphasizes how the errors made in the different solution steps must be balanced for efficiency. For the second model a discontinuous Galerkin discretization is proposed and the agreement between theoretical and numerical results shown.

Acknowledgements. I thank my advisor Eberhard Bänsch for his support and my co-advisor Helmut Abels for his valuable feedback. I thank Thomas Richter for proposing this thesis' topic and his advice during the initial phase of my doctorate. I thank the members of my working group AM3 for their help and the congenial atmosphere. I gratefully acknowledge the financial support by the Deutsche Forschungsgemeinschaft as part of the RTG 2339 "Interfaces, Complex Structures, and Singular Limits". I thank the IntComSin supervisors for organizing stimulating lectures and talks and the IntComSin students for the sociable visits to Weltenburg. Finally, I thank my friends and family for their ongoing support of my endeavors.

Contents

1 Introduction **1**
- 1.1 Overview . . . 1
- 1.2 Sketch of the Multiscale Analysis for Plaque Growth . . . 2
- 1.3 Outline . . . 3
- 1.4 Notation . . . 4

2 Models for Atherosclerosis **7**
- 2.1 The Disease Atherosclerosis . . . 7
- 2.2 Mathematical Models for Atherosclerosis . . . 13
- 2.3 The Model by Yang et. al. . . . 33

3 Periodically-Forced PDE-ODE Fast-Slow Systems **49**
- 3.1 Notation and Assumptions . . . 50
- 3.2 Examples . . . 52
- 3.3 Preliminary Results . . . 56
- 3.4 Proof of Multiscale Convergence . . . 58
- 3.5 Averaging of Forces and Quasi-Static Limit . . . 64

4 Multiscale Analysis of a Simplified Plaque Model **67**
- 4.1 The Plaque Model . . . 67
- 4.2 Analysis on a Fixed Timescale . . . 76
- 4.3 Singular Limit . . . 86

5 Numerics for the Simplified Plaque Model **93**
- 5.1 Problem Description . . . 93
- 5.2 Numerical Realization of Fast-Slow and Limit Systems . . . 97
- 5.3 Calculation of Periodic Solutions . . . 105
- 5.4 Temporal Error Analysis for the Limit System . . . 132

6 Multiscale Analysis of a Permeable Membrane Model **139**
- 6.1 Problem Description . . . 140
- 6.2 Analysis of the Stationary Problem . . . 142
- 6.3 Analysis of the Instationary Problem . . . 153
- 6.4 Numerics . . . 161

Bibliography **175**

Chapter 1

Introduction

1.1 Overview

Atherosclerosis is a cardiovascular disease in which plaque builds up inside an artery's wall. This can lead to a severe restriction of blood flow and can cause heart attacks or strokes, some of the leading causes of death in the world [GBD18]. Almost everybody is affected by some, mostly asymptomatic and benign, stages of this disease, which begins in adolescence and progresses over decades. This motivates a better understanding of this diseases' progression and risk assessments through mathematical models and subsequent numerical simulations.

The disease features processes happening over vastly different timescales. While progression happens over decades, the wall shear stress exerted by the blood on the artery wall is hypothesized to play an important role in the progression but varies on a sub-second timescale due to the pulsatile nature of the blood flow. This poses numerical challenges since the fast processes would have to be fully resolved over long timescales in direct approximations. While many ad-hoc solutions to this problem have been proposed, the implicit assumptions behind these simplifications have received little attention.

This thesis is concerned with the analysis and numerics of two aspects of a plaque model by Yang, Jäger, Neuss-Radu and Richter [Yan+15] which was the initial motivation for this work. The first aspect is slow plaque growth, controlled by fast wall shear stresses due to the pulsatile blood flow. To allow rigorous analysis this model is simplified as an ordinary differential equation for the plaque growth state depending on the (integrated) wall shear stress of a Stokes equation with oscillating boundary conditions and non-cylindrical domain depending on the plaque state. The second model is concerned with fast advection of substances in the artery with slow diffusion through the damaged, permeable wall. This model consists of a coupled system of advection-diffusion and diffusion-reaction partial differential equations.

To develop efficient numerical approximations to these models we use a typical strategy in multiscale analysis. We first express the scale separation by a small number $0 < \varepsilon \ll 1$, in the sense that the separation between the scales increases as $\varepsilon \to 0$. Treating ε as a variable parameter instead of a fixed constant, we then investigate the solution behavior as $\varepsilon \to 0$, with the hope that the corresponding solutions converge, in some appropriate sense, and that

their limit satisfies another equation which can be solved efficiently.

All models investigated in this thesis are of a singular perturbation type, meaning that their mathematical structure changes in the limit $\varepsilon \to 0$ such that some initial or boundary values can no longer be satisfied. The first model has a time-periodic fluid inflow, being driven by the periodic heart beat, and multiscale averaging techniques are employed to prove convergence to the limit system. The second model changes from a coupled parabolic-parabolic to a coupled hyperbolic-parabolic system in the limit. Established estimates for the fast advection limit in one domain are combined with trace and interpolation techniques to prove convergence in the other domain.

Since the limit equation is solved as an approximation to the original model, the quantification of the rate of convergence in terms of ε will be a focus of the analysis. The first model also leads to a non-standard limit equation, which requires the solution of a time-periodic (Navier–)Stokes equation in each step, the numerical solution of which and overall error estimates will be major topics of the numerical discussion.

Both models are simplifications such that a rigorous multiscale analysis is possible. Consequentially their applicability to the medical problem is limited and for this reason the numerical simulations are performed to illustrate and complement the analysis without focusing on accurate medical parameters. It is the hope that these tools can nevertheless be employed in more complex models, even when a rigorous theory is out of reach, where e.g. the validity of underlying assumptions could be checked numerically.

1.2 Sketch of the Multiscale Analysis for Plaque Growth

We sketch the multiscale analysis for the plaque growth model to illustrate the techniques and results mentioned in the overview. To keep this section brief we will not be concerned with technical definitions or details, which can be found in Chapters 3 and 4.

The simplified plaque growth model assumes that the plaque is described by a finite dimensional state $q \in Q$, e.g. the height of the plaque relative to original wall, whose evolution is governed by an ordinary differential equation depending on the wall shear stress exerted by the blood on the artery wall. The blood flow geometry depends on the plaque state, coupling both equations. Expressing the slowness of growth compared to the blood flow by $0 < \varepsilon \ll 1$, the problem then is to find plaque state q_ε, fluid velocity v_ε and fluid pressure q_ε such that

$$\frac{\mathrm{d}}{\mathrm{d}t} q_\varepsilon = \varepsilon g(q_\varepsilon, v_\varepsilon) \quad \text{in } I, \tag{1.1a}$$

$$\partial_t v_\varepsilon - \Delta v_\varepsilon + \nabla p_\varepsilon = f(t) \quad \text{in } \Omega^I_{q_\varepsilon}, \tag{1.1b}$$

supplemented with appropriate boundary and initial conditions, where $I := (0, \varepsilon^{-1}\mathcal{T})$ for some $\mathcal{T} > 0$, f is a 1-periodic function representing the periodic inflow of blood and $\Omega^I_{q_\varepsilon}$ is the non-cylindrical domain due to the plaque evolution, $\Omega^I_{q_\varepsilon} := \{(t, x) \mid t \in I, x \in \Omega_{q_\varepsilon(t)}\}$, for a given family of domains $\{\Omega_q\}_{q \in Q}$. The Stokes equation is used in eq. (1.1b) for simplicity and, as mentioned in the overview, the parameter ε is not a-priori given but must be identified in real models. The variable q_ε is slow, whereas v_ε and p_ε are fast by assumption, which is why eqs. (1.1) are known as a slow-fast system. Equations (1.1) are

formulated on the *fast timescale*, where t denotes multiples of the period of the heart beat. The slow plaque growth is of order $\mathcal{O}(\varepsilon)$ and the investigated time interval has length $\mathcal{O}(\varepsilon^{-1})$, which reflects that we are interested in the evolution on a timescale on which q_ε changes significantly. With the transformation $\tau := \varepsilon t$ the system can equivalently be written on the *slow timescale*

$$\begin{aligned} \tfrac{\mathrm{d}}{\mathrm{d}\tau} q_\varepsilon &= g(q_\varepsilon, v_\varepsilon) && \text{in } \mathcal{I}, \\ \varepsilon \partial_\tau v_\varepsilon - \Delta v_\varepsilon + \nabla p_\varepsilon &= f(\tfrac{\tau}{\varepsilon}) && \text{in } \Omega_{q_\varepsilon}^{\mathcal{I}}, \end{aligned}$$

where $\mathcal{I} := (0, \mathcal{T})$. Note that since $\varepsilon \partial_\tau v_\varepsilon = \mathcal{O}(1)$ we have $\partial_\tau v_\varepsilon = \mathcal{O}(\varepsilon^{-1})$.

Without resorting to tools like asymptotic expansions, we can see from eq. (1.1a) that $q_\varepsilon \approx$ const for short times (on the fast timescale) as $\varepsilon \to 0$, formally setting $\varepsilon = 0$ in eq. (1.1a). This motivates the investigation of the dynamics of eq. (1.1b) for fixed $\hat{q} \in Q$, where we assume that $\hat{q} \approx q_\varepsilon(t)$ for fixed $t \in I$. Since f is 1-periodic and due to the stability of the Stokes equation, it is reasonable to assume that the solution v_ε for short times then tends to the periodic solution $v_\pi(s; \hat{q})$ of

$$\partial_s v_\pi(s; \hat{q}) - \Delta v_\pi(s; \hat{q}) + \nabla p_\pi(s; \hat{q}) = f(s) \quad \text{in } \Omega_{\hat{q}} \tag{1.3}$$

for $s \in (0, 1)$ a.e. with $v_\pi(0; \hat{q}) = v_\pi(1; \hat{s})$. Note that this is an independent problem with periodic time $s \in (0, 1)$ unrelated to t and τ. It must be stressed that the stability of the parabolic eq. (1.1b) is central for this argument and the validity of the subsequent limit equation.

The assumption $q_\varepsilon \approx$ const is clearly no longer satisfied over longer times, but since v_ε approximates v_π for short times, the effect of v_ε on q_ε can be approximated by v_π. This may convince the reader that as $\varepsilon \to 0$ the behavior of q_ε may be approximated by the solution q_0 to the limit equation

$$\frac{\mathrm{d}}{\mathrm{d}\tau} q_0(\tau) = \int_0^1 g(q_0(\tau), v_\pi(s; q_0(\tau)))\, \mathrm{d}s \quad \text{for } \tau \in \mathcal{I} \tag{1.4}$$

which we will call averaging type limit. Since q_0 is independent of ε this equation is naturally formulated on the slow timescale. Note that eq. (1.3) is implicitly solved for fixed $q_0(\tau)$ in the limit equation, which is known as a cell-problem in the spatial homogenization theory and makes this equation non-standard to solve numerically. Furthermore, note that the action of g with periodic argument v_π is averaged, and not the periodic solution v_π itself. For the linear Stokes equation this (incorrect) averaging of v_π is equivalent to solving the stationary problem with averaged inflow boundary conditions, which is a common approach in the literature, see Chapter 2.

Formalizing the previous intuitive reasoning we will show in Chapter 4 that

$$\sup_{t \in (0, \varepsilon^{-1}\mathcal{T})} |q_\varepsilon(t) - q_0(t)| \leq C\varepsilon$$

with constant $C > 0$ depending on the data, which is the quality of approximation typically found in the averaging literature.

1.3 Outline

This thesis is composed of three parts which can be read independently. The first is a review of the disease atherosclerosis and its mathematical models

in Chapter 2. The final section of Chapter 2 discusses the model by Yang et. al. which motivated the two models in this thesis and contains a non-dimensionalization to identify the magnitude of parameters. Chapter 3 and Chapter 4 are concerned with the mathematical analysis of the multiscale convergence for the model of slow plaque growth influenced by fast, oscillatory wall shear stress given by the solution of the Stokes equation. The techniques for the proof of multiscale convergence are first discussed in an abstract framework in Chapter 3 to highlight the major techniques and assumptions. The extension to the growth problem, being technically involved due to the moving domains, is made in Chapter 4. The limit equation which appears in this context requires the solution of time-periodic fluid equations on a family of domains. The numerical solution of this problem and error estimates for the discretized limit equation are major topics of the numerical Chapter 5. The final part of this thesis is a model of fast advection coupled through a permeable interface with slow diffusion, discussed in Chapter 6. Under strong assumptions on the inflow and advection field, satisfied in the setting of Yang et. al., this model is analyzed using established techniques for fast advection limits, combined with trace and interpolation techniques to prove convergence in the interior of the wall. In the final section of Chapter 6 a discontinuous Galerkin discretization of this problem is discussed and numerical results show the agreement with the theoretical predictions.

1.4 Notation

As already done in the sketch of the multiscale analysis above, we will investigate our models on either fast or slow timescale, e.g. the timescale of the heart beat compared to the timescale of the plaque growth. We will denote by $t \in I := (0,T)$ with $T > 0$ the fast and by $\tau \in \mathcal{I} := (0,\mathcal{T})$ with $\mathcal{T} > 0$ the slow timescale. Denoting the timescale separation parameter by $0 < \varepsilon \ll 1$, these scales will be formally related by the transformation $\tau = \varepsilon t$. In particular $T = \varepsilon^{-1}\mathcal{T}$, where the length of the slow timescale $\mathcal{T} > 0$ will be independent of ε in our convergence results. We will not notationally distinguish between the functions $t \mapsto f(t)$ and $\tau \mapsto f(\tau)$, but the scaling should be evident out of context and through the used notation for the argument. We remark that in some parts of the literature the roles of t and τ are reversed, i.e. t denotes the slow and τ the fast time variable.

We denote by $C > 0$ a generic constant which is always independent of ε but may change with each occurrence. We will commonly write $a \lesssim b$ if $a \leq Cb$. We write $\overline{A}$ for the closure and A° for the interior of a set A in some topological space and denote by $\mathbb{1}_A$ the associated indicator function. The spatial dimension is denoted by $d \in \{2,3\}$ and the Euclidean distance between a point $x \in \mathbb{R}^d$ and a set $A \subset \mathbb{R}^d$ by $\mathrm{d}(x,A)$. We use the following notations for vector calculus: We write $\mathrm{I} \in \mathbb{R}^{d\times d}$ for the identity matrix and $\operatorname{Cof} A := \det A A^{-\intercal}$ for the cofactor matrix of some invertible matrix $A \in \mathbb{R}^{d\times d}$. For a vector field u we denote by $(\nabla u)_{ij} = \partial_j u_i$ with $i,j = 1,\dots,d$ the Jacobian matrix and by $\operatorname{div} u := \sum_i \partial_i u_i$ the divergence. For a matrix (representation of a tensor) field A we write $(\operatorname{div} A)_i := \sum_j \partial_j A_{ij}$ for $i = 1,\dots,d$.

In Chapters 2 and 6, where phenomena both inside the region of free blood flow (the lumen) and inside the artery wall are examined, we will write $\Omega_f \subset \mathbb{R}^d$

for the fluid and $\Omega_s \subset \mathbb{R}^d$ for the structure domain. This follows the notation from [Yan+15], but note that in some reviewed models in Section 2.2 fluid flow is also modelled in the wall as a porous medium. We will denote quantities defined on Ω_f and Ω_s with subscripts f and s, respectively, e.g. write v_f for the fluid velocity in Ω_f and v_s for the deformation velocity in Ω_s. The exterior unit normal vector on the boundary of Ω_f and Ω_s is denoted by $\mathfrak{n}_f$, respectively $\mathfrak{n}_s$.

The abstract examples for the theory developed in Chapter 3 are defined on a single domain $\Omega \subset \mathbb{R}^d$ and no subscripts are used. In the simplified model from Chapters 4 and 5 only the fluid domain is considered, but this domain depends on the plaque state $q \in Q$ for $Q \subset R^n$ for some $n \in \mathbb{N}$ and is written as $\Omega_q = \Omega_{f,q}$, i.e. omitting the subscript f. For some function $f\colon \mathcal{D}(f) \to Y$ with sets X, Y and $\mathcal{D}(f) \subset X \times Q$ we will use the notation $f_q(x) := f(x; q)$ if $(x, q) \in \mathcal{D}(f)$, where we write $f(x; q)$ to convey that q is often a fixed parameter.

For some generic domain $\Omega \subset \mathbb{R}^d$, we will denote by $L^p(\Omega)$, $H^s(\Omega)$, $W^{s,p}(\Omega)$ for $1 \leq p \leq \infty$ and $s \geq 0$ the usual Lebesgue and Sobolev spaces, and by $L^p(I, X)$, etc. for some Banach space X the corresponding Bochner spaces. We will denote the scalar products on $L^2(\Omega)$, $L^2(\Omega_f)$ and $L^2(\Omega_s)$ by $(\cdot\,, \cdot)$, $(\cdot\,, \cdot)_f$ and $(\cdot\,, \cdot)_s$ respectively. For the family of (fluid) domains Ω_q studied in Chapters 4 and 5 we write $(\cdot\,, \cdot)_q$ for the $L^2(\Omega_q)$ scalar product.

For Sobolev spaces a subscript 0 will denote the subspace with homogeneous Dirichlet boundary conditions, e.g. $H^1_0(\Omega) := \{u \in H^1(\Omega) \mid u = 0 \text{ on } \partial\Omega\}$. For Lebesgue spaces a subscript 0 will indicate the subspace of functions with zero mean, e.g. $L^2_0(\Omega) := \{p \in L^2(\Omega) \mid \int_\Omega p \,\mathrm{d}x = 0\}$. The space $H^{-1}(\Omega)$ will denote the dual of $H^1_0(\Omega)$. Subspaces of solenoidal, i.e. divergence-free, functions will be denoted by σ, e.g. $H^1_{0,\sigma}(\Omega) := \{u \in H^1_0(\Omega) \mid \operatorname{div} u = 0\}$. For functions in $L^p(\Omega)$ the divergence must be understood in the sense of distributions. We will omit the spatial dimension of objects if it is clear from the context, e.g. write $v_f \in H^1(\Omega)$ for the fluid velocity field instead of $v_f \in H^1(\Omega, \mathbb{R}^d) \cong [H^1(\Omega)]^d$. For a Banach space X we denote by $C_\pi(X) := \{u \in C(\mathbb{R}, X) \mid u(t + 1) = u(t)\ \forall t \in \mathbb{R}\}$ the set of continuous, 1-periodic, X-valued functions.

Chapter 2

Models for Atherosclerosis

We start with a brief summary of the disease atherosclerosis and involved structures in Section 2.1, focusing on the influence of the dynamics of blood flow (hemodynamics) and the causes of plaque growth. No prior knowledge is assumed. In Section 2.2 we review mathematical models for atherosclerosis which cover different processes and stages of the disease. Three foci of this review are the influence of the wall shear stress, the realization of growth and the ad-hoc resolution of the problem of multiple timescales as discussed in the introduction. The final Section 2.3 discusses one specific model by Yang et. al. [Yan+15] which was the motivation for this thesis. A non-dimensionalization is performed to highlight how different timescales emerge through parameter magnitudes.

2.1 The Disease Atherosclerosis

Atherosclerosis is a cardiovascular disease in which plaque builds up inside the artery's wall which can cause a narrowing (stenosis) the region of blood flow [GJ10]. Extreme stenosis or events like a rupture of the plaque may reduce blood flow sufficiently to cause a heart attack or stroke [Her+16], which are leading causes of death in the world [GBD18]. Atherosclerosis develops over a span of decades, with initial stages of the disease found in some locations as early as in the first decade of life [Sta99]. The disease is also ubiquitous: In one study it was found in 95% of the subjects after the fourth decade of life [Sta99]. The initial stages are benign and asymptomatic, the likelihood of a progression towards later, malign stages is driven by several accepted risk factors, such as smoking, adiposity, high blood pressure, blood cholesterol, diabetes mellitus, age, sex, personal and family history [Her+16; GJ10].

Mortality due diseases caused by atherosclerosis has drastically declined since the middle of the 20^{th} century in high-income countries [Her+16]. Today, critically blocked arteries are either opened up with stents or bypassed [Moh+13] and progression slowed down using statins [Ped16]. But even with optimal treatment, recurrent events occur in 10% to 20% of cases in the first 12 months after acute syndromes, highlighting the need for further research [LBT16]. This research is hindered by the slow progression of the disease, difficulties of in-vivo monitoring and deficits of laboratory animal models [NWS08].

The description of processes involved in atherosclerosis fills volumes, so only

an overview can be given here. We refer to [GJ10; LBT16] for a more detailed exposition.

Review of Structures Involved in Atherosclerosis

Arteries

Arteries transport blood away from the heart. They enclose the blood flow region (lumen) with a wall subdivided into three enveloping layers of tissue: The innermost tunica intima, tunica media and outermost tunica adventitia. The initial stages of atherosclerosis occur in the tunica intima, but later stages can extend into tunica media and adventitia [Sta99]. Arteries differ substantially in function and composition. Arteries closest to the heart, like the aorta, are the largest and elastic to stretch in response to the blood pulse. Their walls have their own blood vessels (vasa vasorum) which enter either through the intima or adventitia [RL07]. Medium-sized arteries for blood distribution are muscular, but may still be exposed to considerable external movement, like the coronary arteries which are attached to the heart. Atherosclerosis is uncommon in smaller arteries [Ros99]. The intima, normally thin compared to the other layers, can thicken with age [Sta+92], either focally (eccentric thickening), common near bifurcation points and at the entrances of branch vessels [Sta99], or uniformly (diffuse thickening). Regions with intimal thickening are associated to altered mechanical stress and susceptible to atherosclerosis, but the thickening itself is not considered part of the disease [Sta+92].

The tunicas are separated by elastic tissue [SK04]. The tunica intima is delimited from the lumen by a contiguous mono-layer of cells, called endothelium, which acts as a permeability barrier [Sta+92]. The endothelium is supported by an extracellular matrix, below which lie layers of smooth muscle cells, although these may be missing in some cases and thickness of extracellular matrix and muscle cell layers varies significantly with intimal thickening [Sta+92]. The tunica media contains layers of smooth muscle cells supported by an extracellular matrix with elastic fibres which control the elastic behavior of large arteries [SK04]. The adventitia is a collection of smooth muscle and other cells embedded into a loose matrix containing elastic fibres [SK04].

Blood

Blood is a suspension of particles in a plasma containing, among other things, platelets, red and white blood cells. Blood is a non-Newtonian fluid with shear-thinning, viscoelastic and, albeit controversial, yield stress behaviors, see [RSK08] also for the remainder of this paragraph. These effects are mainly caused by red blood cells, which are oval biconcave disks that can deform, aggregate and align. Under low shear rates, they stack into a structure called rouleaux, which themselves can form complex three-dimensional networks. These structures take seconds to minutes to form and disintegrate under high shear rates, so they can only occur in regions which experience low shear rates due to stagnation or recirculation over longer times. Due to the complexity of blood rheology, simplified models are often employed. A common, but drastic, simplification is the use of a Newtonian model in large and medium sized arteries, which is known to cause artifacts e.g. behind a stenosis [QVZ02b].

Lipoproteins

A function of blood of particular importance for atherosclerosis is the transport of lipids, such as cholesterol. Since lipids are hydrophobic, they are enclosed by proteins in a complex called lipoprotein. Two important characteristics of lipoproteins are their density and comprising proteins. Very low (VLDL), intermediate (IDL) and low density lipoproteins (LDL) contain apoB-proteins, whereas high density lipoproteins (HDL) contain apoA-proteins. While this classification is already a simplification of much more heterogeneous particles with complicated dynamics [Hüb+08], we focus for simplicity only on the atherogenic LDL and atheroprotective HDL [GJ10].

Progression of Atherosclerosis

There is not one single sequence of events in atherosclerosis. Using the progression scheme proposed in [Sta+94; Sta+95; Sta00] one can roughly distinguish between early and advanced stages. Early stages are benign and asymptomatic, whereas advanced stages can be malign with symptoms such as chest pain (angina pectoris) or sudden, possibly but not necessarily fatal, events like heart attack (myocardial infarction) or (ischemic) stroke [Sta00]. Early stages can regress to normal, advanced stages are characterized by irreversible disruption of the wall's structure and geometry with the possibility of stabilization, i.e. a halting of progression, but not regression [Sta+95; Sta00].

Early Stages: Fatty Streak, Lipid Accumulation

Atherosclerosis is an inflammatory response to a dysfunction of the artery wall [LRM02]. The initial event which leads to atherosclerosis is still disputed [SK04] and some authors distinguish between initial stages based on the presence or absence of intimal thickening [Vir+00]. According to the response-to-retention hypothesis the retention of LDL in the intima, and other lipoproteins with diameter $< 70\,\text{nm}$ containing apoB, is the initial event in atherosclerosis [TWB07]. Regions prone to atherosclerosis differ not in the permeability but retention of lipoproteins [SC89a; SC89b], this retention predates the occurrence of immune cells [TWB07; NWS08] and is enhanced by external stimuli such as mechanical strain [NWS08]. The response-to-injury hypothesis stresses the importance of altered endothelial function, e.g. loss of nitric oxide production important for vascular homeostasis, caused by the risk factors described above through different pathways and wall shear stress [GJ10]. This causes in particular monocytes, a part of the innate immune system and a subset of the white blood cells in the blood stream, to be attracted into the wall through a process of adhering to, rolling along and transmigrating through the wall [GL15]. Wall shear stress alters the expression of genes involved in this process, e.g. low shear stress increases the expression of adhesion molecule genes [Ros99].

Inside the wall, monocytes differentiate into macrophages and take up the previously retained LDL [Ros99]. The uptake of LDL in its native state is tightly regulated by the macrophage's LDL receptor, but this regulation is circumvented in atherosclerosis through the so called scavenger receptor pathway [SK04]. This pathway requires chemically modified LDL, e.g. oxidized LDL (oxLDL), and the importance of the process of chemical modification in the

intima is stressed by the oxidative modification hypothesis [SK04]. In a "protective response that backfires" [SN13], macrophages can thus engorge excessive amounts of LDL and turn into foam cells, so called due to their foamy appearance under the microscope. Foam cells are a hallmark of early atherosclerosis and make up the fatty streak [Sta+92]. Foam cells eventually die and leave extracellular lipids in the wall, which together with cell debris form small pools in the wall [Sta00]. The occurrence of small, isolated lipid pools marks the final stage of early atherosclerosis [Sta00]. Through the process of reverse cholesterol transport, which utilizes HDL, lipids can be transported out of the wall [GJ10] which can lead to a regression of the diseased wall back to normal [Sta00].

Advanced Stages: Plaque Formation, Stabilization, Rupture

If the accumulation of lipids outpaces the reverse transport, the small lipid pools join to a larger, confluent pool called lipid core, whose occurrence marks the first stage of advanced atherosclerosis [Sta+92]. Since lipid cores also accumulate debris from dying cells they are also referred to as (lipid-rich) necrotic cores. After the formation of a lipid core, smooth muscle cells migrate into the area separating the core from the lumen, forming a protective, fibrous cap [GJ10]. Together with the lipid core the cap constitutes the atheromatous plaque, which may cause a hardening (sclerosis) of the wall and gives the disease its name.

The further progression of the disease is largely influenced by size and composition of the cap and core. The plaque can be unstable if it has a thin cap with thickness typically less than 100 µm[1] [CW14] overlying an extensive lipid core, typically 30%–50% of total plaque area [Vir+05]. Instability can also occur if the cap is structurally weakened by infiltrating macrophages, by the death of muscle cells or through the formation of microvessels [GJ10]. Stable plaque, in absence of the prior phenomena, can undergo calcification or fibration, where the lipid core is slowly mineralized or the lipids removed by reverse cholesterol transport and replaced by fibrous, reparative tissue [Sta+95].

Unstable plaque may fissure or rupture. Fissuring may be seen as precursor or subtype of rupture and can cause blood to enter the plaque (intraplaque hemorrhage) [Vir+00]. A rupture exposes material from the lipid core to the blood stream, in which case platelets in the blood activate and aggregate, leading to the formation of a blood clot (thrombus) [Vir+00]. A thrombus can stay in place or travel downstream which can either lead to a fatal reduction of blood flow, manifesting e.g. as a heart attack or stroke, but can also be nonfatal and even asymptomatic [Vir+00]. In focal (eccentric) plaques, fissures and ruptures are most common in the shoulder regions where the cap is thinnest and most infiltrated by foam cells [Vir+00; Ben+14]. Multiple, nonfatal and asymptomatic thrombi can occur, which are then incorporated into the healing plaque, leading to a complicated plaque structure and composition [Vir+00].

A thrombus can also arise from a mere erosion of the most luminal part of the cap [Vir+00]. Plaque erosion is defined as occurrence of a thrombus without signs of rupture [Vir+00]. The term "erosion" is used since typically large parts of the endothelial layer are absent, a situation not observed in

[1] A thickness less than 65 µm is commonly used to define thin, unstable plaque, e.g. in [Vir+00], but this number has recently come under scrutiny [CW14]. Under exertion, rupture has been observed in caps with thickness up to 160 µm [CW14].

advanced plaques without thrombosis [Vir+00]. Plaque erosion occurs in about 40% of cases of sudden coronary death [Vir+00], but "the mechanisms leading to thrombus without rupture is one of the most important unresolved questions within atherosclerosis research" [Ben+14].

To quantify the previous statements, it was found in [Dav92] that 19% of subjects with sudden coronary death had only a stenosis of $> 75\%$ cross-sectional area (or $> 50\%$ diameter), while 8% had fissures and the remaining 73% had a thrombus. A rupture was the origin of the thrombus in 65% of the cases in another study [Vir+00]. Ruptured plaques are on average large [Ben+14], but the severity of stenosis leading to clinical events is still disputed [Nic+13] due to rapid changes in plaque prior to clinical events, difficulties and discrepancies in determining a reference state [FS96; Nic+13].

Mechanisms of Plaque Growth, Stenosis, Remodelling

It is necessary to distinguish growth of the plaque and the resulting stenosis, where we use the term plaque in this context also for the initial stages. Not only because plaque can grow by replacement or alteration of healthy tissue without overall increase in size, but also because arteries can compensate plaque growth through arterial remodeling.

Arterial remodelling is an adaption of vessel size over weeks to months [Dav95], controlled by the endothelium, to maintain normal blood flow characteristics such as wall shear stress, see [War+00] also for the remainder of this paragraph. Outward arterial remodelling can compensate plaque growth and thus postpone the development of a flow-limiting stenosis. The extend of remodelling varies locally, hypothesized due to variability of endothelial response, local flow characteristics and wall composition. Plaques with large soft lipid core, i.e. those prone to rupture, exhibit more outward remodeling than those which are fibrous and calcified. The latter plaque type can even experience inward remodeling, which reinforces the stenosis, a phenomena which can also occur during healing from a thrombus. It is uncertain whether the association between outward remodeling and rupture-prone plaques is causal, which would make outward remodeling a "double-edged sword" [War+00]. Nonetheless, outward remodeling hides the type of plaque most vulnerable to rupture in angiography, a common imaging technique, and may render them asymptomatic until rupture, preventing detection and treatment.

Up until the formation of a fibric cap, the size of the stenosis is mainly determined by the size of the lipid core [Sta00]. Due to outward expansion by arterial remodelling, these initial stages "will not obstruct the lumen much" [Sta00] and growth is steady. In advanced stages, growth happens by lipid accumulation, smooth muscle cell and collagen increase and healing from thrombosis, while remodeling is impeded by the cap and other structures, which leads to more severe stenosis [Sta+95; Sta00]. The progression of stenosis in advanced plaque can be both steady or occur in sudden bursts [Yok+99], where the latter is associated with the healing of thrombi [Sta00].

Arterial remodeling necessitates a distinction between stenosis relative to the pre-disease state, which is in practise hard to determine [War+00], and stenosis relative to the remodeled artery, taking some feature as reference for a hypothetical cross-sectional area without plaque [War+00]. Further ambiguity arises since stenosis can be measured in terms of area or diameter of arteries

[War+00; Gla+87], where the latter is ill-defined for non-circular arteries or non-uniform stenosis. One seminal result about the influence of remodeling on atherosclerosis states that coronary arteries can compensate up to 40% of stenosis, measured in terms of the area relative to the remodeled artery [Gla+87].

Biomechanics in Atherosclerosis

Although a direct correlation between sites of low and oscillatory wall shear stress and predisposition for atherosclerosis is "less robust than commonly assumed" [PSW13], blood dynamics influences normal endothelial function and atherosclerosis threefold: First, endothelial cells sense mechanical forces to control endothelial function [Dav95]. Second, blood flow indirectly controls the concentration of chemical substances and blood particles in the vicinity of the wall through advection and diffusion, e.g. by increasing residence times near flow stagnation points [Dav95]. Third, mechanical stress on the plaque plays a central role in plaque rupture [CW14].

Exposed to laminar flow over multiple hours, endothelial cells align and elongate in the direction of mean directional shear stress, otherwise they have an polygonal structure without preferred orientation [Dav95]. Realignment is driven by the cell's exoskeleton and also affects surface and interior topography [Dav95]. Naturally, variations in shear stress at a sub-cellular level, where force transmission and transduction from the surface to the interior takes place, should be taken into account [Dav95]. The effect of the blood flow on the endothelial behavior depend on magnitude, but also on spatial and temporal variations of shear stresses with adaption and filtering to counter overstimulation [Dav95]. The reaction time to changing flow varies from seconds, e.g. for vasodilation which is an immediate change of arterial geometry through muscle relaxation, to hours, e.g. for endothelial cell realignment, or weeks to months for arterial remodelling [Dav95, Tables 1 and 2].

Specifically, endothelial permeability increases under cyclic shear stresses, but decreases with increasing shear stresses through changes in cell junctions functionality [VV07]. Shear stresses can also modify rates of proliferation and apoptosis of endothelial cells, influence oxidative processes, alter smooth muscle cell function, promote immune cell migration and expression of adhesion molecules, although many of these relationships have been observed only in-vitro or ex-vivo [VV07].

In atherosclerosis, these mechanisms are affected by changing flow patterns due to stenosis. Furthermore, advanced stages of atherosclerosis lead to irreversible changes in the artery's structure, thus altering the mechanical properties of the wall [Sta+95]. For example, lipid accumulation weakens the wall through the displacement of muscle cells normally occupying the region and the wall structure is disrupted by newly forming microvessels [Sta99]. The fibric cap, a mechanical protection of the lipid core, can destabilize due to the infiltration by macrophages [Len+91], or can eroded from below by expansion of the lipid core, which lacks support structures to reduce stress on the cap [Ben+14].

Biomechanics plays a central role in plaque rupture. There appears to be a "general agreement that the threshold stress for rupture is 300 kPa" [CW14]. But the previous effects are insufficient to reach such a peak stress in caps of

thickness $< 100\,\mu m$ which have been found to be prone to rupture, in particular for cases of rupture at the cap center instead of shoulders, where around 40% of plaque ruptures occur [CW14]. Multiple mechanisms have been proposed to explain this mismatch, including local stress peaks due to microscopic calcified particles in the cap [CW14] and rupture as response to fatigue [VBD06].

2.2 Mathematical Models for Atherosclerosis

The complexity of atherosclerosis implies that mathematical models necessarily simplify. We focus our review on contemporary models of atherosclerosis which examine both biochemical and biomechanical processes on an artery scale, in contrast to those e.g. investigating cellular signalling pathways. Other reviews for mathematical models of atherosclerosis can be found in e.g. [AN19; Par+16]. Models range in complexity from ordinary differential equations with one to 89 variables [Zoh05; Par+19], to systems of more than a dozen coupled partial differential equations [HF14; CPM14; FH15]. Biomechanical models may include the blood flow in the lumen and through pores of the wall, the (poro-)elastic response of the wall and their fluid-structure interaction. Through transport or changes in endothelial permeability, these biomechanical processes directly influence biochemistry, the accumulation of material and the resulting stenosis in turn affects biomechanics. Biochemical models may include LDL transport in blood and wall, LDL oxidation, uptake of LDL by macrophages, foam cell accumulation and muscle cell migration in the wall. Wall-free models investigate only processes in the lumen, correspondingly lumen-free models only those in the wall.

The realization of a model requires knowledge of parameter values, boundary data, geometries and further measurements for validation. While many parameters are known from experiments, extensive parameter lists can be found for example in [HF14; Par+19], others must be determined through calibration with experimental data from simplified submodels [CSM02; Tho+18], electrical analogies [Pro+05; OKP08] or from microscopic quantities through multiscale arguments using pore models in the endothelium or fiber matrix models for the intima or adventitia [KPZ01; AV06; CV12; CV13]. Due to patient-specific variations and the uncertainty of data acquisition in-vivo, ex-vivo or in-vitro respectively, the sensitivity of models with respect to parameter variations is important to assess [Pro+05]. Computations using patient-specific geometries have become more common in the last two decades [Tan+05; Yan+07; Tan+09; Lea+10; Sio+11; Ten+10; Fil+13; Di +15] using various imaging techniques [AFM17]. Ideally, these should be accompanied by patient-specific boundary data for hemodynamics and mass transport to capture variations due to age, life-style or diseases [AN19]. For wall mechanics a zero-stress states must be determined to account for pre-existing stresses in the geometry at the time of measurement [Hua+09]. Elastography can be used in-vivo to measure elastic strains to determine elastic moduli of the tissue through inverse problems [Oha+14]. Little patient-specific data is available to track progression over longer times, e.g. scans spanning one year used in [Fil+13] or a study of the relation between wall shear stress and plaque growth in [Gib+93] over three years. For sudden events, data is typically only available after clinical manifestations, making e.g. both pre- and post-rupture scans of plaque sparse, necessitating

the manual restoration of post-rupture geometries [Lea+10]. The overview in [AN19, Table 13] shows that most models are validated qualitatively, if at all, with few works striving for quantitative agreement with experimental data [Tho+18].

The following sections review models for different processes involved in atherosclerosis. This facilitates a comparison between models at the cost of a compact presentation of each individual model. We later focus on the influence of wall shear stress, mechanisms of growth and handling of the multiscale-in-time nature of the problem.

Biomechanics of Blood and Wall

Blood, as a suspension of particles in plasma, can be approximated as an incompressible fluid with either Newtonian or non-Newtonian rheology using the Navier–Stokes equation. Denoting by Ω_f the fluid domain, i.e. the lumen, this means that fluid velocity $v_f \colon \Omega_f \to \mathbb{R}^d$ and pressure $p_f \colon \Omega_f \to \mathbb{R}$ satisfy

$$\rho(\partial_t v_f + (v_f \cdot \nabla) v_f) - \operatorname{div} \sigma_f(v_f, p_f) = \rho f, \quad \operatorname{div} v_f = 0 \quad \text{in } \Omega_f$$

with density ρ, forcing f and stress tensor σ depending on the rheology, e.g. $\sigma_f(v_f, p_f) = \mu(\nabla v_f + (\nabla v_f)^\intercal) - p_f \,\mathrm{I}$ with constant dynamic viscosity μ for a Newtonian fluid. Important for many models reviewed later on and central for the first model examined in this thesis is the wall shear stress, defined by

$$\sigma_{\mathrm{WS}} := (\mathrm{I} - \mathfrak{n} \otimes \mathfrak{n}) \sigma_f \mathfrak{n}$$

on the wall section of the boundary $\partial\Omega_f$, i.e. the wall shear stress are the tangential components of the normal stress on the wall. While Newtonian behavior is a good approximation for high-velocity, laminar blood flow, only qualitative agreement for the wall shear stress was found between Newtonian and non-Newtonian models in [SNH17] for unsteady flow in a patient-specific geometry with significant quantitative differences in magnitude and oscillation in regions of stenosis. These effects persist for fluid-structure interaction [Yan+07; HL10; JMS10]. There is no consensus on the modelling of non-Newtonian blood rheology, used models include Quemada [SNH17], Casson [SNH17], Carreau [Yan+07; HL10; JMS10] and Yeleswarapu [HL10] approximations of blood rheology. A discussion, comparison and further references of rheological models for blood can be found in [Joh+04; AV05; Gal+08; FQV09]. The effect of blood rheology in the lumen on LDL concentrations has been investigated in [Nem+12; Ias+16] under steady flow conditions, where [Ias+16] employed a multi-layer wall model and found no significant effect of the blood rheology on LDL concentrations in a bifurcating artery, whereas [Nem+12] used a wall-free model and found that differences were significant at flow separation and reattachment points in a stenosed artery. Neither model examines secondary effects of blood flow, like the influence of wall shear stress on LDL permeability.

The artery wall is a highly anisotropic, layered material with porous and elastic properties, see [Hum02; Ogd09], which is affected by the occurrence and composition of atherosclerosis. In the work reviewed here, the wall is modeled as porous, elastic or poroelastic material and the tunicas and plaque structures inside the wall are either resolved explicitly, with sharp interfaces,

e.g. [Pro+05; Lea+10; CV12; CPM14; Fok16], smoothly varying material coefficients, e.g. [Yan+15], or the wall treated as a homogeneous material, e.g. [OKP08]. [Pro+05] argues that multilayer wall models are necessary to "capture the finest details of the physical problem". In porous models, particularly common in studies of transport processes, blood flow inside the wall is also considered and [BQQ09] argues that "neglecting the porosity of the artery wall means to disregard an important feature." Common models for the blood velocity in porous artery walls are variants of the Darcy law [KV08], which is a linear relationship between flow velocity $v_s \colon \Omega_s \to \mathbb{R}^d$ and the gradient of the pressure $p_s \colon \Omega_s \to \mathbb{R}$ in the structure domain Ω_s, which may encompass the intima and other tunicas. For incompressible fluids, Darcy's law reads

$$v_s = -\frac{K}{\mu}\nabla p_s, \quad \operatorname{div} v_s = 0 \quad \text{in } \Omega_s$$

with permeability K and viscosity μ. The Darcy law is used in e.g. [KPZ01; Sun+06; OKP08; Pro+05; DDP11; Sio+11; Fil+13; CPM14; HF14; FH15]. Variants include the Darcy–Brinkman law which incorporates viscous effects, used in e.g. [SE02; AV06; CV12; CV13; RNF18], or nonlinear power-law models as approximation of non-Newtonian behavior, used in e.g. [Hon+12; DNS15; Ias+16], which have a significant effect on mass transport compared to the linear Darcy law [Hon+12]. The continuity equation $\operatorname{div} v_s = 0$ is modified to accommodate changes in density in [CPM14; HF14; FH15].

In purely elastic models the wall is treated as impenetrable to blood and the interaction between blood flow and elastic wall response is a primary interest [Tan+05; Yan+07; Blu+08; Tan+08; Tan+09; Ten+10; Lea+10; JMS10; Fil+13; FRW16; Yan+15; Yan+17]. The associated equations are rather complex and one example will be given in the presentation of the model by Yang et. al. in the section below. Mathematical and numerical introductions to such fluid-structure interaction problems can be found specifically for biomechanics in e.g. [QF04; HM07; Gal+08] and more generally in [Ric17]. Bulk models for the elastic wall include linear Saint Venant-Kirchhoff models [BQQ09; JMS10; FRW16; Buk+15], Mooney–Rivlin models [Tan+05; Yan+07; Blu+08; Tan+09; Ten+10], with the special case of neo-Hookean models [Yan+15; Yan+17] and more specialized Demiray-type models [Lea+10]. Anisotropic material models and cyclic bending of coronary arteries due to their attachment to the moving heart were found to have a significant effect on wall stresses, but only moderate effects on the fluid velocity and shear stresses in [Tan+09]. Poroelastic models incorporate both porosity and elastic properties of the wall. While some authors model these effects as independent [CV12; Hon+12], the interaction between porosity and elasticity is captured more accurately by the Biot equations, see [BQQ09; Buk+15] and the references therein. [Buk+15] concludes that intramural flow has a significant effect on wall displacement but a fully coupled poroelastic model may not be necessary to achieve this.

The endothelium, of significant importance for atherosclerosis, is treated as a lower-dimensional interface between lumen and wall in a majority of the reviewed work, whereas a bulk description is used in [AV06; CV12; CV13] albeit its single-cell thickness. In fluid-structure interaction with a purely elastic wall, continuity of velocities and mechanical stresses are prescribed across the endothelium. Separate shell or string models for the mechanics of the endothelium itself are uncommon [HL10; Buk+15]. In porous wall models the coupling

between blood flows is more complex, both due to mismatches in number of unknowns between the domains and osmotic effects if the endothelium is considered as a semi-permeable membrane. In models with (Navier–)Stokes–Darcy coupling, the blood velocity in normal direction, denoted by J_v, is assumed to be continuous and satisfies the following relation, which is known in special cases as Starling's law [Tar03] but also as the first Kedem–Katchalsky equation [PPZ09][2]

$$J_v = L_p(\delta p - \sigma_d \delta\pi), \quad \delta\pi := RT\delta c \tag{2.1}$$

where L_p is the hydraulic conductivity, δp the pressure difference across the interface, σ_d the reflection coefficient, $\delta\pi$ the osmotic pressure determined by Van't Hoff's formula with gas constant R, absolute temperature T and (LDL) concentration difference δc. The coupling of J_v to the osmotic pressure is often omitted for simplicity [Pro+05; Sun+06; OKP08; PPZ09; Sio+11; Fil+13] since this decouples the fluid from the concentration equations, circumventing the resolution of their nonlinear coupling numerically [KPZ01]. Equation (2.1) can be supplemented with no-slip conditions in tangential direction for the luminal fluid, as done in [Sun+06; PPZ09; CPM14], but this is "not completely satisfactory for a permeable interface" [DQ09]. Various other tangential coupling conditions have been proposed and analyzed, most famously by Beavers and Joseph who suggested a linear relation between the wall shear stress of luminal fluid and the drop of tangential velocity across the interface

$$\sigma_{\mathrm{WS}} \propto (\mathrm{I} - \mathfrak{n} \otimes \mathfrak{n})(v_f - v_s),$$

we refer to [DQ09] for an extensive discussion. In [SE02; AV06; CV12; CV13] the (Navier–)Stokes equation in the lumen is coupled to a Darcy–Brinkman law in the wall using continuity of velocities and stresses without examining osmotic effects.

Exterior boundary conditions for fluids include Dirichlet inflow, do-nothing outflow, no-slip (see e.g. [Yan+15]) and pressure drop conditions (see e.g. [Yan+07]). Since only a section of the cardiovascular system is studied, fixed boundary conditions might be inadequate replacements for the rest of the circulation. Lumped low dimensional boundary dynamics have been proposed as substitution for the rest of the circulation, such as Windkessel models, see e.g. [Arb+16] and the references therein, but such an approach is not employed in any reviewed model. For the deformation zero-stress boundary conditions are typically employed for simplicity, e.g. in [Yan+07; Tan+08; Tan+09; JMS10], whereas the geometry was fixed in [Yan+15; FRW16]. Even if patient-specific boundary conditions were available, long-time simulations face the difficulty of predicting the evolution of these boundary conditions due to adaption of the cardiovascular system to plaque growth, a point touched upon in [FRW16] where the inflow velocity was ad-hoc coupled to the channel's radius.

Dynamics of Substances

Many substances involved in atherosclerosis are modelled using advection-diffusion-reaction equations, which are discussed in this section abstractly. The

[2] The second Kedem–Katchalsky equation describes solute flux and is formulated in the appropriate section below.

evolution of the i-th substance for $i = 1, \dots, n$ and $n \in \mathbb{N}$ is then governed by the equation

$$\partial_t c^i - \operatorname{div}(D^i \nabla c^i + w^i c^i) = f^i \quad \text{in } \Omega' \in \{\Omega_f, \Omega_s\} \tag{2.2}$$

for $i = 1, \dots, n$ with diffusivity D^i, advection velocity w^i and low-order term f^i, all possibly depending on $c := (c^1, \dots, c^n)$. The stationary variant of eq. (2.2) is often employed, both for simplicity or to account for the fastness of some process compared to others, a heuristic temporal multiscale argument discussed in the section Multiscale Analysis on page 30 below. Even in models investigating both lumen and wall, a substance may only be defined in one region [CPM14]. In multilayer models eq. (2.2) holds in the interior of each tunica and in some models even inside the endothelium and the elastic layer between intima and media [AV06; CV12; CV13], in which case Ω_s is the union of disjoint domains.

The diffusivity D^i is isotropic in all studied models and typically only depends on the domain. An exception is [Yan+15] where macrophage diffusion depends on foam cell concentrations to account for changing wall properties, such that $D^i = D^i(c)$ and eq. (2.2) is quasi-linear. In [Cal+09; Sil+13; CPM14; Yan+15] the diffusion of foam cells is assumed to be negligible such that $D^i := 0$ and eq. (2.2) is a hyperbolic advection-reaction equation.

Inside the lumen the advection field w^i is the blood velocity, $w^i := v_f$. Inside the wall, w^i may account for movements of the geometry due to growth or elastic response, advection by the blood flow and by chemotaxis, i.e. the movement along gradients of signalling species. Due to friction, the advection velocity by blood in the permeable wall is often reduced, e.g. [PPZ09; CV13]. In [CPM14] it is argued that monocytes are so large that advection by blood can be neglected altogether. Chemotaxis is used in [McK+05; Ibr+05; HF14; FH15] for the movement of monocytes, macrophages, T-cells and smooth muscle cells along (normalized) gradients of other species. Mathematically, this implies $w^i = w^i(\nabla c)$ and eq. (2.2) can be seen as a Keller–Segel type system.

The low-order term f^i can model sources and sinks to account for unresolved external processes, but commonly also depends on c to model various reactive processes, e.g. monocytes maturing into macrophages or LDL consumption by macrophages.

For substances defined in both lumen and wall, coupling conditions between the domains are necessary. It is assumed that the interface acts as a semi-permeable membrane for the species c^i, where the solute flux

$$J_s^i := (D^i \nabla c^i + w^i c^i) \cdot \mathfrak{n}$$

is assumed to be continuous across the interface and to satisfy the second Kedem–Katchalsky equation [KK58]

$$J_s^i = \mathcal{P}^i \delta c^i + J_v (1 - \sigma_f^i) \bar{c}^i \tag{2.3}$$

with permeability $\mathcal{P}$, concentration difference $\delta c^i = c_1^i - c_2^i$ across the interface, normal velocity flux J_v from eq. (2.1), reflection coefficient $0 \le \sigma_f^i \le 1$ modelling a sieving of molecules at the interface and average concentration $\bar{c}^i = \bar{c}^i(c_1^i, c_2^i)$ inside the membrane. The determination of $\bar{c}^i$ is "delicate" [PPZ09]. Based on thermodynamical considerations, [KK58] proposed

$$\bar{c}^i := \frac{c_1^i - c_2^i}{\ln(c_1^i) - \ln(c_2^i)} \approx \frac{c_1^i + c_2^i}{2} \tag{2.4}$$

where the approximation holds if $c_1^i \approx c_2^i$. In [PGH63] $\overline{c}^i$ is instead chosen as the average over the solution of a one-dimensional advection-diffusion problem across the endothelium, leading to [PPZ09]

$$\overline{c}^i := \left(\frac{\exp(\mathrm{Pe}^i)}{\exp(\mathrm{Pe}^i) - 1} - \frac{1}{\mathrm{Pe}^i} \right) c_1^i + \left(\frac{1}{\mathrm{Pe}^i} - \frac{1}{\exp(\mathrm{Pe}^i) - 1} \right) c_2^i, \tag{2.5}$$

with Péclet number

$$\mathrm{Pe}^i = \frac{L_p(1 - \sigma_f^i)(p_1 - p_2)l}{\mathcal{P}^i}$$

of the one-dimensional problem with interface thickness l. This choice of $\overline{c}^i$ would introduce additional nonlinearities, but for simplicity a constant approximation of Pe^i is usually employed. The equation for solute flux J_s^i with $\overline{c}^i$ as in eq. (2.5) is also known as Patlak equation [DSB08] and is employed in e.g. [OKP08; DDP11; CPM14]. A more in-depth discussion of the transport laws can be found in [Tar03; DSB08; PPZ09; LM10].

The permeability $\mathcal{P}^i$ may depend on the wall shear stress for LDL and monocyte transport across the endothelium. Some models for LDL transport also investigate different pathways for LDL transport across the interface, employing the Kedem–Katchalsky equation for each pathway and then adding the resulting fluxes. The exact mechanisms of endothelial transport depend on the substance, which is unsurprising given that e.g. monocytes have a size comparable to endothelial cells (16 µm to 22 µm diameter), which is orders of magnitude larger than LDL (22 nm to 27 nm diameter). The specific mechanisms and models, in particular relations between wall shear stress and permeability, are discussed in the corresponding sections below.

A simplified version of the second Kedem–Katchalsky eq. (2.3) is

$$J_s^i = \mathcal{P}^i \, \delta c^i \tag{2.6}$$

which arises from eq. (2.3) by formally setting $J_v := 0$ or $\sigma_f^i := 1$. Such a coupling condition is proposed in [McK+05] for LDL and in [Yan+15] for monocyte flux since no blood flow is studied inside the wall. The coupling condition from eq. (2.6) with wall-shear stress dependent permeability $\mathcal{P}^i$ was also examined in an abstract framework for mass transfer in [RPP97; QVZ02b] with oxygen transport as an example. Equation (2.6) also arises in the study of the Neumann sieve problem, which investigates the limit of a pure diffusion problem with a perforated interface as the size of perforations approaches zero, see [Cio+08, Section 5] and the references therein.

Standard Dirichlet and Neumann conditions are typically employed on exterior boundaries. Other boundary conditions are discussed below, e.g. the lumen-free model [HF14] uses the Kedem–Katchalsky eq. (2.6) for various substances with fixed lumen concentration, leading to Robin-type boundary conditions.

LDL and HDL

The uptake of oxidized LDL or otherwise modified LDL by macrophages is a central feature of atherosclerosis, and thus LDL a central component of most disease models. Spatial models for LDL concentrations employ the advection-diffusion-reaction eq. (2.2) with advection due to the blood flow or movements

due to plaque growth, although the latter effect is omitted in some models [Sio+11; Fil+13; HF14] but not others [Cal+09; DDP11; Sil+13; CPM14]. The following sections describe transport across the endothelium in fluid-wall models for LDL, in particular the influence of wall shear stress on this process, oxidation models, reverse cholesterol transport and other consequences in the presence of HDL.

Transport of LDL across the Endothelium

The transport of LDL across the endothelium is the focus of many works, being the sole process modelled e.g. in [Pro+05; Sun+06; AV06; OKP08; CV12; CV13]. For models with a permeable wall, the Kedem–Katchalsky equation is usually employed [Pro+05; Sun+06; AV06; OKP08; Ges+11; Sio+11; DDP11; CV12; CV13; Fil+13; CPM14]. Since the following discussion only involves the LDL concentration c^i we drop the superscript i for simplicity. The Kedem–Katchalsky equations, eqs. (2.1) and (2.3) are then

$$J_v = L_p(\delta p - \sigma_d \delta\pi), \quad J_s = \mathcal{P}\delta c + J_v(1-\sigma_f)\bar{c} \tag{2.7}$$

with the average concentration $\bar{c}$ as in eq. (2.4) or eq. (2.5). As noted in the section above, the osmotic pressure $\delta\pi$ in the velocity flux is often omitted for simplicity. In e.g. [OKP08; DDP11; CPM14] it is also argued that the concentration of LDL inside the lumen is so small that it can be neglected in the concentration jump δc in eq. (2.7).

Transport across the endothelium happens over three pathways [Tar03]: Normal endothelial junctions (found between healthy endothelial cells), leaky junctions (larger paths which open up during endothelial cell division or death) and vesicular pathways (transport through the cells using small vesicles). Not every transport process uses every pathway: volume flux does not occur over vesicular pathways and LDL is too large to fit through normal endothelial junctions. This is reflected in the model proposed in [OKP08] which is also used in [DDP11; CPM14]. There, the different pathways are realized by additive composition of velocity and solute fluxes,

$$J_v = J_{v,nj} + J_{v,lj}, \quad J_s = J_{s,lj} + J_{s,v},$$

where the subscripts denote contributions from normal junctions (nj), leaky junctions (lj), and vesicular pathways (v). For every pathway, the Kedem–Katchalsky eq. (2.7) are employed with $\bar{c}$ as in the Patlak variant from eq. (2.5), setting formally $J_{v,v} := 0$ and ignoring osmotic effects. Making the a priori assumption that the LDL concentration inside the wall is much smaller than the concentration in the lumen, the corresponding term in the concentration jump δc is omitted in [OKP08]. The distinction of pathways allows for a specific modelling of the relation between wall shear stress and endothelial permeability as follows. The permeability of leaky junctions $\mathcal{P}_{lj}$ was modelled in [OKP08] as

$$\mathcal{P}_{lj} = a_1 + a_2 \exp(a_3 \exp(-b_1|\sigma_{\mathrm{WS}}|) + a_4 \exp(-b_2|\sigma_{\mathrm{WS}}|))$$

with constants $a_1, \dots, a_4, b_1, b_2 > 0$ determined from pore theory and experimental data which linked the fraction of leaky junctions to the amount of mitotic cells, the amount of mitotic cells to the cell shape and the cell shape to the wall shear stress. A relation between mechanical stresses and permeability

is proposed in [CV12] and used e.g. in [DNS15]. This model again uses pore theory but while the fraction of leaky junctions is now assumed constant, the width of these junctions depends on the strain inside the elastic wall. This effect alone leads to an increase of permeability with increasing mechanical forces, contradicting other observations. Since leaky junctions are also a pathway for blood itself, both the permeability models in [OKP08] and [CV12] should create nonlinear couplings on the boundary for the fluid equation, but this is not discussed.

A more direct relation between permeability and wall shear stress was used in [Ges+11; Gab+14] based on the experiment in [Him+04]. Observing the circulation of a stained substance (albumin) in the blood, [Him+04] found that measured optical density OD of the wall, indicating wall penetration, could be related to time-averaged wall shear stress $\overline{\sigma_{\mathrm{WS}}}$ by $\mathrm{OD} \propto \overline{\sigma_{\mathrm{WS}}}^{-\gamma}$ with constant $\gamma > 0$. Under the assumption that optical density is proportional to permeability [Him+04], an analogous power-law relation between σ_{WS} and $\mathcal{P}$ was used for LDL transport in [Ges+11; Gab+14]:

$$\mathcal{P} := \mathcal{P}_0 |\sigma_{\mathrm{WS}}|^{-\gamma}$$

with constant $\mathcal{P}_0 > 0$ and the same power γ from the optical density relation. Yet another permeability relation is proposed in [Fil+13], given by

$$\mathcal{P} := a_0 \log(1 + a_1/(|\sigma_{\mathrm{WS}}| + a_2))$$

with parameters a_0, a_1 and a_2 whose value and origin is not elaborated. A simpler approach to LDL transport is investigated in [Cal+09] and its extension [Sil+13], where neither blood in the wall nor LDL in the lumen is examined. They prescribe a flux of (immediately oxidized) LDL on the endothelium into the wall by

$$J_s = \mathcal{P}\, c_f$$

with fixed LDL concentration c_f in the lumen and wall shear stress dependent permeability function $\mathcal{P}$. In particular, the solute flux does not depend on the concentration difference. In [Cal+09], $\mathcal{P}$ is a "Hill function"

$$\mathcal{P} := \sqrt{\frac{(|\sigma_{\mathrm{WS}}| - (1 + \sigma^0_{\mathrm{WS}}))_+ (1 + 3\sigma^0_{\mathrm{WS}} - |\sigma_{\mathrm{WS}}|)_+}{(\sigma^0_{\mathrm{WS}})^2}}$$

for suitable $\sigma^0_{\mathrm{WS}} > 0$ and [Sil+13] describes $\mathcal{P}$ as "a characteristic function, such that in the area of low wall shear stress we have penetration of LDL, and otherwise we have no penetration" [Sil+13], which could be realized by[3]

$$\mathcal{P} := \mathcal{P}_0 \mathbb{1}_{\{|\sigma_{\mathrm{WS}}| \le \sigma^0_{\mathrm{WS}}\}}$$

with parameter $\mathcal{P}_0$ and a wall shear stress threshold $\sigma^0_{\mathrm{WS}} > 0$.

Yet another influence of wall shear stress is described in [Sun+06], where it is argued that not the permeability but the hydraulic conductivity L_p should depend on σ_{WS}. Fitted to experimental data, the relation reads

$$L_p := a_0 \ln(|\sigma_{\mathrm{WS}}| + a_1) + a_2$$

[3] The equation is the author's guess based on the textual description, no formula is given in [Sil+13].

with parameters $a_0, a_1, a_2 > 0$. In view of eq. (2.7) this relation only indirectly influences LDL transport by changing the velocity field, in particular since the model also omits the osmotic pressure in the equation for J_v.

In conclusion, many relations between wall shear stress and endothelial properties have been proposed for a wide variety of models. Further assessment and comparison of these relations is required.

LDL Oxidation

The oxidation of LDL is an important mechanism in atherosclerosis since it makes LDL susceptible for consumption by macrophages through the scavenger pathways. LDL oxidation is due to the reaction of free radicals with LDL and inhibited in the presence of antioxidants, a process modeled in great detail with multiple stages of oxidation using ordinary differential equations in [CSM02]. Models for LDL oxidation include [McK+05; Ibr+05; Sio+11; CPM14; HF14; FH15], in [Cal+09; DDP11; BD12; Sil+13; Di +15; CBM17] it is assumed that LDL immediately oxidizes inside the intima, at least on the studied timescale. The rate of oxidation is greatly reduced in the lumen, such that all models except for [McK+05] view it a phenomenon in the intima only. In [McK+05; HF14; FH15] the amount of free radicals is assumed to be limited and an independent solution component, whereas a constant amount of free radicals and hence rate of oxidation is used in [Ibr+05; Sio+11; CPM14].

HDL and Reverse Cholesterol Transport

HDL influences the progression of atherosclerosis through multiple mechanisms, for example it reacts with free radicals in the intima and thus removes radicals which otherwise could oxidize LDL. This is realized in [CSM02; McK+05; HF14; FH15] where radical concentrations and oxidation are explicitly modeled. In [CBM17] this mechanism is approximated by HDL-dependent influx of oxidized LDL, but this artificially only depends on HDL boundary concentrations. A second effect of HDL is anti-inflammatory. It inhibits adhesion of monocytes at the endothelium and is realized by an HDL-dependent monocyte influx condition at the endothelium in [CBM17] only. The most prominent effect of HDL is reverse cholesterol transport, in which HDL removes oxidized LDL from foam cells in the intima. This phenomena is examined in [FH15; CBM17], where reverse cholesterol transport is modeled as a regress of foam cells to macrophages in the presence of HDL.

The risk of plaque development in terms of initial LDL and HDL concentrations are investigated in [HF14]. This model was extended in [FH15] to include reverse cholesterol transport and the effect of different drug treatments of animal experiments were reproduces qualitatively, including a regression of stenosis after an increase of reverse cholesterol transport. Reverse cholesterol transport is also the focus in [CBM17], where it was found that HDL is most effective in the earliest stages of the disease. These models strive for qualitative agreement with experimental data, a model which focuses on quantitative results using ordinary differential equations can be found in [Tho+18].

Immune Response

The presence of oxidized LDL leads to the activation of the immune system, the components of which are modelled in widely varying detail. For example, in [Ibr+05; EGV07] all substances involved in the immune response are modelled as a single variable, whereas [HF14; FH15] distinguishes monocytes, macrophages, foam cells, T-cells and multiple chemoattractants and signalling proteins, each modelled by variants of eq. (2.2).

Monocytes are recruited from the lumen and differentiate to macrophages inside the wall. Monocytes inside the lumen are only explicitly modelled in [CPM14; Yan+15; Yan+15], other models study monocytes / macrophages only in the intima even if other parts of the model contain processes inside the lumen, e.g. [McK+05]. The differentiation from monocytes into macrophages is modelled explicitly in [McK+05; BD12; CPM14], whereas [Cal+09; Sil+13; Yan+15; Yan+17] consider monocytes to be immediately differentiated inside the lumen. In [HF14] only the activation of macrophages by the signalling protein interferon IFN-γ, released by T-cells, is investigated. In the extension [FH15] these pro-inflammatory macrophages (M1) are distinguished from anti-inflammatory macrophages (M2) which are the result of reverse cholesterol transport from foam cells.

Macrophages take up oxidized or otherwise modified LDL. If a sufficient amount of lipid is bound, macrophages turn into foam cells [Cal+09; BD12; Sil+13; CPM14; CBM17], which is modelled e.g. in [Sil+13] as a mass action law with rate of conversion from macrophages into foam cells being proportional to macrophage and oxidized LDL concentrations. The model proposed in [Yan+15; Yan+17] does not include LDL and instead assumes that macrophages turn into foam cells at a constant rate. Even simpler is the model in [FRW16] where only foam cells with a direct dependence on the wall shear stress are investigated. Foam cells return to the macrophage stage in [FH15] through reverse cholesterol transport. Instead of foam cells, [McK+05; OTM10] take the amount of lipid bound by macrophages as a measure of lesion size.

T-cells are investigated explicitly only in [HF14; FH15], where they are activated by macrophages in the presence of interleukin-12 which is secreted by macrophages, foam cells and smooth muscle cells.

There is no consensus about which substances are affected by advection, even while accounting for differences due to advection by growth which could be argued to be small. Macrophages are advected in [Cal+09; Sio+11; Fil+13; Sil+13] but not in [DDP11; CPM14]. Foam cells are advected in [Cal+09; Sil+13] but not in [CPM14]. Smooth muscle cells are advected in [HF14] but not in [CPM14]. If explicitly mentioned, the omission of advection is often based on the size of substances, e.g. [CPM14]. Signalling proteins, of varied origin, are not affected by advection in any model [Cal+09; Sio+11; Fil+13; Sil+13; CPM14; HF14].

The diffusion of macrophages is modelled as dependent on foam cell concentration in [Yan+15; Yan+17] due to changes in wall properties due to increased foam cell concentrations. Foam cells diffuse very slowly in [HF14; FH15] and not at all in [Cal+09; Sil+13; CPM14; Yan+15; Yan+17].

Cytokines and Chemotaxis

The recruitment and movement of immune cells is controlled through signalling proteins (cytokines). Chemotactic cytokines (chemokines) can induce chemotaxis, i.e. the advection of one species along the gradient of another, the chemoattractant. Chemotaxis of immune cells is modelled in [McK+05; Ibr+05; HF14; FH15; CBM17] with varying chemoattractants. In [McK+05] monocytes, macrophages, T-cells and smooth muscle cells undergo chemotaxis with a single chemoattractant produced by macrophages, T-cells and smooth muscle cells for simplicity. [Ibr+05] treats oxidized LDL as additional chemoattractant. In [CBM17] macrophages have modified LDL as a sole chemoattractant. A distinction of chemoattractants is made in [HF14; FH15] where macrophages undergo chemotaxis with respect to the monocyte chemoattractant protein (MCP-1), which is produced by endothelial cells under the influence of oxidized LDL. T-cells undergo chemotaxis in [McK+05] but not in [HF14; FH15].

Signalling proteins are also modelled in [Cal+09; Sio+11; Fil+13; Sil+13; CBM17] where they control the recruitment of monocytes at the endothelium instead of inducing chemotaxis. This mechanism is also studied in the chemotaxis models from [Ibr+05; CBM17]. Cytokine production depends on both macrophage and oxidized LDL concentration, but external cytokines are recruited at the intima in [Cal+09; Sil+13] if the oxidized LDL crosses a threshold value, which is modelled as a bulk domain phenomenon in [Sio+11; Fil+13].

The recruitment of immune cells by cytokines is simplified as a source term in [EGV07] depending on cytokine concentrations. Without explicit models for cytokines, the recruitment of immune cells in the presence of oxidized LDL is also approximated by a source term in [CPM14]. The production of cytokines is also investigated in the ordinary differential equation model by [OTM10] as a production rate of macrophages, depending on levels of oxidized LDL and macrophages. A similar approach is used in [BD12] while accounting for the influence of the wall shear stress computed from a Poiseuille flow profile.

Transport of Monocytes across the Endothelium

Monocytes roll along, adhere to and then transmigrate through the endothelium either in the intercellular space or, less frequently, through endothelial cells [GL15]. The transmigration requires active remodeling of monocytes and endothelium [GL15] and multiple processes are influenced by wall shear stress, e.g. the expression of adhesion molecules such as ICAM-1 and VCAM-1 [WH10].

The process of adhesion is explicitly, but still phenomenologically, only treated in the ordinary differential equation model [ZHB04], where a balance equation is solved to determine the velocity below which monocytes are likely to become arrested at the endothelium. This critical velocity is compared to the actual advection velocity of the monocytes, which can be directly computed from the Poiseuille-type flow profile in this model but is also closely related to the wall shear stress.

In spatial models, monocytes in the lumen are only explicitly modelled in [CPM14; Yan+15; Yan+17]. We denote quantities related to monocytes with a superscript “m”, e.g. use c^{m} for the monocyte concentration and J_s^{m} for the

monocyte flux across the endothelium. In [Yan+15; Yan+17] the coupling condition eq. (2.6), i.e.

$$J_s^{\mathrm{m}} := \mathcal{P}^{\mathrm{m}}\, \delta c^{\mathrm{m}},$$

is used for monocyte flux where $\mathcal{P}^{\mathrm{m}}$ is a fixed function on the interface modelling a damaged portion of the endothelium. Instead of the concentration difference, [CPM14] uses only the lumen monocyte concentration. Emulating the activation of cytokines in the presence of oxidized LDL with a dependence on wall shear stress, they model the monocyte flux J_s^{m} as

$$J_s^{\mathrm{m}} = \mathcal{P}^{\mathrm{m}}\, c_f^{\mathrm{m}}, \quad \mathcal{P}^{\mathrm{m}} := \mathcal{P}_0 \frac{c_s^{\mathrm{ox}}}{1 + |\sigma_{\mathrm{WS}}|/\sigma_{\mathrm{WS}}^0}$$

with parameter $\mathcal{P}_0 > 0$, and concentrations c_f^{m} and c_s^{ox} for monocytes in the lumen and oxidized LDL in the wall, respectively. A direct dependence on the oxidized LDL concentration is proposed in the lumen-free model [HF14; FH15] as well, where the monocyte flux J_s^{m} is a boundary condition. Instead of wall shear stress, the anti-inflammatory effect of HDL is considered, yielding

$$\mathcal{P}^{\mathrm{m}} := \mathcal{P}_0 \frac{c_s^{\mathrm{ox}}}{1 + c_s^{\mathrm{h}}}$$

where c_s^{h} denotes the HDL concentration inside the wall. While [McK+05] investigates a constant influx of monocytes, the remaining lumen-free models for monocytes use a dependence on signalling molecules. In [CBM17] both endothelium-stimulating cytokines, which increase adhesion molecule production, and monocyte chemoattractants influence monocyte flux, given by

$$J_s^{\mathrm{m}} = \sigma_{\mathrm{m}} \frac{1 + c_s^{\mathrm{h}}/\alpha_{\mathrm{m}}}{1 + c_s^{\mathrm{h}}/\gamma_{\mathrm{m}}} (1 + A c_s^{\mathrm{q}})(c_s^{\mathrm{p}} - c_f^{\mathrm{p}}) \mathbb{1}_{\{c_s^{\mathrm{p}} \geq c_f^{\mathrm{p}}\}}$$

with parameters $\sigma_{\mathrm{m}}, \alpha_{\mathrm{m}}, \gamma_{\mathrm{m}}, A > 0$ and concentrations c^{q}, c^{p} of endothelium-stimulating cytokines and monocyte chemoattractant respectively, where the concentration c_f^{p} is fixed. A monocyte influx depending on cytokine concentrations is also proposed in [Ibr+05; EGV07; Cal+09; Sil+13] with no influx below a threshold in [Ibr+05; CBM17].

No model except [CPM14] investigates a dependence on wall shear stress. Such a dependence is the single ingredient in the simplified model of [FRW16] for foam cell accumulation, where no monocytes, macrophages or LDL are studied. The foam cell concentration c_s^{f} is spatially constant in [FRW16] and driven by the ordinary differential equation

$$\frac{\mathrm{d}}{\mathrm{d}t} c_s^{\mathrm{f}} = \frac{\gamma_0}{1 + \overline{\sigma_{\mathrm{WS}}}/\overline{\sigma_{\mathrm{WS}}^0}}, \quad \overline{\sigma_{\mathrm{WS}}} := \int_\Gamma |\sigma_{\mathrm{WS}}| \,\mathrm{d}o.$$

with parameter $\gamma_0 > 0$ and reference value $\overline{\sigma_{\mathrm{WS}}^0} > 0$. The focus of this model are changes of geometry due to plaque growth, such that the domain, and in particular the interface Γ, is evolving in time and implicitly depends on c_s^{f}.

All of these monocyte flux relations are phenomenological in nature and the modelling of monocytes crossing the endothelium has received less attention than the related question for LDL, with the need for more experimental data. Sensitivity analysis of the parameters were performed in [HF14] and a bifurcation analysis in [CBM17]. The parameter used in [CPM14] were calibrated from experimental data, whereas e.g. [Ibr+05] chose parameter values ad-hoc.

Plaque Cap Formation and Plaque Growth

Smooth Muscle Cells and PDGF

Central to fibrous cap formation is the migration and proliferation of smooth muscle cells. [CPM14] distinguishes between contractile and synthetic smooth muscle cells, with the latter responsible for the synthesis of extracellular matrix. The conversion from contractile to synthetic type is regulated by a cytokine secreted by macrophages in the presence of oxidized LDL. Modelled using eq. (2.2) with no or small diffusion, e.g. [CPM14; HF14], smooth muscle cells undergo chemotaxis in [McK+05; Ibr+05; Fok12b; HF14; FH15; Wat+18; Wat+20]. A generic chemoattractant is employed in [McK+05; Ibr+05], attraction to (generic) immune cells in [Ibr+05], while [HF14; FH15] study more explicitly attraction to MCP-1, produced by endothelial cells, to the extracellular matrix and to the platelet-derived growth factor (PDGF).

Smooth muscle cells originate only from the media and thus zero flux conditions are used at the endothelium. The inflow of smooth muscle cells from the media into the intima is controlled by the chemoattractant in [Ibr+05], with no influx for chemoattractants below a threshold value. While [McK+05] proposes a coupling of muscle cell influx to the rate of deformation of the internal elastic lamina, a layer separating intima from media, no specifics are given. Robin boundary conditions are used in [HF14; FH15] with fixed muscle cell concentration in the media. In [Wat+20] only the influx of muscle cells by chemotaxis driven by PDGF is investigated. The model in [CPM14] studies neither advective nor diffusive effects on both types of muscle cells, leading to (spatially varying) ordinary differential equations with reaction and source terms, which consequently allow no boundary conditions.

PDGF is a "potent stimulator of both SMC [smooth muscle cell] migration and mitosis [cell division]" [Wat+18] and is employed as sole chemoattractant for smooth muscle cells in [Fok12b; Wat+18; Wat+20]. In [Fok12b; Wat+18; Wat+20] the source of PDGF are platelets at injured regions of the endothelium, realized as Dirichlet boundary conditions in [Fok12b] and Neumann boundary conditions in [Wat+18; Wat+20]. Despite its name, PDGF not only originates from endothelial cells and adherent platelets but is also assumed to be produced by macrophages, foam cells and smooth muscle cells in the intima. This mechanism is the only source of PDGF in [HF14; FH15] where zero flux conditions for the growth factor at the endothelium are used, contrasting the models [Fok12b; Wat+18; Wat+20].

The interaction between PDGF and smooth muscle cells is a central component in the model [Fok12b] for plaque growth and in the two- and three-phase models [Wat+18; Wat+20] for fibrous cap formation where smooth muscle cells are treated as a single phase and only PDGF as chemoattractant since it "is likely to be the dominant chemoattractant in fibrous cap formation" [Wat+18].

Extracellular Matrix and Necrotic Core

The extracellular matrix (ECM) and its degradation by matrix metalloproteinase (MMP) is modelled in [HF14; FH15] and incorporated into plaque growth. The main structural protein of the ECM is collagen, which is studied instead of ECM in [McK+05; CPM14]. Collagen is there modelled as immobile, produced by (synthetic) smooth muscle cells and degraded by T-cells and

macrophages in [McK+05], whereas in [CPM14] degradation is constant. The model for smooth muscle cells and PDGF from [Wat+18] is extended significantly in [Wat+20], where the extracellular matrix is included as another phase which, among other things, inhibits the movement of smooth muscle cells. This extension also models the transforming growth factor TGF-β which regulates collagen production by smooth muscle cells.

Many models feature death or degradation of substances, e.g. [McK+05; Ibr+05; Fok12a; CPM14; HF14; FH15; CBM17], but explicit models for the evolution, including removal, of debris or the formation of a necrotic core are rare. The necrotic core is modelled in [McK+05] as the remainder of degradation of macrophages and their bound lipid, smooth muscle cells and T-cells, but the necrotic core has no influence on other processes. Debris is modelled in [Ibr+05] as degradation of immune cells and smooth muscle cells with a further, unspecified, nonlinear relation between debris production or removal based on the concentration of oxidized LDL. The modelling of the necrotic core is the focus of [Fok12a], where the interplay between macrophage death rate and local available oxygen is investigated as central mechanism for necrotic core growth, with the assumption that the plaque is deplete of oxygen (hypoxic). The oxygen is there modelled as separate variable with degeneration and consumption by macrophages. Another phenomenological description of the necrotic core is used in [Bel+09] with an ordinary differential equation relating the change in its volume to the mechanical stress exerted on the fibrous cap due to the effect of stress on cytokine production.

Realization of Plaque Growth

Atherosclerotic plaque grows due to the accumulation of material, the migration and proliferation of cells in the process of the disease, in particular smooth muscle cells forming the fibrous cap. While growth can be understood as a mere replacement of normal wall material with components of atherosclerotic plaque, like the expansion of a necrotic core inside the wall [Fok12a], we focus on growth which influences the wall geometry. Wall remodelling is explicitly studied in [Bel+09; Isl17; Fok16], but not in any of the other models concerned with plaque growth. Sudden bursts of material accumulation during thrombus healing in the late stages of the disease are not investigated in any model. In particular, growth is modelled as a steady, slow process.

The growth of biological material is a complex subject in itself, see e.g. [JC12]. The reviewed models are phenomenological and based on the principle of volume increase due to the accumulation of material. Materials which are used as source for growth include LDL [Ges+11; BD12; Gab+14], monocytes/macrophages [ZHB04; BD12; HF14; FH15], foam cells [Sio+11; BD12; CPM14; HF14; FH15; Yan+15; Yan+17; FRW16; DDP11; Di +15][4], smooth muscle cells [Fok12b; CPM14; HF14; FH15], collagen or ECM [CPM14; HF14; FH15] and T-cells [HF14; FH15]. In [Zoh05; LT10] a direct relation between wall shear stress and growth rate are used. Biologically, foam cells and formation of a necrotic core are responsible for growth in early stages, whereas smooth muscle cells and the extracellular matrix are additional sources of growth in

[4]The realization of plaque growth is not elaborated in [DDP11; Di +15] but a formula depending on the foam cell volume is given in the review [AN19, Table 12].

advanced stages of the disease. Some of these relations must be seen as simplifications, e.g. LDL influx drives processes leading to growth.

In the ordinary differential equation models [ZHB04; Zoh05; BD12] plaque growth reduces the arterial radius used in the analytical approximation of the blood velocity using Poiseuille-type flow profiles. Growth as decrease of arterial radius was also used in [Fok12b] where smooth muscle cell proliferation due to the platelet-derived growth factor (PDGF) was modeled using a partial differential equations, with growth then coupled by spatial integration to the other variables. The other models use spatially varying growth. In [Cal+09; Sil+13] an unknown height function was used to describe the endothelial surface, with height depending on the integrated material below the surface. A more explicit description of the plaque region was used in [Bel+09; Isl17], where both upper and lower boundaries of the plaque region are prescribed with some parameters and material accumulation leads to two phases of growth, once into the lumen and afterwards into the wall to account for the accumulated plaque volume. More algorithmic approaches to growth were used in [LT10; Ges+11; Gab+14] where local increase of wall thickness are related to the local wall shear stress, derived from simplified transport models [Ges+11; Gab+14] or linear relation between growth and wall shear stress [LT10] derived from experimental data [Gib+93]. A similar model for growth as wall thickness increase was used in [DDP11; Di +15][5]. Using experimental data, [Fil+13] parameter-fitted different models of domain deformation to plaque geometries measured after 3 and 12 months.

The previous models describe growth through the deformation of the endothelial surface. Bulk growth models use a continuum model for the wall deformation inside the wall. The fluid-structure interaction models in [Yan+15; Yan+17; FRW16] use the method of multiple natural configurations [RHM94; AM02; RS04] which leads to a decomposition of the deformation gradient

$$\mathrm{I} + \nabla u =: F \stackrel{!}{=} F_e F_g \tag{2.8}$$

into elastic response F_e and growth tensor F_g. In both models, growth is treated as isotropic: $F_g = g\,\mathrm{I}$ with $g \geq 1$ in [Yan+15; Yan+17] being the solution of another differential equation modelling the material accumulation and in [FRW16] being a given bump function weighted with the solution of an ordinary differential equation.

The decomposition eq. (2.8) was also used in [CPM14; Fok16], although [CPM14] only specifies the resulting equation for $\operatorname{div} u$ and not a constitutive equation. In [HF14; FH15], where only the wall is studied, plaque growth is modeled as a Darcy equation with free boundary at the endothelium where $\sigma = \gamma\kappa$ with wall pressure σ, parameter γ and mean curvature κ. Darcy's law is also used by [Sio+11; Fil+13] for the growth velocity. The models [Sio+11; Fil+13; CPM14] distinguish between growth velocity field and blood velocity, although the latter is unspecified in [Sio+11; Fil+13], whereas [HF14; FH15] use a single velocity field. The physical motivation to model growth by Darcy's equation is unclear to the author.

[5] See footnote[4] on page 26.

Plaque Vulnerability and Rupture Prediction

Different models have been proposed to predict the time frame, risk and location of plaque rupture. They focus on complementary mechanisms such as extreme stress [ZHB04; Tan+05; Ten+10; Lea+10], mechanical fatigue [VBD06] and weakening of the tissue [Bel+09; HF14; FH15; Wat+18]. The rupture itself is not modelled and hence the models are valid at most up until rupture. We refer to [AH13; CW14] for an in-depth review of the biomechanics of plaque rupture.

A phenomenological model for plaque rupture with ordinary differential equations was proposed in [ZHB04] where the plaque is assumed to rupture if the wall pressure, computed from a simple kinematic model, exceeds a given threshold value.

The articles [Tan+05; Ten+10; Lea+10] are concerned with the predictive capabilities of models employing fluid-structure interactions in patient-specific geometries to determine plaque vulnerability. These models sudy detailed but fixed geometries with different mechanical properties for the plaque components and based on the observation that "the endothelial damage caused by extreme shear stress is now suspected to contribute to rupture due to both mechanical and biological effects" [Lea+10]. In [Tan+05] the usage of local, instead of global, maxima of wall stress for possible sites of plaque rupture is proposed. A computational plaque vulnerability index based on this stress was examined and found to be in good agreement with a classical vulnerability measurement from manual histopathological observations. [Ten+10] found numerically that wall stress is more closely associated with sites of plaque rupture than the fluid shear stress in 3D fluid-structure interaction problems using in-vivo MRI data. A relation between areas of strongly elevated wall stress and rupture location was also found in [Lea+10] where pre- and post-rupture MRI scans were employed. [Lea+10] also warns that imaging resolution and erroneous feature identification can have a substantial influence on measured stresses.

The maximal stresses reached in such models are less than the amount assumed to be necessary for mechanical failure and they do not occur in shoulder regions of the plaque, where signs of rupture are often found. Multiple explanations of this mismatch have been proposed. In [VBD06] mechanical fatigue, i.e. mechanical failure as response to repetitive loading, was studied using crack propagation models. The evolution of cracks inside the intima, as precursors to rupture, is examined under various geometrical, mechanical and cardiovascular configurations. Another mechanism which may explain this mismatch is the occurrence of microscopic inclusions (microcalcifications) inside the wall. In the numerical model [Blu+08] it was found that microcalcifications in the plaque cap significantly increase the peak stress, whereas others observed more ambiguous effects of calcifications [Hos+09], see [AH13] for further discussion.

The previous models focus on plaque vulnerability and rupture due to mechanical influences. The model [Wat+20] was proposed for plaque cap formation with a multiphase model for the distribution of smooth muscle cells and extracellular matrix. The authors remark that an extensions of this model could also allow insight into the development of vulnerable plaque where the cap degrades, they emphasize the critical role of the growth factor TGF-β for the plaque's stability. In [Bel+09] the degradation of the plaque cap by MMP is the focus using an model consisting of ordinary differential equations for

cap thickness, cap stress, MMP concentration and lipid core volume, based on phenomenological observations e.g. that MMP reduces the cap thickness. The degradation of the ECM by MMP is also examined in [HF14; FH15], but late stages of the disease were not studied there.

Mathematical Analysis

Naturally there is a trade-off between complexity and mathematical tractability of mathematical models. Existence, stability, regularity and other analytical results are restricted to simpler models. For example, the question of existence of solutions to fluid-structure interaction problems employed in many of the reviewed models is still open. This also affects numerical analysis, such as existence of discrete solutions or convergence of numerical algorithms, the latter requiring regularity of the continuous problem.

In [QVZ02b] a two-compartment model of an advection-diffusion equation in the lumen coupled to a diffusion equation in the wall is analyzed. The equations are coupled using eq. (2.6) with permeability $\mathcal{P}$ depending on the wall shear stress. If the blood velocity field, itself solution to the Navier–Stokes equation, is regular enough, existence, uniqueness and stability of solutions is proven. For the numerical implementation of this problem a domain decomposition approach, splitting the domain into lumen and wall, is natural. An analysis of convergence and other properties of these methods is carried out in [QVZ02b; QVZ02a]. The previous analysis is limited to linear problems, nonlinear coupling conditions between advection-diffusion equations inspired by the Kedem–Katchalsky equation with given velocity field were analyzed in [CZ06]. The results in [CZ06] have the caveat that e.g. existence was proven under the condition that one domain is surrounding the other.

The model in [QVZ02b; QVZ02a] only considers a fluid in the lumen and no flow inside the wall. The analysis and numerical realization of the Navier–Stokes–Darcy system is reviewed in [DQ09], including a derivation of tangential interface coupling conditions from homogenization. The coupling of fluid and concentration equations as induced by the Kedem–Katchalsky equations, e.g. including osmotic effects, has not been found. Furthermore, many of the reviewed models with wall shear stress dependent LDL transport feature nonlinearities which have not been investigated.

Some of the models incorporate chemotaxis, we only refer to [Hor03] for an overview of the rich mathematical theory for Keller–Segel systems including effects such as blow-up in finite time. For most species relevant for atherosclerosis, the diffusion inside the blood flow is much smaller than advection, i.e. the Peclét number is large. For processes at the endothelium this leads to the occurrence of boundary layers which are naturally characterized by the wall shear stress [DTW01]. Boundary layer analysis was used in [DTW01] for platelets and in [Pla+06; Pla+07] for substances related to calcium signalling.

The uncertainty associated with most parameters requires further investigation. Sensitivity analysis was performed in e.g. [CSM02; Pro+05; OKP08; CV13; HF14; Wat+18; Tho+18; Wat+20], either using deterministic or random sampling. Bifurcation analysis was carried out in e.g. [CSM02; Pla+06; OTM10; BD12; Fok12b; CBM17] either analytic or with the help of numerical tools such as AUTO [Doe+20]. Such analysis is useful for both mathematical validation and medical predictions, e.g. [Ibr+05] found a stability criterion

"consistent with observed features" where the disease progresses if the immune response cannot compensate increase of debris and [OTM10] showed that in their model macrophage proliferation and LDL uptake are more important in the intima than LDL influx. Note that the medical interpretation of long-term behavior requires that the model assumptions remain valid in that time frame.

Most articles contain only a brief discussion of the numerical realization of the presented model, discussing at most questions of temporal and mesh convergence. Articles focused on the details of numerical implementation are rarer, detailed exposition of the numerical realization for fluid-structure problems be found in e.g. [FRW16; Yan+17]. In [GKO14] a (compact) DG method is proposed as higher-order discretization of the advection-reaction-diffusion model from [Ibr+05]. Numerical descriptions and convergence results for iterative schemes for coupled advection-diffusion equations can be found in the already mentioned articles [QVZ02b; QVZ02a]. An analysis of existence and convergence of discrete solutions for similar problems can be found in [CGJ16] for a DG discretization, allowing for certain nonlinearities in the coupling condition.

Multiscale Analysis

Several aspects of atherosclerosis happen on vastly different timescales, such as blood flow and growth as mentioned in the introduction, for other examples we refer to the overview in [Di +15, Figure 2] and the timescales of wall shear stress responses listed in [Dav95, Table 1 and 2]. Inclusion of these multiscale phenomena can lead to excessive costs for direct numerical simulations of these models, the goal of the present section is to investigate how this difficulty is handled in the literature. This comes with the caveat that not all authors explicitly mention multiple scales as reason for their simplifications and use e.g. a stationary inflow profile without explanation.

We distinguish between ad-hoc, formal and rigorous multiscale analysis. Ad-hoc methods might simplify out of necessity, e.g. replacing an oscillating with a stationary inflow profile, or use experimental data to model the temporally macroscopic behavior. The latter approach can be seen as directly modelling the limit behavior of the unknown model. Formal and rigorous approaches, the latter pursued in this thesis, derive computationally less expensive approximations of the original model through formal or rigorous arguments, but this typically requires simplifications which reduce the biological applicability.

To describe the behavior of a system with multiple timescales we use the terminology of quasi-static and averaging type limits. An averaging type limit was already discussed in Section 1.2, where the fast variable shows a periodic asymptotic behavior if the slow variable is kept fixed and the action of this fast behavior is averaged in the limit equation, see eq. (1.4). This was discussed for the model considered in this thesis but formally extends to other systems of course. In a quasi-static limit the fast variable has a stationary asymptotic behavior if the slow variable is kept fixed, for simplicity we discuss this type of limit by augmenting the example from Section 1.2. If we assume that the fluid boundary conditions are simplified as stationary, then eqs. (1.1) reads

$$\begin{aligned} \tfrac{\mathrm{d}}{\mathrm{d}t} q_\varepsilon &= \varepsilon g(q_\varepsilon, v_\varepsilon) && \text{in } I, \\ \partial_t v_\varepsilon - \Delta v_\varepsilon + \nabla p_\varepsilon &= f && \text{in } \Omega^I_{q_\varepsilon}, \end{aligned}$$

with stationary f. Fixing the slow variable $q_\varepsilon \approx \hat{q} \in Q$ on a small time interval, the behavior of v_ε is then approximated by the solution $v_\infty(\hat{q})$ to the stationary equation

$$-\Delta v_\infty(\hat{q}) + \nabla p_\infty(\hat{q}) = f \quad \text{in } \Omega_{\hat{q}}. \tag{2.9}$$

The plaque state q_ε is then, as $\varepsilon \to 0$, approximated by the solution q_0 to

$$\tfrac{\mathrm{d}}{\mathrm{d}\tau} q_0(\tau) = g(q_0(\tau), v_\infty(q_0(\tau))) \quad \text{for } \tau \in \mathcal{I}. \tag{2.10}$$

Thus each evaluation of the right-hand side of the limit equation requires the solution to eq. (2.9), which is a static equation which depends on the evolving data $q_0(\tau)$, which is why we refer to eq. (2.10) as quasi-static limit.

The simplification of taking steady instead of pulsatile flow boundary conditions is common [Ges+11; DDP11; CV12; Gab+14; CPM14; Yan+15]. At least for the first model analyzed in this thesis we will see that an averaging of the inflow profile only leads to an accurate approximation if all processes are linear. This does not mean that a periodic inflow must have a significant impact in every model, e.g. [CV12] compared periodic and steady inflow conditions for their model found only small differences. [DDP11; Gab+14; Di +15] iterate between solving steady-state equations for all model components, then updating the geometry based on these solutions. Due to the domain evolution the equations for all model components are quasi-static. In [Ges+11] only LDL accumulation and intimal thickness are treated as variables and it is argued that the differential equation for LDL accumulation can be solved with fixed intimal thickness which "evolves very slowly", effectively making the LDL evolution quasi-static. The numerical calculations in [Yan+15; Yan+17] use a quasi-static approach for fluid velocity and fluid concentrations, but assume that structure concentration and deformation are instationary, the latter incorporating the deformation due to domain growth. A similar decomposition in stationary processes in the lumen and instationary processes inside the wall is used in [CPM14], but there the processes in the lumen are solved only once and are hence not quasi-static. This approach leads to inconsistencies, e.g. the wall shear stress which influences permeability is only computed in the initial geometry and the Kedem–Katchalsky equations for the LDL concentrations cannot be satisfied since the concentration in one domain is stationary.

Quasi-static limits were also studied in other models without fluid flow [Fok12b; Fok16; Wat+18; Wat+20]. In [Fok12a] the growth factor PDGF is only solved in the stationary setting, in [Fok16] the mechanics are quasi-static and both models feature slowly evolving domains. In the model for PDGF and smooth muscle cells in [Wat+18] it is also assumed that PDGF can be considered in a quasi-static state compared to the timescale of smooth muscle cell migration. The same reasoning is extended to TGF-β in [Wat+20].

The effect of time-periodic advection of a concentration field was studied in [Hon+12], although under the assumption that the advection velocity and the periodic component of the concentration field are small. Under these assumptions it was then argued that the average part of the concentration field satisfies the stationary equation with averaged advection velocity.

The body of literature studying flow problems with time-periodic boundary conditions is smaller, most of which use ad-hoc approaches to model the temporally macroscopic behavior directly. These use experimental observations that temporal variations of the wall shear stress have been linked to the risk

of plaque development, we refer to the critical review in [PSW13]. Multiple quantities have been used to characterize the temporal variations of the wall shear stress, writing $\overline{\cdot}$ for the average over one heart beat, these include

- the time averaged wall shear stress (TAWSS) $\overline{|\sigma_{\mathrm{WS}}|}$,
- the magnitude of the mean wall shear stress $|\overline{\sigma_{\mathrm{WS}}}|$,
- the oscillatory shear stress (OSI) $\frac{1}{2}\left(1 - \frac{|\overline{\sigma_{\mathrm{WS}}}|}{\overline{|\sigma_{\mathrm{WS}}|}}\right)$,
- the relative residence time (RRT) $|\overline{\sigma_{\mathrm{WS}}}|^{-1}$.

Other sources also examine the mean of the wall shear stress component perpendicular to $\overline{\sigma_{\mathrm{WS}}}$ [Ghi+17], the mean of the surface gradient of the wall shear stress and quantities related to the Fourier transform of the wall shear stress [LAS09]. All these quantities implicitly depend on the spatial position.

The OSI is the most prominent of these quantities. It varies between 0, where σ_{WS} is collinear to $\overline{\sigma_{\mathrm{WS}}}$ throughout the cycle, and $\frac{1}{2}$, where $\overline{\sigma_{\mathrm{WS}}} = 0$. The OSI is in particular insensitive to the magnitude of the shear stress. A physical interpretation of the relative residence time is given in [Him+04, Appendix] by a Taylor expansion of the particle position near the wall, the OSI then measures the influence of the time averaged wall shear stress on the residence time.

A relation between endothelial permeability and oscillatory shear index has been used in [Him+04; Fil+13] and proposed in [McK+05]. A direct relation between TAWSS and the growth of plaque is assumed in [LT10]. The resulting equation is similar to the limit investigated for the first model in this thesis, but in [LT10] an initial value problem (with periodic boundary conditions) is solved instead of a time-periodic problem.

A natural mathematical question for these ad-hoc approaches is, whether sensible temporally microscopic models can be devised which yield such relations in the multiscale limit $\varepsilon \to 0$, just as e.g. Darcy's law can be derived from a multiscale analysis of Stokes flow in porous media [San80, Appendix]. The averaging theory developed for the first model in this thesis immediately allows for microscale problems to yield limits involving the TAWSS.

The multiscale nature of slow plaque growth and fast fluid flow is the focus of [FRW16; FR20]. In [FRW16] a fluid-structure-interaction problem with growth is studied, similar to the model of Yang et. al. discussed below. Two heuristic multiscale approaches are suggested. The first uses a temporally averaged inflow velocity and repeatedly solves a stationary fluid-structure interaction problem for fixed growth and afterwards updates the growth using the wall shear stress from the quasi-static fluid flow. The second approach uses the quasi-static problem only to calculate initial values for the fast fluid-structure interaction problem with time-periodic inflow conditions. This problem is solved on a fixed short time interval, i.e. not explicitly until a periodic state is reached. In contrast to the averaging type limit, the wall shear stress is averaged in time and not the action of the shear stress. While significant differences between the two approaches were observed, no comparison with a fully resolved simulation was carried out.

In [FR20] the timescale separation was an even stronger focus with a further reduction of the model from [FRW16], omitting the structure equation and

instead using an analytical describing of the domain deformation depending on an unknown growth parameter, very similar to the first model discussed in this thesis. The proposed limit equation solves the time-periodic fluid problem on a fixed domain and the evolution of the domain growth now agrees with the averaging type limit from Section 1.2. While the derivation of the limit system is slightly different than the approach discussed in this thesis, the final form is identical except for the initial values. The rigorous analysis in [FR20] is limited to fast-slow systems of ordinary differential equations. While it is argued in [FR20] that the partial differential equation could be recovered from an eigenvalue decomposition, this is questionable due to the non-autonomous nature of the problem.

In summary, while the multiscale aspect of the problem has received considerable attention in the literature, most models employ ad-hoc quasi-static limits which ignore the periodicity of the blood flow. While this is only one of many simplification which models necessarily have to make, the effect of it requires further investigation. Rigorous analysis may be impossible for most models, but an examination of the expected fast scale behavior could increase the accuracy of atherosclerosis models.

2.3 The Model by Yang et. al.

The inspiration for this thesis was the model investigated by Yang, Jäger, Neuss-Radu and Richter in [Yan+15; Yan+17], see also the thesis [Yan14]. We will present this model in greater detail in this section and perform a non-dimensionalization to highlight the timescale separation, which will motivate the two models studied in this thesis. The work by Yang et. al. models early stages of the disease and features fluid-structure interaction, monocytes in the blood, which immediately differentiate into macrophages once inside the lumen and turn into foam cells at a fixed rate, thus leading to growth of the plaque.

Dimensional Plaque Model

We first describe the geometry, list the unknowns and then briefly discuss each aspect of the model. The numbered equations constitute the final model. Parameters, boundary and initial values can be found in Table 2.1, some of the notation has been slightly adapted from [Yan+15] for consistency with other parts of this thesis. The parameter values have been collected from the literature, see [Yan+15] for the references.

Geometry

The geometry is purely two dimensional, in contrast to a full three dimensional or rotational-symmetric formulation. A sketch of such a geometry and the notation employed in this thesis is depicted in Figure 2.2. Note that there is a mismatch between the three dimensional parameters listed in Table 2.1 and the two dimensional geometry which is not addressed in [Yan+15]. The geometry consists of a fixed, bounded domain $\Omega \subset \mathbb{R}^2$ subdivided into a fluid domain $\Omega_f(t)$ and a structure domain $\Omega_s(t)$ for each $t \in \overline{I}$, $I := (0, T)$, with $T > 0$, in the sense that

$$\overline{\Omega} = \overline{\Omega_f(t)} \cup \overline{\Omega_s(t)}, \quad \Omega_f(t) \cap \Omega_s(t) = \varnothing.$$

Geometry	
Initial artery diameter	$5\,\mathrm{mm}$
Initial wall thickness	$0.5\,\mathrm{mm}$
Permeable wall section length	$2.5\,\mathrm{mm}$
Transition layer thickness	$\delta = 0.0625\,\mathrm{mm}$
Blood	
Density	$\rho_f = 1 \times 10^{-3}\,\mathrm{g\,mm^{-3}}$
Kinematic viscosity	$\nu = 3\,\mathrm{mm^2\,s^{-1}}$
Initial velocity	$v_f^0 = 48y(5-y)\mathrm{mm\,s^{-1}}$
Inflow velocity	$v_f^D = v_f^D$
Wall	
Density	$\rho_s = 1.06 \times 10^{-3}\,\mathrm{g\,mm^{-3}}$
Shear modulus (healthy tissue)	$\mu_{s,h} = 1 \times 10^5\,\mathrm{g\,mm^{-1}\,s^{-2}}$
Shear modulus (diseased tissue)	$\mu_{s,d} = 0.05 \times \mu_{s,h}$
Shear modulus parameter	$\alpha_\mu = 0.1\,\mathrm{mm^3}$
Growth	
Growth coefficient	$\gamma = 1 \times 10^{-6}\,\mathrm{g}$
Biology	
Monocyte diffusion	$D_f = 1 \times 10^{-6}\,\mathrm{mm^2\,s^{-1}}$
Macrophage diffusion rate (healthy tissue)	$D_{s,h} = 1 \times 10^{-7}\,\mathrm{mm^2\,s^{-1}}$
Macrophage diffusion rate (diseased tissue)	$D_{s,d} = 5 \times D_{s,h}$
Macrophage diffusion parameter	$\alpha_D = 0.1\,\mathrm{mm^3}$
Interface permeability	$\xi_0 = 1 \times 10^{-4}\,\mathrm{mm\,s^{-1}}$
Reaction coefficient	$\beta_0 = 1 \times 10^{-7}\,\mathrm{s^{-1}}$
Initial concentration	$c_f^0 = 540\,\mathrm{mm^{-3}}$
Inflow concentration	$c_f^D = c_f^0$

Table 2.1: Original values for geometry measurements, parameters, boundary functions and initial values as given in [Yan+15].

The fluid domain represents the lumen, the structure domain represents the intima and their evolution is driven by the elastic response and growth and is thus unknown. The endothelium is the interface between both domains and is denoted by $\Gamma(t)$ and defined by

$$\Gamma(t) := \partial\Omega_f(t) \cap \partial\Omega_s(t).$$

This interface is assumed to consist of a damaged part $\Gamma_1(t)$ which is permeable to monocytes, and an impermeable part $\Gamma_2(t)$, such that

$$\Gamma(t) = \overline{\Gamma_1(t)} \cup \overline{\Gamma_2(t)}, \quad \Gamma_1(t) \cap \Gamma_2(t) = \varnothing.$$

It is assumed that $\Gamma_1(t)$ and $\Gamma_2(t)$ are measurable and that the 1-dimensional Lebesgue measure of $\Gamma_1(t)$ is non-zero. We denote the non-cylindrical space-time domain by

$$\Omega_f^I := \{(t,x) \mid t \in I, x \in \Omega_f(t)\}$$

and analogously Ω_s^I and Γ^I.

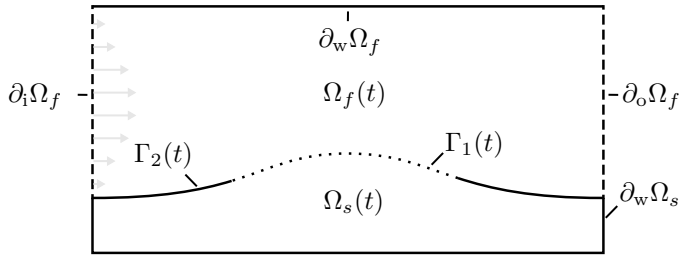

Figure 2.2: Notation used for the geometry of the model by Yang et. al.

The exterior boundaries of $\Omega_f(t)$ and $\Omega_s(t)$ are time-independent since Ω is by assumption. The exterior boundary of $\Omega_f(t)$, i.e. $\partial\Omega_f(t)\backslash\Gamma(t)$, is subdivided into disjoint sets; an inflow boundary $\partial_{\mathrm{i}}\Omega_f$, an outflow boundary $\partial_{\mathrm{o}}\Omega_f$ and a boundary $\partial_{\mathrm{w}}\Omega_f$ consisting of the wall opposite to $\Omega_s(t)$ which is assumed to be healthy. In particular, $\partial_{\mathrm{w}}\Omega_f$ is fixed and hence cannot show an elastic response to the blood flow, which is a simplification to save computational resources. The exterior boundary of $\Omega_s(t)$ is denoted by $\partial_{\mathrm{w}}\Omega_s$. It is assumed that $\partial_{\mathrm{i}}\Omega_f$, $\partial_{\mathrm{o}}\Omega_f$, $\partial_{\mathrm{w}}\Omega_f$ and $\partial_{\mathrm{w}}\Omega_s$ have non-zero 1-dimensional Lebesgue measures. The exterior normal of $\Omega_f(t)$ and $\Omega_s(t)$ is denoted by $\mathfrak{n}_f$ and $\mathfrak{n}_s$ respectively. On the interface then $\mathfrak{n}_f = -\mathfrak{n}_s$.

Given an initial decomposition of Ω into $\Omega_f(0)$ and $\Omega_s(0)$ we can describe the evolution of the subdomains through the deformation field

$$\hat{u}_s \colon \hat{\Omega}_s \to \mathbb{R}^2,$$

later characterized as solution to the elasticity equation, where we use the initial structure domain as reference domain

$$\hat{\Omega}_s := \Omega_s(0).$$

Under the assumption that the deformation field is regular enough, preserves the exterior boundary of $\hat{\Omega}_s$ and is injective, we can define the associated transformation

$$\Phi_s(t) \colon \overline{\Omega}_s \ni \hat{x} \mapsto \hat{x} + \hat{u}(t, \hat{x}) \in \mathbb{R}^2 \tag{2.11}$$

and define the decomposition of the domain Ω for $t > 0$ as

$$\Omega_s(t) := (\Phi_s(t))(\hat{\Omega}_s), \quad \Omega_f(t) := (\Omega \setminus \Omega_s(t))^\circ$$

where $(\cdot)^\circ$ denotes the interior of a set. Here and in the following we will denote quantities defined using the reference coordinates with a hat, in particular $\hat{\Gamma} := \Gamma(0)$. We may switch between these two coordinate systems for any function and write e.g. either $\hat{c}_s(t, \hat{x})$ or $c_s(t, x)$ for the macrophage concentration in the intima, where one is the pullback of the other under Φ_s, respectively Φ_s^{-1}.[6] Space-independent parameters will always be written without a hat. We follow standard notation and denote the deformation gradient and its determinant by

$$\hat{F}_s := \hat{\nabla}\Phi_s \quad \text{and} \quad \hat{J}_s := \det(\hat{F}_s),$$

[6]For vector fields this pullback must be understood in the sense of a pullback of the coordinate functions, not the usual field pullback in differential geometry.

omitting the time t for notational simplicity.

The elastic stress depends on the deformation gradient with respect to these reference coordinates, the defining property of elasticity [Cia88]. This makes a formulation of the elasticity equation in the coordinates of $\hat{\Omega}_s$ natural. The Eulerian formulation of the Navier–Stokes equation on the non-cylindrical space-time domain Ω_f^I requires no transformation, but a pullback to a cylindrical space-time domain $I \times \hat{\Omega}_f$ with $\hat{\Omega}_f := \Omega_f(0)$ is nevertheless useful for a mathematical treatment or numerical implementation. For a clearer presentation we will not perform such a pullback here, the calculations can be found in a slightly different context in Chapter 4, but we briefly describe the arbitrary Lagrangian-Eulerian (ALE) method used in [Yan+15] such that the reader may follow both sources. In the ALE method, $\hat{u}_s$ is continuously extended to $\overline{\Omega}_f(t)$ by some $\hat{u}_f$ which is sufficiently regular and preserves the outer boundary of Ω. The extension can be chosen arbitrary, e.g. a harmonic extension, but the choice can affect the time on which the extension has the required regularity, in particular injectivity, see [Ric17] for a discussion. The Navier–Stokes equation can then be pulled back to $I \times \hat{\Omega}_f$ with the Piola transformation, which preserves solenoidality of v_f, details can be found in Chapter 4.

List of Unknowns

The model consists of the following unknowns inside the fluid domain / lumen:

- v_f: blood velocity,
- p_f: blood pressure,
- c_f: monocyte concentration.

Inside the structure domain, i.e. intima, the unknowns are

- $\hat{u}_s$: wall deformation,
- $\hat{v}_s$: wall velocity,
- $\hat{p}_s$: wall pressure,
- $\hat{c}_s$: macrophage concentration,
- $\hat{c}_s^*$: foam cell concentration,
- $\hat{g}_s$: growth factor.

Blood Flow

For the blood flow the standard incompressible Navier–Stokes equation is employed for simplicity, we refer to the discussion in the review for drawbacks and alternatives to this model of blood flow. The equations are then

$$\left.\begin{aligned} \rho_f \partial_t v_f + \rho_f (v_f \cdot \nabla) v_f - \operatorname{div} \sigma_f &= 0, \\ \operatorname{div} v_f &= 0 \end{aligned}\right\} \quad \text{in } \Omega_f^I \tag{2.12a}$$

with blood density ρ_f and the Cauchy stress tensor with Newtonian rheology

$$\sigma_f := -p_f I + \rho_f \nu (\nabla v_f + (\nabla v_f)^\intercal) \tag{2.12b}$$

with kinematic viscosity ν. The exterior boundary conditions are Dirichlet inflow conditions on $\partial_{\mathrm{i}}\Omega_f$, no-slip conditions on $\partial_{\mathrm{w}}\Omega_f$ and do-nothing boundary conditions on $\partial_{\mathrm{o}}\Omega_f$:

$$v_f = v_f^D \quad \text{on } I \times \partial_{\mathrm{i}}\Omega_f, \tag{2.12c}$$

$$v_f = 0 \quad \text{on } I \times \partial_{\mathrm{w}}\Omega_f, \tag{2.12d}$$

$$\rho_f \nu \nabla v_f \mathfrak{n}_f - p_f \mathfrak{n}_f = 0 \quad \text{on } I \times \partial_{\mathrm{o}}\Omega_f. \tag{2.12e}$$

A constant-in-time inflow velocity v_f^D is used in [Yan+15] to circumvent the problems associated with multiple timescales, a simplification which motivated the investigations of this thesis. The do-nothing condition differs from the natural Neumann condition $\sigma_f \mathfrak{n}_f = 0$ by the omission of the transposed gradient and shows a more realistic outflow behavior compared to the natural Neumann condition if we assume that the blood flow continues in a straight channel beyond the outflow boundary. Do-nothing conditions can have detrimental stability properties if backflow occurs across the outflow boundary [BM14]. The initial blood velocity is a given function

$$v_f(0) = v_f^0 \quad \text{in } \Omega_f(0). \tag{2.12f}$$

Elastic Wall

The elastic behavior of the wall is modelled using an incompressible neo-Hookean material model. Growth is realized in [Yan+15] by the method of multiple natural configurations [RHM94; AM02; RS04], leading to a decomposition of the deformation gradient as

$$\mathrm{I} + \hat{\nabla}\hat{u}_s = \hat{F}_s = \hat{F}_s^e \hat{F}_s^g$$

into elastic response $\hat{F}_s^e$ and growth tensor $\hat{F}_s^g$. The model described here makes the simplifying assumption that growth is isotropic, meaning that

$$\hat{F}_s^g := \hat{g}_s \, \mathrm{I},$$

with some function $\hat{g}_s \geq 1$ whose evolution is described next. We assume that the mass increases only due to the increase of volume whereas the density is constant. Specifically, if $V(t)$ denotes some arbitrary volume in $\Omega_s(t)$ moving with the deformation velocity, we assume that there exists a growth function f_s^g, modelled below, which represents the rate of mass growth per unit volume:

$$\frac{\mathrm{d}}{\mathrm{d}t} \int_{V(t)} \rho_s \, \mathrm{d}x = \int_{V(t)} f_s^g \, \mathrm{d}x$$

with wall density ρ_s, such that by integral transformation of $V(t)$ to $\hat{V}$ we get

$$\int_{\hat{V}} \frac{\mathrm{d}}{\mathrm{d}t} (\rho_s \hat{J}_s) \, \mathrm{d}\hat{x} = \int_{\hat{V}} \hat{f}_s^g \hat{J}_s \, \mathrm{d}x$$

and by variation of $\hat{V}$ we arrive at

$$\frac{\mathrm{d}}{\mathrm{d}t} (\rho_s \hat{J}_s) = \hat{f}_s^g \hat{J}_s \quad \text{in } I \times \hat{\Omega}_s.$$

Since $\hat{J}_s = \hat{J}_s^e \hat{J}_s^g = \hat{J}_s^g = \hat{g}_s^2$ by incompressibility of the elastic response, i.e. $\hat{J}_s^e = 1$, and isotropy of $\hat{F}_s^g$, we arrive at

$$\partial_t \hat{g}_s = \frac{1}{2} \frac{\hat{f}_s^g}{\rho_s} \hat{g}_s \quad \text{in } I \times \hat{\Omega}_s.$$

We remark that the factor changes to $\frac{1}{3}$ for a three dimensional geometry. The growth function $\hat{f}_s^g$ will be related to the macrophage concentration below.

Following introductory texts for elasticity, e.g. [Cia88], the balance of momentum reads

$$\left.\begin{aligned} \hat{J}_s \rho_s \partial_t \hat{v}_s - \widehat{\operatorname{div}}(\hat{J}_s \hat{\sigma}_s \hat{F}_s^{-\intercal}) = 0, \\ \partial_t \hat{u}_s - \hat{v}_s = 0. \end{aligned}\right\} \quad \text{in } I \times \hat{\Omega}_s \tag{2.13a}$$

where the stress tensor $\hat{\sigma}_s$ is assumed to only depend on $\hat{F}_s^e$. For an incompressible neo-Hookean material this means that

$$\hat{\sigma}_s := -\hat{p}_s \, \mathrm{I} + \hat{\mu}_s \left(\hat{F}_s^e (\hat{F}_s^e)^\intercal - \mathrm{I} \right) \tag{2.13b}$$

where the shear modulus $\hat{\mu}_s$ depends on the foam cell concentration $\hat{c}_s^*$ to model the softening of diseased tissue with high foam cell concentrations,

$$\hat{\mu}_s := \mu_{s,d} + (\mu_{s,h} - \mu_{s,d}) \mathrm{e}^{-\alpha_\mu \hat{c}_s^*} \tag{2.13c}$$

with parameters $\mu_{s,h}$, $\mu_{s,d}$ and α_μ. The elastic response tensor $\hat{F}_s^e$ can be expressed using the growth tensor and the deformation gradient as

$$\hat{F}_s^e = \hat{g}_s^{-1} \hat{F}_s = \hat{g}_s^{-1} (\mathrm{I} + \hat{\nabla} \hat{u}_s)$$

such that the equations are formulated only in terms of the unknowns $\hat{u}_s$, $\hat{v}_s$ and $\hat{g}_s$. Finally, the incompressibility of the elastic response yields the constraint

$$\det(\mathrm{I} + \hat{\nabla} \hat{u}_s) = \det(\hat{F}_s) = \det(\hat{F}_s^g) = \hat{g}_s^2 \quad \text{in } I \times \hat{\Omega}_s \tag{2.13d}$$

which is missing in the summary of [Yan+15]. The structure problem has initial conditions

$$\hat{u}_s(0) = 0, \quad \hat{v}_s(0) = 0 \quad \text{in } \hat{\Omega}_s \tag{2.13e}$$

and a fixed deformation at the exterior boundaries

$$\hat{u}_s = 0 \quad \text{on } I \times \partial_{\mathrm{w}} \Omega_s. \tag{2.13f}$$

The fixed exterior boundaries, the isotropic wall behavior and growth are simplifications made in this model. Furthermore, the wall is implicitly assumed to be unstressed in the reference configuration which is not the case in vivo.

Mechanical Interface Coupling Conditions

On the interface $\Gamma(t)$ between $\Omega_f(t)$ and $\Omega_s(t)$ the continuity of velocities and normal stresses is assumed:

$$v_f = v_s \quad \text{and} \quad \sigma_f \mathfrak{n}_f + \sigma_s \mathfrak{n}_s = 0 \quad \text{on } \Gamma^I. \tag{2.14}$$

Growth Law

The growth function is assumed to depend linearly on the macrophage concentration $\hat{c}_s$, i.e.

$$\hat{f}_s^g := \gamma\hat{\beta}\hat{c}_s,$$

with growth factor γ. The factor $\hat{\beta}\hat{c}_s$ will later also denote the rate at which macrophages turn into foam cells. In summary, $\hat{g}_s$ satisfies the spatially varying ordinary differential equation

$$\partial_t\hat{g}_s = \frac{1}{2}\frac{\gamma\bar{\beta}}{\rho_s}\hat{c}_s\hat{g}_s \quad \text{in } I\times\hat{\Omega}_s. \tag{2.15a}$$

Note that unless $\bar{c}_s$ vanishes the variable $\hat{g}_s$ can be expected to grow exponentially. Assuming that no growth occurred prior to the initial time of the model, the initial condition for $\hat{g}_s$ reads

$$\hat{g}_s(0) = 1 \quad \text{in } \hat{\Omega}_s. \tag{2.15b}$$

Monocytes, Macrophages and Foam Cells

The monocyte concentration c_f undergoes advection by the blood and diffusion inside the lumen

$$\partial_t c_f + v_f\cdot\nabla c_f - D_f\Delta c_f = 0 \quad \text{in } \Omega_f^I. \tag{2.16a}$$

Once inside the lumen, the interface condition will be discussed below, monocytes are assumed to differentiate into macrophages immediately and c_s denotes the macrophage concentration. The macrophages are advected by the velocity of the structure and diffuse. Macrophages turn into foam cells at a fixed rate, independent of e.g. LDL concentrations which are not examined in this model. These processes are realized by

$$\partial_t c_s + \operatorname{div}(v_s c_s) - \operatorname{div}(D_s\nabla c_s) = -\beta c_s \quad \text{in } \Omega_s^I \tag{2.16b}$$

with diffusion rate D_s which is higher in regions with high foam cell concentrations c_s^*:

$$D_s := D_{s,d} + (D_{s,h} - D_{s,d})\mathrm{e}^{-\alpha_D c_s^*} \tag{2.16c}$$

with parameters $D_{s,d}$, $D_{s,h}$ and α_D. It is argued in [Yan+15] that no conversion from macrophages to foam cells takes place in a region around the interface consisting of endothelium and a layer of smooth muscle cells, such that[7]

$$\beta = \beta_0\mathbb{1}_{\Omega_{s,\delta}^I} \tag{2.16d}$$

with reaction coefficient β_0 and $\Omega_{s,\delta}(t) := (\Phi_s(t))(\hat{\Omega}_{s,\delta})$, where $\hat{\Omega}_{s,\delta} := \{\hat{x}\in\hat{\Omega}_s \mid \mathrm{d}(\hat{x},\hat{\Gamma})\geq\delta\}$ with transition layer thickness $\delta>0$. Foam cells only occur inside the wall and are advected by the wall's movement and produced through macrophages. No diffusion is assumed to occur, leading to

$$\partial_t c_s^* + \operatorname{div}(v_s c_s^*) = \beta c_s \quad \text{in } \Omega_s^I. \tag{2.16e}$$

[7] This is the author's guess based on the textual description given in [Yan+15].

The concentration of monocytes in the lumen is assumed to be some given function, whereas no macrophages and foam cells are assumed to be inside the intima at the beginning.

$$c_f(0) = c_f^0 \quad \text{in } \Omega_f(0), \quad c_s(0) = 0 \quad \text{and} \quad c_s^*(0) = 0 \quad \text{in } \Omega_s(0). \tag{2.16f}$$

New monocytes flow into the lumen at the inflow boundary, all other exterior boundaries are assumed to be homogeneous diffusive Neumann boundaries:

$$c_f = c_f^D \quad \text{on } I \times \partial_{\mathrm{i}}\Omega_f, \tag{2.16g}$$
$$D_f \nabla c_f \cdot \mathfrak{n}_f = 0 \quad \text{on } I \times (\partial_{\mathrm{o}}\Omega_f \cup \partial_{\mathrm{w}}\Omega_f), \tag{2.16h}$$
$$D_s \nabla c_s \cdot \mathfrak{n}_s = 0 \quad \text{on } I \times \partial_{\mathrm{w}}\Omega_s. \tag{2.16i}$$

We note that the deformation and hence the velocity across $\partial_{\mathrm{w}}\Omega_s$ is zero.

On the interface, monocytes and macrophages are coupled through continuity of fluxes and the simplified Kedem–Katchalsky eq. (2.6), i.e.

$$D_f \nabla c_f \cdot \mathfrak{n}_f + D_s \nabla c_s \cdot \mathfrak{n}_s = 0 \quad \text{on } \Gamma^I, \tag{2.16j}$$
$$D_f \nabla c_f \cdot \mathfrak{n}_f + \xi(c_f - c_s) = 0 \quad \text{on } \Gamma^I. \tag{2.16k}$$

The permeability function ξ has been chosen as a scaled indicator function on the damaged portion of the endothelium, i.e.

$$\xi := \xi_0 \mathbb{1}_{\Gamma_1^I} \quad \text{on } \Gamma^I \tag{2.16l}$$

with constant permeability ξ_0. The permeability is in particular independent of the wall shear stress.

Non-Dimensional Plaque Model

We rescale the time and the spatial coordinates of both moving and reference domains according to

$$t = T\bar{t}, \quad x = L\bar{x}, \quad \hat{x} = L\mathring{\hat{x}}.$$

The partial derivatives then transform as

$$\partial_t = \frac{1}{T}\partial_{\bar{t}}, \quad \partial_x = \frac{1}{L}\partial_{\bar{x}}, \quad \partial_{\hat{x}} = \frac{1}{L}\partial_{\mathring{\hat{x}}}$$

with obvious extensions to ∇, $\hat{\nabla}$, div, $\widehat{\mathrm{div}}$, Δ and $\hat{\Delta}$. We use an analogous notation for the rescaled domains, boundaries and the interface,

$$\bar{I} := \frac{1}{T} I, \quad \bar{\Omega}_f(t) := \frac{1}{L}\Omega_f(t), \quad \mathring{\hat{\Omega}}_s := \frac{1}{L}\hat{\Omega}_s, \quad \text{etc.}$$

The bar will not denote the closure of any set in the following, such that no confusion can arise. On their respective domains, we make the following Ansatz for the unknowns:

$$\begin{aligned}
&v_f(t,x) = V\bar{v}_f(\bar{t},\bar{x}), && \hat{u}_s(t,\hat{x}) = L\mathring{\hat{u}}_s(\bar{t},\mathring{\hat{x}}), && \hat{v}_s(t,\hat{x}) = V\mathring{\hat{v}}_s(\bar{t},\mathring{\hat{x}}),\\
&p_f(t,x) = P_f\bar{p}_f(\bar{t},\bar{x}), && \hat{p}_s(t,\hat{x}) = P_s\mathring{\hat{p}}_s(\bar{t},\mathring{\hat{x}}), && \hat{g}_s(t,\hat{x}) = \mathring{\hat{g}}_s(\bar{t},\mathring{\hat{x}}),\\
&c_f(t,x) = C\bar{c}_f(\bar{t},\bar{x}), && c_s(t,x) = C\bar{c}_s(\bar{t},\bar{x}), && c_s^*(t,x) = C\bar{c}_s^*(\bar{t},\bar{x}).
\end{aligned}$$

	dimensional	non-dimensional
moving domain	x	$\bar{x}$
reference domain	$\hat{x}$	$\hat{\bar{x}} = \hat{\bar{x}}$

(a) Notation for coordinates.

	dimensional	non-dimensional
moving domain	$v_s(t, x)$	$V\bar{v}_s(\bar{t}, \bar{x})$
reference domain	$\hat{v}_s(t, \hat{x})$	$V\hat{\bar{v}}_s(\bar{t}, \hat{\bar{x}})$

(b) Notation and scaling behavior of functions.

Table 2.3: Enumeration of the notation for the four coordinates systems used in the structure domain. Only the two moving coordinate systems are used in the fluid domain.

Where we used the same scaling for v_f and $\hat{v}_s$ due to their continuity, the natural scaling by L for the deformation and that $\hat{g}_s$ is already dimensionless and normalized to 1. The same scaling for all concentrations is used, where C, contrary to the notation used in other parts of this thesis, does of course not denote a generic constant but the reference concentration.

Since we later want to examine oscillating blood flow we perform the non-dimensionalization with a natural reference time T of period length. Using artery diameter and maximum inflow velocity as reference values for L and V this implies that, in contrast to the stationary setting, no relation is assumed between L, V and T, a mismatch which is expressed through the Strouhal number St below. The concentrations will be normalized by the inflow monocyte concentration.

The amount of notation can be overwhelming at first. Four coordinate systems are employed in the structure domain, consisting of all combinations of moving vs. reference coordinates (indicated by a hat, $\hat{\cdot}$) and dimensional vs. non-dimensional coordinates (indicated by a bar, $\bar{\cdot}$), where $\hat{\bar{\cdot}}$ is a visual shorthand for $\hat{\cdot}$-and-$\bar{\cdot}$. This is summarized in Table 2.3. We will freely change between all four coordinate systems in the following, with the caveat that non-dimensional quantities are also rescaled. This also holds for parameters, e.g. we denote the (space-dependent) macrophage-to-foam cell conversion rate by β, $\hat{\beta}$, $\bar{\beta}$ and $\hat{\bar{\beta}}$ with to-be-defined rescaling of $\bar{\beta}$ and $\hat{\bar{\beta}}$. A rescaling of constant parameters will also be denoted by a bar, e.g. α_D vs. $\bar{\alpha}_D$, except for well-known nondimensional parameters such as the Reynolds, Strouhal or Péclet numbers.

We again number only the equations belonging to the final non-dimensional model. The values of non-dimensional parameters, defined throughout the next section, can be found in Table 2.4. The multiscale behavior of the model is discussed, using the non-dimensionalization, at the end of the section.

Reference Values		*Order*
Reference time	$T = 1\,\mathrm{s}$	–
Reference length	$L = 5\,\mathrm{mm}$	–
Reference velocity	$V = 300\,\mathrm{mms}^{-1}$	–
Reference concentration	$C = 540\,\mathrm{mm}^{-3}$	–
Geometry		
Initial artery diameter	1	–
Initial wall thickness	0.1	–
Permeable wall section length	0.5	–
Transition layer thickness	$\bar{\delta} = 0.0125$	–
Time		
Period length	1	$\mathcal{O}(1)$
Blood		
Strouhal number	$St = 0.01\bar{6}$	$\mathcal{O}(1)$
Reynolds number	$Re = 500$	$\mathcal{O}(1)$
Womersley number	$\alpha \approx 7.1$	$\mathcal{O}(1)$
Initial velocity	$\bar{v}_f^0 = 4\bar{y}(1-\bar{y})$	$\mathcal{O}(1)$
Inflow velocity	$\bar{v}_f^D = \bar{v}_f^D$	$\mathcal{O}(1)$
Wall		
Shear modulus (healthy tissue)	$\bar{\mu}_{s,h} = 1048$	$\mathcal{O}(1)$
Shear modulus (diseased tissue)	$\bar{\mu}_{s,d} = 0.05 \times \bar{\mu}_{s,h}$	$\mathcal{O}(1)$
Shear modulus parameter	$\bar{\alpha}_\mu = 54$	$\mathcal{O}(1)$
Blood and Wall		
Structure-to-fluid density ratio	$\rho_{s:f} = 1.06$	$\mathcal{O}(1)$
Growth		
Growth coefficient	$\bar{\gamma} = 0.5094$	$\mathcal{O}(1)$
Biology		
Monocyte Péclet number	$Pe_f = 1.5 \times 10^9$	$\mathcal{O}(\varepsilon^{-1})$
Macrophage Péclet number (healthy)	$Pe_{s,h} = 1.5 \times 10^{10}$	$\mathcal{O}(\varepsilon^{-1})$
Macrophage Péclet number (diseased)	$Pe_{s,d} = 0.2 \times Pe_{s,h}$	$\mathcal{O}(\varepsilon^{-1})$
Macrophage diffusion parameter	$\bar{\alpha}_D = 54$	$\mathcal{O}(1)$
Interface permeability	$\bar{\xi}_0 = 3.\bar{3} \times 10^{-7}$	$\mathcal{O}(\varepsilon)$
Reaction coefficient	$\bar{\beta}_0 = 1.\bar{6} \times 10^{-9}$	$\mathcal{O}(\varepsilon)$
Initial concentration	$\bar{c}_f^0 = 1$	$\mathcal{O}(1)$
Inflow concentration	$\bar{c}_f^D = \bar{c}_f^0$	$\mathcal{O}(1)$

Table 2.4: Nondimensional values for geometry measurements, parameters, boundary functions and initial values. The last column is a suggested scaling behavior for a small parameter ε as discussed in the section Multiscale Behavior of the Model by Yang et. al on page 46.

Blood Flow

Transforming the Navier–Stokes equation (2.12a) by the rules above, we get

$$\frac{\rho_f V}{T}\partial_{\bar{t}}\bar{v}_f + \frac{\rho_f V^2}{L}(\bar{v}_f\cdot\bar{\nabla})\bar{v}_f - \frac{1}{L}\overline{\operatorname{div}}\left[-P_f\bar{p}_f I + \frac{\rho_f \nu V}{L}(\bar{\nabla}\bar{v}_f + \bar{\nabla}\bar{v}_f^{\intercal})\right] = 0$$

in $\bar{\Omega}_f^{\bar{I}}$. Rescaling by $L/(\rho_f V^2)$ and using that the solenoidality is unaffected by the transformation, we arrive at

$$\left.\begin{aligned} St\,\partial_{\bar{t}}\bar{v}_f + (\bar{v}_f\cdot\bar{\nabla})\bar{v}_f - \overline{\operatorname{div}}\;\bar{\sigma}_f &= 0,\\ \overline{\operatorname{div}}\;\bar{v}_f &= 0 \end{aligned}\right\} \quad \text{in } \bar{\Omega}_f^{\bar{I}} \tag{2.17a}$$

with Strouhal number St, expressing the ratio of the time it takes the reference velocity to cross the reference length to the period, and Reynold's number Re defined by

$$St := \frac{L}{VT}, \quad Re := \frac{VL}{\nu}$$

and rescaled stress tensor

$$\bar{\sigma}_f := -\bar{p}_f I + \frac{1}{Re}(\bar{\nabla}\bar{v}_f + (\bar{\nabla}\bar{v}_f)^{\intercal}) \tag{2.17b}$$

for the pressure scaling $P_f := \rho_f V^2$. Another popular non-dimensional measure of pulsatile flows is the Womersley number, defined by $\alpha := \sqrt{2\pi\, Re\, St}$ and often used instead of the Strouhal number. The boundary and initial conditions from eqs. (2.12c) to (2.12f) can be rescaled similarly, such that

$$\bar{v}_f = \bar{v}_f^D \quad \text{on } \bar{I}\times\partial_{\mathrm{i}}\bar{\Omega}_f, \tag{2.17c}$$

$$\bar{v}_f = 0 \quad \text{on } \bar{I}\times\partial_{\mathrm{w}}\bar{\Omega}_f, \tag{2.17d}$$

$$\frac{1}{Re}\bar{\nabla}\bar{v}_f\bar{\mathfrak{n}}_f - \bar{p}_f\bar{\mathfrak{n}}_f = 0 \quad \text{on } \bar{I}\times\partial_{\mathrm{o}}\bar{\Omega}_f \tag{2.17e}$$

and

$$\bar{v}_f(0) = \bar{v}_f^0 \quad \text{in } \bar{\Omega}_f(0). \tag{2.17f}$$

Elastic Wall

By the chosen scaling of $\mathring{u}_s$ we have

$$\mathring{F}_s = \mathrm{I} + \frac{U}{L}\mathring{\nabla}\mathring{u}_s = \mathrm{I} + \mathring{\nabla}\mathring{u}_s \quad \text{and} \quad \mathring{J}_s = \det(\mathring{F}_s)$$

such that these quantities are unaffected by the scaling. The structure equation from eq. (2.13a) then transform to

$$\left.\begin{aligned} \mathring{J}_s\frac{\rho_s V}{T}\partial_{\bar{t}}\mathring{v}_s - \frac{1}{L}\mathring{\operatorname{div}}\left[\mathring{J}_s\left(-P_s\mathring{p}_s\,\mathrm{I} + \hat{\mu}_s\left(\mathring{F}_s^e(\mathring{F}_s^e)^{\intercal} - \mathrm{I}\right)\right)\mathring{F}_s^{-\intercal}\right] &= 0,\\ \frac{L}{T}\partial_{\bar{t}}\mathring{u}_s - V\mathring{v}_s &= 0 \end{aligned}\right\} \text{ in } \bar{I}\times\mathring{\Omega}_s.$$

Rescaling the first equation by $L/(\rho_s V^2)$ and the second by $1/V$ leads to

$$\left.\begin{aligned} \mathring{J}_s\, St\,\partial_{\bar{t}}\mathring{v}_s - \mathring{\operatorname{div}}(\mathring{J}_s\mathring{\sigma}_s\mathring{F}_s^{-\intercal}) &= 0,\\ St\,\partial_{\bar{t}}\mathring{u}_s - \mathring{v}_s &= 0 \end{aligned}\right\} \quad \text{in } \bar{I}\times\mathring{\Omega}_s \tag{2.18a}$$

with stress tensor

$$\mathring{\sigma}_s := -\mathring{p}_s \mathrm{I} + \mathring{\mu}_s \left(\mathring{F}_s^e (\mathring{F}_s^e)^\intercal - \mathrm{I} \right), \quad \mathring{F}_s^e = \mathring{g}_s^{-1} \mathring{F}_s \tag{2.18b}$$

if $P_s := \rho_s V^2$ and dimensionless shear modulus

$$\mathring{\mu}_s := \bar{\mu}_{s,d} + (\bar{\mu}_{s,h} - \bar{\mu}_{s,d}) \mathrm{e}^{-\bar{\alpha}_\mu \mathring{c}_s^*}, \tag{2.18c}$$

with dimensionless parameters

$$\bar{\mu}_{s,h} := \frac{\mu_{s,h}}{\rho_s V^2}, \quad \bar{\mu}_{s,d} := \frac{\mu_{s,d}}{\rho_s V^2} \quad \text{and} \quad \bar{\alpha}_\mu := C\alpha_\mu.$$

The incompressibility condition is completely analogous to eq. (2.13d), i.e.

$$\det(\mathrm{I} + \mathring{\nabla} \mathring{u}_s) = \mathring{g}_s^2 \quad \text{in } \bar{I} \times \mathring{\Omega}_s, \tag{2.18d}$$

as are the initial conditions

$$\mathring{u}_s(0) = 0, \quad \mathring{v}_s(0) = 0 \quad \text{in } \mathring{\Omega}_s \tag{2.18e}$$

and the exterior boundary condition

$$\mathring{u}_s = 0 \quad \text{on } \bar{I} \times \partial_{\mathrm{w}} \bar{\Omega}_s. \tag{2.18f}$$

Mechanical Interface Coupling Conditions

For the interface condition eq. (2.14) we note that the scaling of the stress tensors during the non-dimensionalization, eqs. (2.17b) and (2.18b), differed by the factors ρ_f and ρ_s, respectively. This leads to the coupling conditions

$$\bar{v}_f = \bar{v}_s \quad \text{and} \quad \bar{\sigma}_f \bar{\mathfrak{n}}_f + \rho_{s:f} \bar{\sigma}_s \bar{\mathfrak{n}}_s = 0 \quad \text{on } \bar{\Gamma}^{\bar{I}} \tag{2.19}$$

with density ratio

$$\rho_{s:f} := \frac{\rho_s}{\rho_f}.$$

Growth Law

The growth law from eq. (2.15a) transforms according to

$$\frac{1}{T} \partial_{\bar{t}} \mathring{g}_s = \frac{1}{2} \frac{\mathring{\beta} V}{L} \frac{\gamma C}{\rho_s} \mathring{c}_s \mathring{g}_s \quad \text{in } \bar{I} \times \mathring{\Omega}_s$$

where we used the nondimensional macrophage-to-foam cell conversion rate

$$\mathring{\beta} := \bar{\beta}_0 \mathbb{1}_{\bar{I} \times \mathring{\Omega}_{s,\bar{\delta}}} \tag{2.20a}$$

where $\bar{\delta} := \frac{\delta}{L}$, $\mathring{\Omega}_{s,\bar{\delta}} := \{\mathring{x} \in \mathring{\Omega}_s \mid \mathrm{d}(\mathring{x}, \mathring{\Gamma}) \geq \bar{\delta}\}$ and

$$\bar{\beta}_0 := \beta_0 \frac{L}{V}.$$

The reason for this rescaling will become apparent in the section for the biological processes below. With nondimensional growth rate

$$\bar{\gamma} := \frac{\gamma C}{\rho_s}$$

we can hence conclude that

$$St\,\partial_{\bar{t}}\mathring{\bar{g}}_s = \tfrac{1}{2}\mathring{\bar{\beta}}\mathring{\bar{\gamma}}\mathring{\bar{c}}_s\mathring{\bar{g}}_s \quad \text{in } \bar{I}\times\mathring{\bar{\Omega}}_s. \tag{2.20b}$$

We keep the factor $\frac{1}{2}$ separate due to its link with the spatial dimension. The initial condition from eq. (2.15b) is unchanged,

$$\mathring{\bar{g}}_s(0) = 1 \quad \text{in } \mathring{\bar{\Omega}}_s. \tag{2.20c}$$

Monocytes, Macrophages and Foam Cells

The monocyte equation eq. (2.16a) transforms to

$$\frac{C}{T}\partial_{\bar{t}}\bar{c}_f + \frac{VC}{L}\bar{v}_f\cdot\bar{\nabla}\bar{c}_f - \frac{D_f C}{L^2}\bar{\Delta}\bar{c}_f = 0 \quad \text{in } \bar{\Omega}_f^{\bar{I}}$$

and rescaling by $L/(VC)$ yields

$$St\,\partial_{\bar{t}}\bar{c}_f + \bar{v}_f\cdot\bar{\nabla}\bar{c}_f - \frac{1}{Pe_f}\bar{\Delta}\bar{c}_f = 0 \quad \text{in } \bar{\Omega}_f^{\bar{I}} \tag{2.21a}$$

with fluid Péclet number

$$Pe_f := \frac{VL}{D_f}.$$

With the same arguments, the macrophage eq. (2.16b) transforms to

$$St\,\partial_{\bar{t}}\bar{c}_s + \overline{\operatorname{div}}(\bar{v}_s\bar{c}_s) - \overline{\operatorname{div}}\left(\frac{1}{Pe_s}\bar{\nabla}\bar{c}_s\right) = -\bar{\beta}\bar{c}_s \quad \text{in } \bar{\Omega}_s^{\bar{I}} \tag{2.21b}$$

where the scaling used here motivated the definition of $\bar{\beta}$ in eq. (2.20a). The (inverse of the) structure Péclet number is given by

$$Pe_s^{-1} := Pe_{s,d}^{-1} + \left(Pe_{s,h}^{-1} - Pe_{s,d}^{-1}\right)\mathrm{e}^{-\bar{\alpha}_D\bar{c}_s^*} \quad \text{in } \bar{\Omega}_s^{\bar{I}} \tag{2.21c}$$

with Péclet numbers of healthy and diseased wall and $\bar{\alpha}_D$ defined through

$$Pe_{s,h}^{-1} := \frac{VL}{D_{s,h}}, \quad Pe_{s,d}^{-1} := \frac{VL}{D_{s,d}}, \quad \bar{\alpha}_D := \alpha_D C.$$

The transformation of the foam cell eq. (2.16e) is analogous,

$$St\,\partial_{\bar{t}}\bar{c}_s^* + \overline{\operatorname{div}}(\bar{v}_s\bar{c}_s^*) = \bar{\beta}\bar{c}_s \quad \text{in } \bar{\Omega}_s^{\bar{I}}. \tag{2.21d}$$

The initial conditions can be rewritten as

$$\bar{c}_f(0) = \bar{c}_f^0 \quad \text{in } \bar{\Omega}_f(0), \quad \bar{c}_s(0) = 0 \quad \text{and} \quad \bar{c}_s^*(0) = 0 \quad \text{in } \bar{\Omega}_s(0) \tag{2.21e}$$

and the exterior boundary conditions transform to

$$\bar{c}_f = \bar{c}_f^D \quad \text{on } \bar{I} \times \partial_{\mathrm{i}} \bar{\Omega}_f, \tag{2.21f}$$

$$\frac{1}{Pe_f} \bar{\nabla} \bar{c}_f \cdot \bar{\mathfrak{n}}_f = 0 \quad \text{on } \bar{I} \times (\partial_{\mathrm{o}} \bar{\Omega}_f \cup \partial_{\mathrm{w}} \bar{\Omega}_f), \tag{2.21g}$$

$$\frac{1}{Pe_s} \bar{\nabla} \bar{c}_s \cdot \bar{\mathfrak{n}}_s = 0 \quad \text{on } \bar{I} \times \partial_{\mathrm{w}} \bar{\Omega}_s. \tag{2.21h}$$

On the interface we have for the first coupling condition from eq. (2.16j), after scaling by $1/V$, that

$$\frac{1}{Pe_f} \bar{\nabla} \bar{c}_f \cdot \bar{\mathfrak{n}}_f + \frac{1}{Pe_s} \bar{\nabla} \bar{c}_s \cdot \bar{\mathfrak{n}}_s = 0 \quad \text{on } \bar{\Gamma}^{\bar{I}} \tag{2.21i}$$

and for the second interface condition, eq. (2.16k), with the same scaling that

$$\frac{1}{Pe_f} \bar{\nabla} \bar{c}_f \cdot \bar{\mathfrak{n}}_f + \bar{\xi}(\bar{c}_f - \bar{c}_s) = 0 \quad \text{on } \bar{\Gamma}^{\bar{I}} \tag{2.21j}$$

with permeability function

$$\bar{\xi} := \bar{\xi}_0 \mathbb{1}_{\bar{\Gamma}_1^{\bar{I}}} \quad \text{on } \bar{\Gamma}^{\bar{I}}, \quad \text{where} \quad \bar{\xi}_0 := \frac{\xi_0}{V}. \tag{2.21k}$$

Multiscale Behavior of the Model by Yang et. al.

The normalization of geometry and unknowns facilitates a clearer identification of the scales in the model of Yang et. al. through the magnitude of the nondimensional parameters. The assumption of normalization is evident for $\bar{v}_f$, $\mathring{\bar{u}}_s$, $\bar{c}_f$, $\bar{c}_s$ and $\mathring{\bar{g}}_s$ from the given data but requires further discussion for $\mathring{\bar{v}}_s$ and $\bar{c}_s^*$. The scaling of v_s by the reference fluid velocity is natural due to the velocity continuity assumption at the interface, but the structure velocity deep inside the wall could be mainly determined by the slow growth velocity, which could lead to widely varying magnitudes for $\mathring{\bar{v}}_s$ and is one of the reasons why the structure equation is excluded from the analysis in this thesis. The reference value for the foam cell concentration c_s^* was chosen as identical to that of c_f and c_s. Ignoring advection there holds $St\, \partial_{\bar{t}} \bar{c}_s^* \approx \bar{\beta} \bar{c}_s$ and thus, assuming $\bar{c}_s \approx 1$, we have that $\partial_{\bar{t}} \bar{c}_s^* = \bar{\beta} / St = 1 \times 10^{-7}$ such that $\bar{c}_s^* \approx 1$ after $1 \times 10^7 \times T \approx 4$ months, which is a reasonable time frame.

To identify the scales in this problem we wish to introduce a small parameter ε and relate the magnitude of the physical parameters to it. A suggestion for such a scaling can be found in the last column of Table 2.4 if $\varepsilon := 10^{-8}$. Here, most parameters are of order 1 except for the Péclet numbers, which are of order ε^{-1}, and the permeability and the macrophage-to-foam cell conversion rate, which are of order ε. Since the inverse of the Péclet number is the diffusion factor, we in fact identify two orders, namely $\mathcal{O}(1)$ and $\mathcal{O}(\varepsilon)$.

Both the value of ε and the scaling of parameters in ε are somewhat arbitrary for this complex problem and, for example, more than two orders could have been introduced with a larger ε. The choice made here balances a reduction of the magnitudes of parameters sharing an order while maintaining a small value of ε. This only matters if the limit $\varepsilon \to 0$ is examined, where e.g. the magnitude of ε controls the error between original model and limit system.

Fundamentally, the choice of scaling is more art than science. The chosen scaling appears to be sensible for the models studied here in the sense that a limit exists, that some central properties of the original model are preserved and that the numerical solution of the limit system is feasible. Even though the scaling from Table 2.4 appears natural to the author, superiority to other approaches is not claimed.

Returning to the suggested scaling, the $\mathcal{O}(1)$-scale could be described as fast processes happening with the speed of the heart beat, since the period length has been normalized to 1, whereas the $\mathcal{O}(\varepsilon)$-scale are slow processes happening at the speed of growth, since growth increases with rate $\bar{\gamma}\bar{\beta}_0 = \mathcal{O}(\varepsilon)$. While we focus on the temporal effect of these parameters, they also dictate the spatial scales, e.g. the high Péclet numbers lead to the occurrence of boundary layers near the endothelium. Slow are hence the growth of the plaque, the diffusion of monocytes and macrophages, their migration across the endothelium and the conversion of macrophages into foam cells. This motivates us to look at two complementing multiscale models, both omitting the fluid-structure interaction due to its complexity. We first examine the coupling of the fast fluid flow to the slow growth. In the model of Yang et. al. such a coupling is very indirect, with the fluid only influencing the delivery of monocytes to the vicinity of the endothelium. We will instead study a more direct coupling through the wall shear stress. Specifically, we will assume that the growth rate directly depends on the wall shear stress while omitting monocytes, macrophages and foam cells. This is complemented by a second model which only examines the interaction between monocytes and macrophages, where the monocytes are advected by a fast velocity field but permeate through the endothelium only through slow diffusive fluxes.

Chapter 3

Periodically-Forced PDE-ODE Fast-Slow Systems

Motivated by the non-dimensional model presented in Section 2.3, we wish to investigate the interaction between slow growth and fast fluid field. By a significant simplification of the original model we couple the wall shear stress of the fluid field directly to a growth variable which influences the fluid domain, i.e. omitting monocytes, macrophages, foam cells and the elastic wall behavior. The analysis of such a model is still involved since the multiscale convergence happens on moving geometries under the low regularity of the wall shear stress.

To discuss the multiscale convergence without these technical details the present chapter investigates an even simpler model of a coupled system of slow ordinary and fast partial differential equations, the prototype being the system

$$\begin{aligned} q_\varepsilon'(t) &= \varepsilon g(q_\varepsilon(t), u_\varepsilon(t)), & q_\varepsilon(0) &= q^0, \\ \partial_t u_\varepsilon(t) + A(q_\varepsilon(t))u_\varepsilon(t) &= f(t), & u_\varepsilon(0) &= u^0, \end{aligned}$$

on a timescale $t \in (0, \varepsilon^{-1}\mathcal{T})$ for some $\mathcal{T} > 0$ with a small parameter $0 < \varepsilon \ll 1$. The slow variable q_ε solves an ordinary differential equation and represents the growth in the plaque model. The fast variable u_ε solves a partial differential equation with elliptic operators $A(\cdot)$ depending on the slow state q_ε and is driven by a 1-periodic forcing f. The partial differential equation can be seen as a simplification of the fluid equation on a moving domain which is pulled back to the reference domain and hence has coefficients depending on the deformation field, which itself depends on q_ε. The forcing f represents the periodic boundary conditions. Since such a transformation is discussed in detail in the next chapter, we will only study model problems in the present chapter, which could be of independent interest.

The main result of this chapter is that

$$\|q_\varepsilon - q_0\|_{C([0,\varepsilon^{-1}\mathcal{T}])} = \mathcal{O}(\varepsilon)$$

where q_0 solves the averaging-type limit equation

$$q_0'(t) = \varepsilon \int_0^1 g(q_0(t), u_\pi(s; q_0(t)))\,\mathrm{d}s, \quad q_0(0) = q^0$$

and $u_\pi(\cdot; q)$ for fixed $q \in Q$ is the time-periodic solution to

$$\partial_t u_\pi(t; q) + A(q)u_\pi(t; q) = f(t), \quad u_\pi(0; q) = u_\pi(1; q),$$

see Theorem 3.1.1 below. Except for a boundary layer at $t = 0$ the fast variable u_ε is close to $u_\pi(\cdot; q_0)$, see Lemma 3.4.7.

The investigation of slow-fast systems of nonlinear ordinary differential equations started with the seminal papers of Tikhonov [Tik48], [Tik52] and has expanded significantly since then, e.g. with the geometric singular perturbation theory of Fenichel [Fen79], see [Kue15] for a modern introduction and review. In this setting it is assumed that the fast flow, i.e. the dynamical system where the slow components are considered fixed, tends to an equilibrium. If the fast flow has a cyclic limit behavior, as in our situation, the limit equation has an averaging structure. This kind of slow-fast system was first analyzed by Pontryagin and Rodygin in [PR60] for autonomous ordinary differential equations and is closely linked to the theory of averaging, see e.g. the monograph by Sanders et. al. [SVM07].

For partial differential equations, the theory is much less well-developed, see e.g. [Kue15] and [SVM07] for historical overviews. For single parabolic partial differential equations, temporal singular perturbations for non-autonomous systems have been investigated, in particular with respect to the persistence and perturbation of attractors and invariant manifolds, e.g. by Vishik and collaborators [BV92], [VC07], [CV01], [CPV08], see also [CLR13] and [Hen81]. To our knowledge, there are few investigations of slow-fast systems of coupled partial or ordinary and partial differential equations. Henry [Hen81] treats the following problem, where both components are evolving slowly compared to their differential operator and forcing:

$$\begin{aligned} q_\varepsilon'(t) &= \varepsilon g(t, q_\varepsilon(t), u_\varepsilon(t)), & q_\varepsilon(0) &= q^0, \\ \partial_t u_\varepsilon(t) + \varepsilon A(t, q_\varepsilon(t)) u_\varepsilon(t) &= \varepsilon f(t, u_\varepsilon(t), q_\varepsilon(t)), & u_\varepsilon(0) &= u^0 \end{aligned}$$

with A, f, $\mathrm{D}_u f$ and g having a well-defined average in time, among other requirements. In this setting both components evolve with averaged forcing in the limit.

The goal of the present work is to prove convergence to the limit equation of order $\mathcal{O}(\varepsilon)$ under the assumption of Lipschitz continuity of the involved objects. In contrast to the existing literature our approach is elementary in its techniques but requires little regularity while still yielding quantitative estimates. This is not only of interest in itself but also important for the numerical realization. To emphasize the dynamical nature of our result, we present it in a framework where the fast process is described by a general evolution process. We will first state general assumptions on the fast process under which we can prove first-order convergence, give the proof of the convergence result, first for bounded and then for unbounded right-hand sides g of the ordinary differential equation. We then discuss how, under the assumption of linearity, the averaging reduces to a quasi-static equation with an averaged forcing.

3.1 Notation and Assumptions

Let $Q \subset \mathbb{R}^n$ for $n \in \mathbb{N}$ be a connected, bounded and open set and denote the norm on $\mathbb{R}^n$ by $|\cdot|$. Let X denote a Banach space with norm $\|\cdot\|$. We remind that $C_\pi(X)$ denotes the set of continuous 1-periodic, X-valued functions.

Let $\mathcal{U} := \{U(t,s;q) \mid t \geq s, q \in C(\mathbb{R},Q)\} \subset C(X,X)$ be a parametrized evolution process[1]: A family of maps such that $\mathcal{U}(q) = \{U(t,s;q); t \geq s\}$ is an evolution process for each $q \in C(\mathbb{R},Q)$:

- $U(t,t;q) = \mathrm{Id}_X$ for all $t \in \mathbb{R}$,
- $U(t,s;q) = U(t,r;q)U(r,s;q)$ for all $t \geq r \geq s$,
- $(t,s,u^0) \mapsto U(t,s;q)u^0$ is continuous for $t \geq s$, $u^0 \in X$.

Furthermore, $\mathcal{U}$ is assumed to be local-in-time in the sense that for $t \geq s$ and $q, \tilde{q} \in C(\mathbb{R},Q)$ with $q \equiv \tilde{q}$ on $[s,t]$ there holds $U(t,s;q) = U(t,s;\tilde{q})$, i.e. the evolution depends only on the present values of q. By this property, we can write $U(t,s;q)$ for any function $q \in C([s,t],Q)$ with $t \geq s$. We also assume:

A1. The evolution operator is exponentially stable in the sense that there exists $\alpha > 0$ such that

$$\|U(t,s;q)u^0 - U(t,s;q)\tilde{u}^0\| \lesssim \mathrm{e}^{-\alpha(t-s)}\|u^0 - \tilde{u}^0\|$$

for any $s < t$, $u^0, \tilde{u}^0 \in X$ and $q \in C([s,t],Q)$.

A2. The operator is Lipschitz continuous with respect to q in the sense that there exists a monotone function $\lambda\colon \mathbb{R}_+ \to \mathbb{R}_+$ such that

$$\|U(t,s;q)u^0 - U(t,s;\tilde{q})u^0\| \lesssim \|q - \tilde{q}\|_{C([s,t])}\left(\|u^0\| + \lambda(t-s)\right)$$

for $s < t$, $u^0 \in X$ and $q, \tilde{q} \in C([s,t],Q)$.

A3. The process is 1-periodic for each $q \in Q$:

$$U(t+1,s+1;q) = U(t,s;q)$$

for any $s < t$.

We investigate the following problem: For uniformly Lipschitz continuous function $g\colon Q \times X \to \mathbb{R}^n$ we search for a solution $q_\varepsilon\colon [0,\varepsilon^{-1}\mathcal{T}) \to Q$ of the ordinary differential equation

$$q_\varepsilon'(t) = \varepsilon g(q_\varepsilon(t), U(t,0;q_\varepsilon)u^0), \quad q_\varepsilon(0) = q^0 \tag{3.1}$$

with initial value $q^0 \in Q$ and $u^0 \in X$. In our examples, U is the solution operator to a non-autonomous partial differential equation in the sense that $U(t,s;q)u^0 = u(t)$ with u being the solution of

$$\partial_t u(t) + A(q(t))u(t) = f(t), \quad u(s) = u^0$$

where A is a q-dependent elliptic operator and f is 1-periodic, see the examples below for more details. We may thus think of eq. (3.1) as a condensation of

$$\begin{aligned} q_\varepsilon'(t) &= \varepsilon g(q_\varepsilon(t), u_\varepsilon(t)), & q_\varepsilon(0) &= q^0, \\ \partial_t u_\varepsilon(t) + A(q_\varepsilon(t))u_\varepsilon(t) &= f(t), & u_\varepsilon(0) &= u^0. \end{aligned}$$

A simple consequence of assumptions (A1) and (A3) is, see Lemma 3.3.1, that for any $q \in Q$ there exists $u_\pi^0(q) \in X$ such that $u_\pi(t;q) := U(t,0;q)u_\pi^0(q)$ is 1-periodic. With this notation, our main result is the following:

[1] Due to the requirement $t \geq s$ they could be called *semi*-processes, but we skip the prefix.

Theorem 3.1.1. *For any $q^0 \in Q$ and $u^0 \in X$ there exists $\mathcal{T} > 0$ such that for all $0 < \varepsilon < \varepsilon^*$ with ε^* small enough the solution $q_\varepsilon \colon [0, \varepsilon^{-1}\mathcal{T}] \to Q$ of*

$$q_\varepsilon'(t) = \varepsilon g(q_\varepsilon(t), U(t, 0; q_\varepsilon)u^0), \quad q_\varepsilon(0) = q^0 \tag{3.1}$$

exists and converges to the, also existing, solution $q_0 \colon [0, \varepsilon^{-1}\mathcal{T}] \to Q$ of

$$q_0'(t) = \varepsilon \int_0^1 g(q_0(t), u_\pi(s; q_0(t)))\,\mathrm{d}s, \quad q_0(0) = q^0 \tag{3.2}$$

in the sense that

$$\|q_\varepsilon(t) - q_0(t)\| \lesssim \varepsilon$$

for all $t \in [0, \varepsilon^{-1}\mathcal{T}]$.

3.2 Examples

Before we continue to the proof of our main theorem, we give some examples of evolution processes which satisfy the assumptions above.

Let X be a Hilbert space with scalar product $(\cdot, \cdot)$. Let V be a separable, reflexive Banach space, densely embedded in X. Hence $V \hookrightarrow X \hookrightarrow V^*$ by the usual identification of X with X^*. The norms on V and V^* are denoted as $\|\cdot\|_V$ and $\|\cdot\|_{V^*}$, the duality product between V and V^* by $\langle \cdot, \cdot \rangle$. We define $W(s,t) := \{u \in L^2(s,t;V); \partial_t u \in L^2(s,t;V^*)\}$, being a Banach space with norm $\|u\|_{W(s,t)} := \|u\|_{L^2(s,t;V)} + \|\partial_t u\|_{L^2(s,t;V^*)}$ and note that $W(s,t) \hookrightarrow C([s,t], X)$.

We will examine families of monotone operators, see [Sho96] for an introduction to monotone operators. Let $A \colon Q \to \{V \to V^*\}$ be a family of operators, such that

B1. For each $q \in Q$, $A(q)$ is radially continuous.

B2. The family is uniformly strongly monotone: There exists $\gamma > 0$ such that

$$\langle A(q)u - A(q)v, u - v\rangle \geq \gamma \|u - v\|_V^2$$

for all $q \in Q$ and $u, v \in V$.

B3. The family has uniform linear growth: There exists $M > 0$ such that

$$\|A(q)u\|_{V^*} \leq M(\|u\|_V + 1)$$

for all $q \in Q$ and $u \in V$.

B4. The map A is Lipschitz continuous in the sense that there is $L > 0$ with

$$\|A(q)u - A(\tilde{q})u\|_{V^*} \leq L|q - \tilde{q}|(\|u\|_V + 1)$$

for all $q, \tilde{q} \in Q$ and $u \in V$.

Note that (B4) implies (B3) if for one $q \in Q$ the operator $A(q)$ grows linearly.

The evolution process U is generated by the solutions of the periodically-forced parabolic equation with operators A: For $f \in L^2(0,1;V^*)$ and $u^0 \in X$ we define $U(t,s;q)u^0 := u(t)$, where u is the solution to

$$\partial_r u(r) + A(q(r))u(r) = f(r) \quad \text{for } r \in (s,t) \text{ a.e.}, \quad u(s) = u^0, \tag{3.3}$$

with f extended periodically to $\mathbb{R}$. We first give some more specific examples of operator families A with the above properties, then prove well-posedness of the associated process and its fulfillment of our assumptions (A1)–(A3).

Remark 3.2.1. We could also study for $1 < p < \infty$ the setting corresponding to

$$W(s,t) := \{u \in L^p(I,V) \mid \partial_t u \in [L^p(I,V)]^* \cong L^q(I,V^*)\}$$

for $\frac{1}{p} + \frac{1}{q} = 1$, with appropriate changes to the assumptions. ◇

Example 3.2.2. In case of linear operators $A\colon Q \to \mathcal{L}(V,V^*)$, (B1) – (B4) reduce to uniform coercivity and boundedness, i.e. there exists $\gamma > 0$ and $M > 0$ such that

$$\langle A(q)u, u\rangle \geq \gamma \|u\|_V^2, \quad \|A(q)u\|_{V^*} \leq M\|u\|_V$$

for all $q \in Q$ and $u \in V$, together with Lipschitz continuity of A: There is $L > 0$ such that for all $q, \tilde{q} \in Q$ we have

$$\|A(q) - A(\tilde{q})\|_{\mathcal{L}(V,V^*)} \leq L|q - \tilde{q}|. \qquad \diamond$$

Example 3.2.3. Let $A_0\colon V \to V^*$ be radially continuous and strongly monotone, which reduces to coercivity if $A_0 \in \mathcal{L}(V,V^*)$. Let $\alpha\colon Q \to \mathbb{R}$ be Lipschitz continuous such that $\underline{\alpha} \leq \alpha(\cdot) \leq \overline{\alpha}$ for $0 < \underline{\alpha} < \overline{\alpha} < \infty$. Then $A(q) := \alpha(q)A_0$ is an operator family satisfying (B1) – (B4). ◇

Example 3.2.4. Let $\Omega \subset \mathbb{R}^d$ with $d \in \mathbb{N}$ be a bounded Lipschitz domain and $V := H_0^1(\Omega)$, $X := L^2(\Omega)$. Let $K\colon Q \to L^\infty(\Omega, \mathcal{L}(\mathbb{R}^d, \mathbb{R}^d))$ be Lipschitz continuous and $K(q)$ be (q,x)-uniformly bounded and positive definite matrices, i.e. there exists $\gamma > 0$ and $M > 0$ such that

$$[K(q)](x)\xi \cdot \xi \geq \gamma|\xi|^2, \quad \|K(q)\|_{L^\infty(\Omega,\mathcal{L}(\mathbb{R}^d,\mathbb{R}^d))} \leq M$$

for all $q \in Q$, $\xi \in \mathbb{R}^d$ and $x \in \Omega$ almost everywhere. Then the family of operators $A(q) := -\operatorname{div}(K(q)\nabla\cdot)$ satisfies (B1) – (B4), since by Example 3.2.2 we have to check:

- The family is uniformly bounded by M: Since for $q \in Q$ and $u, v \in V$ we have $(K(q)\nabla u, \nabla v) \leq \|K(q)\|_{L^\infty(\Omega,\mathcal{L}(\mathbb{R}^d,\mathbb{R}^d))}\|\nabla u\|\|\nabla v\|$, there holds

$$\|A(q)\|_{\mathcal{L}(V,V^*)} \leq \|K(q)\|_{L^\infty(\Omega,\mathcal{L}(\mathbb{R}^d,\mathbb{R}^d))} \leq M.$$

- The operators are uniformly coercive: Since K is uniformly positive definite, we have for all $q \in Q$ and $u \in V$:

$$\langle A(q)u, u\rangle = (K(q)\nabla u, \nabla u) \geq \gamma\|\nabla u\|^2.$$

- The map $q \mapsto A(q)$ is Lipschitz continuous, since for $q, \tilde{q} \in Q$

$$\|A(q) - A(\tilde{q})\|_{\mathcal{L}(V,V^*)} \leq \|K(q) - K(\tilde{q})\|_{L^\infty(\Omega,\mathcal{L}(\mathbb{R}^d,\mathbb{R}^d))} \lesssim |q - \tilde{q}|. \qquad \diamond$$

Example 3.2.5. Let $\Omega \subset \mathbb{R}^d$ with $d \in \mathbb{N}$ be a bounded Lipschitz domain, $V := H^1_{0,\sigma}(\Omega)$ and $X := L^2_\sigma(\Omega)$ be the solenoidal function spaces, i.e. those spaces with vanishing (weak) divergence. Let $P\colon L^2(\Omega) \to L^2_\sigma(\Omega)$ denote the Helmholtz projection. Then the Stokes operator, $A_0 := -P\Delta \in \mathcal{L}(V, V^*)$, is coercive and hence Stokes' problem with slowly changing viscosities falls into the described framework by Example 3.2.3. ◇

Lemma 3.2.6. *The evolution process U is well-defined in the sense that for $t \geq s$, $q \in C([s,t], Q)$ and $u^0 \in X$ a unique solution $u \in W(s,t) \hookrightarrow C([s,t], X)$ to problem (3.3) exists. We have the a-priori estimate*

$$\|u\|_{L^\infty(s,t;X)} + \|u\|_{L^2(s,t;V)} \lesssim \|u^0\| + \|f\|_{L^2(s,t;V^*)}.$$

Proof. Note that for fixed $q \in Q$, we have by strong monotonicity (B2) for $u \in V$:

$$\langle A(q)u, u\rangle = \langle A(q)u - A(q)0, u - 0\rangle + \langle A(q)0, u\rangle \geq (\gamma\|u\|_V - M)\|u\|_V$$

where we used that $\|A(q)0\|_{V^*} \leq M$ due to (B3). Hence $\langle A(q)u, u\rangle \|u\|_V^{-1} \to \infty$ for $\|u\|_V \to \infty$ and $A(q)$ is coercive with constants independent of q. Existence of solutions for this particular non-autonomous Cauchy problem then follows from standard theory, see e.g. [Sho96, Proposition III.4.1]. Uniqueness follows from the proof of exponential stability, see below. For the a-priori estimate, we test as usual with the solution u itself, to arrive at

$$\frac{1}{2}\frac{\mathrm{d}}{\mathrm{d}r}\|u(r)\|^2 + \langle A(q(r))u(r), u(r)\rangle = \langle f(r), u(r)\rangle$$

and apply the coercivity estimate from above, to get

$$\frac{1}{2}\frac{\mathrm{d}}{\mathrm{d}r}\|u(r)\|^2 + \gamma\|u(r)\|_V^2 \leq (\|f(r)\|_{V^*} + M)\|u(r)\|_V.$$

The estimate then follows by application of Young's inequality with suitable constants and integration in time. □

Lemma 3.2.7. *The process is exponential stable as assumed by (A1).*

Proof. Let $s < t$, $q \in C([s,t], Q)$ and $u^0, \tilde{u}^0 \in X$. Let $u(t) := U(t,s;q)u^0$ and $\tilde{u}(t) := U(t,s;q)\tilde{u}^0$, such that both satisfy the corresponding eq. (3.3). Then

$$\frac{1}{2}\frac{\mathrm{d}}{\mathrm{d}t}\|u - \tilde{u}\|^2 + \langle A(q)u - A\tilde{u}, u - \tilde{u}\rangle = 0, \quad u(s) - \tilde{u}(s) = u^0 - \tilde{u}^0$$

and strong monotonicity (B2) and $V \hookrightarrow X$ yield $\frac{\mathrm{d}}{\mathrm{d}t}\|u - \tilde{u}\|^2 + \|u - \tilde{u}\|^2 \lesssim 0$. By Gronwall's inequality, this gives as claimed

$$\|u(t) - \tilde{u}(t)\|^2 \leq \mathrm{e}^{-C(t-s)}\|u^0 - \tilde{u}^0\|.$$ □

Lemma 3.2.8. *The assumption (A2) of Lipschitz continuity is satisfied.*

Proof. Let $s < t$, $q, \tilde{q} \in C([s,t], Q)$ and $u^0 \in X$. Let $u(t) := U(t,s;q)u^0$ and $\tilde{u}(t) := U(t,s;\tilde{q})u^0$, such that both satisfy the corresponding eq. (3.3). Then

$$\partial_r(u - \tilde{u})(r) + A(q(r))u(r) - A(q(r))\tilde{u}(r) = A(\tilde{q}(r))\tilde{u}(r) - A(q(r))\tilde{u}(r)$$

with $u(s) - \tilde{u}(s) = 0$. By arguments as in the preceding results, this yields

$$\|u(t) - \tilde{u}(t)\| \lesssim \|A(q)\tilde{u} - A(\tilde{q})\tilde{u}\|_{L^2(s,t;V^*)}.$$

Applying the Lipschitz assumption (B4) pointwise, we have

$$\|A(q)\tilde{u} - A(\tilde{q})\tilde{u}\|_{L^2(s,t;V^*)} \lesssim \|q - \tilde{q}\|_{C([s,t])}(\|\tilde{u}\|_{L^2(s,t;V)} + \sqrt{t-s}).$$

Together with the a-priori estimate for $\tilde{u}$ and using the periodicity of f, this yields (A2). □

Lemma 3.2.9. *The process is* 1*-periodic as assumed by* (A3).

Proof. This is evident due to the 1-periodicity of f. □

We conclude this overview with a simple application of Theorem 3.1.1.

Example 3.2.10. With $\Omega := (-1,1)^2$ and $Q := (1,2)$ consider the problem

$$\partial_t u_\varepsilon(t,x) - (1 + q_\varepsilon(t))\Delta u_\varepsilon(t,x) = \sin(2\pi t)\sin(\pi x_1)\sin(\pi x_2) \quad \text{in } \Omega, \tag{3.4a}$$

$$q_\varepsilon'(t) = \varepsilon\|u_\varepsilon(t)\|_{L^2(\Omega)} q_\varepsilon(t)(2 - q_\varepsilon(t)) \tag{3.4b}$$

with initial values $u_\varepsilon(0) = 0$, $q_\varepsilon(0) = q^0 = 1$ and $u_\varepsilon = 0$ on $\partial\Omega$. The fast equation is of the type investigated in Example 3.2.4 and hence a process with $X = L^2(\Omega)$. The right-hand g of the slow equation is Lipschitz continuous in X and Q but unbounded. Applying Theorem 3.1.1[2] the limit equation is

$$q_0'(t) = \varepsilon \left(\int_0^1 \|u_\pi(s; q_0(t))\|_{L^2(\Omega)} \, \mathrm{d}s \right) q_0(t)(2 - q_0(t)) \tag{3.5}$$

with $u_\pi(\cdot; q)$ for $q \in Q$ being the 1-periodic solution to

$$\partial_s u_\pi(s,x;q) - (1+q)\Delta u_\pi(s,x;q) = \sin(2\pi s)\sin(\pi x_1)\sin(\pi x_2).$$

The periodic problem has an autonomous differential operator, in contrast to the original non-autonomous problem. We can in particular apply a simple eigenfunction decomposition of the periodic problem to see that it has the explicit solution

$$u_\pi(s,x;q) = \frac{1}{2\pi} \frac{\pi(1+q)\sin(2\pi s) - \cos(2\pi s)}{\pi^2(1+q)^2 + 1} \sin(\pi x_1)\sin(\pi x_2)$$

and hence the time-average of the norm is given by

$$\int_0^1 \|u_\pi(s; q_0(t))\|_{L^2(\Omega)} \, \mathrm{d}s = \frac{1}{\pi^2\sqrt{\pi^2(1+q)^2 + 1}}.$$

Therefore, the limit eq. (3.5) can be written explicitly as

$$q_0'(t) = \varepsilon \frac{q_0(t)(2 - q_0(t))}{\pi^2\sqrt{\pi^2(1+q_0(t))^2 + 1}}, \quad q_0(0) = 1. \tag{3.6}$$

Thus only the solution of a simple ordinary differential equation, instead of the coupled, oscillatory system of partial and ordinary differential equations, is necessary. ◇

[2] While $q^0 \in \partial Q$ is not included in the theory, this is of course only a formal problem since the right-hand side of eq. (3.4b) is non-negative and zero only if $u_\varepsilon = 0$ such that $q_\varepsilon(t) \in Q$ for $t > 0$.

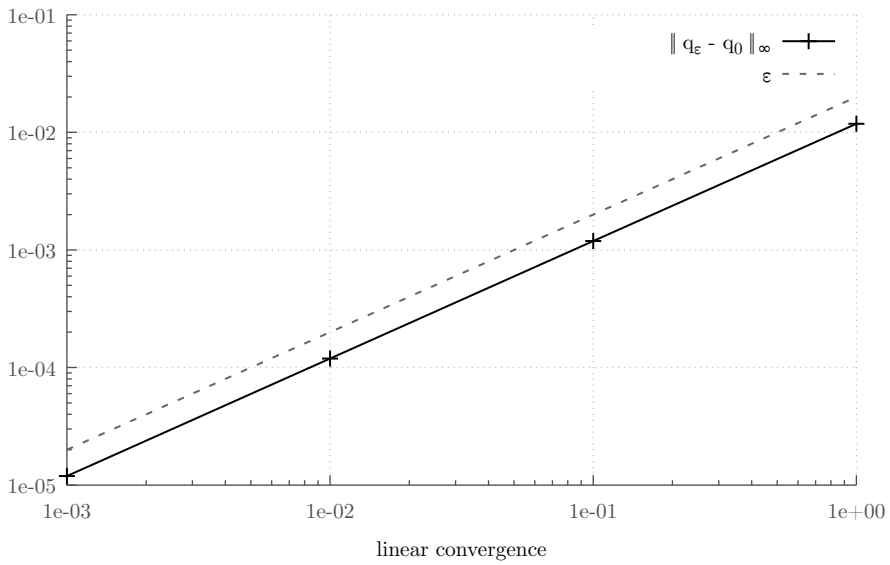

Figure 3.1: Error between the numerical solutions to q_ε and q_0 from Example 3.2.10 in terms of ε together with a reference linear convergence (dashed line).

We also investigated the convergence in Example 3.2.10 numerically, but keep this section brief and refer to Chapter 5 for a discussion of the issues when solving the limit equation for the more interesting plaque problem on moving domains. For the fast-slow system we used the second-order backward difference scheme (BDF2) for the temporal discretization and quadratic finite elements on a quadrilateral mesh for the spatial discretization. Temporal and spatial resolution were chosen such that the numerical discretization errors could be neglected. The direct numerical simulation was carried out using the finite element library deal.II [Alz+18], the limit eq. (3.6) was solved in MATLAB. As can be seen in Figure 3.1, the results are in good agreement with the theory.

3.3 Preliminary Results

We briefly gather some consequences of our assumptions:

Lemma 3.3.1. *For every $q \in Q$ there exists a unique $u_\pi^0(q) \in X$ such that the function $u_\pi(t;q) := U(t,0;q)u_\pi^0(q)$ is 1-periodic.*

Proof. Fix $q \in Q$. Then $u_\pi^0(q)$ is the fixed-point of the Poincaré map

$$P\colon X \to X, \quad u \mapsto U(1,0;q)u$$

due to the periodicity assumption (A3). The same assumption yields

$$P^k := P \circ \cdots \circ P = U(k,0;q)$$

for $k \in \mathbb{N}$. The exponential stability assumption (A1) implies

$$\|P^k(u) - P^k(\tilde{u})\| \leq C\mathrm{e}^{-\alpha k}\|u - \tilde{u}\|.$$

Hence for sufficiently large k we have $C\mathrm{e}^{-\alpha k} < 1$ and P^k is a contraction. Thus P has a unique fixed-point by Banach's theorem, which is $u^0_\pi(q)$. □

Lemma 3.3.2. *The map*

$$Q \ni q \mapsto u_\pi(\,\cdot\,; q) \in C_\pi(X)$$

is Lipschitz-continuous. In particular, $q \mapsto u^0_\pi(q)$ is Lipschitz-continuous.

Proof. We first prove the second statement, the Lipschitz continuity of $q \mapsto u^0_\pi(q)$. Let $q, \tilde{q} \in Q$ and let $L \in \mathbb{N}$ be fixed. The periodicity yields

$$\begin{aligned}\|u^0_\pi(q) - u^0_\pi(\tilde{q})\| &= \|U(L,0;q)u^0_\pi(q) - U(L,0;\tilde{q})u^0_\pi(\tilde{q})\| \\ &\leq \|U(L,0;q)u^0_\pi(q) - U(L,0;\tilde{q})u^0_\pi(q)\| \\ &\quad + \|U(L,0;\tilde{q})u^0_\pi(q) - U(L,0;\tilde{q})u^0_\pi(\tilde{q})\|.\end{aligned}$$

Application of our assumptions (A1) and (A2) hence implies

$$\|u^0_\pi(q) - u^0_\pi(\tilde{q})\| \leq C|q - \tilde{q}|\left(\|u^0_\pi(q)\| + \lambda(L)\right) + C\mathrm{e}^{-\alpha L}\|u^0_\pi(q) - u^0_\pi(\tilde{q})\|.$$

Choosing L large enough such that $C\mathrm{e}^{-\alpha L} < 1$ we get

$$\|u^0_\pi(q) - u^0_\pi(\tilde{q})\| \lesssim |q - \tilde{q}|\left(\|u^0_\pi(q)\| + 1\right).$$

Since Q is bounded, this yields as claimed that $\|u^0_\pi(q) - u^0_\pi(\tilde{q})\| \lesssim |q - \tilde{q}|$. Now consider any $t \in [0, 1)$. Then with (A1) and (A2) as above, we get

$$\begin{aligned}\|u_\pi(t;q) - u_\pi(t;\tilde{q})\| &= \|U(t,0;q)u^0_\pi(q) - U(t,0;\tilde{q})u^0_\pi(\tilde{q})\| \\ &\lesssim |q - \tilde{q}|\left(\|u^0_\pi(q)\| + \lambda(t)\right) + \mathrm{e}^{-\alpha t}\|u^0_\pi(q) - u^0_\pi(\tilde{q})\|\end{aligned}$$

and the Lipschitz estimate for $\|u^0_\pi(q) - u^0_\pi(\tilde{q})\|$ yields the claim

$$\|u_\pi(t;q) - u_\pi(t;\tilde{q})\| \lesssim |q - \tilde{q}|.$$ □

Lemma 3.3.3. *The periodic trajectories are uniformly bounded in q, i.e. $\|u_\pi(t;q)\| \lesssim 1$ for all $t \in [0,1)$ and $q \in Q$.*

Proof. By Lemma 3.3.2 and periodicity we have that

$$\mathbb{R}/\mathbb{Z} \times Q \ni (t,q) \mapsto u_\pi(t;q) \in X$$

is uniformly continuous and hence the claim follows since all periodic trajectories are contained in the range of this mapping and $Q \times \mathbb{R}/\mathbb{Z}$ is bounded. □

For completeness' sake, we now prove that a solution q_ε of eq. (3.1) exists until q_ε leaves Q. The interval of existence may depend on ε and we assume that g is bounded. These restrictions are lifted for sufficiently small ε by our main result.

Lemma 3.3.4. *Assume that g is bounded. For any $\varepsilon > 0$ there exists $T_\varepsilon > 0$ such that the solution q_ε of eq. (3.1) exists on $I_\varepsilon = [0, T_\varepsilon)$. If the maximal interval of existence is finite, then $\lim_{t \uparrow T_\varepsilon} q_\varepsilon(t) \in \partial Q$.*

Proof. Let g be bounded by $M > 0$ and $I_\varepsilon := [0, T_\varepsilon)$ with $T_\varepsilon > 0$ to be chosen later. We use a fixed-point argument and consider the set

$$C_\varepsilon := \{q \in C(I_\varepsilon, Q) \mid q(0) = q^0, |q(t) - q(s)| \leq \varepsilon M|t - s| \ \forall t, s \in I_\varepsilon\}.$$

Then q_ε is a fixed-point of the map

$$S_\varepsilon \colon C_\varepsilon \to C_\varepsilon, \quad [S_\varepsilon(q)](t) := q^0 + \varepsilon \int_0^t g(q(s), U(s, 0; q)u^0)\,\mathrm{d}s.$$

Due to the boundedness assumption on g, i.e. $|g| \leq M$, this map is well-defined for T_ε small enough such that $B_\rho(q^0) \subset Q$ with $\rho := \varepsilon T_\varepsilon M$. To apply the Banach fixed-point theorem, we prove the Lipschitz continuity of S_ε. Let $q, \tilde{q} \in C_\varepsilon$. We have for any $t \in I_\varepsilon$ that

$$\begin{aligned}
|[S_\varepsilon(q)](t) - [S_\varepsilon(\tilde{q})](t)| &\leq \varepsilon \int_0^t |g(q(s), U(s, 0; q)u^0) - g(\tilde{q}(s), U(s, 0; \tilde{q}))|\,\mathrm{d}s \\
&\lesssim \varepsilon \int_0^t \left(|q(s) - \tilde{q}(s)| + \|U(s, 0; q)u^0 - U(s, 0; \tilde{q})u^0\|\right)\mathrm{d}s \\
&\lesssim \varepsilon T_\varepsilon \left(\|q - \tilde{q}\|_{C(I_\varepsilon)} + \|U(\,\cdot\,, 0; q)u^0 - U(\,\cdot\,, 0; \tilde{q})u^0\|_{C(I_\varepsilon, X)}\right).
\end{aligned}$$

By the Lipschitz assumption (A2) we have

$$\|U(\,\cdot\,, 0; q)u^0 - U(\,\cdot\,, 0; \tilde{q})u^0\|_{C(I_\varepsilon, X)} \lesssim \|q - \tilde{q}\|_{C(I_\varepsilon)} \left(\|u^0\| + \lambda(T_\varepsilon)\right).$$

Thus for the initial Lipschitz estimate:

$$\|S_\varepsilon(q) - S_\varepsilon(\tilde{q})\|_{C(I_\varepsilon)} \lesssim \varepsilon T_\varepsilon \|q - \tilde{q}\|_{C(I_\varepsilon)} \left(1 + \lambda(T_\varepsilon)\right).$$

With T_ε sufficiently small, this implies that S_ε is a contraction and hence Banach's fixed-point theorem yields existence and uniqueness of q_ε.

For the breakdown result, note that by g's boundedness, $\lim_{t \uparrow T_\varepsilon} q_\varepsilon(t)$ exists. If $q_\varepsilon(T_\varepsilon) \in Q$ we could extend q_ε beyond T_ε locally, contradicting the maximality of T_ε. Hence $q_\varepsilon(T_\varepsilon) \in \partial Q$. □

3.4 Proof of Multiscale Convergence

We use the following classical result for averaging of an ordinary differential equations with periodic right-hand side, cf. [SVM07, Theorem 2.8.1]:

Theorem 3.4.1. *Let $Q \subset \mathbb{R}^n$ be connected, bounded and open. Let $f \colon \mathbb{R} \times Q \to \mathbb{R}^n$ be 1-periodic, continuous in its first and uniformly Lipschitz continuous in its second argument. Then for any $x^0 \in Q$ there is a $\mathcal{T} > 0$ such that a solution $x_0 \colon [0, \varepsilon^{-1}\mathcal{T}] \to Q$ of*

$$x_0'(t) = \varepsilon \overline{f}(x_0(t)) := \varepsilon \int_0^1 f(s, x_0(t))\,\mathrm{d}s, \quad x_0(0) = x^0$$

exists. The solution x_0 is a first order approximation of the solution x_ε of

$$x_\varepsilon'(t) = \varepsilon f(t, x_\varepsilon(t)), \quad x_\varepsilon(0) = x^0$$

in the sense that there is an $\varepsilon^* > 0$ such that for any $0 < \varepsilon < \varepsilon^*$ the solution x_ε exists for all $t \in [0, \varepsilon^{-1}\mathcal{T}]$ and there holds

$$\max_{t \in [0, \varepsilon^{-1}\mathcal{T}]} |x_\varepsilon(t) - x_0(t)| \lesssim \varepsilon.$$

Proof. The existence of limit solutions on the $\mathcal{O}(\varepsilon^{-1})$-timescale follows by rescaling to slow time, $\tau := \varepsilon t$, and using that $x \mapsto \int_0^1 f(s,x)\,\mathrm{d}s$ is Lipschitz continuous, since f is. The main ingredient for the averaging result is a comparison of x_0 and x_ε by keeping x_ε fixed on small intervals, see [Art07] for details. □

Corollary 3.4.2. *There exists $\mathcal{T} > 0$ independent of ε such that the limit equation*

$$q_0'(t) = \varepsilon \int_0^1 g(q_0(t), u_\pi(s; q_0(t)))\,\mathrm{d}s, \quad q_0(0) = q^0 \tag{3.2}$$

has a unique solution $q_0 \colon [0, \varepsilon^{-1}\mathcal{T}] \to Q$. Furthermore, there is an $\varepsilon^* > 0$ such that for all $0 < \varepsilon < \varepsilon^*$ the solution $q_{\varepsilon,\pi}$ of

$$q_{\varepsilon,\pi}'(t) = \varepsilon g(q_{\varepsilon,\pi}(t), u_\pi(t; q_{\varepsilon,\pi}(t))), \quad q_{\varepsilon,\pi}(0) = q^0. \tag{3.7}$$

exists for $t \in [0, \varepsilon^{-1}\mathcal{T}]$ with

$$\max_{t \in [0, \varepsilon^{-1}\mathcal{T}]} |q_{\varepsilon,\pi}(t) - q_0(t)| \lesssim \varepsilon.$$

Proof. Define $G(t,q) := g(q, u_\pi(t;q))$. Then $q_{\varepsilon,\pi}'(t) = \varepsilon G(t, q_{\varepsilon,\pi}(t))$ and G is continuous and 1-periodic in t and Lipschitz continuous in q, the latter following from the Lipschitz continuity of g by assumption and of u_π by Lemma 3.3.2. The time-average of G is the right-hand side of the limit equation and hence we can apply the averaging theorem. □

With this result, it remains to prove that q_ε is close to $q_{\varepsilon,\pi}$. For this, we first make the additional assumption that g is bounded by $M > 0$. By careful analysis of the constants involved, we will lift this restriction later on. To this end, let the constant in $\lesssim$ be independent of M. We will first prove that $u_\varepsilon(t) := U(t,0;q_\varepsilon)u^0$ reaches an ε-neighborhood of $u_\pi(t; q_\varepsilon(t), \varepsilon)$ after a boundary layer of size $\mathcal{O}(|\ln \varepsilon|)$ and stays there, i.e. u_ε is slaved to u_π.

Lemma 3.4.3. *Let $K \in \mathbb{N}$ and $(a_k)_{k=0}^K$ be non-negative with $a_k \le b a_{k-1} + c$ for $b, c \ge 0$ and $k = 1, \dots, K$. Then $a_k \le b^k a_0 + c \sum_{j=0}^{k-1} b^j$ for $k = 1, \dots, K$.*

Proof. Follows by induction. □

Lemma 3.4.4. *There exists $C > 0$ such that there holds*

$$\|U(t,0;q_\varepsilon)u^0 - u_\pi(t; q_\varepsilon(t))\| \lesssim \mathrm{e}^{-\alpha t}\|u^0 - u_\pi^0(q^0)\| + \varepsilon M$$

for all $t \in I_\varepsilon$ with constants independent of $|I_\varepsilon|$.

Proof. First, using the assumption of exponential stability A1 we get

$$\|U(t,0;q_\varepsilon)u^0 - U(t,0;q_\varepsilon)u_\pi^0(q^0)\| \lesssim \mathrm{e}^{-\alpha t}\|u^0 - u_\pi^0(q^0)\|.$$

Hence it remains to prove that $\|U(t,0;q_\varepsilon)u_\pi^0(q^0) - u_\pi(t;q_\varepsilon(t))\| \lesssim \varepsilon M$. For this, let $L \in \mathbb{N}$ and the constant in $\lesssim$ in the following be independent of L. Let $I_k := [t_k, t_{k+1})$ for $k = 0, \dots, K$ with $0 = t_0 < t_1 < \dots < t_{K+1} = T_\varepsilon$ such that $|I_k| = L$ for $k = 0, \dots, K-1$ and $|I_K| \le L$.

Let $t \in I_k$ for $k = 0, \dots, K$ and define $q_\varepsilon^k := q_\varepsilon(t_k)$. Note that by the boundedness assumption on g and since $t - t_k \le L$ we have

$$|q_\varepsilon(t) - q_\varepsilon^k| = |q_\varepsilon(t) - q_\varepsilon(t_k)| \le \varepsilon \int_{t_k}^t |g(q_\varepsilon(s), u_\varepsilon(s))|\,\mathrm{d}s \le \varepsilon L M. \tag{3.8}$$

We estimate

$$\begin{aligned}&\|U(t,0;q_\varepsilon)u_\pi^0(q^0) - u_\pi(t;q_\varepsilon(t))\|\\ &\quad\le \|U(t,0;q_\varepsilon)u_\pi^0(q^0) - u_\pi(t;q_\varepsilon^k)\| + \|u_\pi(t;q_\varepsilon(t)) - u_\pi(t;q_\varepsilon^k)\|.\end{aligned}$$

The Lipschitz property of u_π by Lemma 3.3.2 and ineq. (3.8) yields

$$\|u_\pi(t;q_\varepsilon(t)) - u_\pi(t;q_\varepsilon^k)\| \lesssim |q_\varepsilon(t) - q_\varepsilon^k| \lesssim \varepsilon LM$$

and hence

$$\|U(t,0;q_\varepsilon)u_\pi^0(q^0) - u_\pi(t;q_\varepsilon(t))\| \le \|U(t,0;q_\varepsilon)u_\pi^0(q^0) - u_\pi(t;q_\varepsilon^k)\| + \varepsilon LM.$$

To estimate the first term on the right we add and subtract $U(t,t_k;q_\varepsilon)u_\pi^0(q_\varepsilon^k)$:

$$\begin{aligned}\|U(t,0;q_\varepsilon)u_\pi^0(q^0) - u_\pi(t;q_\varepsilon^k)\| \le{}& \|U(t,0;q_\varepsilon)u_\pi^0(q^0) - U(t,t_k;q_\varepsilon)u_\pi^0(q_\varepsilon^k)\|\\ &+ \|U(t,t_k;q_\varepsilon)u_\pi^0(q_\varepsilon^k) - u_\pi(t;q_\varepsilon^k)\|. \qquad (3.9)\end{aligned}$$

For the first term, we split the evolution on $[0,t]$ into $[0,t_k]$ and the remainder $[t_k,t]$. Using the assumption of exponential stability (A1) this results in

$$\begin{aligned}&\|U(t,0;q_\varepsilon)u_\pi^0(q^0) - U(t,t_k;q_\varepsilon)u_\pi^0(q_\varepsilon^k)\|\\ &\quad\lesssim \mathrm{e}^{-\alpha(t-t_k)}\|U(t_k,0;q_\varepsilon)u_\pi^0(q^0) - u_\pi^0(q_\varepsilon^k)\|. \qquad (3.10)\end{aligned}$$

For the second term the periodicity and $t_k \in \mathbb{N}$ imply

$$u_\pi(t;q_\varepsilon^k) = U(t,t_k;q_\varepsilon^k)u_\pi(t_k;q_\varepsilon^k) = U(t,t_k;q_\varepsilon^k)u_\pi^0(q_\varepsilon^k)$$

and thus the Lipschitz assumption (A2) yields

$$\begin{aligned}\|U(t,t_k;q_\varepsilon)u_\pi^0(q_\varepsilon^k) - u_\pi(t;q_\varepsilon^k)\| &\lesssim \|q_\varepsilon - q_\varepsilon^k\|_{C(t_k,t)}\left(\|u_\pi^0(q_\varepsilon^k)\| + \lambda(L)\right)\\ &\lesssim \varepsilon L(1+\lambda(L))M\|u_\pi(\,\cdot\,;q_\varepsilon^k)\|_{C_\pi(X)}\\ &\lesssim \varepsilon L\lambda(L)M,\end{aligned}$$

where we used Lemma 3.3.3 and assumed, without restriction of generality, that $\lambda(L) \ge 1$. Using the last estimate and ineq. (3.10) in ineq. (3.9) leads to

$$\begin{aligned}&\|U(t,0;q_\varepsilon)u_\pi^0(q^0) - u_\pi(t;q_\varepsilon(t))\|\\ &\quad\lesssim \mathrm{e}^{-\alpha(t-t_k)}\|U(t_k,0;q_\varepsilon)u_\pi^0(q^0) - u_\pi^0(q_\varepsilon^k)\| + \varepsilon L\lambda(L)M \qquad (3.11)\end{aligned}$$

for any $t \in I_k$. By passing to the limit $t \uparrow t_{k+1}$ for $k < K$ this yields

$$\begin{aligned}&\|U(t_{k+1},0;q_\varepsilon)u_\pi^0(q^0) - u_\pi(t_{k+1};q_\varepsilon^{k+1})\|\\ &\quad\lesssim \mathrm{e}^{-\alpha L}\|U(t_k,0;q_\varepsilon)u_\pi^0(q^0) - u_\pi^0(q_\varepsilon^k)\| + \varepsilon L\lambda(L)M.\end{aligned}$$

This is an inequality of the form of Lemma 3.4.3. Together with

$$\|U(t_k,0;q_\varepsilon)u_\pi^0(q^0) - u_\pi^0(q_\varepsilon^k)\| = 0$$

for $k = 0$, an application of this lemma yields for $k = 0,\dots,K$ that

$$\|U(t_k,0;q_\varepsilon)u_\pi^0(q^0) - u_\pi(t_k;q_\varepsilon^k)\| \lesssim \varepsilon L\lambda(L)M\sum_{j=0}^{k-1}(C\mathrm{e}^{-\alpha L})^j$$

with a constant C independent of L and M. We may choose L independent of M such that $C\mathrm{e}^{-\alpha L} < 1$. This implies, with $\lesssim$ now depending on L, that

$$\|U(t_k, 0; q_\varepsilon)u_\pi^0(q^0) - u_\pi(t_k; q_\varepsilon^k)\| \lesssim \varepsilon M$$

for $k = 0, \dots, K$. Using this estimate in ineq. (3.11) yields the claimed bound for all $t \in I_k$ and concludes the proof. □

We now use the previous result to establish that q_ε is close to $q_{\varepsilon,\pi}$, where $q_{\varepsilon,\pi}$ was defined, repeated here for convenience, as solution of

$$q'_{\varepsilon,\pi}(t) = \varepsilon g(q_{\varepsilon,\pi}(t), u_\pi(t; q_{\varepsilon,\pi}(t))), \quad q_{\varepsilon,\pi}(0) = q^0. \tag{3.7}$$

Lemma 3.4.5. *Let $\mathcal{T} > 0$ be fixed and $|I_\varepsilon| \le \varepsilon^{-1}\mathcal{T}$. Then we have*

$$\max_{t\in I_\varepsilon} |q_\varepsilon(t) - q_{\varepsilon,\pi}(t)| \lesssim \varepsilon M,$$

with constant depending on $\mathcal{T}$.

Proof. Using the Lipschitz continuity of g and u_π, we have for $t \in I_\varepsilon$ that

$$\begin{aligned}
|q_\varepsilon(t) - q_{\varepsilon,\pi}(t)| &\lesssim \varepsilon \int_0^t |q_\varepsilon(s) - q_{\varepsilon,\pi}(s)| + \|u_\varepsilon(s) - u_\pi(s; q_{\varepsilon,\pi}(s))\| \,\mathrm{d}s \\
&\lesssim \varepsilon \int_0^t |q_\varepsilon(s) - q_{\varepsilon,\pi}(s)| \,\mathrm{d}s + \varepsilon \int_0^t \|u_\varepsilon(s) - u_\pi(s; q_\varepsilon(s))\| \,\mathrm{d}s \\
&\quad + \varepsilon \int_0^t \|u_\pi(s; q_\varepsilon(s)) - u_\pi(s; q_{\varepsilon,\pi}(s))\| \,\mathrm{d}s.
\end{aligned}$$

For the second term we use our estimate from Lemma 3.4.4 to see that

$$\varepsilon \int_0^t \|u_\varepsilon(s) - u_\pi(s; q_\varepsilon(s))\| \,\mathrm{d}s \lesssim \varepsilon \|u^0 - u_\pi^0(q^0)\| \int_0^t \mathrm{e}^{-\alpha s} \,\mathrm{d}s + \varepsilon^2 M t \lesssim \varepsilon M,$$

since $\int_0^t \mathrm{e}^{-\alpha s} \,\mathrm{d}s \lesssim 1$, independent of t, $t \le \varepsilon^{-1}\mathcal{T}$ and $\|u^0 - u_\pi^0(q^0)\| \lesssim 1$ by Lemma 3.3.3. By Lipschitz continuity of u_π there holds for the third term:

$$\varepsilon \int_0^t \|u_\pi(s; q_\varepsilon(s)) - u_\pi(s; q_{\varepsilon,\pi}(s))\| \,\mathrm{d}s \lesssim \varepsilon \int_0^t |q_\varepsilon(s) - q_{\varepsilon,\pi}(s)| \,\mathrm{d}s.$$

Combination of these estimate gives

$$|q_\varepsilon(t) - q_{\varepsilon,\pi}(t)| \lesssim \varepsilon \int_0^t |q_\varepsilon(s) - q_{\varepsilon,\pi}(s)| \,\mathrm{d}s + \varepsilon M$$

and application of Gronwall's inequality yields the claimed estimate

$$|q_\varepsilon(t) - q_{\varepsilon,\pi}(t)| \le \varepsilon M \mathrm{e}^{C\varepsilon t} \lesssim \varepsilon M,$$

where we used again that $t \le \varepsilon^{-1}\mathcal{T}$. □

Corollary 3.4.6. *There exists $\mathcal{T} > 0$, $\varepsilon^* = \varepsilon^*(M) > 0$ such that for $0 < \varepsilon < \varepsilon^*$ the solution q_ε exists on $[0, \varepsilon^{-1}\mathcal{T}]$ and there holds*

$$\max_{t\in[0,\varepsilon^{-1}\mathcal{T}]} |q_\varepsilon(t) - q_0(t)| \lesssim \varepsilon M.$$

Proof. By the previous result and Corollary 3.4.2 we see that the estimate is valid on a possibly ε-dependent interval I_ε for ε small enough. It remains to prove that the interval of existence may be extended to $[0, \varepsilon^{-1}\mathcal{T}]$. Since the trajectory of the averaged equation $\Gamma_0 := q_0([0, \varepsilon^{-1}\mathcal{T}])$ is compact and contained in Q, we can find $\eta > 0$ such that a η-neighborhood of Γ_0 is contained in Q. Choosing ε^* small enough such that $\varepsilon M \lesssim \eta$ for all $0 < \varepsilon < \varepsilon^*$ the previous corollary implies that q_ε cannot leave this neighborhood (and hence Q) for any such ε. By Lemma 3.3.4 solutions only cease to exist if q_ε crosses the boundary of Ω. Hence for all $0 < \varepsilon < \varepsilon^*$ the solution q_ε must exist at least until $\varepsilon^{-1}\mathcal{T}$. □

A simple consequence of our results is an estimate on the fast component, albeit limited by a boundary layer at $t = 0$:

Lemma 3.4.7. *For any $\delta \in (0, \mathcal{T})$ there exists $\varepsilon^* = \varepsilon^*(\delta, M) > 0$, such that for all $0 < \varepsilon < \varepsilon^*$ there holds*

$$\max_{t \in [\varepsilon^{-1}\delta, \varepsilon^{-1}\mathcal{T}]} \|U(t, 0; q_\varepsilon)u^0 - u_\pi(t; q_0(t))\| \lesssim \varepsilon M.$$

Proof. By Lemma 3.4.4, we have for $t \in [0, \varepsilon^{-1}\mathcal{T}]$ that

$$\|U(t, 0; q_\varepsilon)u^0 - u_\pi(t; q_\varepsilon(t))\| \lesssim \mathrm{e}^{-\alpha t}\|u^0 - u^0_\pi\| + \varepsilon M.$$

Using the Lipschitz continuity of u_π and the estimate for $q_\varepsilon - q_0$ from the Corollary 3.4.6, we hence get

$$\begin{aligned}
&\|U(t, 0; q_\varepsilon)u^0 - u_\pi(t; q_0(t))\| \\
&\quad \le \|U(t, 0; q_\varepsilon)u^0 - u_\pi(t; q_\varepsilon(t))\| + \|u_\pi(t; q_\varepsilon(t)) - u_\pi(t; q_0(t))\| \\
&\quad \lesssim \mathrm{e}^{-\alpha t}\|u^0 - u^0_\pi\| + \varepsilon M + |q_\varepsilon(t) - q_0(t)| \\
&\quad \lesssim \mathrm{e}^{-\alpha t}\|u^0 - u^0_\pi\| + \varepsilon M.
\end{aligned}$$

For $t \ge t^*(\varepsilon) = -\alpha^{-1}\ln(\varepsilon(1+M))$ we have $\mathrm{e}^{-\alpha t} \le \varepsilon(1+M)$. Since $\varepsilon^{-1}\delta > t^*(\varepsilon)$ for all $0 < \varepsilon < \varepsilon^*$ if $\varepsilon^* = \varepsilon^*(\delta, M)$ is sufficiently small, the claimed estimate follows. □

Proof for unbounded g

We will now prove that one can drop the assumption of g being bounded. We reduce this to the previous case by replacing g with a bounded function g_R outside a ball of radius R in X. Careful analysis of the preceding estimates then shows that for R sufficiently large and ε sufficiently small this change has no effect on the solutions.

Lemma 3.4.8. *For $R > 0$ define $P_R \colon X \to X$ by $P_R(u) := u$ for $\|u\| \le R$ and $P_R(u) := R\frac{u}{\|u\|}$ for $\|u\| > R$. Then P_R is Lipschitz continuous with constant 1.*

Proof. Let $u_1, u_2 \in X$ and assume without restriction of generality that $\|u_1\| \le \|u_2\|$. If $\|u_2\| \le R$ we have $\|P_R(u_1) - P_R(u_2)\| = \|u_1 - u_2\|$. For the case $\|u_2\| > R$ and $\|u_1\| < R$ let $v \in X$ denote the orthogonal projection of u_1 onto $\mathbb{R}u_2$. Then it is easy to see that $\|v - P_R(u_2)\| \le \|v - u_2\|$ and hence

$$\|P_R(u_1) - P_R(u_2)\|^2 = \|u_1 - P_R(u_2)\|^2 \le \|u_1 - v\|^2 + \|v - u_2\|^2 = \|u_1 - u_2\|^2.$$

If $\|u_1\| > R$ first assume that $\|u_1\| = \|u_2\|$, i.e. there exists $\hat{\alpha} > R$ such that $u_1 = \hat{\alpha}\frac{u_1}{\|u_1\|}$ and $u_2 = \hat{\alpha}\frac{u_2}{\|u_2\|}$. Since $\alpha \mapsto \alpha\|\frac{u_1}{\|u_1\|} - \frac{u_2}{\|u_2\|}\|$ is increasing the claim follows since $\hat{\alpha} > R$. In the last case, $R < \|u_1\| < \|u_2\|$, we use the already proven cases together with $P_R \circ P_{\|u_1\|} = P_R$ to see that

$$\begin{aligned}\|u_1 - u_2\| &\geq \|u_1 - P_{\|u_1\|}(u_2)\| \geq \|P_R(u_1) - [P_R \circ P_{\|u_1\|}](u_2)\| \\ &\geq \|P_R(u_1) - P_R(u_2)\|.\end{aligned}$$ □

Lemma 3.4.9. *For any $R > 0$ there exists a bounded, Lipschitz continuous function $g_R\colon Q \times X \to \mathbb{R}^n$ such that $g_R(q,u) = g(q,u)$ for all $q \in Q$ and $\|u\| \leq R$ with the same Lipschitz constant as g.*

Proof. Define $g_R(q,u) := g(q, P_R(u))$. Then $g_R(u) = g(u)$ for $\|u\| \leq R$ and the Lipschitz continuity follows from the previous lemma. Since

$$|g_R(q,u)| = |g(q - q^0 + q^0, P_R(u-0))| \lesssim |q - q^0| + \|P_R(u)\| + |g(q^0, 0)| \lesssim 1 + R,$$

where we used that Q is bounded, g_R is bounded. □

Lemma 3.4.10. *For $R > 0$ large enough the limit solution q_0 solves*

$$q_0'(t) = \varepsilon \int_0^1 g_R(q_0(t), u_\pi(s; q_0(t)))\,\mathrm{d}s, \quad q_0(0) = q^0$$

for all $t \in [0, \varepsilon^{-1}\mathcal{T}]$.

Proof. The set $\Gamma := \{u_\pi(s; q_0(t)) \mid s \in [0,1], t \in [0, \varepsilon^{-1}\mathcal{T}]\} \subset X$ is bounded. Hence we can choose $R > 0$ large enough such that $\|u\| \leq R$ for all $u \in \Gamma$ and hence $g(q_0(t), u_\pi(s; q_0(t))) = g_R(q_0(t), u_\pi(s; q_0(t)))$. □

Now let $q_{\varepsilon,R}$ denote the solution with right-hand side g_R where $R > 0$ is at least as large as required by the previous lemma. For the bound $M > 0$ of g we have $M \lesssim 1 + R \lesssim R$ for R sufficiently large. Then by the results of the previous section there is an $\varepsilon^*(R) > 0$ such that for all $0 < \varepsilon < \varepsilon^*$ the solution $q_{\varepsilon,R}$ exists for $[0, \varepsilon^{-1}\mathcal{T}]$ and there holds

$$\begin{aligned}\|q_{\varepsilon,R}(t) - q_0(t)\| &\lesssim \varepsilon R, \\ \|U(t,0;q_{\varepsilon,R})u^0 - u_\pi(t; q_{\varepsilon,R}(t))\| &\lesssim \mathrm{e}^{-\alpha t}\|u^0 - u_\pi^0\| + \varepsilon R\end{aligned}$$

for all $t \in [0, \varepsilon^{-1}\mathcal{T}]$, where we implicitly used that q_0 is also the solution of the limit equation for g_R. With R-independent constants $C > 0$ we get

$$\begin{aligned}\|U(t,0;q_{\varepsilon,R})u^0\| &\leq C\left(\|u^0 - u_\pi^0\| + \|u_\pi(t; q_{\varepsilon,R}(t))\| + \varepsilon R\right) \\ &\leq C\left(\|u^0 - u_\pi^0\| + \|u_\pi(t; q_0(t))\| + |q_{\varepsilon,R}(t) - q_0(t)| + \varepsilon R\right) \\ &\leq C\left(\|u^0 - u_\pi^0\| + \|u_\pi(t; q_0(t))\| + \varepsilon R\right).\end{aligned}$$

Fixing $R > 0$ such that $C\left(\|u^0 - u_\pi^0\| + \|u_\pi(t; q_0(t))\|\right) \leq \frac{R}{2}$ and making the corresponding $\varepsilon^*(R) > 0$ small enough such that $\frac{1}{2} + C\varepsilon \leq 1$ holds for all $0 < \varepsilon < \varepsilon^*$ we get $\|U(t,0;q_{\varepsilon,R})u^0\| \leq R$ for all $t \in [0, \varepsilon^{-1}\mathcal{T}]$ and hence

$$q_{\varepsilon,R}(t)' = \varepsilon g_R(q_{\varepsilon,R}(t), U(t,0;q_{\varepsilon,R})u^0) = \varepsilon g(q_{\varepsilon,R}(t), U(t,0;q_{\varepsilon,R})u^0).$$

But this implies that $q_{\varepsilon,R}$ for such R and $0 < \varepsilon < \varepsilon^*$ solves the original eq. (3.1), hence $q_{\varepsilon,R} = q_\varepsilon$ and of course the estimates from the previous section still hold.

3.5 Averaging of Forces and Quasi-Static Limit

Let us finally return to the initial example, where the fast process is induced by a periodically-forced partial differential equation:

$$\begin{aligned} q_\varepsilon'(t) &= \varepsilon g(q_\varepsilon(t), u_\varepsilon(t)), & q_\varepsilon(0) &= q^0, \\ \partial_t u_\varepsilon(t) + A(q_\varepsilon(t))u_\varepsilon(t) &= f(t), & u_\varepsilon(0) &= u^0. \end{aligned}$$

The simplest heuristical method to remove the fast oscillations is to average the periodic right-hand side f. For this, we assume that $A(\cdot)$ is a family of linear operators as in Example 3.2.2. If we replace f by $\bar{f} := \int_0^1 f(t)\,\mathrm{d}t$, our system reads

$$\begin{aligned} \bar{q}_\varepsilon'(t) &= \varepsilon g(\bar{q}_\varepsilon(t), \bar{u}_\varepsilon(t)), & \bar{q}_\varepsilon(0) &= q^0, \\ \partial_t \bar{u}_\varepsilon(t) + A(\bar{q}_\varepsilon(t))\bar{u}_\varepsilon(t) &= \bar{f}, & \bar{u}_\varepsilon(0) &= u^0. \end{aligned}$$

Now for fixed $q \in Q$, the fast equation is $\partial_t u(t) + A(q)u(t) = \bar{f}$ and tends to a stationary limit point, independent of its initial value by exponential stability. Thus, the limit equation has the form

$$\bar{q}_0'(t) = \varepsilon g(\bar{q}_0(t), u_\infty(\bar{q}_0(t))), \quad \bar{q}_0(0) = q^0$$

where $u_\infty(q)$ for $q \in Q$ is defined as solution of $A(q)u_\infty(q) = \overline{f}$.

This quasi-static limit is one heuristic to circumvent the resolution of the fast-timescale, see e.g. [Yan+15]. This approach is similar to crude averaging as described in [SVM07, chapter 2.7] and does not always yield the correct result, see e.g. Example 3.5.2 below. There holds, however:

Lemma 3.5.1. *If we assume that $A(\cdot)$ are linear operators as in Example 3.2.2 and g is linear in u, we have $q_0 = \bar{q}_0$. The limit equation for q_0 can hence be simplified as*

$$q_0'(t) = \varepsilon g(q_0(t), u_\infty(q_0(t))), \quad q_0(0) = q^0$$

where $u_\infty(q)$ for $q \in Q$ is the solution of

$$A(q)u_\infty(q) = \int_0^1 f(t)\,\mathrm{d}t.$$

Proof. The linearity of g in u implies that

$$q_0'(t) = \varepsilon g\left(q_0(t), \int_0^1 u_\pi(s; q_0(t))\,\mathrm{d}s\right).$$

Taking the time-average of the differential equation for u_π, using the linearity of $A(\cdot)$, yields that

$$\int_0^1 \partial_s u_\pi(s)\,\mathrm{d}s + A(q)\left(\int_0^1 u_\pi(s; q)\,\mathrm{d}s\right) = \int_0^1 f(t)\,\mathrm{d}t$$

and the first term vanishes due to the periodicity of u_π, thus

$$A(q)\left(\int_0^1 u_\pi(s; q)\,\mathrm{d}s\right) = \int_0^1 f(t)\,\mathrm{d}t$$

and hence $\int_0^1 u_\pi(s; q)\,\mathrm{d}s = u_\infty(q)$, yielding as claimed $q_0 = \bar{q}_0$. □

Example 3.5.2. Example 3.2.10 also yields a counter-example that the quasi-static limit may not approximate q_ε even if the fast equation is linear. Specifically, the right-hand side for u_ε from eq. (3.4a) has zero average, $\bar{f} = 0$, and hence $u_\infty(q) = 0$ for all $q \in Q$, which implies $\bar{q}_0 \equiv q^0 = 1$. Solving either eq. (3.6) for q_0 numerically or observing that $q_0' \geq C\varepsilon$ if q_0 is bounded away from 2 we see that $|\bar{q}_0 - q_0| = \mathcal{O}(1)$ and hence $|\bar{q}_0 - q_\varepsilon| = \mathcal{O}(1)$. ◇

Chapter 4

Multiscale Analysis of a Simplified Plaque Model

We now adopt the techniques from the last chapter to a model coupling fast Stokes flow on a slowly evolving domain with wall shear stress dependent growth as presented in the introduction. The use of the Stokes instead of Navier–Stokes equation is a simplification, the equations are still nonlinear due to the solution-dependent evolving domain. Compared to the theory from the previous chapter, the two primary challenges are the pullback of the Stokes flow to the fixed geometry and the low regularity of the wall shear stress. The main result of this chapter is the multiscale convergence result from Theorem 4.3.9 which is of the same type as Theorem 3.1.1 from the last chapter, i.e. the growth in the multiscale model converges to an averaging-type limit system with error $\mathcal{O}(\varepsilon)$. Due to the solution-dependent non-cylindrical domain, the mathematical description of the model is notationally more involved and is discussed in Section 4.1. The existence of solutions and further properties of the model with a fixed scale is proven in Section 4.2 and the convergence to the singular limit is investigated in Section 4.3.

4.1 The Plaque Model

Our model consists of blood flow confined in an artery with geometry changing due to the growth of plaque. The blood flow is the solution to a Stokes equation with periodic forcing due the heart beat. The plaque is described through a finite dimensional state, e.g. its maximum height, whereas shape and location are prescribed. This state influences the artery's geometry. It evolves according to an ordinary differential equation depending on the wall shear stress, similar to the model investigated in [FR20]. We refer to the review from Section 2.2 for proposed relations between the wall shear stress and the wall's permeability but only assume here that large shear stresses reduce the permeability of the damaged wall and hence the available material for growth. If we choose the heart beat period as unit time, the timescale separation is indicated by a very small rate of change for the plaque state. We do not claim that our model is able to accurately predict plaque growth, since a relation between growth rate and wall shear stress is at most phenomenological.

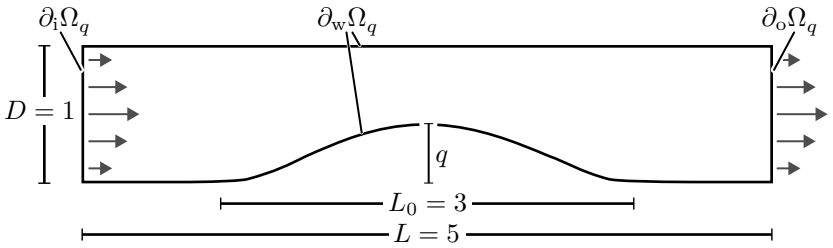

Figure 4.1: Sketch of the 2D geometry Ω_q from Example 4.1.2 with the measurements as used in the numerical simulations. The plaque bump has variable height q.

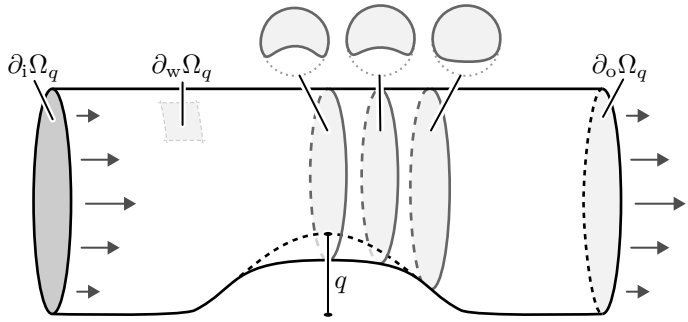

Figure 4.2: Sketch of the 3D geometry Ω_q from Example 4.1.3. The plaque bump has variable height q.

Plaque State

Let the bounded domain $Q \subset \mathbb{R}^n$ denote the parameter set describing the plaque. In the example investigated below the height is the only parameter so that we choose $Q := (0, q_{\max}) \subset \mathbb{R}$ for given $q_{\max} > 0$. Higher dimensional parameter sets could describe other geometric characteristics of the plaque or discrete, but spatially distributed heights, which could be seen as an already spatially discretized surface differential equation.

Geometry

The artery's geometry depends on the state $q \in Q$ of the plaque,

$$\Omega_q := \Phi_q(\Omega) = \Phi(\Omega; q),$$

where $\Omega \subset \mathbb{R}^d$ is the *reference domain* and Φ is a given transformation

$$\Phi \colon \overline{\Omega} \times Q \to \mathbb{R}^d, \quad (x, q) \mapsto \Phi(x; q) = \Phi_q(x).$$

The boundary of Ω is divided into wall boundary $\partial_w\Omega$, inflow boundary $\partial_i\Omega$ and outflow boundary $\partial_o\Omega$ (outflow) with $\overline{\partial_w\Omega} \cup \overline{\partial_i\Omega} \cup \overline{\partial_o\Omega} = \partial\Omega$. Each connected component of $\partial_w\Omega$, $\partial_i\Omega$ and $\partial_o\Omega$ has non-zero measure and in- and outflow boundaries are not adjacent, $\overline{\partial_i\Omega} \cap \overline{\partial_o\Omega} = \varnothing$. We abbreviate $\partial_{io}\Omega := \partial_i\Omega \cup \partial_o\Omega$ and assume that $\partial_{io}\Omega$ is planar, so that that the unit exterior normal

$\mathfrak{n}$ is constant on each connected component. For regularity of solutions we assume that $\partial_{\mathrm{w}}\Omega$ is C^3-regular and that $\partial_{\mathrm{w}}\Omega$ and $\partial_{\mathrm{io}}\Omega$ meet at a 90° angle.

The transformation Φ_q is assumed to be C^3-diffeomorphism for fixed q:

$$\Phi_q \colon \overline{\Omega} \to \overline{\Omega}_q \text{ is bijective}, \quad \Phi_q \in C^3(\overline{\Omega}), \quad \Phi_q^{-1} \in C^3(\overline{\Omega}_q).$$

We assume that there is a relatively open neighborhood $\Omega' \subset \overline{\Omega}$ of $\partial_{\mathrm{io}}\Omega \subset \Omega'$ such that $\Phi_q|_{\Omega'} = \mathrm{Id}_{\Omega'}$ for all $q \in Q$. Writing for $q \in Q$ $\partial_{\mathrm{w}}\Omega_q := \Phi_q(\partial_{\mathrm{w}}\Omega)$, $\partial_{\mathrm{i}}\Omega_q := \Phi_q(\partial_{\mathrm{i}}\Omega)$ and $\partial_{\mathrm{o}}\Omega_q := \Phi_q(\partial_{\mathrm{o}}\Omega)$ this assumption not only implies $\partial_{\mathrm{i}}\Omega_q = \partial_{\mathrm{i}}\Omega$ and $\partial_{\mathrm{o}}\Omega_q = \partial_{\mathrm{o}}\Omega$ but also that the boundaries $\partial_{\mathrm{w}}\Omega_q$ and $\partial_{\mathrm{io}}\Omega_q$ remain orthogonal. As for the regularity of Φ in q, we assume Lipschitz continuity in the sense that

$$\|\Phi_{q_1} - \Phi_{q_2}\|_{C^3(\overline{\Omega})} \lesssim |q_1 - q_2|$$

for $q_1, q_2 \in Q$. Furthermore, $\|\Phi_q^{-1}\|_{C^3(\overline{\Omega}_q)}$ is assumed to be uniformly bounded in q.

Remark 4.1.1. In view of our application, we make no assumption that Φ_q is locally or globally volume preserving, so that $\det \nabla \Phi_q \neq 1$ in general. At least global volume preservation is necessary if Dirichlet boundary values are imposed on the whole boundary due to the fluid's incompressibility, making it a common assumption in the literature, e.g. in [Saa06; IW77] and see also the discussions in [MT82]. ◇

For a given evolution of state $q \in C(\overline{I}, Q)$ with $I := (0, T)$ where $T > 0$ we interpret, with slight abuse of notation,Φ_q in this case as either

$$I \times \Omega \ni (t, x) \mapsto (t, \Phi(x; q(t)) \quad \text{or} \quad I \ni t \mapsto \Phi(\,\cdot\,; q(t)).$$

Example 4.1.2. For $d = 2$ we consider a configuration as in Figure 4.1, with a rectangular reference domain

$$\Omega := (-\tfrac{L}{2}, \tfrac{L}{2}) \times (0, 1) \subset \mathbb{R}^2$$

of length $L := 5$. The boundary is subdivided as indicated in Figure 4.1. Let $q \in Q := [0, q_{\max})$ for $q_{\max} < 1$ and $\eta \colon \mathbb{R} \to \mathbb{R}_{\geq 0}$ be the smooth bump function

$$\eta(s) := \begin{cases} \exp(\frac{s^2}{s^2-1}) & \text{if } |s| < 1, \\ 0 & \text{else} \end{cases}$$

such that $\operatorname{supp} \eta = [-1, 1]$ and $\max \eta = \eta(0) = 1$. For $(x, y) \in \overline{\Omega}$ and $q \in Q$ let

$$\Phi_q(x, y) := \big(x, y + q\eta(\tfrac{2x}{L_0})(1 - y)\big)^{\mathsf{T}}$$

for plaque width $L_0 := 3$. The compact support of η yields that $\Phi_q = \mathrm{Id}$ near in- and outflow boundaries. Since $q_{\max} < 1$ the map Φ_q is injective on $\overline{\Omega}$. Since $\Phi_q = \Phi^1 + q\Phi^2$ with Φ^1 and Φ^2 smooth, the Lipschitz assumption follows. The inverse of Φ_q for $(x, y) \in \overline{\Omega}_q$ is given by

$$\Phi_q^{-1}(x, y) = \left(x, \left(1 - q\eta(\tfrac{2x}{L_0})\right)^{-1}(y - 1) + 1\right)^{\mathsf{T}}.$$

Since $1 - q\eta(\frac{2x}{L_0})$ is uniformly bounded away from 0 due to $q < q_{\max} < 1$ and $\max \eta = 1$, the inverse is smooth and $\|\Phi_q^{-1}\|_{C^3(\overline{\Omega}_q)}$ is bounded uniformly in q. ◇

Example 4.1.3. For $d = 3$ we consider a configuration as in Figure 4.2, with a cylindrical reference domain

$$\Omega := (-\tfrac{L}{2}, \tfrac{L}{2}) \times \{(y, z) \in \mathbb{R}^2 \mid y^2 + z^2 \leq 1\} \subset \mathbb{R}^3$$

of radius $R = 1$ and length $L > 0$. The boundary is subdivided as indicated in Figure 4.2. Let $q \in Q := (0, q_{\max})$ for $q_{\max} < 2$. With η being a compactly supported bump function as in Example 4.1.2, we define the (x, z)-bump function

$$\varphi(x, z) := \eta(\tfrac{2x}{L_0})\eta(z) \in [0, 1]$$

where $0 < L_0 < L$ is the length of the plaque. For $(x, y, z) \in \overline{\Omega}$ and $q \in Q$ let

$$\Phi_q(x, y, z) := \left(x, y + \frac{q\varphi(x, z)}{2}\left(\sqrt{1 - z^2} - y\right), z\right)^{\mathsf{T}}.$$

The inverse of Φ_q for $(x, y, z) \in \overline{\Omega}_q$ is given by

$$\Phi_q^{-1}(x, y, z) = \left(x, \left(1 - \frac{q\varphi(x, z)}{2}\right)^{-1}\left(y - \sqrt{1 - z^2}\right) + \sqrt{1 - z^2}, z\right)^{\mathsf{T}}.$$

The claimed properties of Φ_q follow just as in Example 4.1.2. ◇

Strong Formulation

Let $q\colon I \to Q$, $v\colon \Omega_q^I \to \mathbb{R}^d$ and $p\colon \Omega_q^I \to \mathbb{R}$ be sufficiently regular functions, such that v and p satisfy the Stokes equations

$$St\,\partial_t v - Re^{-1}\,\Delta v + \nabla p = 0, \quad \operatorname{div} v = 0, \quad v(0) = v^0 \tag{4.1}$$

in the non-cylindrical space-time domain Ω_q^I defined by

$$\Omega_q^I := \{(t, x) \mid t \in I, x \in \Omega_{q(t)}\}$$

with Strouhal number $St > 0$ and Reynolds numbers $Re > 0$, initial velocity $v^0\colon \Omega_{q^0} \to \mathbb{R}^d$ and initial plaque state $q^0 \in Q$. The boundary conditions for v will be described below. The plaque state q is assumed to satisfy the ordinary differential equation

$$q'(t) = \varepsilon g(q(t), v(t)), \quad q(0) = q^0 \tag{4.2}$$

for $0 < \varepsilon \ll 1$ and a bounded function g discussed in Section 4.1. We emphasize that g maps the whole function $v(t)\colon \Omega_{q(t)} \to \mathbb{R}^d$ to a single value in $\mathbb{R}^n$. For the moment we omit the subscript ε indicating the dependence on ε.

It remains to supply boundary conditions for v. For simplicity we assume that $\partial_{\mathrm{i}}\Omega$ and $\partial_{\mathrm{o}}\Omega$ have exactly one connected component, on which we assume that the pressure drop is prescribed:

$$\frac{1}{|\partial_{\mathrm{i}}\Omega|}\int_{\partial_{\mathrm{i}}\Omega} p(t, x)\,\mathrm{d}o = P_{\mathrm{in}}(t), \quad \frac{1}{|\partial_{\mathrm{o}}\Omega|}\int_{\partial_{\mathrm{o}}\Omega} p(t, x)\,\mathrm{d}o = P_{\mathrm{out}}(t),$$

with $P_{\mathrm{in}}, P_{\mathrm{out}}\colon \mathbb{R} \to \mathbb{R}$ being 1-periodic. By [HRT96, Section 3] and implicitly using that $\partial_{\mathrm{i}}\Omega$ and $\partial_{\mathrm{o}}\Omega$ are planar, this can be realized with the boundary condition

$$Re^{-1}\,\partial_{\mathfrak{n}} v - p\mathfrak{n} = -P_{\mathrm{io}}\mathfrak{n} \quad \text{on } I \times \partial_{\mathrm{io}}\Omega$$

with $P_{\text{io}} = P_{\text{in}}$ on $\partial_{\text{i}}\Omega$ and $P_{\text{io}} = P_{\text{out}}$ on $\partial_{\text{o}}\Omega$. On the wall a no-slip boundary condition implies that v matches the boundary velocity due to the domain's movement:

$$v(t,x) = \partial_q \Phi(\Phi^{-1}(x;q(t));q(t))q'(t) \quad \text{for } t \in I \text{ and } x \in \partial_{\text{w}}\Omega_{q(t)}.$$

Since q' is of order $\mathcal{O}(\varepsilon)$, this boundary condition can be seen as a regular perturbation of homogeneous boundary values. For simplicity we ignore these regular perturbations in the present analysis and assume

$$v(t,x) = 0 \quad \text{for } t \in I \text{ and } x \in \partial_{\text{w}}\Omega_{q(t)}.$$

Due to the possibility of in- and outflow this simplification is compatible with the incompressibility of the fluid even if the total volume of the fluid changes.

Rate of Growth

Let $q \in Q = (0, q_{\max})$ model the height of the plaque. We remind of the definition of the wall shear stress

$$\sigma_{\text{WS}} = (\mathrm{I} - \mathfrak{n} \otimes \mathfrak{n})\sigma\mathfrak{n} := 2\,Re^{-1}(\mathrm{I} - \mathfrak{n} \otimes \mathfrak{n})\nabla^s v\mathfrak{n}$$

where $\sigma = 2\,Re^{-1}\,\nabla^s v - p\,\mathrm{I}$ is the full stress tensor with symmetric gradient $\nabla^s v := \frac{1}{2}(\nabla v + (\nabla v)^{\intercal})$. A number of possible relations between wall shear stress and permeability to LDL or monocytes has been discussed in the review from Section 2.2, most of which decrease permeability with increasing wall shear stress. A direct relation between wall shear stresses and growth is at most phenomenological. In the models [FRW16; FR20] a stress-growth relation g similar to

$$g(q,v) = \gamma_0 \int_{\partial_{\text{w}}\Omega_q} \left(1 + \frac{|\sigma_{\text{WS}}|}{\sigma^0_{\text{WS}}}\right)^{-1} \mathrm{d}o \tag{4.3}$$

is used where $q \in Q$ and $v\colon \Omega_q \to \mathbb{R}^d$ sufficiently regular with given $\gamma_0 > 0$ and reference shear stress $\sigma^0_{\text{WS}} > 0$. The theory we develop allows a large class of stress-growth relations, but we take eq. (4.3) as a prototype for now since the abstract assumptions are easier to formulate after a pullback to a fixed domain, see eq. (4.8) and ineq. (4.9). We note that $x \mapsto (1+x)^{-1}$ is a monotone decreasing function tending to 0 as $x \to \infty$, and in particular bounded, which reflects our assumption that (local) permeability decreases with increasing shear stresses.

Pullback Equations

For the analysis we pull the equation back to the reference domain Ω following e.g. [Saa06]. This allows us to investigate non-autonomous operators on cylindrical domains. To preserve solenoidality of v we use the Piola transformation. In contrast to [Saa06] we do not study volume-preserving transformations, hence the Piola transformation is slightly more complicated.

We abbreviate $F_q := \nabla \Phi_q$ and $J_q := \det F_q$. Let $f\colon \Omega_q \to \mathbb{R}$, $v\colon \Omega_q \to \mathbb{R}^d$, $A\colon \Omega_q \to \mathbb{R}^{d\times d}$ denote sufficiently smooth functions. Then

$$\begin{aligned}
(\nabla f)\circ\Phi_q &= \nabla_q(f\circ\Phi_q) &&:= F_q^{-\mathsf{T}}\nabla(f\circ\Phi_q),\\
(\nabla v)\circ\Phi_q &= \nabla_q(v\circ\Phi_q) &&:= \nabla(v\circ\Phi_q)F_q^{-1},\\
(\operatorname{div} v)\circ\Phi_q &= \operatorname{div}_q(v\circ\Phi_q) &&:= \operatorname{tr}(\nabla_q(v\circ\Phi_q)),\\
(\Delta v)\circ\Phi_q &= \Delta_q(v\circ\Phi_q) &&:= \operatorname{div}_q(\nabla_q(v\circ\Phi_q)),\\
(\operatorname{div} A)\circ\Phi_q &= \operatorname{div}_q(A\circ\Phi_q) &&:= J_q^{-1}\operatorname{div}(A\circ\Phi_q \operatorname{Cof} F_q),
\end{aligned}$$

This last transformation uses the Piola identity $\operatorname{div}(\operatorname{Cof} F_q) = 0$, see [Cia88, Theorem 1.7-1]. This identity also motivates the Piola transformation

$$\mathcal{P}_q v := \operatorname{Cof} F_q^{\mathsf{T}}(v\circ\Phi_q) \tag{4.4}$$

since from the Piola identity it follows that

$$\operatorname{div}(\mathcal{P}_q v) = J_q \operatorname{div}_q(v\circ\Phi_q) = J_q(\operatorname{div} v)\circ\Phi_q \tag{4.5}$$

and thus $\operatorname{div} v = 0$ if and only if $\operatorname{div}(\mathcal{P}_q v) = 0$. The inverse of $\mathcal{P}_q$ is given by

$$\mathcal{P}_q^{-1}\hat{v} := (\hat{v}\cdot\operatorname{Cof} F_q^{-1})\circ\Phi_q^{-1} = (\operatorname{Cof} F_q^{-\mathsf{T}}\hat{v})\circ\Phi_q^{-1}$$

for sufficiently smooth $\hat{v}\colon \Omega \to \mathbb{R}^d$. We transform the Stokes equation (4.1)

$$\begin{pmatrix} St\,\partial_t - Re^{-1}\Delta & \nabla \\ \operatorname{div} & \end{pmatrix}\begin{pmatrix} v \\ p \end{pmatrix} = 0$$

to one in new variables $\hat{v}\colon I\times\Omega\to\mathbb{R}^d$, $\hat{p}\colon I\times\Omega\to\mathbb{R}$ on a cylindrical domain. Specifically, using the notation $\Phi_q^*(f) := f\circ\Phi_q$ for the pullback, we transform

$$\begin{pmatrix} \mathcal{P}_q & \\ & \Phi_q^* \end{pmatrix}\begin{pmatrix} St\,\partial_t - Re^{-1}\Delta & \nabla \\ \operatorname{div} & \end{pmatrix}\begin{pmatrix} \mathcal{P}_q^{-1} & \\ & (\Phi_q^{-1})^* \end{pmatrix}\begin{pmatrix} \hat{v} \\ \hat{p} \end{pmatrix} = 0 \tag{4.6}$$

We now want to derive a more explicit expression for eq. (4.6). Abbreviating

$$(\partial_t\Phi_q)(t,x) := \tfrac{\mathrm{d}}{\mathrm{d}t}\Phi(x;q(t)) = \partial_q\Phi(x;q(t))q'(t).$$

we use the identity

$$\partial_t(v\circ\Phi_q) = (\partial_t v)\circ\Phi_q + (\nabla v)\circ\Phi_q\partial_t\Phi_q = (\partial_t v)\circ\Phi_q + \nabla_q(v\circ\Phi_q)\partial_t\Phi_q.$$

which implies for the ∂_t-term in eq. (4.6)

$$\begin{aligned}
\mathcal{P}_q\partial_t(\mathcal{P}_q^{-1}\hat{v}) &= \operatorname{Cof} F_q^{\mathsf{T}}(\partial_t(\mathcal{P}_q^{-1}\hat{v}))\circ\Phi_q\\
&= \operatorname{Cof} F_q^{\mathsf{T}}(\partial_t(\mathcal{P}_q^{-1}\hat{v}\circ\Phi_q) - \nabla_q(\mathcal{P}_q^{-1}\hat{v}\circ\Phi_q)\partial_t\Phi_q)\\
&= \operatorname{Cof} F_q^{\mathsf{T}}(\partial_t(\operatorname{Cof} F_q^{-\mathsf{T}}\hat{v}) - \nabla_q(\operatorname{Cof} F_q^{-\mathsf{T}}\hat{v})\partial_t\Phi_q).
\end{aligned}$$

For the first term on the right we use the identity

$$\partial_t\hat{v} = \partial_t(\operatorname{Cof} F_q^{\mathsf{T}}\operatorname{Cof} F_q^{-\mathsf{T}}\hat{v}) = \partial_t(\operatorname{Cof} F_q^{\mathsf{T}})\operatorname{Cof} F_q^{-\mathsf{T}}\hat{v} + \operatorname{Cof} F_q^{\mathsf{T}}\partial_t(\operatorname{Cof} F_q^{-\mathsf{T}}\hat{v}).$$

For the second term we use a similar trick. We write $(\nabla' A)_{ijk} := \partial_j A_{ik}$ for a matrix-field A, but note that $(\nabla' A)(Bx) \neq ((\nabla' A)B)x$ for $B \in \mathbb{R}^{d\times d}$, $x \in \mathbb{R}^d$. Then

$$\nabla \hat{v} = \nabla(\operatorname{Cof} F_q^{\mathsf{T}} \operatorname{Cof} F_q^{-\mathsf{T}} \hat{v}) = \nabla' \operatorname{Cof} F_q^{\mathsf{T}} (\operatorname{Cof} F_q^{-\mathsf{T}} \hat{v}) + \operatorname{Cof} F_q^{\mathsf{T}} \nabla (\operatorname{Cof} F_q^{-\mathsf{T}} \hat{v}).$$

These identities together yield

$$\begin{aligned}\mathcal{P}_q \partial_t (\mathcal{P}_q^{-1} \hat{v}) = \partial_t \hat{v} - \partial_t \operatorname{Cof} F_q^{\mathsf{T}} \operatorname{Cof} F_q^{-\mathsf{T}} \hat{v} - \nabla_q \hat{v} \partial_t \Phi_q \\ + (\nabla' \operatorname{Cof} F_q^{\mathsf{T}} (\operatorname{Cof} F_q^{-\mathsf{T}} \hat{v})) F_q^{-1} \partial_t \Phi_q.\end{aligned}$$

By the chain rule, all terms except the first yield a factor q' of order $\mathcal{O}(\varepsilon)$. These are regular perturbations and, as with the wall boundary values, we omit these terms:

$$\mathcal{P}_q \partial_t (\mathcal{P}_q^{-1} \hat{v}) = \partial_t \hat{v} + \mathcal{O}(\varepsilon).$$

The transformation of the Laplace term in eq. (4.6) can be written as

$$\mathcal{P}_q(\Delta(\mathcal{P}_q^{-1} \hat{v})) = \operatorname{Cof} F_q^{\mathsf{T}} \Delta_q (\operatorname{Cof} F_q^{-\mathsf{T}} \hat{v}).$$

For the pressure term in eq. (4.6) we get

$$\mathcal{P}_q(\nabla(\hat{p} \circ \Phi_q^{-1})) = \operatorname{Cof} F_q^{\mathsf{T}} (\nabla(\hat{p} \circ \Phi_q^{-1})) \circ \Phi_q = \operatorname{Cof} F_q^{\mathsf{T}} \nabla_q \hat{p}.$$

The second equation of eq. (4.6) transforms according to

$$\Phi_q^*(\operatorname{div}(\mathcal{P}_q^{-1} \hat{v})) = \operatorname{div}_q(\mathcal{P}_q^{-1} \hat{v} \circ \Phi_q) = \operatorname{div}_q(\hat{v} \cdot \operatorname{Cof} F_q^{-\mathsf{T}}) = J_q \operatorname{div} \hat{v}$$

and for the condition of solenoidality the factor J_q can be omitted.

In regard to the boundary values we note that since $\Phi = \mathrm{Id}$ near $\partial_{\mathrm{io}}\Omega$ the corresponding boundary values remain unchanged by the transformation. The, due to our simplification, homogeneous boundary values on $\partial_{\mathrm{w}}\Omega_q$ are mapped to homogeneous values on $\partial_{\mathrm{w}}\Omega$.

To express the plaque state eq. (4.2) in terms of $\hat{v}$, more information about the right-hand side g is needed. For the example from eq. (4.3) we have

$$\hat{g}(q, \hat{v}) = \gamma_0 \int_{\partial_{\mathrm{w}}\Omega} \left(1 + \frac{|\sigma_{\mathrm{WS}}| \circ \Phi_q}{\sigma_{\mathrm{WS}}^0}\right)^{-1} |\operatorname{Cof} F_q \mathfrak{n}| \, \mathrm{d}o \tag{4.7}$$

with the transformed wall shear stress

$$|\sigma_{\mathrm{WS}}| \circ \Phi_q = 2\, Re^{-1} \left| \left(\mathrm{I} - \tfrac{\operatorname{Cof} F_q \mathfrak{n}}{|\operatorname{Cof} F_q \mathfrak{n}|} \otimes \tfrac{\operatorname{Cof} F_q \mathfrak{n}}{|\operatorname{Cof} F_q \mathfrak{n}|}\right) \nabla_q^s (\operatorname{Cof} F_q^{-\mathsf{T}} \hat{v}) \right|.$$

Here we used the transformation rule

$$(\mathrm{d}o) \circ \Phi_q = |\operatorname{Cof} F_q \mathfrak{n}| \, \mathrm{d}o, \quad \mathfrak{n} \circ \Phi_q = \frac{\operatorname{Cof} F_q \mathfrak{n}}{|\operatorname{Cof} F_q \mathfrak{n}|},$$

see [Cia88]. The state equation can be expressed in terms of $\hat{v}$ as

$$q'(t) = \varepsilon \hat{g}(q(t), \hat{v}(t)).$$

Our theory does not assume $\hat{g}$ to be given by eq. (4.7) but only that

$$\hat{g} \colon Q \times H^2(\Omega) \to \mathbb{R}^n \quad \text{bounded} \tag{4.8}$$

and $\hat{g}$ is Lipschitz continuous in the sense that for $q_1, q_2 \in Q$ and $v_1, v_2 \in H^2(\Omega)$ there holds

$$|\hat{g}(q_1, v_1) - \hat{g}(q_2, v_2)| \lesssim (1 + \|v_i\|_{H^2(\Omega)})|q_1 - q_2| + \|v_1 - v_2\|_{H^2(\Omega)} \tag{4.9}$$

for $i \in \{1, 2\}$. This assumption is weaker than the one made in Chapter 3 since the Lipschitz constant is allowed to depend on v_i.

Lemma 4.1.4. *For g from eq. (4.3) with transformation $\hat{g}$ given by eq. (4.7) the previous assumptions are satisfied.*

Proof. It is clear that g is well-defined for $v \in H^2(\Omega)$ and bounded. To verify the Lipschitz condition from ineq. (4.9), we simplify by setting $\sigma^0_{\mathrm{WS}} = \gamma_0 = Re = 1$. Then

$$\begin{aligned}
&|\hat{g}(q_1, v) - \hat{g}(q_2, v)| \\
&\quad \leq \int_{\partial_{\mathrm{w}}\Omega} (1 + |\sigma_{\mathrm{WS}}| \circ \Phi_{q_1})^{-1} |\,|\operatorname{Cof} F_{q_1}\mathfrak{n}| - |\operatorname{Cof} F_{q_2}\mathfrak{n}|\,| \,\mathrm{d}o \\
&\qquad + \int_{\partial_{\mathrm{w}}\Omega} |(1 + |\sigma_{\mathrm{WS}}| \circ \Phi_{q_1})^{-1} - (1 + |\sigma_{\mathrm{WS}}| \circ \Phi_{q_2})^{-1}| |\operatorname{Cof} F_{q_2}\mathfrak{n}| \,\mathrm{d}o.
\end{aligned}$$

The first term on the right-hand side can be estimated by $|q_1 - q_2|$ with fixed constant. For the second term we use the following estimate for $x, y \geq 0$:

$$|(1 + x)^{-1} - (1 + y)^{-1}| \leq |x - y|. \tag{4.10}$$

This implies

$$\begin{aligned}
&\int_{\partial_{\mathrm{w}}\Omega} |(1 + |\sigma_{\mathrm{WS}}| \circ \Phi_{q_1})^{-1} - (1 + |\sigma_{\mathrm{WS}}| \circ \Phi_{q_2})^{-1}| |\operatorname{Cof} F_{q_2}\mathfrak{n}| \,\mathrm{d}o \\
&\quad \lesssim \int_{\partial_{\mathrm{w}}\Omega} ||\sigma_{\mathrm{WS}}| \circ \Phi_{q_1} - |\sigma_{\mathrm{WS}}| \circ \Phi_{q_2}| \,\mathrm{d}o.
\end{aligned} \tag{4.11}$$

Writing $T_q := \mathrm{I} - |\operatorname{Cof} F_q\mathfrak{n}|^{-2}(\operatorname{Cof} F_q\mathfrak{n}) \otimes (\operatorname{Cof} F_q\mathfrak{n})$ for the (transformed) tangential projection and using the expression for $\sigma_{\mathrm{WS}} \circ \Phi_q$ from above, we can estimate

$$\begin{aligned}
||\sigma_{\mathrm{WS}}| \circ \Phi_{q_1} - |\sigma_{\mathrm{WS}}| \circ \Phi_{q_2}| &\lesssim |T_{q_1} - T_{q_2}||\nabla^s_{q_1}(\operatorname{Cof} F_{q_1}^{-\intercal}\hat{v})| \\
&\quad + |T_{q_2}||(\nabla^s_{q_1} - \nabla^s_{q_2})(\operatorname{Cof} F_{q_1}^{-\intercal}\hat{v})| + |T_{q_2}||\nabla^s_{q_2}((\operatorname{Cof} F_{q_1}^{-\intercal} - \operatorname{Cof} F_{q_2}^{-\intercal})\hat{v})|.
\end{aligned}$$

Using the Lipschitz assumptions of Φ_q, this implies

$$||\sigma_{\mathrm{WS}}| \circ \Phi_{q_1} - |\sigma_{\mathrm{WS}}| \circ \Phi_{q_2}| \lesssim |q_1 - q_2|(|v| + |\nabla v|).$$

Inserting this estimate in ineq. (4.11) yields

$$\begin{aligned}
&\int_{\partial_{\mathrm{w}}\Omega} |(1 + |\sigma_{\mathrm{WS}}| \circ \Phi_{q_1})^{-1} - (1 + |\sigma_{\mathrm{WS}}| \circ \Phi_{q_2})^{-1}| |\operatorname{Cof} F_{q_2}\mathfrak{n}| \,\mathrm{d}o \\
&\quad \lesssim |q_1 - q_2| \int_{\partial_{\mathrm{w}}\Omega} |v| + |\nabla v| \,\mathrm{d}o \lesssim |q_1 - q_2| \|v\|_{H^2(\Omega)}.
\end{aligned}$$

For the second estimate, we write $\sigma_{\mathrm{WS},1}$, respectively $\sigma_{\mathrm{WS},2}$, for the wall-shear stress of v_1, respectively v_2. Then by ineq. (4.10) and the expression for $\sigma_{\mathrm{WS}} \circ \Phi_q$ we conclude

$$\begin{aligned}
&|\hat{g}(q, v_1) - \hat{g}(q, v_2)| \\
&\quad \leq \int_{\partial_{\mathrm{w}}\Omega} |(1 + |\sigma_{\mathrm{WS},1}| \circ \Phi_q)^{-1} - (1 + |\sigma_{\mathrm{WS},2}| \circ \Phi_q)^{-1}| \, |\operatorname{Cof} F_q \mathfrak{n}| \, \mathrm{d}o \\
&\quad \lesssim \int_{\partial_{\mathrm{w}}\Omega} ||\sigma_{\mathrm{WS},1}| \circ \Phi_q - |\sigma_{\mathrm{WS},2}| \circ \Phi_q| \, \mathrm{d}o \\
&\quad \lesssim \|v_1 - v_2\|_{H^2(\Omega)}.
\end{aligned}$$

□

Extension of Boundary Values

To reduce the problem to one with homogeneous boundary values let P_{io} be regular enough such that there is $p_{\mathrm{io}} \in L^2(0,1; H^1(\Omega))$ with $p_{\mathrm{io}}|_{\partial_{\mathrm{io}}\Omega} = P_{\mathrm{io}}$. Setting $\hat{p} = p_{\mathrm{io}} + \hat{p}_0$ we have

$$Re^{-1} \nabla^s \hat{v}\mathfrak{n} - \hat{p}_0 \mathfrak{n} = Re^{-1} \nabla^s \hat{v}\mathfrak{n} - \hat{p}\mathfrak{n} + p_{\mathrm{io}}\mathfrak{n} = -p_{\mathrm{io}}\mathfrak{n} + p_{\mathrm{io}}\mathfrak{n} = 0$$

on $\partial_{\mathrm{io}}\Omega$ and thus $(\hat{v}, \hat{p}_0)$ solves the Stokes' equation with homogeneous boundary values and right-hand side

$$f(t; q) := -\operatorname{Cof} F_q^{\intercal} \nabla_q p_{\mathrm{io}}(t) \quad \text{for } t \in (0,1) \text{ a.e.} \tag{4.12}$$

For any $I := (0, T)$ with $T > 0$ and $q \in C(\overline{I}, Q)$ we have

$$\{I \ni t \mapsto f(t; q(t))\} \in L^2(I, L^2(\Omega))$$

by the regularity assumptions on p_{io} and Φ_q.

Summary, Simplified Notation

We will not study the solution on the non-cylindrical domain anymore, hence we omit the hats in our notation but add a subscript ε to emphasize the dependency on ε. Furthermore, we examine the problem with homogeneous boundary values and omit the regular perturbations of order $\mathcal{O}(\varepsilon)$. Specifically, we write $(v_\varepsilon, p_\varepsilon)$ instead of $(\hat{v}, \hat{p}_0)$ and g instead of $\hat{g}$.

Problem 4.1.5. *Let $0 < \varepsilon \ll 1$ and $I := (0, T)$ with $T > 0$. Given $q^0 \in Q$ and $v^0 \in \mathcal{V} \subset H^1(\Omega)$, $\mathcal{V}$ introduced later, find $q_\varepsilon \in C^{0,1}(\overline{I}, Q)$, $v_\varepsilon \in L^2(I, H^2(\Omega)) \cap H^1(I, L^2(\Omega))$ and $p_\varepsilon \in L^2(I, H^1(\Omega))$ such that*

$$\left.\begin{aligned} St\, \partial_t v_\varepsilon - Re^{-1} \operatorname{Cof} F_{q_\varepsilon}^{\intercal} \Delta_{q_\varepsilon} (\operatorname{Cof} F_{q_\varepsilon}^{-\intercal} v_\varepsilon) + \operatorname{Cof} F_{q_\varepsilon}^{\intercal} \nabla_{q_\varepsilon} p_\varepsilon = f(q_\varepsilon), \\ \operatorname{div} v_\varepsilon = 0 \end{aligned}\right\} \text{ in } I \times \Omega,$$

where f is given by eq. (4.12), with initial condition $v_\varepsilon(0) = v^0$ and boundary values

$$\begin{aligned} Re^{-1} \partial_{\mathfrak{n}} v_\varepsilon - p_\varepsilon \mathfrak{n} = 0 \quad &\text{on } I \times \partial_{io}\Omega, \\ v_\varepsilon = 0 \quad &\text{on } I \times \partial_{w}\Omega. \end{aligned}$$

The plaque state q_ε must satisfy the ordinary differential equation

$$q_\varepsilon' = \varepsilon g(q_\varepsilon, v_\varepsilon)$$

with initial condition $q_\varepsilon(0) = q^0$ where g satisfies eq. (4.8) and ineq. (4.9).

For the following analysis we will always set $St = Re = 1$.

4.2 Analysis on a Fixed Timescale

In this section we analyze Problem 4.1.5 for fixed ε. We first study the fluid equation for given $q \in C(\overline{I}, Q)$ which occupies most of this section, the existence of solutions to the full model follows by a fixed-point argument. For the fluid equation we follow the approach by [Saa06]: To investigate the non-autonomous equation, we study the autonomous equation for a fixed state $q \in Q$ and use [Saa06, Theorem 1.4] to conclude existence and regularity for the non-autonomous problem. The autonomous problem is induced by the Piola transform of the Stokes operator on Ω_q, which is why we first examine this operator, the main challenge being the mixed boundary conditions.

Stokes Operator on Ω_q

We begin by studying the domain and action of the Stokes operator with mixed boundary conditions, which requires several preparatory results. We define the approximation space

$$C^\infty_{\sigma,\mathrm{w}}(\overline{\Omega}) := \{\varphi \in C^\infty(\overline{\Omega}) \mid \operatorname{div}\varphi = 0,\ \operatorname{supp}\varphi \cap \partial_{\mathrm{w}}\Omega = \varnothing\}$$

with an analogous definition for Ω_q with $q \in Q$. We write

$$\mathcal{H} := \overline{C^\infty_{\sigma,\mathrm{w}}(\overline{\Omega})}^{\|\cdot\|_{L^2(\Omega)}}, \quad \mathcal{V} := \overline{C^\infty_{\sigma,\mathrm{w}}(\overline{\Omega})}^{\|\cdot\|_{H^1(\Omega)}}, \quad \mathcal{V}^+ := \mathcal{V} \cap H^2(\Omega)$$

and analogously $\mathcal{H}_q$, $\mathcal{V}_q$ and $\mathcal{V}_q^+$ if the domain is Ω_q. By construction, $\mathcal{V} \hookrightarrow \mathcal{H}$ continuously and densely. We also use the spaces

$$C^\infty_{\mathrm{io}}(\overline{\Omega}) := \{\varphi \in C^\infty(\overline{\Omega}) \mid \operatorname{supp}\varphi \cap \partial_{\mathrm{io}}\Omega = \varnothing\}, \quad \mathcal{W} := \overline{C^\infty_{\mathrm{io}}(\overline{\Omega})}^{\|\cdot\|_{H^1(\Omega)}}$$

and define analogously $\mathcal{W}_q$.

Lemma 4.2.1 (Generalized normal trace, [Soh01, Section II.1.2])**.** *On the Banach space*

$$E(\Omega) := \{v \in L^2(\Omega) \mid \operatorname{div} v \in L^2(\Omega)\}$$

with norm $\|v\|_{E(\Omega)} := \|v\|_{L^2(\Omega)} + \|\operatorname{div} v\|_{L^2(\Omega)}$ there exists a bounded linear operator

$$E(\Omega) \to H^{-\frac{1}{2}}(\partial\Omega), \quad v \mapsto v \cdot \mathfrak{n}$$

which extends the classical normal trace in the sense that for $v \in C^\infty(\overline{\Omega})$ and $\varphi \in H^{\frac{1}{2}}(\Omega)$ there holds

$$(v \cdot \mathfrak{n})(\varphi) = (v \cdot \mathfrak{n}, \varphi)_{\partial\Omega}$$

and for any $v \in E(\Omega)$ and $\varphi \in H^1(\Omega)$ there holds the generalized Green's formula

$$(\operatorname{div} v, \varphi) + (v, \nabla\varphi) = \langle v \cdot \mathfrak{n}, \varphi\rangle_{\partial\Omega} := (v \cdot \mathfrak{n})(\varphi).$$

Proof. See e.g. [Soh01, Section II.1.2]. □

Lemma 4.2.2. *There holds*

$$\begin{aligned}\mathcal{H} &= \{v \in L^2(\Omega) \mid \operatorname{div} v = 0,\ \langle v \cdot \mathfrak{n}, \varphi\rangle_{\partial\Omega} = 0\ \forall \varphi \in \mathcal{W}\},\\ \mathcal{V} &= \{v \in H^1(\Omega) \mid \operatorname{div} v = 0,\ v|_{\partial_w\Omega} = 0\},\\ \mathcal{W} &= \{v \in H^1(\Omega) \mid v|_{\partial_{io}\Omega} = 0\}.\end{aligned}$$

Analogous results are valid for $\mathcal{H}_q$, $\mathcal{V}_q$ and $\mathcal{W}_q$.

Proof. Let $\tilde{\mathcal{H}}$, $\tilde{\mathcal{V}}$ and $\tilde{\mathcal{W}}$ denote the sets on the right of the claimed equalities. The inclusions $\mathcal{V} \subset \tilde{\mathcal{V}}$ and $\mathcal{W} \subset \tilde{\mathcal{W}}$ follow by continuity of the divergence and trace operator on $H^1(\Omega)$. To prove $\tilde{\mathcal{W}} \subset \mathcal{W}$ we extend Ω to a Lipschitz domain $\hat{\Omega}$ by extruding $\partial_{\mathrm{io}}\Omega$ in normal direction. Then for $v \in \tilde{\mathcal{W}}$ there exists $\hat{v} \in H^1_0(\hat{\Omega})$ such that $\hat{v}|_\Omega = v$. By density of $C^\infty_0(\hat{\Omega})$ in $H^1_0(\hat{\Omega})$ there are $\hat{\varphi}_k \in C^\infty_0(\hat{\Omega})$ with $\hat{\varphi}_k \to \hat{v}$ in $H^1(\hat{\Omega})$, which implies $\varphi_k := \hat{\varphi}_k|_\Omega \to v$ in $H^1(\Omega)$ and $\varphi_k \in C^\infty(\overline{\Omega})$, $\operatorname{supp}\varphi_k \cap \partial_{\mathrm{io}}\Omega = \varnothing$, hence $v \in \mathcal{W}$.

To prove that $v \in \tilde{\mathcal{V}}$ lies in $\mathcal{V}$ we modify an argument from [Hey76, Section 3]. Since $\partial_{\mathrm{w}}\Omega$ is C^3, an argument as in [PS16, Section 2.3] implies that $\sigma > 0$ exists for which

$$\Lambda\colon \overline{\partial_{\mathrm{w}}\Omega} \times [0,\sigma) \to \mathbb{R}^d, \quad (y,d) \mapsto y - d\mathfrak{n}_y$$

is a C^2-diffeomorphism onto its image $\Lambda(\overline{\partial_{\mathrm{w}}\Omega} \times [0,\sigma)) = \{x \in \overline{\Omega} \mid \mathrm{d}(x, \partial_{\mathrm{w}}\Omega) < \sigma\}$ since the boundaries $\partial_{\mathrm{w}}\Omega$ and $\partial_{\mathrm{io}}\Omega$ are orthogonal and $\partial_{\mathrm{io}}\Omega$ is planar. We write $\Lambda^{-1} = (\pi, \delta)$. We define the shrinking transformation for $\theta \in (0,1]$ and $x \in \overline{\Omega}$ by

$$\Psi_\theta(x) = \begin{cases} x & \text{if } \mathrm{d}(x, \partial_{\mathrm{w}}\Omega) \geq \sigma,\\ \pi(x) - \eta_\theta(\delta(x))\mathfrak{n}_{\pi(x)} & \text{else}\end{cases}$$

where $\eta_\theta(d) := d + \frac{1}{3}(1-\theta)\sigma^{-2}(\sigma - d)^3$, following [Hey76]. Then $\eta_1(d) = d$ and η_θ is strictly monotone increasing with $\eta_\theta(\sigma) = \sigma$, $\eta'_\theta(\sigma) = \eta''_\theta(\sigma) = 0$ for all θ. This implies that ψ_θ is C^2-diffeomorphism onto its image denoted by $\overline{\Omega}_\theta$. Then $\overline{\Omega}_\theta \subset \overline{\Omega}$ and since $\eta_\theta(0) > 0$ for $\theta < 1$, $\overline{\Omega}_\theta \cap \partial_{\mathrm{w}}\Omega = \varnothing$ for $\theta < 1$. Let v_θ denote the image of v under the inverse Piola transformation induced by Ψ_θ, identified with its extension by zero to $\overline{\Omega}$. Then by [Hey76], $v_\theta \in H^1_\sigma(\Omega)$, $\operatorname{supp} v_\theta \cap \partial_{\mathrm{w}}\Omega = \varnothing$ and $\|v - v_\theta\|_{H^1(\Omega)} \to 0$ as $\theta \to 1$.

Let $v_{\theta,\rho}$ denote the mollification of v_θ, extended constant in normal direction $\partial_{\mathrm{io}}\Omega$, with some mollification kernel of width $0 < \rho < \rho_0(\theta)$. Then $\operatorname{div} v_{\theta,\rho} = 0$ and $\operatorname{supp} v_{\theta,\rho} \cap \partial_{\mathrm{w}}\Omega = \varnothing$ for small ρ. Thus $v_{\theta,\rho} \in C^\infty_{\sigma,\mathrm{w}}(\overline{\Omega})$ and $\|v_\theta - v_{\theta,\rho}\|_{H^1(\Omega)} \to 0$ for $\rho \to 0$. Hence there are θ_k and ρ_k such that

$$\|v - v_{\theta_k,\rho_k}\|_{H^1(\Omega)} \leq \|v - v_{\theta_k}\|_{H^1(\Omega)} + \|v_{\theta_k} - v_{\theta_k,\rho_k}\|_{H^1(\Omega)} \to 0$$

for $k \to \infty$, implying $v \in \mathcal{V}$.

Let $v \in \mathcal{H}$. Then $v_k \in C^\infty_{\sigma,\mathrm{w}}(\overline{\Omega})$ exists with $\|v - v_k\|_{L^2(\Omega)} \to 0$. Using the definition of distributional divergence, this is sufficient to prove $\operatorname{div} v = 0$ and hence $v \cdot \mathfrak{n}$ is well-defined in the generalized sense above. For $\varphi \in \mathcal{W}$ there holds

$$\langle v \cdot \mathfrak{n}, \varphi\rangle_{\partial\Omega} = (v, \nabla\varphi) = \lim_{k\to\infty}(v_k, \nabla\varphi) = \lim_{k\to\infty}(v_k \cdot \mathfrak{n}, \varphi)_{\partial\Omega} = 0$$

since $v_k|_{\partial_{\mathrm{w}}\Omega} = 0$ and $\varphi|_{\partial_{\mathrm{io}}\Omega} = 0$. Hence $v \in \mathcal{H}$ implies $v \in \tilde{\mathcal{H}}$.

For the final implication $\tilde{\mathcal{H}} \subset \mathcal{H}$ we use a technique similar to [Tem01, Theorem 1.4], using a characterization of the orthogonal complement of $\mathcal{H}$. We claim that

$$\mathcal{H}^\perp = \{\nabla p \mid p \in \mathcal{W}\}.$$

With slight abuse of notation let $\tilde{\mathcal{H}}^\perp$ denote the right-hand side of this identity (and not the orthogonal complement of $\tilde{\mathcal{H}}$). If $v \in \tilde{\mathcal{H}}^\perp$, i.e. $v = \nabla p$ for $p \in \mathcal{W}$, then we must prove that $(v, \varphi) = 0$ for all $\varphi \in \mathcal{H}$. Let $\varphi_k \in C^\infty_{\sigma,\mathrm{w}}(\overline{\Omega})$ be such that $\varphi_k \to \varphi$ in $L^2(\Omega)$ for $k \to \infty$, then

$$(v, \varphi) = \lim_{k\to\infty} (v, \varphi_k) = \lim_{k\to\infty} (\nabla p, \varphi_k) = \lim_{k\to\infty} (-(p, \operatorname{div} \varphi_k) + (p\mathfrak{n}, \varphi_k)_{\partial\Omega}) = 0$$

since $-(p, \operatorname{div} \varphi_k) = 0$ and $(p\mathfrak{n}, \varphi_k)_{\partial\Omega} = 0$ for $\varphi_k|_{\partial_{\mathrm{w}}\Omega} = 0$ and $p|_{\partial_{\mathrm{io}}\Omega} = 0$. We can thus conclude $v \in \mathcal{H}^\perp$. For $\mathcal{H}^\perp \subset \tilde{\mathcal{H}}^\perp$ let $v \in \mathcal{H}^\perp$. The functional

$$F_v \colon L^2(\Omega) \to L^2(\Omega), \quad \varphi \mapsto (v, \varphi)$$

can be restricted to $H^{-1}(\Omega)$ and by the orthogonality assumption $F_v(\varphi) = 0$ for all $\varphi \in C^\infty_0(\Omega)$ with $\operatorname{div} \varphi = 0$. By a standard argument, [Tem01, Proposition 1.2], and using the continuity of F_v in $L^2(\Omega)$, this implies that there is $\tilde{p} \in H^1(\Omega)$ such that $(v, \varphi) = F_v(\varphi) = (\nabla \tilde{p}, \varphi)$ for $\varphi \in H^1_0(\Omega)$, i.e. $v = \nabla \tilde{p}$.

We prove that there is $c \in \mathbb{R}$ such that $p := \tilde{p} - c$ satisfies $p|_{\partial_{\mathrm{io}}\Omega} = 0$, an argument similar to one in [MMW11, Theorem 6.8]. Orthogonality yields that

$$0 = (v, \varphi) = (\nabla \tilde{p}, \varphi) = -(\tilde{p}, \operatorname{div} \varphi) + (\tilde{p}\mathfrak{n}, \varphi)_{\partial\Omega} = (\tilde{p}\mathfrak{n}, \varphi)_{\partial\Omega} \tag{4.13}$$

for all $\varphi \in C^\infty_{\sigma,\mathrm{w}}(\overline{\Omega})$ and by density for all $\varphi \in \mathcal{V}$. This identity only depends on $\varphi|_{\partial\Omega}$, characterized as follows:

$$\{\varphi|_{\partial\Omega} \mid \varphi \in \mathcal{V}\} = \{\varphi \in H^{\frac{1}{2}}(\partial\Omega) \mid \varphi|_{\partial_{\mathrm{w}}\Omega} = 0, \int_{\partial\Omega} \varphi \cdot \mathfrak{n} \,\mathrm{d}o = 0\}. \tag{4.14}$$

The inclusion $\subset$ follows from $\mathcal{V} = \tilde{\mathcal{V}}$ and the divergence theorem. If $\varphi \in H^{\frac{1}{2}}(\partial\Omega)$ with $\varphi|_{\partial_{\mathrm{w}}\Omega} = 0$ and $\int_{\partial\Omega} \varphi \cdot \mathfrak{n} \,\mathrm{d}o = 0$ let $\mathrm{E}\,\varphi$ denote any $H^1(\Omega)$ extension of φ and let $\varphi \in H^1_0(\Omega)$ solve $\operatorname{div} \varphi = -\operatorname{div}(\mathrm{E}\,\varphi)$, which is well-defined since $\int_\Omega \operatorname{div}(\mathrm{E}\,\varphi) \,\mathrm{d}x = \int_{\partial\Omega} \mathrm{E}\,\varphi \cdot \mathfrak{n} \,\mathrm{d}o = \int_{\partial\Omega} \varphi \cdot \mathfrak{n} \,\mathrm{d}o = 0$. Then $\mathrm{E}\,\varphi + \varphi \in \mathcal{V}$ restricted to $\partial\Omega$ is φ, proving $\supset$.

Back to the construction of p: Fix $\varphi_0 \in H^{\frac{1}{2}}(\partial\Omega)$ satisfying $\varphi_0|_{\partial_{\mathrm{w}}\Omega} = 0$ and $\int_{\partial\Omega} \varphi_0 \cdot \mathfrak{n} \,\mathrm{d}o = 1$. Then for any $\varphi \in H^{\frac{1}{2}}(\partial\Omega)$ with $\varphi|_{\partial_{\mathrm{w}}\Omega} = 0$ set $\eta := \int_{\partial\Omega} \varphi \cdot \mathfrak{n} \,\mathrm{d}o$ so that $\varphi - \eta\varphi_0$ is the trace of a function in $\mathcal{V}$ by eq. (4.14), hence eq. (4.13) implies

$$(\tilde{p}\mathfrak{n}, \varphi)_{\partial\Omega} = (\tilde{p}\mathfrak{n}, \varphi - \eta\varphi_0)_{\partial\Omega} + (\tilde{p}\mathfrak{n}, \eta\varphi_0)_{\partial\Omega} = (\tilde{p}\mathfrak{n}, \eta\varphi_0)_{\partial\Omega} = (c\mathfrak{n}, \varphi_0)_{\partial\Omega}$$

with $c := (\tilde{p}\mathfrak{n}, \varphi_0)_{\partial\Omega}$. Therefore $p := \tilde{p} - c$ satisfies $(p\mathfrak{n}, \varphi)_{\partial\Omega} = 0$ for all $\varphi \in H^1(\Omega)$ with $\varphi|_{\partial_{\mathrm{w}}\Omega} = 0$. By the fundamental lemma this implies $p|_{\partial_{\mathrm{io}}\Omega} = 0$ and thus finally $\mathcal{H}^\perp \supset \tilde{\mathcal{H}}^\perp$.

With this characterization of $\mathcal{H}^\perp$ we come back to the proof of $\mathcal{H} = \tilde{\mathcal{H}}$. Since $\mathcal{H} \subset \tilde{\mathcal{H}}$ was already proven, there exists an orthogonal complement $\mathcal{H}^\triangledown$ of $\mathcal{H}$ in $\tilde{\mathcal{H}}$. Then $\mathcal{H} = \tilde{\mathcal{H}}$ follows if $\mathcal{H}^\triangledown = \{0\}$. If $v \in \mathcal{H}^\triangledown$, then $v \in \tilde{\mathcal{H}}$, i.e.

$\operatorname{div} v = 0$ and $\langle v \cdot \mathfrak{n}, \varphi \rangle = 0$ for all $\varphi \in \mathcal{W}$. But by orthogonality, $v \in \mathcal{H}^{\perp}$, thus $v = \nabla p$ with $p \in \mathcal{W}$. Combining these conditions yields that p satisfies

$$(\nabla p, \nabla \varphi) = 0 \quad \forall \varphi \in \mathcal{W}$$

which implies $p = 0$, i.e. $v = \nabla p = 0$. We conclude $\mathcal{H}^{\nabla} = \{0\}$ and thus $\mathcal{H} = \tilde{\mathcal{H}}$. □

Remark 4.2.3. Since for $\varphi \in \mathcal{W}$ there holds $\varphi|_{\partial_{\mathrm{io}}\Omega} = 0$, the condition $\langle v \cdot \mathfrak{n}, \varphi \rangle_{\partial\Omega} = 0$ in the characterization of $\mathcal{H}$ in Lemma 4.2.2 can be interpreted as weak version of $v \cdot \mathfrak{n}|_{\partial_{\mathrm{w}}\Omega} = 0$. ◇

Definition 4.2.4. For given $q \in Q$ we define the Stokes operator on Ω_q,

$$\tilde{A}_q \colon \mathcal{D}(\tilde{A}_q) \subset \mathcal{H}_q \to \mathcal{H}_q,$$

as follows: $v \in \mathcal{D}(\tilde{A}_q)$ if and only if $v \in \mathcal{V}_q$ and there is $f \in \mathcal{H}_q$ satisfying

$$(\nabla v, \nabla \varphi)_q = (f, \varphi)_q \quad \forall \varphi \in \mathcal{V}_q.$$

Set $\tilde{A}_q v := f$. ◇

That $\tilde{A}_q$ is well-defined, i.e. the uniqueness of f associated to $v \in \mathcal{D}(\tilde{A}_q)$ in the definition above, is a particular consequence of the following lemma.

Lemma 4.2.5. *For each $q \in Q$, $\tilde{A}_q$ is a positive, self-adjoint operator with dense domain induced by the coercive symmetric bilinear form*

$$\mathcal{V}_q \times \mathcal{V}_q \to \mathbb{R}, \quad (v, \varphi) \mapsto (\nabla v, \nabla \varphi)_q. \tag{4.15}$$

Proof. It is clear that the form is symmetric and bilinear. The claimed properties of $\tilde{A}_q$ now follow from [Soh01, Lemma II.3.2.1]. □

Lemma 4.2.6. *For each $v \in \mathcal{V}_q^+$ with $(\mathrm{I} - \mathfrak{n} \otimes \mathfrak{n})\partial_{\mathfrak{n}} v = 0$ on $\partial_{io}\Omega_q$ there exists a unique $p \in H^1(\Omega_q)$ such that*

$$-\Delta v + \nabla p \in \mathcal{H}_q \quad \text{and} \quad \partial_{\mathfrak{n}} v - p\mathfrak{n} = 0 \text{ on } \partial_{io}\Omega_q$$

given as solution to

$$(\nabla p, \nabla \xi)_q = \langle \Delta v \cdot \mathfrak{n}, \xi \rangle_{\partial\Omega_q} = (\Delta v, \nabla \xi)_q \quad \forall \xi \in \mathcal{W}_q$$

with boundary condition $p = \partial_{\mathfrak{n}} v \cdot \mathfrak{n}$ on $\partial_{io}\Omega_q$.

Remark 4.2.7. Since $\Delta v \in E(\Omega_q)$ the normal trace $\Delta v \cdot \mathfrak{n}$ is well-defined in the sense of Lemma 4.2.1. ◇

Proof of Lemma 4.2.6. For $-\Delta v + \nabla p \in \mathcal{H}_q$ to hold it suffices by Lemma 4.2.2 that

$$\operatorname{div}(-\Delta v + \nabla p) = 0 \text{ in } \Omega_q, \quad \langle (-\Delta v + \nabla p) \cdot \mathfrak{n}, \xi \rangle_{\partial\Omega} = 0 \text{ for } \xi \in \mathcal{W}_q$$

which can be rewritten, using $\operatorname{div}(\Delta v) = \Delta(\operatorname{div} v) = 0$, as

$$(\nabla p, \nabla \xi)_q = \langle \nabla p \cdot \mathfrak{n}, \xi \rangle_{\partial\Omega_q} = \langle \Delta v \cdot \mathfrak{n}, \xi \rangle_{\partial\Omega_q} \quad \forall \xi \in \mathcal{W}_q.$$

Writing $p = p_0 + p_D$ with $p_0 \in \mathcal{W}_q$ and $p_D \in H^1(\Omega_q)$ extending the boundary values $\partial_{\mathfrak{n}} v \cdot \mathfrak{n} \in H^{\frac{1}{2}}(\partial_{\mathrm{io}}\Omega_q)$, standard Hilbert space theory yields the existence and uniqueness of p_0 and hence p, since Poincaré's inequality holds on $\mathcal{W}_q$. Using the assumption $(\mathrm{I} - \mathfrak{n} \otimes \mathfrak{n})\partial_{\mathfrak{n}} v = 0$ on $\partial_{\mathrm{io}}\Omega_q$, it follows that

$$\partial_{\mathfrak{n}} v - p\mathfrak{n} = \mathfrak{n} \otimes \mathfrak{n}\, \partial_{\mathfrak{n}} v - p\mathfrak{n} = (\partial_{\mathfrak{n}} v \cdot \mathfrak{n} - p)\mathfrak{n} = 0 \quad \text{on } \partial_{\mathrm{io}}\Omega_q,$$

since by construction $p = \partial_{\mathfrak{n}} v \cdot \mathfrak{n}$ on $\partial_{\mathrm{io}}\Omega_q$. □

Using this lemma and regularity results for the mixed-boundary Stokes problem, we arrive at the following characterization of $\tilde{A}_q$:

Lemma 4.2.8. *There holds*

$$\mathcal{D}(\tilde{A}_q) = \{v \in \mathcal{V}_q^+ \mid (\mathrm{I} - \mathfrak{n} \otimes \mathfrak{n})\partial_{\mathfrak{n}} v = 0 \text{ on } \partial_{io}\Omega_q\}$$

and for $v \in \mathcal{D}(\tilde{A}_q)$ the action of $\tilde{A}_q$ is described by

$$\tilde{A}_q v = -\Delta v + \nabla p$$

with p being the (unique) pressure p associated to v from Lemma 4.2.6.

Proof. Let $v \in \mathcal{V}_q^+$ with $(\mathrm{I} - \mathfrak{n} \otimes \mathfrak{n})\partial_{\mathfrak{n}} v = 0$ on $\partial_{\mathrm{io}}\Omega_q$ and $p \in H^1(\Omega_q)$ as given by Lemma 4.2.6. For $\varphi \in \mathcal{V}_q$ there holds

$$(-\Delta v + \nabla p, \varphi)_q = (\nabla v, \nabla \varphi)_q - (p, \operatorname{div} \varphi)_q - (\partial_{\mathfrak{n}} v - p\mathfrak{n}, \varphi)_{\partial_{\mathrm{io}}\Omega_q} = (\nabla v, \nabla \varphi)_q$$

using that $\operatorname{div} \varphi = 0$, $\varphi|_{\partial_{\mathrm{w}}\Omega_q} = 0$ and the boundary condition on $\partial_{\mathrm{io}}\Omega_q$. This implies that

$$\mathcal{V}_q \ni \varphi \mapsto (\nabla v, \nabla \varphi)_q = (-\Delta v + \nabla p, \varphi)_q$$

is continuous in $\mathcal{H}_q$. Thus $v \in \mathcal{D}(\tilde{A}_q)$ and the claimed representation for $\tilde{A}_q v$ holds. If $v \in \mathcal{D}(\tilde{A}_q)$ then $(\nabla v, \nabla \varphi)_q = (\tilde{A}_q v, \varphi)_q$ for $\varphi \in \mathcal{V}_q$. It follows that $v \in H^2(\Omega_q)$ and thus $v \in \mathcal{V}_q^+$ by a regularity result for the Stokes equation from [BK16, Theorem A.1] if $d = 2$ and [Ben14, Corollary 3] if $d = 3$ due to our assumption that the change of boundary type happens at points where these boundaries are orthogonal. To prove that the tangential components of $\partial_{\mathfrak{n}} v$ vanish, we note that

$$\left[\varphi \mapsto (\nabla v, \nabla \varphi)_q - (\tilde{A}_q v, \varphi)_q\right] \in H^{-1}(\Omega_q)$$

vanishes on $C^\infty_{0,\sigma}(\Omega_q) \subset \mathcal{V}_q$, thus there is $\tilde{p} \in L^2(\Omega_q)$ such that

$$(\nabla v, \nabla \varphi)_q - (\tilde{p}, \operatorname{div} \varphi)_q = (\tilde{A}_q v, \varphi)_q \quad \forall \varphi \in H^1_0(\Omega_q).$$

In fact, $\tilde{p} \in H^1(\Omega_q)$ since $\nabla \tilde{p} = \tilde{A}_q v + \Delta v$ in the sense of distributions. And hence, through partial integration and using the density of $H^1_0(\Omega_q)$ in $L^2(\Omega_q)$, there holds $-\Delta v + \nabla \tilde{p} = \tilde{A}_q v$ a.e. in Ω_q. This implies that

$$(\partial_{\mathfrak{n}} v - \tilde{p}\mathfrak{n}, \varphi)_{\partial\Omega_q} = (\nabla v, \nabla \varphi)_q - (\tilde{p}, \operatorname{div} \varphi)_q + (\Delta v - \nabla \tilde{p}, \varphi)_q = 0$$

for all $\varphi \in \mathcal{V}_q$. Similar arguments as in the proof of Lemma 4.2.2 then imply that there is $c \in \mathbb{R}$ such that with $p := \tilde{p} + c$ there holds $\partial_{\mathfrak{n}} v = p\mathfrak{n}$ and thus $(\mathrm{I} - \mathfrak{n} \otimes \mathfrak{n})\partial_{\mathfrak{n}} v = 0$ on $\partial_{\mathrm{io}}\Omega_q$. □

Lemma 4.2.9. *$\tilde{A}_q$ is a boundedly invertible, sectorial operator and has maximal regularity.*

Proof. The invertibility follows using arguments similar to the case of homogeneous Dirichlet boundary values in [Soh01, Theorem III.2.1.1]. That $\tilde{A}_q$ is a sectorial operator is standard, e.g. [Sch12, Corollary 3.23]. The maximal regularity follows since $\tilde{A}_q$ is induced by a symmetric, coercive and continuous bilinear form, see e.g. [ADF17]. □

Non-Autonomous Stokes Operator

Lemma 4.2.10. *The operator $\mathcal{P}_q$ induces an isomorphism between $\mathcal{X}_q$ and $\mathcal{X}$ for $\mathcal{X} \in \{\mathcal{H}, \mathcal{V}, \mathcal{V}^+\}$ and $q \in Q$ with constants independent of q.*

Proof. Let $v \in \mathcal{H}_q$. By construction $\operatorname{div}(\mathcal{P}_q v) = 0$. It remains to check the validity of the weak boundary condition. For $\varphi \in \mathcal{W}$ we have

$$\begin{aligned}\langle \mathcal{P}_q v \cdot \mathfrak{n}, \varphi\rangle_{\partial\Omega} = (\mathcal{P}_q v, \nabla\varphi) = (v \circ \Phi_q, \operatorname{Cof} F_q \nabla\varphi) = \int_\Omega J_q (v \circ \Phi_q) \cdot \nabla_q \varphi \,\mathrm{d}x \\ = \int_{\Omega_q} v \cdot \nabla(\varphi \circ \Phi_q^{-1}) \,\mathrm{d}x = \langle v \cdot \mathfrak{n}, \varphi \circ \Phi_q^{-1}\rangle_{\partial\Omega_q}\end{aligned}$$

and since the pullback by Φ_q^{-1} induces an isomorphism between $\mathcal{W}$ and $\mathcal{W}_q$, for each $\psi \in \mathcal{W}_q$ we find $\varphi \in \mathcal{W}$ such that $\psi = \varphi \circ \Phi_q^{-1}$, which implies that

$$0 = \langle \mathcal{P}_q v \cdot \mathfrak{n}, \varphi\rangle_{\partial\Omega} = \langle v \cdot \mathfrak{n}, \psi\rangle_{\partial\Omega_q}$$

holds for all $\psi \in \mathcal{W}$ as required. The argument that $\mathcal{P}_q^{-1}$ maps $\mathcal{H}$ to $\mathcal{H}_q$ is analogous. For the more regular spaces $\mathcal{X} = \mathcal{V}$ and $\mathcal{X} = \mathcal{V}^+$ we proceed similarly but can use standard trace theory to argue that the boundary values are preserved. We note that the occurrence of F_q in the definition of $\mathcal{P}_q$ requires Φ_q to be a C^3-diffeomorphism for $\mathcal{P}_q$ to be an isomorphism between H^2-subspaces. The independence of the constants from q follows by the uniform bounds on Φ_q, Φ_q^{-1} and their derivatives. □

Definition 4.2.11. For $q \in Q$ we define the pullback Stokes operator

$$A_q \colon \mathcal{D}(A_q) := \mathcal{P}_q^{-1}\mathcal{D}(\tilde{A}_q) \subset \mathcal{H} \to \mathcal{H}$$

by

$$A_q v := \mathcal{P}_q \circ \tilde{A}_q \circ \mathcal{P}_q^{-1}. \qquad \diamond$$

Lemma 4.2.12. *The domain of A_q is independent of q and given by*

$$\mathcal{D}(A) := \mathcal{D}(A_q) = \{v \in \mathcal{V}^+ \mid (\mathrm{I} - \mathfrak{n} \otimes \mathfrak{n})\partial_{\mathfrak{n}} v = 0 \text{ on } \partial_{io}\Omega\}.$$

Furthermore, the operator norm of A_q is equivalent to the $H^2(\Omega)$-norm with constants independent of q.

Proof. We have

$$\mathcal{D}(A_q) = \mathcal{P}_q^{-1}\mathcal{D}(\tilde{A}_q) = \mathcal{P}_q^{-1}\{v \in \mathcal{V}_q^+ \mid (\mathrm{I} - \mathfrak{n} \otimes \mathfrak{n})\partial_{\mathfrak{n}} v = 0 \text{ on } \partial_{\mathrm{io}}\Omega_q\}$$

by Lemma 4.2.8. The characterization of $\mathcal{D}(A_q)$ follows since $\mathcal{P}_q^{-1} \colon \mathcal{V}_q^+ \to \mathcal{V}^+$ is an isomorphism by Lemma 4.2.10 and $\Phi_q = \mathrm{Id}$ in a neighborhood of $\partial_{\mathrm{io}}\Omega$ by assumption. The independence of the constants follows by the respective statements for $\mathcal{D}(\tilde{A}_q)$ and $\mathcal{P}_q$. □

Corollary 4.2.13. *$(A_q)_{q\in Q}$ is a family of boundedly invertible, sectorial operators of maximal regularity.*

To apply [Saa06, Theorem 1.4] and for our multiscale analysis we need:

Lemma 4.2.14. *The map $A\colon Q \to \mathcal{L}(\mathcal{D}(A), \mathcal{H})$, $q \mapsto A_q$ is Lipschitz continuous.*

Proof. We must prove that for given q_1, $q_2 \in Q$ and $v \in \mathcal{D}(A)$ there holds

$$\|A_{q_1} v - A_{q_2} v\| = \|(\mathcal{P}_{q_1} \circ \tilde{A}_{q_1} \circ \mathcal{P}_{q_1}^{-1} - \mathcal{P}_{q_2} \circ \tilde{A}_{q_2} \circ \mathcal{P}_{q_2}^{-1})v\| \lesssim |q_1 - q_2| \|v\|_{\mathcal{D}(A)}.$$

We use the representation of $\tilde{A}_q v = -\Delta v + \nabla p$ for $v \in \mathcal{D}(\tilde{A}_q)$ for $q \in Q$ from Lemma 4.2.8 with p being the pressure associated to v by Lemma 4.2.6. For the Laplacian, we have seen for fixed $q \in Q$ that

$$\mathcal{P}_q(\Delta(\mathcal{P}_q^{-1} v)) = \operatorname{Cof} F_q^{\intercal} \Delta_q (\operatorname{Cof} F_q^{-\intercal} v) = F_q^{-1} \operatorname{div}(\nabla(\operatorname{Cof} F_q^{-\intercal} v) F_q^{-1} \operatorname{Cof} F_q).$$

Elementary but lengthy calculations yield that for $x \in \Omega$ and $i = 1, \dots, d$

$$[\mathcal{P}_q(\Delta(\mathcal{P}_q^{-1} v))]_i(x) = \sum_{j=1}^{d} \sum_{|\alpha| \le 2} \partial^\alpha v_j(x) a_{ij}^\alpha(x; q)$$

with coefficient functions $a_{ij}^\alpha(\cdot; q)$ containing derivatives of Φ_q up to order $3 - |\alpha|$. By assumption $q \mapsto \Phi_q \in C^3(\overline{\Omega})$ is Lipschitz continuous, it follows that $q \mapsto a_{ij}^\alpha(\cdot; q) \in C(\overline{\Omega}, \mathbb{R})$ is Lipschitz continuous as well. Thus

$$\begin{aligned} &|[\mathcal{P}_{q_1}(\Delta(\mathcal{P}_{q_1}^{-1} v)) - \mathcal{P}_{q_2}(\Delta(\mathcal{P}_{q_2}^{-1} v))]_i(x)| \\ &\quad \le \sum_{j=1}^{d} \sum_{|\alpha| \le 2} |\partial^\alpha v_j(x)| |a_{ij}^\alpha(x; q_1) - a_{ij}^\alpha(x; q_2)| \lesssim |q_1 - q_2| \sum_{j=1}^{d} \sum_{|\alpha| \le 2} |\partial^\alpha v_j(x)| \end{aligned}$$

and we can conclude

$$\|\mathcal{P}_{q_1}(\Delta(\mathcal{P}_{q_1}^{-1} v)) - \mathcal{P}_{q_2}(\Delta(\mathcal{P}_{q_2}^{-1} v))\| \lesssim |q_1 - q_2| \|v\|_{H^2(\Omega)} \lesssim |q_1 - q_2| \|v\|_{\mathcal{D}(A)}.$$

Let $p_i \in H^1(\Omega_{q_i})$ denote the pressure associated to $\mathcal{P}_{q_i}^{-1} v$ by Lemma 4.2.6 for $i = 1, 2$. With the transformation law for scalar gradients there holds

$$\begin{aligned} \|\mathcal{P}_{q_1}(\nabla p_1) - \mathcal{P}_{q_2}(\nabla p_2)\| &= \|\operatorname{Cof} F_{q_1}^{\intercal} \nabla_{q_1}(p_1 \circ \Phi_{q_1}) - \operatorname{Cof} F_{q_2}^{\intercal} \nabla_{q_2}(p_2 \circ \Phi_{q_2})\| \\ &\le \|(\operatorname{Cof} F_{q_1}^{\intercal} F_{q_1}^{-\intercal} - \operatorname{Cof} F_{q_2}^{\intercal} F_{q_2}^{-\intercal}) \nabla(p_1 \circ \Phi_{q_1})\| \\ &\quad + \|\operatorname{Cof} F_{q_2}^{\intercal} F_{q_2}^{-\intercal} \nabla(p_1 \circ \Phi_{q_1} - p_2 \circ \Phi_{q_2})\|. \end{aligned}$$

The first term on the right can be estimated by

$$\begin{aligned} \|(\operatorname{Cof} F_{q_1}^{\intercal} F_{q_1}^{-\intercal} - \operatorname{Cof} F_{q_2}^{\intercal} F_{q_2}^{-\intercal}) \nabla(p_1 \circ \Phi_{q_1})\| &\lesssim |q_1 - q_2| \|\nabla_{q_1}(p_1 \circ \Phi_{q_1})\| \\ &\lesssim |q_1 - q_2| \|\nabla p_1\|_{q_1}. \end{aligned}$$

By construction of p_1 and standard techniques for elliptic equations, there holds

$$\|\nabla p_1\|_{q_1} \lesssim \|\mathcal{P}_{q_1}^{-1} v\|_{\mathcal{D}(\tilde{A}_{q_1})} \lesssim \|v\|_{\mathcal{D}(A)}.$$

For the second term on the right we must estimate $\|\nabla(p_1 \circ \Phi_{q_1} - p_2 \circ \Phi_{q_2})\|$. We transform the equation defining p_i,

$$(\nabla p_i, \nabla \xi)_{q_i} = (\Delta(\mathcal{P}_{q_i}^{-1} v), \nabla \xi)_{q_i} \quad \forall \xi \in \mathcal{W}_{q_i}$$

to the reference domain

$$(J_{q_i} \nabla_{q_i}(p_i \circ \Phi_{q_i}), \nabla_{q_i}(\xi \circ \Phi_{q_i})) = (J_{q_i}(\Delta((\mathcal{P}_{q_i}^{-1} v) \circ \Phi_{q_i}), \nabla_{q_i}(\xi \circ \Phi_{q_i})) \quad \forall \xi \in \mathcal{W}_{q_i}.$$

Since $\Phi_{q_i} \colon \mathcal{W} \to \mathcal{W}_{q_i}$ is an isomorphism and by definition of $\mathcal{P}_{q_i}$, equivalently

$$(J_{q_i} F_{q_i}^{-1} F_{q_i}^{-\intercal} \nabla(p_i \circ \Phi_{q_i}), \nabla \xi) = (\mathcal{P}_{q_i}(\Delta(\mathcal{P}_{q_i}^{-1} v)), \nabla \xi) \quad \forall \xi \in \mathcal{W}.$$

Subtracting these equations for $i = 1, 2$ and some algebraic manipulations yield

$$\begin{aligned}
&(J_{q_2} \nabla_{q_2}(p_1 \circ \Phi_{q_1} - p_2 \circ \Phi_{q_2}), \nabla_{q_2} \xi) \\
&\quad = (\mathcal{P}_{q_1}(\Delta(\mathcal{P}_{q_1}^{-1} v)) - \mathcal{P}_{q_2}(\Delta(\mathcal{P}_{q_2}^{-1} v)), \nabla \xi) \\
&\qquad + ((F_{q_2}^{-1} \operatorname{Cof} F_{q_2} - F_{q_1}^{-1} \operatorname{Cof} F_{q_1}) \nabla(p_1 \circ \Phi_{q_1}), \nabla \xi).
\end{aligned}$$

Since $\Phi_{q_i} = \mathrm{Id}$ near $\partial_{\mathrm{io}}\Omega$ there holds $p_1 \circ \Phi_{q_1} = p_2 \circ \Phi_{q_2}$ on $\partial_{\mathrm{io}}\Omega$. Hence $\xi = p_1 \circ \Phi_{q_1} - p_2 \circ \Phi_{q_2} \in \mathcal{W}$ is a test function. Using the established estimate for the Laplace difference for the first term on the right and the Lipschitz continuity of Φ_q together with $\|\nabla p_1\|_{q_1} \lesssim \|v\|_{\mathcal{D}(A)}$ for the second term on the right yields

$$\|\nabla(p_1 \circ \Phi_{q_1} - p_2 \circ \Phi_{q_2})\| \lesssim |q_1 - q_2| \|v\|_{\mathcal{D}(A)}.$$

Combining these two estimates for the two terms of A_q, we get as claimed

$$\|A_{q_1} v - A_{q_2} v\| \lesssim |q_1 - q_2| \|v\|_{\mathcal{D}(A)}. \qquad \square$$

Theorem 4.2.15. *For given $q \in C(\overline{I}, Q)$, where $I := (0, T)$ with $T > 0$, the non-autonomous operator $A_{q(\cdot)} := \{t \mapsto A_{q(t)}\}$ is maximal regular: For each $v^0 \in \mathcal{V}$ and $f \in L^2(I, \mathcal{H})$, not necessarily given by eq. (4.12), there exists a unique $v \in H^1(I, \mathcal{H}) \cap L^2(I, \mathcal{D}(A))$ such that*

$$\partial_t v(t) + A_{q(t)} v(t) = f(t), \quad v(0) = v^0$$

for $t \in I$ a.e. with the estimate

$$\|\partial_t v\|_{L^2(I,\mathcal{H})} + \|v\|_{L^2(I,\mathcal{D}(A))} \lesssim \|v^0\|_{\mathcal{V}} + \|f\|_{L^2(I,\mathcal{H})}. \tag{4.16}$$

The constants are in particular independent of q and T.

Proof. This is a consequence of [Saa06, Theorem 1.4], whose assumptions were verified in Corollary 4.2.13 and Lemma 4.2.14. The arguments in [Saa06] that the continuity of $t \mapsto A(t)$ guarantees uniform bounds for the constants can be applied to the Lipschitz continuous map $Q \ni q \mapsto A_q$, yielding bounds independent of $q(\cdot)$. $\square$

Coupled Problem

With the previous result for the fluid equation with given state, we prove existence and uniqueness of solutions using a fixed-point iteration for q.

Problem 4.2.16 (Fixed scale problem)**.** *Given $\varepsilon > 0$, $T > 0$, $v^0 \in \mathcal{V}$ and $q^0 \in Q$, find $v_\varepsilon \in L^2(I, \mathcal{D}(A)) \cap H^1(I, \mathcal{H})$ and $q_\varepsilon \in C^{0,1}(I, Q)$ where $I := (0, T)$ such that*

$$\partial_t v_\varepsilon(t) + A_{q_\varepsilon(t)} v(t) = f(t; q_\varepsilon(t)), \qquad v_\varepsilon(0) = v^0, \tag{4.17a}$$

$$q_\varepsilon'(t) = \varepsilon g(q_\varepsilon(t), v_\varepsilon(t)), \qquad q_\varepsilon(0) = q^0. \tag{4.17b}$$

Except for Corollary 4.2.20 the ε-dependence is of no importance for the results of this section, which is why we set $\varepsilon = 1$ and write v and q instead of v_ε and q_ε.

Lemma 4.2.17. *Given $v^0 \in \mathcal{V}$ and $q \in C(\overline{I}, Q)$ for $I := (0, T)$ with $T > 0$ there exists a unique solution $v \in L^2(I, \mathcal{D}(A)) \cap H^1(I, \mathcal{H})$ to*

$$\partial_t v(t) + A_{q(t)} v(t) = f(t; q(t)), \quad v(0) = v^0 \tag{4.18}$$

satisfying

$$\|\partial_t v\|_{L^2(I,\mathcal{H})} + \|v\|_{L^2(I,\mathcal{D}(A))} \lesssim \|v^0\|_{\mathcal{V}} + \|p_{io}\|_{L^2(I,H^1(\Omega))} \tag{4.19}$$

with constant independent of q.

Proof. The result follows immediately from Theorem 4.2.15 and ineq. (4.16) using the definition of $f(t; q)$ from eq. (4.12). □

Lemma 4.2.18. *Let q_1 and $q_2 \in C(\overline{I}, Q)$ for $I := (0, T)$ with some $T > 0$. Let v_1, v_2 be the corresponding solutions to eq. (4.18) with the same initial value $v^0 \in \mathcal{V}$. Then*

$$\begin{aligned} &\|\partial_t(v_1 - v_2)\|_{L^2(I,\mathcal{H})} + \|v_1 - v_2\|_{L^2(I,\mathcal{D}(A))} \\ &\quad\lesssim \left(\|v^0\|_{\mathcal{V}} + \|p_{io}\|_{L^2(I,H^1(\Omega))}\right) \|q_1 - q_2\|_{C(\overline{I},Q)}. \end{aligned} \tag{4.20}$$

Proof. By eq. (4.18), $w := v_1 - v_2$ satisfies, omitting the time as argument,

$$\partial_t w + A_{q_1} w = f(q_1) - f(q_2) + (A_{q_2} - A_{q_1}) v_2,$$

with initial value $w(0) = 0$. The maximal regularity from ineq. (4.16) implies

$$\begin{aligned} &\|\partial_t w\|_{L^2(I,\mathcal{H})} + \|w\|_{L^2(I,\mathcal{D}(A))} \\ &\quad\lesssim \|f(q_1) - f(q_2)\|_{L^2(I,L^2(\Omega))} + \|(A_{q_2} - A_{q_1}) v_2\|_{L^2(I,\mathcal{H})}. \end{aligned} \tag{4.21}$$

By definition of f in eq. (4.12) there holds

$$\begin{aligned} &\|f(q_1) - f(q_2)\|_{L^2(I,L^2(\Omega))} \\ &\quad= \|\operatorname{Cof} F_{q_1}^\intercal \nabla_{q_1} p_{\mathrm{io}} - \operatorname{Cof} F_{q_2}^\intercal \nabla_{q_2} p_{\mathrm{io}}\|_{L^2(I,L^2(\Omega))} \\ &\quad\le \|p_{\mathrm{io}}\|_{L^2(I,H^1(\Omega))} \|\operatorname{Cof} F_{q_1}^\intercal F_{q_1}^{-\intercal} - \operatorname{Cof} F_{q_2}^\intercal F_{q_2}^{-\intercal}\|_{L^\infty(I,L^\infty(\Omega))} \\ &\quad\lesssim \|p_{\mathrm{io}}\|_{L^2(I,H^1(\Omega))} \|q_1 - q_2\|_{C(\overline{I},Q)}. \end{aligned}$$

Using the Lipschitz-continuity of $q \mapsto A_q$ by Lemma 4.2.14 in space and ineq. (4.19) for v_2, for the other term on the right-hand side of ineq. (4.21) there holds

$$\begin{aligned} \|(A_{q_1} - A_{q_2}) v_2\|_{L^2(I,\mathcal{H})} &\lesssim \|v_2\|_{L^2(I,\mathcal{D}(A))} \|q_1 - q_2\|_{C(\overline{I},Q)} \\ &\lesssim \left(\|v^0\|_{\mathcal{V}} + \|p_{\mathrm{io}}\|_{L^2(I,H^1(\Omega))}\right) \|q_1 - q_2\|_{C(\overline{I},Q)}. \end{aligned}$$

Combining the previous results results in the claimed ineq. (4.20). □

Theorem 4.2.19. *For all $v^0 \in \mathcal{V}$, $q^0 \in Q$ there exists $T > 0$ such that Problem 4.2.16 has a unique solution on $I := (0, T)$. If T is chosen maximal with these properties, either $T = \infty$ or $q(T) \in \partial Q$.*

Proof. Let $T > 0$ be chosen appropriately later. We study the Picard iteration map

$$\mathcal{F}\colon \mathcal{U} \to \mathcal{U}, \quad \mathcal{U} \ni \tilde{q} \mapsto \left\{ I \ni t \mapsto q^0 + \int_0^t g(\tilde{q}(s), \tilde{v}(s))\,\mathrm{d}s \right\} \in \mathcal{U}$$

where $\mathcal{U} \subset C(\overline{I}, \mathbb{R}^n)$ is defined below and $\tilde{v}$ is a solution to eq. (4.18) for a fixed plaque state $\tilde{q}$, i.e.

$$\partial_t \tilde{v}(t) + A_{\tilde{q}(t)}\tilde{v}(t) = f(t; \tilde{q}(t)), \quad \tilde{v}(0) = v^0.$$

By Lemma 4.2.17 there is a unique $\tilde{v}$ with these properties and $\tilde{v} \in L^2(I, \mathcal{D}(A))$. By boundedness of g this implies $\mathcal{F}(\tilde{q}) \in W^{1,\infty}(I, Q) \cong C^{0,1}(\overline{I}, Q)$. Let $\rho = \rho(q^0) > 0$ be such that $\overline{B_\rho(q^0)} \subset Q$ and define

$$\mathcal{U} := \{q \in C(\overline{I}, Q) \mid \|q - q^0\|_{C(\overline{I},Q)} \le \rho\}.$$

By definition of ρ it follows that $\mathcal{U}$ is well-defined and a closed subset of $C(\overline{I}, \mathbb{R}^n)$, hence a complete metric space with $\|\cdot\|_{C(\overline{I},Q)}$. If $M > 0$ denotes the bound of g, $\mathcal{F}$ is well-defined for $T \le \rho M^{-1}$. Let $\tilde{q}_1, \tilde{q}_2 \in \mathcal{U}$ and $\tilde{v}_1$, $\tilde{v}_2$ be the solutions to eq. (4.18). The Lipschitz assumption on g from ineq. (4.9) implies

$$\begin{aligned}
\|\mathcal{F}(\tilde{q}_1) - \mathcal{F}(\tilde{q}_2)\|_{C(\overline{I},Q)} &\le \max_{t\in\overline{I}} \int_0^t |g(\tilde{q}_1(s), \tilde{v}_1(s)) - g(\tilde{q}_2(s), \tilde{v}_2(s))|\,\mathrm{d}s \\
&\lesssim \max_{t\in\overline{I}} \int_0^t |\tilde{q}_1(s) - \tilde{q}_2(s)|(1 + \|\tilde{v}_i(s)\|_{\mathcal{D}(A)}) + \|\tilde{v}_1(s) - \tilde{v}_2(s)\|_{\mathcal{D}(A)}\,\mathrm{d}s \\
&\lesssim \|\tilde{q}_1 - \tilde{q}_2\|_{C(\overline{I},Q)}(T + \sqrt{T}\|\tilde{v}_i\|_{L^2(I,\mathcal{D}(A))}) + \sqrt{T}\|\tilde{v}_1 - \tilde{v}_2\|_{L^2(I,\mathcal{D}(A))}
\end{aligned}$$

for $i \in \{1, 2\}$. With the estimate ineq. (4.20) from Lemma 4.2.18 for $\|\tilde{v}_1 - \tilde{v}_2\|_{L^2(I,\mathcal{D}(A))}$ and the bound from ineq. (4.19) for $\|v_i\|_{L^2(I,\mathcal{D}(A))}$, we conclude

$$\|\mathcal{F}(\tilde{q}_1) - \mathcal{F}(\tilde{q}_2)\|_{C(\overline{I},Q)} \lesssim \|\tilde{q}_1 - \tilde{q}_2\|_{C(\overline{I},Q)} \left(T + \sqrt{T}\left(\|v^0\|_{\mathcal{V}} + \|p_{\mathrm{io}}\|_{L^2(I,H^1(\Omega))}\right)\right).$$

Hence for small $T > 0$ depending on $\|v^0\|_{\mathcal{V}}$, $\mathcal{F}$ is a contraction. As a consequence there exists a fixed point $q \in \mathcal{U}$ of $\mathcal{F}$, $q = \mathcal{F}(q) \in C^{0,1}(\overline{I}, Q)$, which together with the solution v of eq. (4.18) solves Problem 4.2.16.

If we assume $T < \infty$ is the maximal time for which a solution exists, we have $q(T) \in \partial Q$ since otherwise Problem 4.2.16 with starting time $T_0 := T$ and initial values $q(T) \in Q$ and $v(T) \in \mathcal{V}$ has a solution on $(T, T + \delta T)$ for some $\delta T > 0$ by the construction carried out before, extending q and v to $(0, T + \delta T)$ and thus contradicting T's maximality.

To prove that the solution to Problem 4.2.16 is unique, let (q_1, v_1) and (q_2, v_2) be two solutions with the same data on a shared interval $I = (0, T)$. If $q := q_1 = q_2$, then $v_1 - v_2$ satisfies $\partial_t(v_1 - v_2) + A_q(v_1 - v_2) = 0$, $(v_1 - v_2)(0) = 0$ and hence $v_1 - v_2 = 0$. Now assume that $q_1 \neq q_2$. Define $\tilde{T} := \inf J$ for $J := \{t \in \overline{I} \mid q_1(t) \neq q_2(t)\}$. The graphs of q_1 and q_2 on $\overline{I}$ are closed in $\overline{I} \times \mathbb{R}^n$ and so is their intersection. This implies that $\overline{I} \setminus J$ is closed and hence J is open

in $\overline{I}$. Thus $\tilde{T} \in \overline{I} \setminus J$ and hence $\tilde{q} := q_1(\tilde{T}) = q_2(\tilde{T})$ and $\tilde{T} < T$. Since $q_1 = q_2$ on $\tilde{I} := (0, \tilde{T})$, by the argument above, $v_1 = v_2$ on $\tilde{I}$ and $\tilde{v} := v_1(\tilde{T}) = v_2(\tilde{T})$. The initial value problem at $\tilde{T}$ with initial values $(\tilde{q}, \tilde{v})$ has a unique solution on $(\tilde{T}, \tilde{T} + \delta T)$ for δT such that $\tilde{T} + \delta T < T$. This implies $q_1 = q_2$ on $(0, \tilde{T} + \delta T)$, contradicting the construction $\tilde{T}$. □

Corollary 4.2.20. *For given $q^0 \in Q$ there exists $\mathcal{T} > 0$ such that for all $v^0 \in \mathcal{V}$ and $\varepsilon > 0$ the solution to Problem 4.2.16 exists at least on $I := (0, \varepsilon^{-1}\mathcal{T})$.*

Proof. With $\rho := \mathrm{d}(q^0, \partial Q) > 0$ and $M > 0$ being the bound of g, the solution q_ε cannot exit Q for $T \leq \varepsilon^{-1}\rho M^{-1}$ and hence the claim follows from Theorem 4.2.19. □

4.3 Singular Limit

Since the wall shear stress has only L^2-regularity in time, we cannot directly use the results from Chapter 3 to prove convergence of q_ε to the solution of a suitably averaged equation. While this loss of regularity requires some changes in the convergence proof, we nevertheless use some key results from Chapter 3. For this, we first prove that the solution v to eq. (4.18) for given q induces a parametric evolution process as introduced in Chapter 3.

Definition 4.3.1. For $t \geq s$, $q \in C(\overline{I}, Q)$ and $v^0 \in \mathcal{V}$ define

$$V(t, s; q)v^0 := v(t)$$

where for $I := (s, t)$, $v \in L^2(I, \mathcal{D}(A)) \cap H^1(I, \mathcal{H}) \hookrightarrow C(\overline{I}, \mathcal{V})$ solves eq. (4.18) with (shifted) initial value $v(s) = v^0$ and given plaque state q. ◇

Lemma 4.3.2. *The set $\{V(t, s; q); t \geq s, q \in C(\mathbb{R}, Q)\} \subset C(\mathcal{V}, \mathcal{V})$ is a local-in-time evolution process as defined in Chapter 3, i.e. satisfies for $q \in C(\mathbb{R}, Q)$ the conditions*

- *$V(t, t; q) = \mathrm{Id}_{\mathcal{V}}$ for all $t \in \mathbb{R}$,*
- *$V(t, s; q) = V(t, r; q)V(r, s; q)$ for all $t \geq r \geq s$,*
- *$(t, s, v^0) \mapsto V(t, s; q)v^0 \in \mathcal{V}$ is continuous for $t \geq s$, $v^0 \in \mathcal{V}$.*

Proof. This follows by definition and Lemma 4.2.17 using that $L^2(I, \mathcal{D}(A)) \cap H^1(I, \mathcal{H}) \hookrightarrow C(\overline{I}, \mathcal{V})$. □

Lemma 4.3.3. *There exists $\alpha > 0$ such that for $q \in C(\overline{I}, Q)$ and v_1, v_2 solving eq. (4.18) with given q and initial values v_1^0, $v_2^0 \in \mathcal{V}$ there holds*

$$\|\partial_t(\mathrm{e}^{\alpha t}(v_1 - v_2))\|_{L^2(I,\mathcal{H})} + \|\mathrm{e}^{\alpha t}(v_1 - v_2)\|_{L^2(I,\mathcal{D}(A))} \lesssim \|v_1^0 - v_2^0\|_{\mathcal{V}}$$

and pointwise-in-time exponential stability holds in $\mathcal{V}$ for $t \in \overline{I}$:

$$\|v_1(t) - v_2(t)\|_{\mathcal{V}} \lesssim \mathrm{e}^{-\alpha t}\|v_1^0 - v_2^0\|_{\mathcal{V}}.$$

Proof. For any $q \in Q$ the bilinear form

$$\mathcal{V}_q \times \mathcal{V}_q \ni (v, \varphi) \mapsto (\nabla v, \nabla \varphi)_q - \alpha(v, \varphi)_q$$

is coercive for $0 < \alpha < C_q$ with $C_q > 0$ depending only on Poincaré's constant and hence $\operatorname{diam}(\Omega_q)$. Since $\operatorname{diam}(\Omega) \lesssim \operatorname{diam}(\Omega_q) \lesssim \operatorname{diam}(\Omega)$ we can find $\alpha > 0$ independent of q such that the bilinear form is coercive for all $q \in Q$.

Analogous to the arguments for the bilinear form (4.15) the form above induces a maximal regular operator $\tilde{A}_{q,\alpha} = \tilde{A}_q - \alpha \operatorname{Id}_{\mathcal{H}_q}$ on $\mathcal{H}_q$ with domain $\mathcal{D}(\tilde{A}_q)$ and operator norm equivalent to $\|\cdot\|_{\mathcal{D}(\tilde{A}_q)}$ for all $q \in Q$, with analogous properties for $A_{q,\alpha} := \mathcal{P}_q \circ \tilde{A}_{q,\alpha} \circ \mathcal{P}_q^{-1} = A_q - \alpha \operatorname{Id}_{\mathcal{H}}$. For $q \in C(\overline{I}, Q)$, $t \mapsto A_{q(t),\alpha}$ is maximal regular, so that the solution to

$$\partial_t w(t) + A_{q(t)} w(t) - \alpha w(t) = 0, \quad w(0) = w^0 \in \mathcal{V} \tag{4.22}$$

obeys the bound

$$\|\partial_t w\|_{L^2(I,\mathcal{H})} + \|w\|_{L^2(I,\mathcal{D}(A))} \lesssim \|w^0\|_{\mathcal{V}}.$$

Now $w := \mathrm{e}^{\alpha t}(v_1(t) - v_2(t))$ satisfies eq. (4.22), which follows by subtraction of the equations for v_1 and v_2 multiplied with $\mathrm{e}^{\alpha t}$. Thus the maximal regularity estimate for w implies the first claimed bounds. The embedding $L^2(I, \mathcal{D}(A)) \cap H^1(I, \mathcal{H}) \hookrightarrow C(\overline{I}, \mathcal{V})$ results in the pointwise-in-time estimates. □

Corollary 4.3.4. *The assumptions A1–A3 from Chapter 3 are satisfied, i.e.*

A1. There is $\alpha > 0$ such that

$$\|V(t,s;q)v^0 - V(t,s;q)\tilde{v}^0\|_{\mathcal{V}} \lesssim \mathrm{e}^{-\alpha(t-s)} \|v^0 - \tilde{v}^0\|_{\mathcal{V}}.$$

A2. There is a monotone function $\lambda \colon \mathbb{R}_{\geq 0} \to \mathbb{R}_{\geq 0}$ such that

$$\|V(t,s;q)v^0 - V(t,s;\tilde{q})v^0\|_{\mathcal{V}} \lesssim \|q - \tilde{q}\|_{C([s,t],Q)} \left(\|v^0\|_{\mathcal{V}} + \lambda(t-s)\right)$$

for $s < t$, $v^0 \in \mathcal{V}$ and $q, \tilde{q} \in C([s,t], Q)$.

A3. For each $q \in Q$ the process is 1-periodic, i.e.

$$V(t+1, s+1; q) = V(t,s;q)$$

for any $s < t$.

Proof. Exponential stability, pointwise in $\mathcal{V}$, was verified in Lemma 4.3.3, the Lipschitz continuity in Lemma 4.2.18 and periodicity follows since the data p_{io} is 1-periodic. □

Lemma 4.3.5. *For each $q \in Q$ there is a unique $v_\pi(\cdot; q) \in L^2(0,1;\mathcal{D}(A)) \cap H^1(0,1;\mathcal{H})$ solving the time-periodic equation*

$$\partial_s v_\pi(s;q) + A_q v_\pi(s;q) = f(s;q), \quad v_\pi(0,q) = v_\pi(1,q).$$

The map

$$Q \ni q \mapsto v_\pi(\cdot;q) \in L^2(0,1;\mathcal{D}(A)) \cap H^1(0,1;\mathcal{H})$$

is Lipschitz continuous.

Proof. By Lemma 3.3.2 a unique periodic solution exists. The Lipschitz continuity in $L^2(0,1;\mathcal{D}(A)) \cap H^1(0,1;\mathcal{H})$ follows from Lemmas 4.3.3 and 4.2.18 together with the Lipschitz continuity of $Q \ni q \mapsto v_\pi(0;q) \in \mathcal{V}$ also proven in Lemma 3.3.2. □

Let us remind of our notation $\tau \in \mathcal{I} := (0, \mathcal{T})$ for $\mathcal{T} > 0$ to denote the slow timescale. For some fixed $0 < \varepsilon \ll 1$ it is related to the fast ε-timescale, where we write $t \in I := (0, T)$ for $T > 0$, by $\tau = \varepsilon t$, $\mathcal{T} = \varepsilon T$. The limit system is naturally formulated in the slow timescale, but we return to the fast scale for the convergence analysis.

Problem 4.3.6 (Limit system)**.** *Given $\mathcal{T} > 0$, $q^0 \in Q$, find $q_0 \in C^{0,1}(\overline{\mathcal{I}}, Q)$ with $\mathcal{I} := (0, \mathcal{T})$ such that for $\tau \in \mathcal{I}$ there holds*

$$q_0'(\tau) = \overline{g}(q_0(\tau)), \quad q_0(0) = q^0$$

where the averaged right-hand side $\overline{g} \colon Q \to \mathbb{R}^n$ is defined by

$$\overline{g}(q) := \int_0^1 g(q, v_\pi(s; q)) \, \mathrm{d}s \tag{4.23}$$

and $v_\pi(\cdot; q)$ for $q \in Q$ denotes the time periodic solution from Lemma 4.3.5.

Lemma 4.3.7. *The function $\overline{g}$ defined in eq. (4.23) is Lipschitz continuous.*

Proof. For $q_1, q_2 \in Q$ there holds for $i \in \{1, 2\}$:

$$\begin{aligned}
&|\overline{g}(q_1) - \overline{g}(q_2)| \\
&\quad \lesssim \int_0^1 |q_1 - q_2|(1 + \|v_\pi(s; q_i)\|_{\mathcal{D}(A)}) + \|v_\pi(s; q_1) - v_\pi(s; q_2)\|_{\mathcal{D}(A)} \, \mathrm{d}s \\
&\quad \lesssim |q_1 - q_2|(1 + \|v_\pi(q_i)\|_{L^2(0,1;\mathcal{D}(A))}) + \|v_\pi(q_1) - v_\pi(q_2)\|_{L^2(0,1;\mathcal{D}(A))} \\
&\quad \lesssim |q_1 - q_2|
\end{aligned}$$

using the Lipschitz-continuity of g, ineq. (4.9), and the Lipschitz continuity of $q \mapsto v_\pi(q) \in L^2(0, 1; \mathcal{D}(A))$ from Lemma 4.3.5. □

Lemma 4.3.8. *For every $q^0 \in Q$ there exists $\mathcal{T} > 0$ such that Problem 4.3.6 has a unique solution $q_0 \in C^{1,1}(\overline{\mathcal{I}}, Q)$ where $\mathcal{I} := (0, \mathcal{T})$. For the maximum time of existence either $\mathcal{T} = \infty$ or $q_0(\mathcal{T}) \in \partial Q$.*

Proof. This follows from standard theory of ordinary differential equations due to the Lipschitz continuity and boundedness of $\overline{g}$ from Lemma 4.3.7. □

Theorem 4.3.9. *For $q^0 \in Q$ and $v^0 \in \mathcal{V}$ there exists $\mathcal{T} > 0$ such that for any $0 < \varepsilon \ll 1$ the solution $(q_\varepsilon, v_\varepsilon)$ to Problem 4.2.16 exists on $I := (0, \varepsilon^{-1}\mathcal{T})$, the solution q_0 to Problem 4.3.6 exists on $\mathcal{I} = (0, \mathcal{T})$ and there holds*

$$\|q_\varepsilon - q_0\|_{C(I,Q)} \lesssim \varepsilon.$$

Proof. By Corollary 4.2.20 there exists $\mathcal{T} > 0$ such that for any $\varepsilon > 0$ Problem 4.2.16 has a solution $(q_\varepsilon, v_\varepsilon)$ on $I := (0, T)$ with $T := T_\varepsilon := \varepsilon^{-1}\mathcal{T}$. By Lemma 4.3.8 the same holds true for q_0 with $\mathcal{T}$ smaller if necessary. For $t \in I$ there holds

$$\begin{aligned}
&|q_\varepsilon(t) - q_0(t)|^2 \\
&\quad \le \varepsilon^2 \Big| \int_0^t g(q_\varepsilon, v_\varepsilon) - \overline{g}(q_0) \, \mathrm{d}s \Big|^2 \\
&\quad \le \varepsilon^2 \Big| \int_0^t g(q_\varepsilon, v_\varepsilon) - g(q_0, v_\varepsilon) \, \mathrm{d}s \Big|^2 + \varepsilon^2 \Big| \int_0^t g(q_0, v_\varepsilon) - \overline{g}(q_0) \, \mathrm{d}s \Big|^2.
\end{aligned} \tag{4.24}$$

For the first term we use the Lipschitz continuity of g, ineq. (4.9), to estimate

$$\begin{aligned}|\int_0^t g(q_\varepsilon) - g(q_0, v_\varepsilon)\,\mathrm{d}s|^2 &\lesssim \left(\int_0^t (1 + \|v_\varepsilon\|_{\mathcal{D}(A)})|q_\varepsilon - q_0|\,\mathrm{d}s\right)^2 \\ &\lesssim (T + \|v_\varepsilon\|^2_{L^2(I,\mathcal{D}(A))}) \int_0^t |q_\varepsilon - q_0|^2\,\mathrm{d}s.\end{aligned}$$

Using ineq. (4.19) and $\|p_{\mathrm{io}}\|^2_{L^2(I,H^1(\Omega))} \lesssim \varepsilon^{-1}\|p_{\mathrm{io}}\|^2_{L^2(0,1;H^1(\Omega))}$ it follows that

$$\|v_\varepsilon\|^2_{L^2(I,\mathcal{D}(A)} \lesssim \|v^0\|^2_{\mathcal{V}} + \|p_{\mathrm{io}}\|^2_{L^2(I,H^1(\Omega))} \lesssim \varepsilon^{-1}$$

which together with $T \lesssim \varepsilon^{-1}$ implies for ineq. (4.24) that

$$|q_\varepsilon(t) - q_0(t)|^2 \lesssim \varepsilon \int_0^t |q_\varepsilon - q_0|^2\,\mathrm{d}s + \varepsilon^2 |\int_0^t g(q_0, v_\varepsilon) - \overline{g}(q_0)\,\mathrm{d}s|^2. \tag{4.25}$$

Our goal is to apply Gronwall's inequality to ineq. (4.25), which yields the claimed estimate if all terms on the right are either of the form of the first term or of order ε^2. We abbreviate $v^0_\pi(q) := v_\pi(0;q)$ and $\tilde{v}_\varepsilon(t) := v(0,t;q_\varepsilon)v^0_\pi(q^0)$. Then there holds

$$\begin{aligned}&|\int_0^t g(q_0, v_\varepsilon) - \overline{g}(q_0)\,\mathrm{d}s| \\ &\quad\le \int_0^t |g(q_0, v_\varepsilon) - g(q_0, \tilde{v}_\varepsilon)|\,\mathrm{d}s + |\int_0^t g(q_0, \tilde{v}_\varepsilon) - \overline{g}(q_0)\,\mathrm{d}s|\end{aligned} \tag{4.26}$$

and the exponential stability estimate from Lemma 4.3.3 implies

$$\begin{aligned}\int_0^t |g(q_0, v_\varepsilon) - g(q_0, \tilde{v}_\varepsilon)|\,\mathrm{d}s &\lesssim \int_0^t \|v_\varepsilon - \tilde{v}_\varepsilon\|_{\mathcal{D}(A)}\,\mathrm{d}s \\ &\lesssim \left(\int_0^t \mathrm{e}^{-2\alpha s}\,\mathrm{d}s\right)^{\frac{1}{2}} \|\mathrm{e}^{\alpha s}(v_\varepsilon - \tilde{v}_\varepsilon)\|_{L^2(0,t;\mathcal{D}(A))} \lesssim \|v^0 - v^0_\pi(q^0)\|_{\mathcal{V}} \lesssim 1.\end{aligned}$$

For the second term on the right of ineq. (4.26) we proceed as in Chapter 3 and split $[0,t]$ into $\lfloor t \rfloor$ intervals of period length 1 and a remainder:

$$\begin{aligned}&|\int_0^t g(q_0, \tilde{v}_\varepsilon) - \overline{g}(q_0)\,\mathrm{d}s|^2 \\ &\quad\lesssim |\sum_{i=1}^{\lfloor t \rfloor} \int_{i-1}^{i} g(q_0, \tilde{v}_\varepsilon) - \overline{g}(q_0)\,\mathrm{d}s|^2 + \int_{\lfloor t \rfloor}^t |g(q_0, \tilde{v}_\varepsilon) - \overline{g}(q_0)|^2\,\mathrm{d}s.\end{aligned}$$

The last term is bounded independent of ε since g, and hence $\overline{g}$, is. We abbreviate e.g. $q^{i-1}_\varepsilon := q_\varepsilon(i-1)$ and split the remaining integrals over full periods

as follows:

$$\int_{i-1}^{i} g(q_0, \tilde{v}_\varepsilon) - \overline{g}(q_0)\,\mathrm{d}s \tag{4.27a}$$

$$= \int_{i-1}^{i} g(q_0, \tilde{v}_\varepsilon) - g(q_0, v_\pi(q_\varepsilon^{i-1}))\,\mathrm{d}s \tag{4.27b}$$

$$+ \int_{i-1}^{i} g(q_0, v_\pi(q_\varepsilon^{i-1})) - g(q_0, v_\pi(q_0^{i-1}))\,\mathrm{d}s \tag{4.27c}$$

$$+ \int_{i-1}^{i} g(q_0, v_\pi(q_0^{i-1})) - g(q_0^{i-1}, v_\pi(q_0^{i-1}))\,\mathrm{d}s \tag{4.27d}$$

$$+ \int_{i-1}^{i} g(q_0^{i-1}, v_\pi(q_0^{i-1})) - \overline{g}(q_0^{i-1})\,\mathrm{d}s \tag{4.27e}$$

$$+ \int_{i-1}^{i} \overline{g}(q_0^{i-1}) - \overline{g}(q_0)\,\mathrm{d}s. \tag{4.27f}$$

The integral in line (4.27e) is zero by definition of $\overline{g}$ since we integrate over one period. Since we sum over $\lfloor t \rfloor \lesssim \varepsilon^{-1}$ periods we require lines (4.27b), (4.27d) and (4.27f) to be of order ε, line (4.27c) will be estimated differently. For line (4.27b) we use Lipschitz continuity of g, such that it remains to estimate

$$\int_{i-1}^{i} \|\tilde{v}_\varepsilon - v_\pi(q_\varepsilon^{i-1})\|_{\mathcal{D}(A)}\,\mathrm{d}s$$
$$\leq \int_{i-1}^{i} \|\tilde{v}_\varepsilon - V^{i-1}(q_\varepsilon)v_\pi^0(q_\varepsilon^{i-1})\|_{\mathcal{D}(A)} + \|V^{i-1}(q_\varepsilon)v_\pi^0(q_\varepsilon^{i-1}) - v_\pi(q_\varepsilon^{i-1})\|_{\mathcal{D}(A)}\,\mathrm{d}s$$

writing $V^{i-1}(q_\varepsilon) := V(\cdot, i-1; q_\varepsilon)$ for the process starting at $i-1$. There holds

$$\int_{i-1}^{i} \|\tilde{v}_\varepsilon - V^{i-1}(q_\varepsilon)v_\pi^0(q_\varepsilon^{i-1})\|_{\mathcal{D}(A)}\,\mathrm{d}s \lesssim \|\tilde{v}_\varepsilon^{i-1} - v_\pi^0(q_\varepsilon^{i-1})\|_{\mathcal{V}} \lesssim \varepsilon$$

since $\|\tilde{v}_\varepsilon(t) - v_\pi(t; q_\varepsilon(t))\|_{\mathcal{V}} \lesssim \varepsilon$ for any $t \in I$ by a simple modification of the argument in Lemma 3.4.4, noting that not the specific form of q_ε but only a Lipschitz constant of order ε is necessary there. For the second term we have

$$\int_{i-1}^{i} \|V^{i-1}(q_\varepsilon)v_\pi^0(q_\varepsilon^{i-1}) - v_\pi(q_\varepsilon^{i-1})\|_{\mathcal{D}(A)}\,\mathrm{d}s \lesssim \|q_\varepsilon - q_\varepsilon^{i-1}\|_{C([i-1,i],Q)} \lesssim \varepsilon.$$

For line (4.27d) the Lipschitz continuity of g by ineq. (4.9) and of $q \mapsto v_\pi(q)$ by Lemma 4.3.5 yield

$$\int_{i-1}^{i} |g(q_0, v_\pi(q_0^{i-1})) - g(q_0^{i-1}, v_\pi(q_0^{i-1}))|\,\mathrm{d}s$$
$$\lesssim \int_{i-1}^{i} (1 + \|v_\pi(q_0^{i-1})\|_{\mathcal{D}(A)})|q_0 - q_0^{i-1}|\,\mathrm{d}s \lesssim \varepsilon(1 + \|v_\pi(q_0^{i-1})\|_{L^2(0,1;\mathcal{D}(A))})$$

and thus by the boundedness of v_π in $L^2(0,1;\mathcal{D}(A))$ the claim. For line (4.27f) the $\mathcal{O}(\varepsilon)$-estimate follows since $\overline{g}$ is Lipschitz continuous by Lemma 4.3.7. For

the last term on line (4.27c) we have by similar techniques as before

$$\begin{aligned}\int_{i-1}^{i} |g(q_0, v_\pi(q_\varepsilon^{i-1})) - g(q_0, v_\pi(q_0^{i-1}))| \,\mathrm{d}s &\lesssim \int_{i-1}^{i} \|v_\pi(q_\varepsilon^{i-1}) - v_\pi(q_0^{i-1})\|_{\mathcal{D}(A)} \,\mathrm{d}s \\ &\lesssim \|v_\pi(q_\varepsilon^{i-1}) - v_\pi(q_0^{i-1})\|_{L^2(0,1;\mathcal{D}(A))} \lesssim |q_\varepsilon^{i-1} - q_0^{i-1}|.\end{aligned}$$

Using the Lipschitz continuity of q_ε and q_0 we have

$$|q_\varepsilon^{i-1} - q_0^{i-1}| \leq \int_{i-1}^{i} |q_\varepsilon^{i-1} - q_\varepsilon| + |q_\varepsilon - q_0| + |q_0^{i-1} - q_0| \,\mathrm{d}s \lesssim \varepsilon + \int_{i-1}^{i} |q_\varepsilon - q_0| \,\mathrm{d}s.$$

Applying these estimates for lines (4.27b) to (4.27f) in ineq. (4.25), we conclude

$$\begin{aligned}&|q_\varepsilon(t) - q_0(t)|^2 \\ &\quad\lesssim \varepsilon \int_0^t |q_\varepsilon(s) - q_0(s)|^2 \,\mathrm{d}s + \varepsilon^2 + \varepsilon^2 \left(\sum_{i=1}^{\lfloor t \rfloor} \int_{i-1}^{i} |q_\varepsilon(s) - q_0(s)| \,\mathrm{d}s \right)^2 \\ &\quad\lesssim \varepsilon \int_0^t |q_\varepsilon(s) - q_0(s)|^2 \,\mathrm{d}s + \varepsilon^2\end{aligned}$$

and thus by Gronwall's inequality the claimed estimate follows:

$$|q_\varepsilon(t) - q_0(t)|^2 \lesssim \varepsilon^2 \mathrm{e}^{C\varepsilon t} \lesssim \varepsilon^2 \mathrm{e}^{C\mathcal{T}}. \qquad \square$$

Chapter 5

Numerics for the Simplified Plaque Model

This chapter is concerned with the numerical solution of the problem described in Chapter 4, i.e. a fluid equation with time-periodic boundary conditions on a slowly moving domain with movement governed by an ordinary differential equation depending on the wall shear stress. In contrast to the theory we will mainly study the Navier–Stokes equation, assuming that analogous results for the multiscale convergence hold. We emphasize that the interest lies in the evolution of the growth, rather than the blood flow for which a simple reconstruction is available.

The motivation for the theory was that the limit equation is much more efficient to solve numerically than the original fast-slow system, at least for ε "sufficiently small". The numerical solution of the limit system is non-standard since each evaluation of the right-hand side of the limit equation for q_0 requires the solution of the time-periodic solution to the Navier–Stokes equation on the domain corresponding to q_0. This chapter consists of a description of the problem and the discretizations used for both fast-slow and limit systems, an error analysis for the temporally semi-discrete limit equation, the numerical convergence results and an improvement, both theoretically and numerically, of an existing method to solve the time-periodic fluid equation.

5.1 Problem Description

For computational simplicity we only study the two-dimensional geometry from Example 4.1.2 from Chapter 4, see also Figure 5.1. To summarize, this domain is a single-channel geometry with dimensionless diameter 1 and length $L := 5$. At the bottom-center a stenosis may develop with base width $L_0 := 3.5$, prescribed bump-shape and height given by the slow variable q. The fluid flows from the inflow boundary $\partial_{\mathrm{i}}\Omega$ on the left to the outflow boundary $\partial_{\mathrm{o}}\Omega$ on the right, the remaining boundary is the fixed wall $\partial_{\mathrm{w}}\Omega_q$. Only the region $\Gamma_q \subset \partial_{\mathrm{w}}\Omega_q$ of the bump is considered damaged and hence permeable, which in our model means that the growth rate depends on the wall shear stress only in this region.

Some physiological parameters such as Reynolds and Strouhal number were taken from the non-dimensionalization of the model by Yang et. al. [Yan+15]

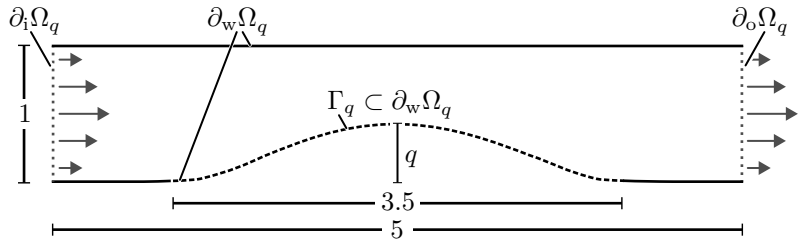

Figure 5.1: Sketch of the problem domain Ω_q for some $q \approx 0.5$ with notation for boundaries and geometric dimensions. The reference domain $\hat{\Omega}$ is a rectangle with the same dimensions. This figure is a repetition of Figure 4.1.

from Section 2.3, but the situation treated here must be viewed as a purely theoretical test case to demonstrate the numerical implementation and acceleration of the proposed multiscale scheme compared to the direct numerical simulation of the original fast-slow problem. Apart from the geometrical simplifications we investigate an exemplary flow profile and wall shear stress to growth rate relation.

We formulate all equations on the unknown moving domain. The problem is then to find fluid velocity v_ε, pressure p_ε and growth q_ε as solution to the following equations. The fluid velocity and pressure is solution to the (dimensionless) Navier–Stokes equation on a moving domain given by

$$\left.\begin{aligned} St\,\partial_t v_\varepsilon + (v_\varepsilon \cdot \nabla) v_\varepsilon - Re^{-1}\,\Delta v_\varepsilon + \nabla p_\varepsilon &= 0, \\ \operatorname{div} v_\varepsilon &= 0, \end{aligned}\right\} \quad \text{in } \Omega^I_{q_\varepsilon} \tag{5.1a}$$

with Strouhal number $St = 0.016$ and Reynolds number $Re = 500$ in the slowly evolving space-time domain

$$\Omega^I_{q_\varepsilon} := \{(t, x) \mid t \in I, x \in \Omega_{q_\varepsilon(t)}\} \tag{5.1b}$$

with plaque state q_ε given by

$$q'_\varepsilon = \varepsilon g(q_\varepsilon, v_\varepsilon) \tag{5.1c}$$

where

$$g(q, v) := \gamma(1 - q) \int_{\Gamma_q} \left(1 + \frac{|\sigma_{\mathrm{WS}}(v)|}{\sigma^0_{\mathrm{WS}}}\right)^{-1} \mathrm{d}o$$

following the example from eq. (4.3) where $\sigma_{\mathrm{WS}}(v)$ is the wall shear stress corresponding to the velocity field v. The parameter $\sigma^0_{\mathrm{WS}} := 0.004$ was chosen such that the integrand over Γ_q has non-trivial behavior, whereas $\gamma := 0.1$ rescales the slow time such that interesting behavior happens for $\tau \in [0, 10]$ and effectively acts as a rescaling of ε.

The initial values chosen for our computations are $q_\varepsilon(0) := 0$ and $v_\varepsilon(0) := 0$ in Ω_0. From a modelling perspective it would be more appropriate to set $v_\varepsilon(0) := v_\pi(0; 0)$ under the assumption that the blood flow prior to our model's initial time is undisturbed and hence periodic. Such an initial value is investigated for a single test case below, but it requires knowledge of the initial

periodic flow, which is unknown in general[1]. The method we present to solve the time-periodic Navier–Stokes problem in our limit equation could be used to determine this initial value, but this would convolute the presentation and computations. This nevertheless highlights that a time-periodic problem should be solved for realistic models even if the fast-slow problem is studied. We remind that the limit system is independent of the choice of initial fluid velocity, so the simplification $v_\varepsilon(0) := 0$ mainly affects the boundary layer behavior for the fast variable v_ε.

On in- and outflow boundaries, a 1-periodic pressure drop is prescribed,

$$Re^{-1}\,\partial_{\mathfrak{n}} v_\varepsilon - p_\varepsilon \mathfrak{n} = -P_{\mathrm{io}}\mathfrak{n} \quad \text{on } I \times \partial_{\mathrm{io}}\Omega \tag{5.1d}$$

with temporally 1-period pressure drop function P_{io} described below. For the wall boundary homogeneous Dirichlet values are used for simplicity

$$v_\varepsilon(t,x) = 0 \quad \text{for } t \in I \text{ and } x \in \partial_{\mathrm{w}}\Omega_{q_\varepsilon(t)}. \tag{5.1e}$$

The pressure drop function is graphed in Figure 5.2 and given by

$$P_{\mathrm{io}}(t,x) = \begin{cases} \frac{p_0}{2}\left(1 - \cos(2\pi(2t - t^2))\right) & \text{for } x \in \partial_{\mathrm{i}}\Omega, \\ 0 & \text{for } x \in \partial_{\mathrm{o}}\Omega \end{cases} \tag{5.2}$$

for $t \in [0,1]$, periodically extended to $\mathbb{R}$. The parameter $p_0 := 0.16$ was chosen such that the induced periodic velocity field has a maximal speed of approximately 1 in the initial geometry while the solution is still stable, see the remarks about the pressure boundary conditions below. The shape of the pressure drop function is intended to only roughly approximate systole (heart contraction) and diastole (refilling of the heart), including the asymmetry of this process.

Translating the multiscale result from Chapter 4 to the present situation for the Navier–Stokes equation we assume that the limit as $\varepsilon \to 0$ is given by the solution to

$$q_0'(\tau) = g_0(q_0(\tau)) \tag{5.3a}$$

with initial value $q_0(0) := 0$ and right-hand side

$$g_0(\hat{q}) := \gamma(1-\hat{q}) \int_0^1 \int_{\Gamma_{\hat{q}}} \left(1 + \frac{|\sigma_{\mathrm{WS},\pi}(s;\hat{q})|}{\sigma^0_{\mathrm{WS}}}\right)^{-1} \mathrm{d}o\,\mathrm{d}s \tag{5.3b}$$

for $\hat{q} \in Q$, where $\sigma_{\mathrm{WS},\pi}(\cdot;\hat{q})$ is the wall shear stress of the solution to the time-periodic Navier–Stokes equation on a cylindrical domain

$$\left.\begin{aligned} St\,\partial_s v_\pi(\hat{q}) + (v_\pi(\hat{q})\cdot\nabla)v_\pi(\hat{q}) - Re^{-1}\,\Delta v_\pi(\hat{q}) + \nabla p_\pi(\hat{q}) &= 0, \\ \operatorname{div} v_\pi(\hat{q}) &= 0, \end{aligned}\right\} \text{ in } (0,1)\times\Omega_{\hat{q}}, \tag{5.3c}$$

omitting the temporal variable $s \in (0,1)$ here, i.e. writing $v_\pi(\hat{q})$ instead of $v_\pi(s;\hat{q})$. This solution is temporally 1-periodic,

$$v_\pi(0;\hat{q}) = v_\pi(1;\hat{q}) \quad \text{in } \Omega_{\hat{q}}, \tag{5.3d}$$

[1] For the straight tube geometry one could use (a spatial projection of) the Womersley flow as an exact solution [Wom55], but such a solution is also only given as a Fourier series depending on the Fourier decomposition of p_{io}.

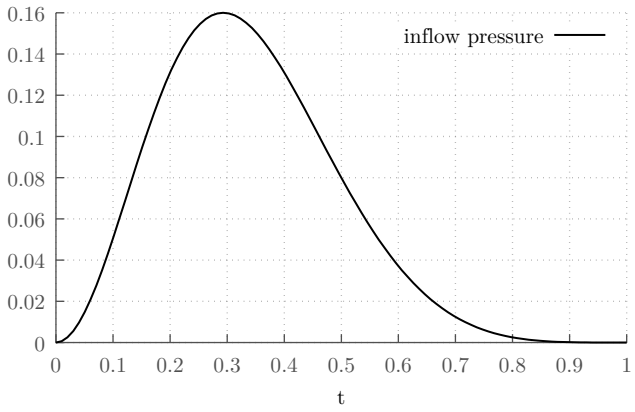

Figure 5.2: Plot of the pressure (drop) at the inflow boundary $\partial_{\mathrm{i}}\Omega$ over one period, see eq. (5.2). A zero pressure is prescribed on the outflow boundary $\partial_{\mathrm{o}}\Omega$.

and has the same boundary conditions as the fast-slow problem, i.e.

$$Re^{-1}\,\partial_{\mathfrak{n}} v_\pi(\hat{q}) - p_\pi(\hat{q})\mathfrak{n} = -P_{\mathrm{io}}\mathfrak{n} \quad \text{on } (0,1)\times\partial_{\mathrm{io}}\Omega, \tag{5.3e}$$

$$v_\pi(\hat{q}) = 0 \quad \text{on } (0,1)\times\partial_{\mathrm{w}}\Omega_{\hat{q}}. \tag{5.3f}$$

We refer to [GK16] for an overview of the theory for the time-periodic Navier–Stokes equation, in particular the existence and uniqueness of weak time-periodic solutions with homogeneous Dirichlet boundary conditions for sufficiently regular right-hand side and domain, assuming the smallness of the data for $d = 3$. Corresponding results for the boundary conditions and domain studied here are not known to the author. In fact, the use of the do-nothing boundary condition on an outflow boundary, as in eq. (5.3e), is known to cause stability issues due to the possibility of uncontrollable backflow, i.e. inflow at nominal outflow boundaries. As a remedy, directional do-nothing conditions have been proposed which add a stabilization only affecting such backflow [BM14] among other approaches [Ber+18]. On inflow boundaries such modifications drastically change the flow profile and are hence unsuitable. Instead, tame problem data and geometry were selected such that no stabilization is necessary.

The behavior of the solutions q_ε and q_0 are plotted in Figure 5.3. These solutions were obtained numerically using the discretization discussed below. All simulations were stopped after the growth variable exceeded a 80%-diameter stenosis, i.e. $q > q_{\max} := 0.8$. In the algorithmic descriptions of the time-stepping schemes this condition is replaced with a fixed number of time steps for simplicity. All errors between solutions in the following were computed on the largest shared time interval.

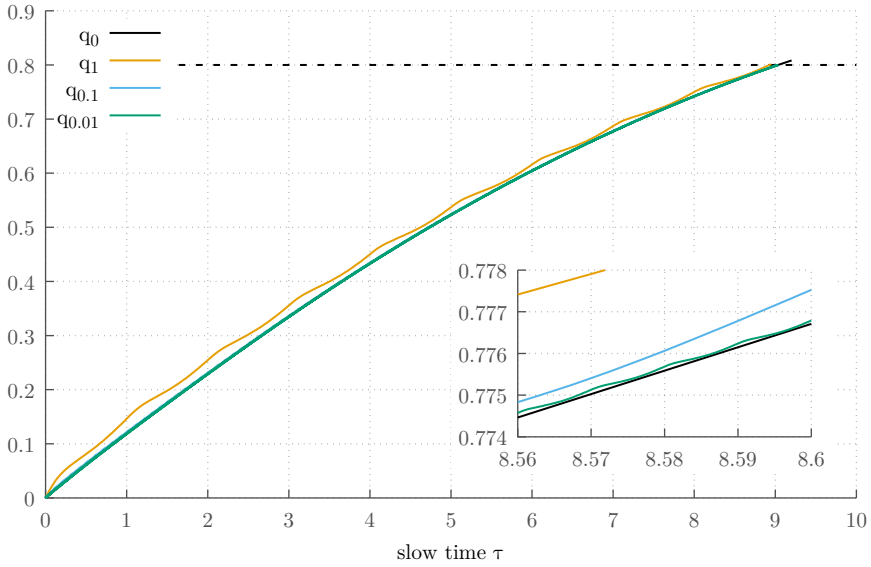

Figure 5.3: Behavior of the solutions q_ε for different values of ε and the limit solution q_0. The simulation is stopped after q exceeded $q_{\max} := 0.8$ (dashed line), the limit system crosses this threshold significantly due to the large step size employed. For small ε, q_ε and q_0 are indistinguishable on this scale, hence a zoomed view is provided.

5.2 Numerical Realization of Fast-Slow and Limit Systems

Spatial Discretization

For both limit and fast-slow equation the solution of the Navier–Stokes equation will be necessary. We will use the same spatial discretization in both cases, employing the inf-sup stable Taylor–Hood P^2/P^1 element on a triangular mesh. We write h for the maximal element diameter and denote the discrete velocity space by $V_h \subset \{v \in H^1(\Omega_0) \mid v|_{\partial_w \Omega} = 0\}$ and the discrete pressure space by $Q_h \subset L^2(\Omega_0)$. The spatial mesh is uniform on the initial geometry Ω_0 and is chosen as very coarse with only 15 522 degrees of freedom for the velocity and 2000 degrees of freedom for the pressure variable. The reason for this low spatial resolution is the very large number of time steps required in particular for the solution of the fast-slow system. Since our focus lies exclusively on the temporal aspects of this problem this is not considered a problem.

The movement of the geometry is implemented as explicit movement of the mesh vertices using the transformation Φ_q and not through a pullback of the equation to the initial geometry. We denote the finite element spaces on such a deformed mesh by $V_{h,q}$ and $Q_{h,q}$. Since the transformation Φ_q of the whole fluid domain is explicitly given, the mesh quality can be controlled easily, in contrast to e.g. ALE methods.

All numerical simulations in this chapter were carried out using a customized version of the FEniCS software v2018.1 [Aln+15; LWH12; Log+12; Aln+14; Kir04; ALM12]. The used (semi-)implicit temporal discretization of the fluid equation leads to nonlinear problems which were solved with a quasi-Newton method using PETSc's SNES package [Bal+] and the resulting linear equations were solved with the direct solver UMFPACK [Dav04].

Temporal Discretization: Fast-Slow System

We compute the solution of the fast-slow system eq. (5.1) for different ε to investigate the numerical convergence behavior of q_ε to q_0. Following the convention used throughout this thesis we will formulate the temporal discretization of the fast-slow system in terms of the fast variable t. For simplicity we employ a uniform temporal discretization with step size $k := \frac{1}{M}$ where $M \in \mathbb{N}$ is the number of temporal steps per period. With total number of time steps $N \in \mathbb{N}$, we denote the individual discrete times on the fast scale by

$$0 = t^0 < t^1 < \cdots < t^{N-1} < t^N = T, \quad t^n := nk.$$

We remark that, since $T = \varepsilon^{-1}\mathcal{T}$, the number of micro steps is proportional to ε^{-1}. We formulate our time-stepping schemes with a fixed N for formal simplicity, but the simulations performed in the following were stopped once the growth q_ε exceeded the threshold $q_{\max} := 0.8$. We write q_ε^n, v_ε^n and p_ε^n for the fully discrete solution at time t^n, i.e. omit the dependence on k and h.

The discretization of the fast-slow system eq. (5.1) is non-trivial due to the coupling of these two equations through the movement of the fluid domain. Since our focus lies on the solution of the limit system, we will propose a straight-forward decoupling scheme employing an explicit Euler method for q_ε and the Crank–Nicolson scheme for the fluid velocity v_ε.

For all $n = 1, \dots, N$ first solve

$$q_\varepsilon^n = q_\varepsilon^{n-1} + \varepsilon k g(q_\varepsilon^{n-1}, v_\varepsilon^{n-1})$$

with initial value $q_\varepsilon^0 := 0$ and then, reminding that $(\,\cdot\,,\,\cdot\,)_{\hat{q}}$ denotes the $L^2(\Omega_{\hat{q}})$ scalar product , the weak version of the Navier–Stokes equation, given as solution to

$$\begin{aligned} &St(v_\varepsilon^n - \tilde{v}_\varepsilon^{n-1}, \varphi)_{q_\varepsilon^n} + \tfrac{k}{2}((v_\varepsilon^n \cdot \nabla)v_\varepsilon^n + (\tilde{v}_\varepsilon^{n-1} \cdot \nabla)\tilde{v}_\varepsilon^{n-1}, \varphi)_{q_\varepsilon^n} \\ &\quad + \tfrac{k}{2}\, Re^{-1}(\nabla v_\varepsilon^n + \nabla \tilde{v}_\varepsilon^{n-1}, \nabla\varphi)_{q_\varepsilon^n} - k(p_\varepsilon^n, \operatorname{div}\varphi)_{q_\varepsilon^n} + k(\operatorname{div} v_\varepsilon^n, \xi)_{q_\varepsilon^n} \\ &\quad = -k(p_{\mathrm{io}}^n \mathfrak{n}, \varphi)_{\partial_{\mathrm{io}}\Omega} \end{aligned}$$

for all $\varphi \in V_{h,q_\varepsilon^n}$ and $\xi \in Q_{h,q_\varepsilon^n}$ with initial value $v_\varepsilon^0 := 0$. Here, $\tilde{v}_\varepsilon^{n-1}$ is the push-forward of v_ε^{n-1} to $\Omega_{q_\varepsilon^n}$ induced by the movement of the vertices of the finite element mesh. As in the multiscale analysis we omitted the advection due to mesh movement of order $\mathcal{O}(\varepsilon)$. Note that the integral over $\Gamma_{\hat{q}}$ in the evaluation of g must be replaced by a quadrature scheme.

The algorithm presented here first evolves q_ε^n and then v_ε^n. Even though a first order discretization is used for the growth equation the observed convergence is of second order as depicted in Figure 5.4, where the error in terms of the step size k has been plotted for $\varepsilon = 0.1$. Evolving first v_ε^n and then q_ε^n

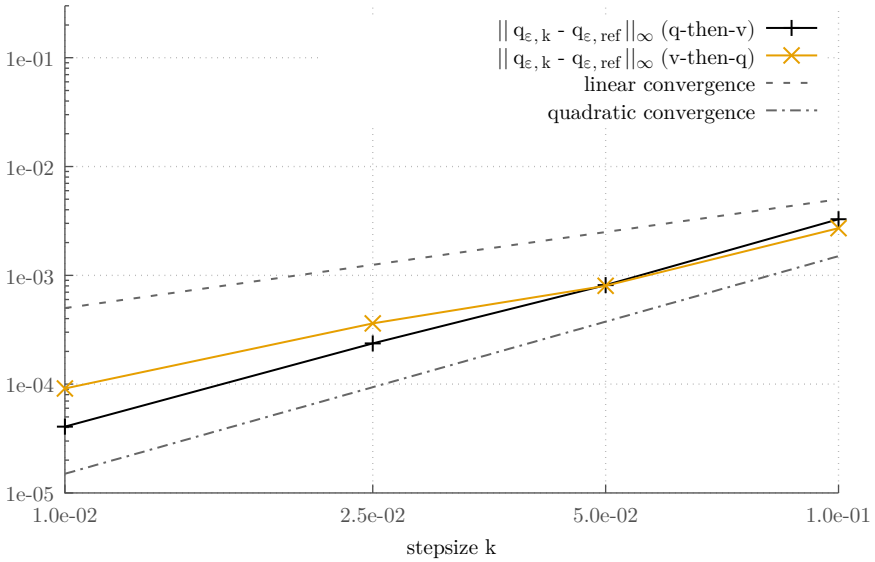

Figure 5.4: Maximal error between q_ε, with $\varepsilon = 0.1$, for different values of k compared to the reference solution with $k_0 := 5 \times 10^{-3}$. Plotted are both orders in which the q_ε and v_ε steps could be taken.

reduces the observed order to $k^{1.5}$, also plotted in Figure 5.4. The reference solution in both cases is the respective solution for $k_0 := 5 \times 10^{-3}$. The reason for this better-than-expected convergence is unknown. Below we will use that the integration scheme corresponding to the implicit Euler method is equivalent to the second-order trapezoidal rule for periodic functions integrated over the full period, which also holds for the explicit Euler method. The improved convergence seen in Figure 5.4 may be related to this effect since the fast changing v_ε^n is close to its periodic orbit, but this is only speculation.

Temporal Discretization: Limit Equation

The evaluation of the right-hand side of eq. (5.3a) for q_0 requires the time-periodic solution of the Navier–Stokes equation for the associated domain. This naturally decomposes the numerical algorithm into macro steps evolving q_0 and micro steps for the temporal discretization of the time-periodic Navier–Stokes equation for the given geometry. These two interlinked time-stepping schemes are illustrated in Figure 5.5.

The decomposition into macro and micro steps naturally fits into the framework of the heterogeneous multiscale method (HMM), see [E+07] for a review. In the nomenclature from [E+07] the problem studied here is of type B, where the macro scale equation, in our case the equation for q_0, is computationally not explicit in the sense that v_π and q_π are unknown and thus the right-hand side of the limit equation cannot be evaluated directly. The solution algorithm we are going to propose computes the associated periodic Navier–Stokes equation in each step and is thus a concurrent coupling method, again following the

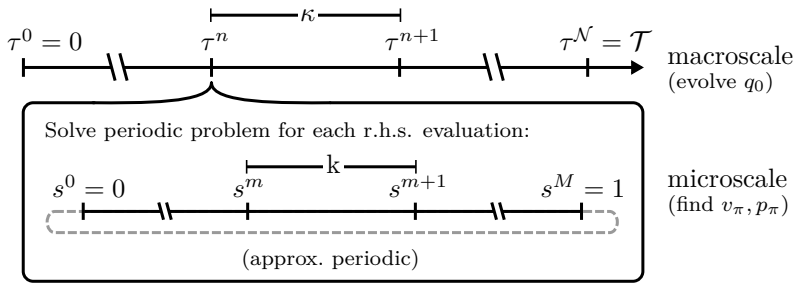

Figure 5.5: Sketch of the solution process for the discrete limit equation. In every macro step, which evolves q_0, each evaluation of the averaging right-hand side requires the solution of the microscale problem, i.e. the solution of the time-periodic Navier–Stokes equation.

nomenclature from [E+07]. Sequential coupling methods, in contrast, would pre-compute the periodic problem for a fixed set of Q and then interpolate between these values, an approach not pursued here.

As indicated in Figure 5.5, we use equidistant temporal meshes for simplicity and use κ for the temporal step size on the macro scale. We denote by q_0^n for $n = 0, \dots, \mathcal{N}$ the discretization of q_0 at time $\tau^n := n\kappa$ with $\mathcal{N} := \mathcal{T}/\kappa$. Note that q_0^n is an approximation to $q_0(\tau^n)$ for $n = 0, \dots, \mathcal{N}$ on the slow timescale, whereas q_ε^n is an approximation of $q_\varepsilon(t^n)$ for $n = 0, \dots, N$ on the fast timescale.

We study only explicit time-stepping schemes for the limit equation for q_0, eq. (5.3a), since otherwise the coupling between q_0 and the time-periodic solution of the Navier–Stokes equation on Ω_{q_0} must be resolved. Discretizing only the macro scale for the moment, the time-stepping schemes studied here are the explicit Euler method

$$q_0^n := q_0^{n-1} + \kappa g_0(q_0^{n-1}) \tag{5.4}$$

and the second-order Runge–Kutta midpoint (RK2) method

$$\delta^{n(1)} := g_0(q_0^{n-1}), \quad \delta^{n(2)} := g_0\left(q_0^{n-1} + \tfrac{\kappa}{2}\delta^{n(1)}\right), \quad q_0^n := q_0^{n-1} + \kappa\delta^{n(2)}. \tag{5.5}$$

The right-hand side g_0 can not be evaluated exactly since $v_\pi(\cdot; \hat{q})$ is unknown. The determination of an approximation for v_π is the topic of the second part of this chapter. Here we only assume that a time-discrete approximation $v_\pi^m(\hat{q})$ at time $s^m := mk$ for $m = 0, \dots, M$ and $k := 1/M$ has been found by a black box solver, where $M \in \mathbb{N}$ is the number of time steps used to resolve a single period.

We will use the second-order Crank–Nicolson method for the temporal discretization of the Navier–Stokes equation, just as for the fast-slow system. For the discretization of the averaging integral in the evaluation of g_0 it is hence plausible to also use a second-order approximation, such as the trapezoidal integration rule, i.e.

$$g_0(\hat{q}) \approx \gamma(1-\hat{q}) \sum_{m=1}^{M} \frac{k}{2} \int_{\Gamma_{\hat{q}}} \left(1 + \frac{|\sigma_{\mathrm{WS},\pi}^m(\hat{q})|}{\sigma_{\mathrm{WS}}^0}\right)^{-1} + \left(1 + \frac{|\sigma_{\mathrm{WS},\pi}^{m-1}(\hat{q})|}{\sigma_{\mathrm{WS}}^0}\right)^{-1} \mathrm{d}o.$$

The periodicity of the integrand allows us to find alternative formulations for this integral. Namely, assuming that $\sigma^0_{\mathrm{WS},\pi} = \sigma^M_{\mathrm{WS},\pi}$, which is only approximatively satisfied in practise, the integral can be rewritten as

$$g_0(\hat{q}) \approx \gamma(1-\hat{q}) \sum_{m=1}^{M} k \int_{\Gamma_{\hat{q}}} \left(1 + \frac{|\sigma^m_{\mathrm{WS},\pi}(\hat{q})|}{\sigma^0_{\mathrm{WS}}}\right)^{-1} \mathrm{d}o \tag{5.6}$$

which is the integral version of the implicit Euler scheme, or explicit Euler scheme if the sum is taken over $m = 0, \ldots, M-1$. This equivalence between midpoint and explicit Euler scheme was alluded to above as a possible explanation why the explicit Euler discretization of the fast-slow system yielded better convergence than expected. While the discretization eq. (5.6) is used for our numerical computations, the approximation

$$g_0(\hat{q}) \approx \gamma(1-\hat{q}) \sum_{m=1}^{M} k \int_{\Gamma_{\hat{q}}} \left(1 + \frac{|\frac{1}{2}(\sigma^m_{\mathrm{WS},\pi}(\hat{q}) + \sigma^{m-1}_{\mathrm{WS},\pi}(\hat{q}))|}{\sigma^0_{\mathrm{WS}}}\right)^{-1} \mathrm{d}o \tag{5.7}$$

is more suitable for the error analysis of the limit system carried out in the last part of this chapter due to the form of error estimates available for the Crank–Nicolson scheme.

After spatial discretization of the Navier–Stokes equation and replacement of the boundary integral with a quadrature rule, this approximation of g_0 will be used in the time-stepping schemes eqs. (5.4) and (5.5). Again, we will omit any indices for the discretization parameters, which would yield unwieldy names such as $q_{0,\kappa,k,h}$. All these parameters will influence the quality of the discretization, the last part of this chapter consists of a sketch of an error analysis for the RK2 scheme. This analysis will show that the right-hand side evaluation for $\delta^{n(2)}$ from eq. (5.5), i.e. the micro problem solution, must be of order $\mathcal{O}(\kappa^2)$, whereas the micro problem solved for $\delta^{n(1)}$ must be only of order $\mathcal{O}(\kappa)$ to balance the overall error to be of order $\mathcal{O}(\kappa^2)$, cf. Theorem 5.4.1. Consequentially, different discretization schemes for the micro solver should be used in the evaluation of $\delta^{n(1)}$ and $\delta^{n(2)}$ for efficiency.

The convergence of the limit solver in terms of the macro step size κ is plotted in Figure 5.6, comparing the discrete solutions for explicit Euler and RK2 schemes to the reference solution which employed the RK2 scheme with $\kappa = 1 \times 10^{-1}$. Here and in the following the errors between functions on different time grids are computed using a linear interpolation to a common, matching grid. For the balanced RK2 scheme the parameters were chosen such that the overall error is balanced, see Theorem 5.4.1 at the end of this chapter. Specifically,

$$M^{(1)} = 6\lceil \kappa^{-1/2} \rceil \quad \text{and} \quad M^{(2)} = 6\lceil \kappa^{-1} \rceil$$

time steps were used in the evaluation of $\tilde{g}_0^{(1)}$ and $\tilde{g}_0^{(2)}$, respectively. For the explicit Euler and unbalanced RK2 scheme a fixed micro discretization was employed which used $M = 40$ time steps per period and stopped once the L^2 error between initial and final value in a period was below 10^{-7}. The convergence behavior for the explicit Euler scheme in Figure 5.6 is of first order as expected. The error for the unbalanced RK2 scheme is of second order, whereas the error for the balanced RK2 scheme is better than expected for $\kappa = 2$ but shows convergence behavior similar to that of the unbalanced scheme for smaller κ, while being much more computationally efficient.

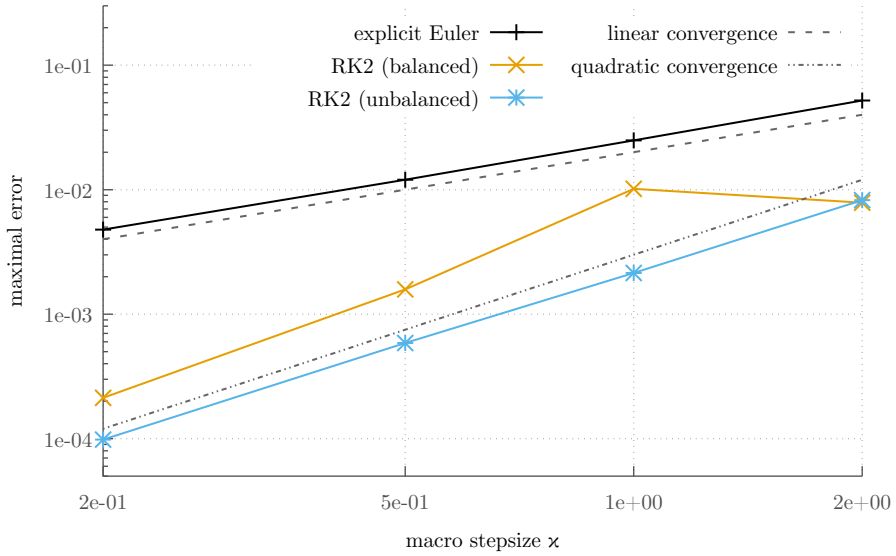

Figure 5.6: Convergence behavior for the solution of the limit equation in the macro step size κ. Plotted are the errors for the solutions using the explicit Euler and RK2 schemes, compared to the reference solution which used the RK2 scheme with $\kappa = 1 \times 10^{-1}$. Two variants of the RK2 discretization are plotted, one striving to balance the overall error and thus reducing the numerical cost (RK2 balanced), the other using a much finer, static discretization (RK2 unbalanced).

Single Period Micro Solvers

Even though the periodic solver has not been discussed yet, we want to investigate an alternative and computationally cheaper micro solver which only evolve the fast initial value problem by a single period while keeping the slow growth variable, i.e. the domain, fixed without taking periodicity into account. This can either be seen as a heuristic approach to solving the fast-slow system if no knowledge of the limit system is available, or as a computational simplification.

Such a single-period micro solver requires initial values for the fast initial value problem at each macro step. The most obvious choice is to use the end value of the micro solver from the previous macro step as new initial value, or rather its push-forward due to the mesh movement. The initial value for the first macro step could either be the initial value of the fast-slow system, in our case simply $v^0 = 0$, or, in view of the known limit structure, the initial value of the periodic solution $v_\pi^0(0)$ in the initial geometry. The determination of this initial value would again require a solution of the periodic problem, but just once.

The result of such a simplification, compared to the reference solution for q_0^n from Figure 5.6, can be found in Figure 5.7. It can be observed that the single period micro solvers also yield convergent solutions, but the convergence

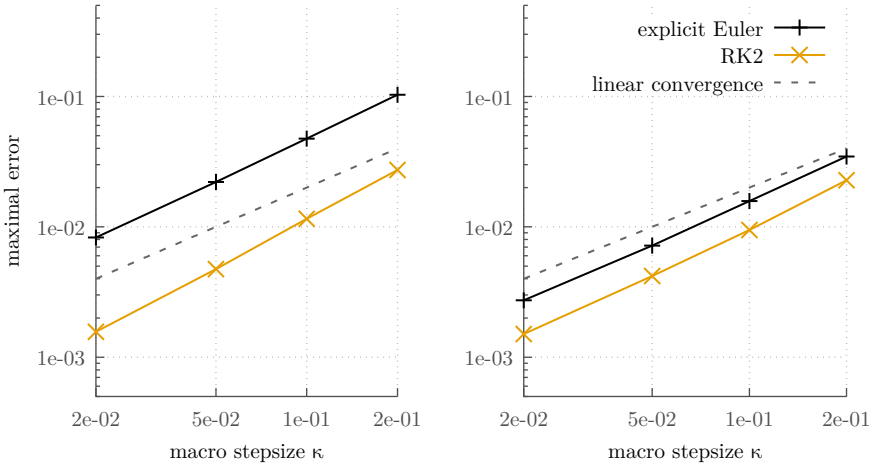

(a) Zero initial value.

(b) Periodic initial value.

Figure 5.7: Error between the reference solution for q_0^n from Figure 5.6 and solutions of the "limit system" if only a single period of the fast equation is evolved per macro step, instead of seeking periodic solutions. Two different initial values for the first micro step are compared.

order for the RK2 discretization is reduced to $\mathcal{O}(\kappa^{1.2})$. The use of a periodic initial value only reduces the overall error, cf. Figure 5.7(b). The convergence in κ may be explained by the fact that the increase in macro steps leads to an increase in the number of computed periods such that the velocity is close to its periodic state. We will see below for the RK2 discretization with $\kappa = 0.2$ that only 2–4 initial value problems must be solved per macro step to achieve quadratic convergence, cf. Figure 5.9, which shows the superiority of using a true periodic solver at least for the RK2 discretization.

Multiscale Convergence and Efficiency

The convergence of the solution of the fast-slow solutions q_ε to the limit solution q_0 can be found in Figure 5.8. In contrast to the theory only a convergence order of ≈ 0.85 could be achieved, where the error stalls if the number of steps per period for the fast-slow system is too small. The reason for this deviation from the theoretical results could not be determined, other tests with the Stokes equation and other temporal norms for the difference $q_\varepsilon - q_0$ yielded the same convergence rate.

To estimate the cost for the solution of the limit equation we need to investigate the cost of solving the periodic micro problem. The algorithm presented below amounts to a variable number of iterations, each consisting of solving an initial value Navier–Stokes problem for a single period and then performing a correction, which is negligible in cost. The number of iterations required per macro step for the RK2 discretization with macro step size $\kappa = 0.2$ is plotted

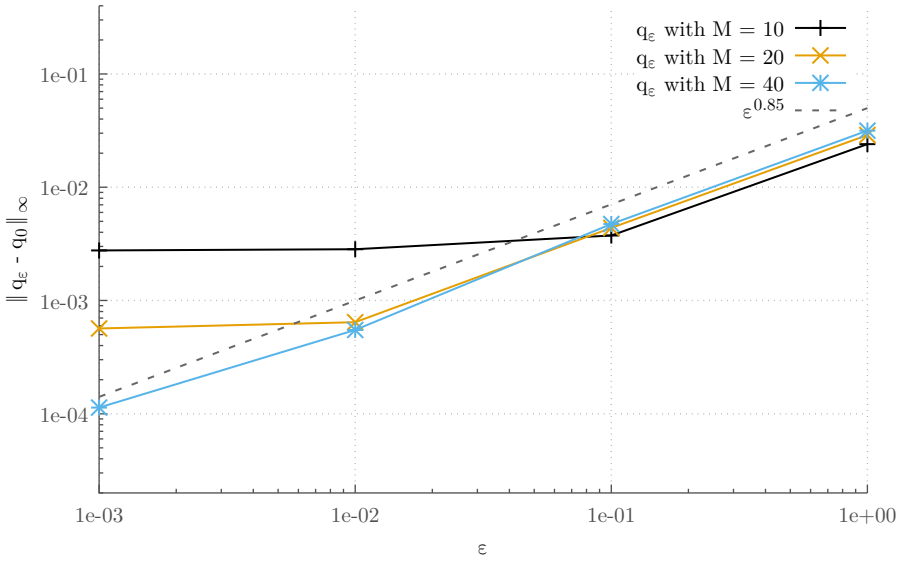

Figure 5.8: Maximal error between the numerical solutions of the fast-slow problem and the reference solution to the limit equation for different number M of time steps per period for the fast-slow problem.

in Figure 5.9. Each macro steps in the RK2 scheme consists of two evaluations of an approximation to g_0, each employing different temporal discretizations and periodicity tolerances. These evaluations are distinguished in Figure 5.9 as $\tilde{g}_0^{(1)}$ and $\tilde{g}_0^{(2)}$ corresponding to the updates $\delta^{n(1)}$ and $\delta^{n(2)}$ from eq. (5.5).

For $\tau \geq 3$ it can be observed in Figure 5.9 that the number of iterations decreases, until just one iteration is needed per evaluation of g_0, a behavior we will later attribute to the reduction of flow velocity due to the closure of the artery. Summing over the numbers from Figure 5.9, a total of 89 iterations were needed for the evaluation of $\tilde{g}_0^{(1)}$ and 97 for $\tilde{g}_0^{(2)}$. Each iteration of $\tilde{g}_0^{(1)}$ consisted of $M^{(1)} = 18$ time steps, yielding a total of 1602 time steps for the evaluation of $\tilde{g}_0^{(1)}$. For $\tilde{g}_0^{(2)}$ a finer discretization with $M^{(2)} = 30$ steps was employed, yielding a total of 2910 time steps. Thus, the main cost of the solution to the limit equation were 4512 time steps of the Navier–Stokes equation. The only tested resolution which yielded appropriate results for $\varepsilon = 10^{-3}$ employed $M = 40$ steps per period for the fast-slow system, see Figure 5.8. This discretization performed a total of 361 473 steps, i.e. 80 times more than the limit system.

This demonstrates the efficiency of the limit system solver. A solution of the fast-slow system for smaller ε is infeasible, in particular for $\varepsilon = 10^{-8}$ as appropriate for the model of Yang et. al. as discussed in Section 2.3. Even for $\varepsilon = 10^{-3}$ the cost of solving the fast-slow system severely limited the spatial resolution which could be employed for these calculations.

Finally we emphasize that the limit system is solved to approximate q_ε for some fixed ε, our case $\varepsilon = 10^{-8}$. This means that the total error consists of

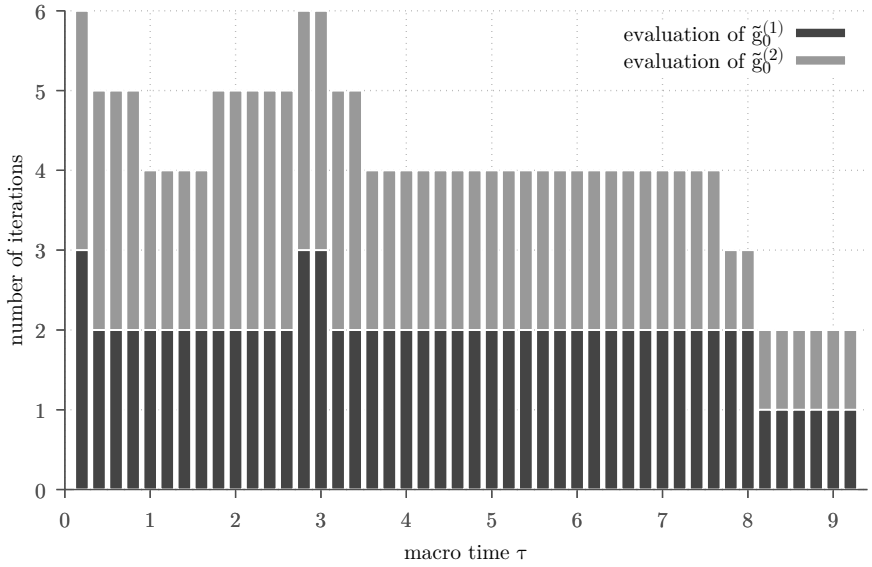

Figure 5.9: Number of iterations until an approximately periodic solution was found in each macro step for the balanced RK2 discretization with step size $\kappa = 0.2$. Each iteration consists primarily of solving an Navier–Stokes initial value problem. Distinguished are the iterations needed for the two evaluations of g_0, denoted here by $\tilde{g}_0^{(1)}$ and $\tilde{g}_0^{(2)}$ for $\delta^{n(1)}$ and $\delta^{n(2)}$ from eq. (5.5), which use different temporal discretizations and periodicity tolerances.

discretization errors for the limit system and the multiscale convergence error,

$$\begin{aligned}\max_{n=1,\dots,\mathcal{N}} |q_0^n - q_\varepsilon(\tau^n)| &\leq \max_{n=1,\dots,\mathcal{N}} |q_0^n - q_0(\tau^n)| + \max_{n=1,\dots,\mathcal{N}} |q_0(\tau^n) - q_\varepsilon(\tau^n)| \\ &\leq \max_{n=1,\dots,\mathcal{N}} |q_0^n - q_0(\tau^n)| + C\varepsilon.\end{aligned}$$

The multiscale error is so small in our application that the corresponding term can be neglected. For applications with larger values of ε it may be appropriate to balance these errors, which would again create a dependency between the limit system discretization and ε. Still, the use of higher order schemes would reduce the computational cost compared to solving the fast-slow system directly.

5.3 Calculation of Periodic Solutions

A numerical method is required to solve the time-periodic micro problem in the limit equation. We quickly review some proposals to solve such time-periodic problems on a continuous level, i.e. with neither temporal nor spatial discretization. Since the slow variable $q \in Q$ is fixed we omit this dependence and denote by $v_\pi(\cdot)$ the solution to the periodic (Navier–)Stokes equation and by $v(\cdot; v^0)$ the solution to the corresponding initial value problem with initial

value v^0. Let

$$\mathcal{S}_0 \colon v^0 \mapsto v(1; v^0) \tag{5.8}$$

denote the map between initial value v^0 and the velocity of the corresponding initial value problem after one period. Later we will introduce a family of related operators $\mathcal{S}_\gamma$ for $\gamma \in [0, 1]$ which explains the subscript. The periodic solution can be characterized as fixed-point of $\mathcal{S}_0$, i.e.

$$v^0 = v_\pi^0 := v_\pi(0) \quad \Leftrightarrow \quad \mathcal{S}_0(v^0) = v^0. \tag{5.9}$$

Assuming exponential stability of the problem, the map $\mathcal{S}_0$ is a contraction. Applying the Picard iteration to this fixed-point problem leads to

$$v_i^0 = \mathcal{S}_0(v_{i-1}^0) = v(1; v_{i-1}^0) \quad \text{for } i \in \mathbb{N} \tag{5.10}$$

with initial guess v_0^0. The sequence $(v_i^0)_{i\in\mathbb{N}}$ thus defined can be characterized by $v_i^0 = v(i; v_0^0)$, i.e. the initial value problem is simply solved for large times and the reason for convergence to v_π^0 is the exponential stability already exploited extensively in our multiscale analysis. This scheme is referred to as forward iteration in [Ric19], but also as direct integration in [Kei+99] and as successive substitution in [JBF03].

It is easy to see for the Stokes equation that the iteration from eq. (5.10) converges linearly and that the rate of convergence depends on the problem parameters, see Lemma 5.3.1 below. For many problems this rate of convergence is very slow, making the forward iteration impractical. For theoretical purposes it can be used to prove the existence of periodic solutions, numerically it can be a building block in more elaborate solvers for nonlinear parabolic problems [Ste79; Pao02]. The method discussed and used in this thesis, the mean correction iteration, is a simple augmentation of the forward iteration guaranteeing a reasonable upper bound for the rate of convergence.

The calculation of periodic solutions can also be seen as a special boundary value problem, for which shooting methods have been developed. For this the fixed-point iteration eq. (5.9) is rewritten as a root finding problem

$$\mathcal{S}_0(v^0) - v^0 = 0$$

and various variants of Newton's method are used to approximate this. While Newton's method leads to a higher order of convergence [Ste79], the drawback of such methods is that at least an approximation of the Jacobian $\mathrm{D}\mathcal{S}_0(v^0)$ must be computed. Neither storage nor computation of the full Jacobian is feasible for spatial resolutions typically encountered in applications. Quasi-Newton methods such as Broyden's rank-one updating scheme of the Jacobian have been found to perform better than theoretically predicted for some applications [NLB99], see also [MPR03] for a review of other strategies for Quasi-Newton methods. Another modification of the shooting strategy for highly nonlinear problems is the replacement of a single shooting step with multiple shooting trajectories, starting from a subdivision of the period interval, which increases stability, see e.g. [SB02].

An optimization based approach is suggested in [AW12; RW18], where time-periodicity is rephrased as

$$\min_{v^0} j(v^0), \quad \text{where } j(v^0) := \tfrac{1}{2}\|v^0 - v(1; v^0)\|^2.$$

Of course $j(v_\pi^0) = 0$. This optimization problem can then be solved using e.g. a gradient descent algorithm, requiring the solution of a primal and adjoint problem per step, both consisting of the simulation of one cycle.

Finally, fully discrete space-time systems are employed in [NP98; Pla+05]. The consideration of all time steps at once has the benefit that periodicity can be enforced directly, but this approach suffers from severe memory requirements in particular for higher spatial dimensions.

Continuous Mean Correction Iteration

The mean correction algorithm augments the forward iteration to guarantee rates of convergence independent of problem parameters.

Mean Correction for the Stokes Equation

For simplicity we assume that the problem is to find the solution of the time-periodic Stokes problem with 1-periodic right-hand side f and homogeneous Dirichlet boundary conditions. Let (v_π, p_π) hence solve

$$\left.\begin{aligned} \partial_s v_\pi(s) - \Delta v_\pi(s) + \nabla p_\pi(s) &= f(s), \\ \operatorname{div} v_\pi(s) &= 0, \end{aligned}\right\} \quad \text{in } (0,1)\times\Omega \tag{5.11}$$

with $v_\pi(0) = v_\pi(1)$ in Ω and $v_\pi(s) = 0$ on $(0,1)\times\partial\Omega$, where we set the dimensionless parameters to one for simplicity. The corresponding initial value problem has solution $v(\cdot; v^0)$ where

$$\left.\begin{aligned} \partial_s v(s; v^0) - \Delta v(s; v^0) + \nabla p(s; v^0) &= f(s), \\ \operatorname{div} v(s; v^0) &= 0, \end{aligned}\right\} \quad \text{in } (0,1)\times\Omega \tag{5.12}$$

with associated pressure $p(\cdot; v^0)$, satisfying $v(0; v^0) = v^0$ in Ω and $v(\cdot; v^0) = 0$ on $(0,1)\times\partial\Omega$.

Reminding of the notation $L^2_\sigma(\Omega)$ for the weakly solenoidal functions in $L^2(\Omega)$ we have the following simple convergence result for the forward iteration, which also carries over almost verbatim to other time-periodic, linear parabolic problems with autonomous operator.

Lemma 5.3.1. *Let the domain Ω be such that the Stokes operator $-P\Delta = A\colon \mathcal{D}(A) \subset L^2_\sigma(\Omega) \to L^2_\sigma(\Omega)$ has domain $\mathcal{D}(A) = H^2(\Omega) \cap H^1_0(\Omega) \cap L^2_\sigma(\Omega)$. Assume that $f \in L^2(0,1; L^2(\Omega))$ (with 1-periodic extension to $\mathbb{R}$). The forward iteration eq. (5.10) then convergences linearly with*

$$\|v_i^0 - v_\pi^0\| \le \mathrm{e}^{-\lambda_1}\|v_{i-1}^0 - v_\pi^0\|$$

where $\lambda_1 > 0$ is the smallest eigenvalue of the Stokes operator.

Proof. The proof is standard, but we repeat it here as preparation for the corresponding results for the mean correction algorithm introduced below. We use the variation of constants representation for the solution to eq. (5.12):

$$v(s; v^0) = \mathrm{e}^{-As}v^0 + \int_0^s \mathrm{e}^{-A(s-r)}Pf(r)\,\mathrm{d}r$$

for $s > 0$, which implies for any v_1^0 and v_2^0 that

$$v(s; v_1^0) - v(s; v_2^0) = \mathrm{e}^{-As}(v_1^0 - v_2^0).$$

By definition of v_i^0 in eq. (5.10) and the fixed-point property of v_0^π we thus get

$$\|v_i^0 - v_\pi^0\| = \|\mathcal{S}_0(v_{i-1}^0) - \mathcal{S}_0(v_\pi^0)\| = \|\mathrm{e}^{-A}(v_{i-1}^0 - v_\pi^0)\|.$$

The last term is estimated using the decomposition of $L^2_\sigma(\Omega)$ into eigenvectors of A. Let $Av_l = \lambda_l$ for $l \in \mathbb{N}$ with ordered eigenvalues $0 < \lambda_1 \leq \lambda_2 \leq \dots$ and corresponding orthonormal eigenvectors $v_l \in \mathcal{D}(A) \subset L^2_\sigma(\Omega)$. With $w := v_{i-1}^0 - v_\pi^0$ we write $w_l := (w, v_l)$. Then

$$\|\mathrm{e}^{-A}w\|^2 = \sum_{l\in\mathbb{N}} \mathrm{e}^{-2\lambda_l}\|w_l\|^2 \leq \mathrm{e}^{-2\lambda_1} \sum_{l\in\mathbb{N}} \|w_l\|^2 = \mathrm{e}^{-2\lambda_1}\|w\|^2$$

and the claim follows. □

We will use the method outlined in [Ric19], although with a small optimization and rephrased as a fixed-point iteration similar to eq. (5.10). We first observe that at least for linear problems the mean value of the periodic solution can be easily computed without knowledge of the periodic solution itself. This can be seen by splitting v_π into mean and oscillatory parts

$$v_\pi = \overline{v_\pi} + \widetilde{v_\pi}, \quad \overline{v_\pi} := \int_0^1 v_\pi(s)\,\mathrm{d}s, \quad \widetilde{v_\pi} := v_\pi - \overline{v_\pi},$$

we use the same notation for p_π and f. Integration of the periodic problem from eq. (5.11) over $(0, 1)$ yields the stationary problem:

$$\left.\begin{aligned} -\Delta\overline{v_\pi} + \nabla\overline{p_\pi} &= \overline{f}, \\ \operatorname{div}\overline{v_\pi} &= 0 \end{aligned}\right\} \quad \text{in } \Omega, \tag{5.13}$$

since $\int_0^1 \partial_s v_\pi \,\mathrm{d}s = v_\pi(1) - v_\pi(0) = 0$, with $\overline{v_\pi} = 0$ on $\partial\Omega$. Note that eq. (5.13) does not require any knowledge of v_π^0. The idea in [Ric19] is now to shift the trajectory $v(\cdot; v^0)$ by a constant such that that the shifted mean value agrees with $\overline{v}_\pi$ and to use this shifted trajectory as initial value for the next iteration. For an improvement of the results in [Ric19] we introduce a relaxation parameter $\gamma \in [0, 1]$ which controls the strength of this shift, with $\gamma = 0$ corresponding to no shifting, i.e. the forward iteration, and $\gamma = 1$ to full shifting as used in [Ric19]. Specifically, we apply the Picard iteration to the map

$$\mathcal{S}_\gamma \colon v^0 \mapsto v(1; v^0) + \gamma\left(\overline{v_\pi} - \overline{v(\cdot; v^0)}\right) \tag{5.14}$$

for which v_π^0 is obviously still the fixed-point. For $\gamma = 0$ this corresponds to the map introduced in eq. (5.8). There holds

$$\overline{v(\cdot; v^0)} + \gamma\left(\overline{v_\pi} - \overline{v(\cdot; v^0)}\right) = (1-\gamma)\overline{v(\cdot; v^0)} + \gamma\overline{v_\pi} \tag{5.15}$$

for all v^0 and the average of the corrected function is thus equal to that of v_π for $\gamma = 1$. Applying the Picard iteration to the fixed-point of eq. (5.14) yields

$$v_i^0 = \mathcal{S}_\gamma(v_{i-1}^0) = v(1; v_{i-1}^0) + \gamma\left(\overline{v_\pi} - \overline{v(\cdot; v^0)}\right),$$

which we reformulate as

$$v_i^0 = v(1; v_{i-1}^0) + \gamma\,\delta_i, \quad \delta_i := \overline{v_\pi} - \overline{v(\cdot; v_{i-1}^0)} \tag{5.16}$$

for some initial guess v_0^0. In other words, we solve the same problem with a shifted initial value, which is the formulation used in [Ric19] for $\gamma = 1$. The linearity of the problem would allow us to study without loss of generality only the case $\overline{v_\pi} = 0$. We won't make this simplification here since it will not work for the Navier–Stokes equation. Furthermore, the shift of the trajectory comes at the price that the Stokes equation is no longer satisfied. Specifically there holds for $w(\cdot) := v(\cdot; v_{i-1}^0) + \gamma\,\delta_i$ that

$$\partial_s w - \Delta w + \nabla q = f + \gamma(w(1) - w(0)), \quad \operatorname{div} w = 0 \tag{5.17}$$

with some associated pressure q. But the right-hand side evidently converges to f as v_{i-1}^0 approaches the fixed-point. Together, eq. (5.15) and eq. (5.17) illustrate the trade-off between choosing γ such that the shifted solution has the correct average ($\gamma = 1$) or satisfies the correct equation ($\gamma = 0$).

Lemma 5.3.2. *Let the assumptions of Lemma 5.3.1 be satisfied. Then the mean correction iteration eq. (5.16) with parameter $\gamma \in [0, 1]$ satisfies*

$$\|v_i^0 - v_\pi^0\| \le \rho \|v_{i-1}^0 - v_\pi^0\| \tag{5.18}$$

with reduction rate ρ given by

$$\rho := \max_{l \in \mathbb{N}} |\tilde{\rho}(\lambda_l; \gamma)|, \quad \tilde{\rho}(\lambda; \gamma) := \mathrm{e}^{-\lambda} + \gamma\lambda^{-1}(\mathrm{e}^{-\lambda} - 1) \tag{5.19}$$

where λ_l are the eigenvalues of the Stokes operator. By taking the supremum over $\lambda > 0$ we can find bounds independent of the Stokes operators' spectrum. One can find numerically that this supremum is minimized for $\gamma_0 \approx 0.79$ where

$$\|v_i^0 - v_\pi^0\| < 0.21 \|v_{i-1}^0 - v_\pi^0\| \tag{5.20}$$

independent of the problem data.

Proof. As in the proof of Lemma 5.3.1 we have

$$v(s; v_1^0) - v(s; v_2^0) = \mathrm{e}^{-As}(v_1^0 - v_2^0)$$

for arbitrary v_1^0 and v_2^0, where $A := -P\Delta$ is the Stokes operator. Since v_π^0 is a fixed-point of $\mathcal{S}_\gamma$ we have

$$\begin{aligned} v_i^0 - v_\pi^0 &= \mathcal{S}_\gamma(v_{i-1}^0) - \mathcal{S}_\gamma(v_\pi^0) \\ &= v(1; v_{i-1}^0) - v_\pi(1) + \gamma\overline{v_\pi(\cdot) - v(\cdot; v_{i-1}^0)} \\ &= \mathrm{e}^{-A}(v_{i-1}^0 - v_\pi^0) + \gamma \int_0^1 \mathrm{e}^{-As}(v_\pi^0 - v_{i-1}^0)\,\mathrm{d}s \\ &= \mathrm{e}^{-A}(v_{i-1}^0 - v_\pi^0) - \gamma A^{-1}(\mathrm{e}^{-A} - \mathrm{Id})(v_\pi^0 - v_{i-1}^0) \end{aligned}$$

and hence

$$v_i^0 - v_\pi^0 = \left(\mathrm{e}^{-A} + \gamma A^{-1}(\mathrm{e}^{-A} - \mathrm{Id})\right)(v_{i-1}^0 - v_\pi^0).$$

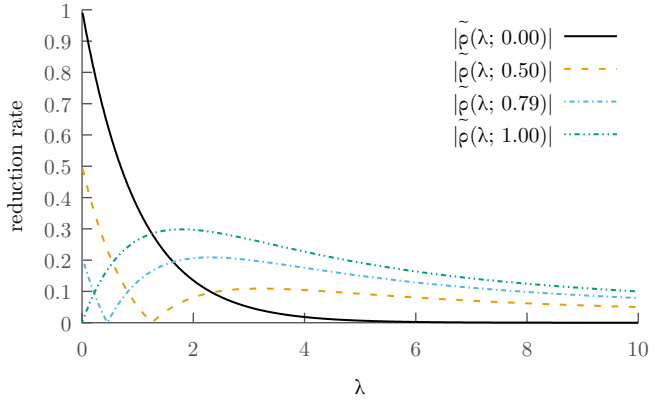

Figure 5.10: The reduction rate of the mean correction iteration eq. (5.16) for different values of γ plotted over the range of possible eigenvalues λ for the Stokes operator, see eq. (5.19). The reduction rate, independent of the eigenvalue distribution, is smallest for $\gamma_0 \approx 0.79$.

With a decomposition of $L^2_\sigma(\Omega)$ using eigenvectors of A, $Av_l = \lambda_l$ for $l \in \mathbb{N}$ with $0 < \lambda_1 \leq \lambda_2 \leq \dots$ and orthonormal $v_l \in \mathcal{D}(A) \subset L^2_\sigma(\Omega)$, we see as in the proof of Lemma 5.3.1 that

$$\|v_i^0 - v_\pi^0\| \leq \max_{l \in \mathbb{N}} \left| e^{-\lambda_l} + \gamma \lambda_l^{-1} (e^{-\lambda_l} - 1) \right| \|v_{i-1}^0 - v_\pi^0\|.$$

This implies the claimed ineq. (5.18) with ρ and $\tilde{\rho}(\lambda; \gamma)$ as in eq. (5.19). By elementary analysis one can prove that the function $\tilde{\rho}(\lambda; \gamma)$ has the asymptotic behavior

$$\lim_{\lambda \to 0} \tilde{\rho}(\lambda; \gamma) = 1 - \gamma \quad \text{and} \quad \lim_{\lambda \to \infty} \tilde{\rho}(\lambda; \gamma) = 0$$

and that there exists exactly one local maximum in $(0, \infty)$. The supremum thus either occurs at this local maximum or at the limit value as $\lambda \to 0$. Computing the value of $\sup |\tilde{\rho}|$ on an equidistant grid for $\gamma \in [0, 1]$ with step size 0.001 we find numerically that $\gamma_0 = 0.791$ has the best reduction rate $r < 0.21$, cf. Figure 5.11, which leads to ineq. (5.20). □

Remark 5.3.3. For $\gamma = 1$, the case examined in [Ric19], the reduction rate is slightly worse with $\rho < 0.3$ as evident from Figure 5.10. While the mean correction iteration guarantees convergence rates independent of the problem parameters, these rates may not be superior to the forward iteration if the smallest eigenvalue of the Stokes operator is "large enough". This can be seen in Figure 5.10 where $|\tilde{\rho}(\lambda; 0)|$ is smaller than any $|\tilde{\rho}(\lambda; \gamma)|$ for fixed γ if λ is large enough. The superiority of the forward iteration to the mean correction in certain cases can also be observed numerically, see e.g. Figure 5.15. Finally, note that $\lim_{\lambda \to 0} \tilde{\rho}(\lambda; \gamma) = 1 - \gamma$ decreases as γ increases, whereas Figure 5.10 indicates that the local maximum of $|\tilde{\rho}(\cdot; \gamma)|$ in the interior increases as γ increases. The optimal γ_0 is thus the point at which these two local maxima are equal with reduction rate $\lim_{\lambda \to 0} \tilde{\rho}(\lambda; \gamma_0) = 1 - \gamma_0 \approx 0.21$. ◇

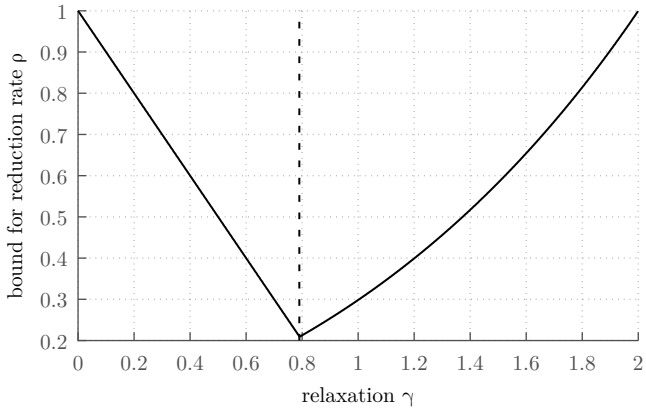

Figure 5.11: Bounds for the reduction rate ρ of the mean correction iteration eq. (5.16) independent of the operator spectrum, computed numerically. While excluded in the analysis, the reduction rate for $1 < \gamma < 2$ is also plotted to show that such over-relaxation has no benefit. The optimal choice of $\gamma_0 \approx 0.79$ is indicated by the dashed line.

Mean Correction for the Navier–Stokes Equation

Let in this section v_π and p_π denote the solution to

$$\left.\begin{aligned} \partial_s v_\pi(s) + (v_\pi(s)\cdot\nabla)v_\pi(s) - \Delta v_\pi(s) + \nabla p_\pi(s) &= f(s), \\ \operatorname{div} v_\pi(s) &= 0, \end{aligned}\right\} \text{ in } (0,1)\times\Omega \tag{5.21}$$

with $v_\pi(0) = v_\pi(1)$ in Ω and $v_\pi(s) = 0$ on $(0,1)\times\partial\Omega$, again omitting all constants for simplicity. As in the linear case, $v(\cdot; v^0)$ denotes the solution of the corresponding initial value problem.

For the Navier–Stokes equation there is no equation for $\overline{v_\pi}$ like eq. (5.13) independent of $\widetilde{v_\pi}$ due to the nonlinear term. With the decomposition $v_\pi = \overline{v_\pi} + \widetilde{v_\pi}$ we have for the nonlinear term

$$(v_\pi\cdot\nabla)v_\pi = (\overline{v_\pi}\cdot\nabla)\overline{v_\pi} + (\overline{v_\pi}\cdot\nabla)\widetilde{v_\pi} + (\widetilde{v_\pi}\cdot\nabla)\overline{v_\pi} + (\widetilde{v_\pi}\cdot\nabla)\widetilde{v_\pi}.$$

Since the mixed terms contain one function independent of time and one with zero mean, taking the mean of this identity yields that

$$\int_0^1 (v_\pi\cdot\nabla)v_\pi \,\mathrm{d}s = (\overline{v_\pi}\cdot\nabla)\overline{v_\pi} + \int_0^1 (\widetilde{v_\pi}\cdot\nabla)\widetilde{v_\pi}\,\mathrm{d}s.$$

This implies that the average of eq. (5.21) satisfies

$$(\overline{v_\pi}\cdot\nabla)\overline{v_\pi} + \int_0^1 (\widetilde{v_\pi}\cdot\nabla)\widetilde{v_\pi}\,\mathrm{d}s - \Delta\overline{v_\pi} + \overline{p_\pi} = \overline{f}. \tag{5.22}$$

Equation (5.22) is known as Reynolds averaged Navier–Stokes (RANS) equation in the context of turbulence analysis, where the decomposition into mean and oscillatory components, although typically for non-periodic solutions, is a

well-known tool under the name Reynolds decomposition, see [Pop00; Foi+01]. The approach in turbulence modelling is to replace the oscillatory nonlinear term, also known as Reynolds stresses, with models depending only on the mean component intended to replicate the effects of turbulent behavior. We are not concerned with turbulent behavior however, such that we handle this term in another way.

With the same Picard iteration approach as in the linear case, we directly study the fixed-point iteration

$$v_i^0 = v(1; v_{i-1}^0) + \gamma\, \delta_i, \quad \delta_i := \overline{v_\pi} - \overline{v(\cdot; v_{i-1}^0)} \tag{5.23}$$

analogous to eq. (5.16). By our discussion above, $\overline{v_\pi}$ and hence δ_i cannot be computed without knowledge of $\widetilde{v_\pi}$. To circumvent this issue, [Ric19] suggests to directly compute (an approximation of) δ_i. With the abbreviations $v_i := v(\cdot; v_{i-1}^0)$ and $p_i := p(\cdot; v_{i-1}^0)$ we note, by the same techniques used in the derivation of eq. (5.22), that

$$v_i(1) - v_i(0) + (\overline{v_i} \cdot \nabla)\overline{v_i} + \int_0^1 (\widetilde{v_i} \cdot \nabla)\widetilde{v_i}\, \mathrm{d}s - \Delta \overline{v_i} + \overline{p_i} = \overline{f} \tag{5.24}$$

which differs in form from eq. (5.22) only in the first two terms due to the non-periodicity of v_i. The corrector $\delta_i = \overline{v_\pi} - \overline{v_i}$ hence satisfies

$$(\overline{v_\pi} \cdot \nabla)\overline{v_\pi} - (\overline{v_i} \cdot \nabla)\overline{v_i} - \Delta \delta_i + \nabla q_i = \int_0^1 (\widetilde{v_i} \cdot \nabla)\widetilde{v_i} - (\widetilde{v_\pi} \cdot \nabla)\widetilde{v_\pi}\, \mathrm{d}s + v_i(1) - v_i(0)$$

with some associated pressure q_i. Using the algebraic identity

$$(\overline{v_\pi} \cdot \nabla)\overline{v_\pi} - (\overline{v_i} \cdot \nabla)\overline{v_i} = (\delta_i \cdot \nabla)\delta_i + (\delta_i \cdot \nabla)\overline{v_i} + (\overline{v_i} \cdot \nabla)\delta_i$$

we can rewrite the first two terms to yield

$$\begin{aligned}(\delta_i \cdot \nabla)\delta_i + (\delta_i \cdot \nabla)\overline{v_i} + (\overline{v_i} \cdot \nabla)\delta_i - \Delta \delta_i + \nabla q_i \\ = \int_0^1 (\widetilde{v_i} \cdot \nabla)\widetilde{v_i} - (\widetilde{v_\pi} \cdot \nabla)\widetilde{v_\pi}\, \mathrm{d}s + v_i(1) - v_i(0).\end{aligned}$$

Now it is argued in [Ric19] that since v_i approaches v_π both the integral over the oscillatory terms on the right-hand side as well as $\delta_i \cdot \nabla \delta_i$ may be neglected, the former out of necessity the latter for simplicity. This leads to the final equation for (an approximation of) δ_i:

$$(\delta_i \cdot \nabla)\overline{v_i} + (\overline{v_i} \cdot \nabla)\delta_i - \Delta \delta_i + \nabla q_\pi = v_i(1) - v_i(0). \tag{5.25}$$

Equations (5.23) and (5.25) constitute the mean correction scheme for the Navier–Stokes equation in the continuous setting.

Discrete Mean Correction Iteration

The numerical realization of the mean correction scheme requires a discretization in both space and time. For the spatial discretization we will use the inf-sup stable Taylor–Hood P^2/P^1 element on triangular meshes just as in the

discretization of the fast-slow system. Our focus lies again in the temporal discretization.

For the presentation in this section we will assume that spatial and temporal discretization remain fixed during the determination of periodic solutions. Computationally more efficient is the use of adaptive discretizations, using less resources if the quality of the approximately periodic solution is poor. We only refer to [JBF03; LST07] for a discussion and further references for adaptive solvers. In Section 5.4 we will discuss how the parameters of the (temporal) micro solver must be tweaked for an overall balance of error in the limit system.

We discuss the numerical results for the following three test cases.

Test Case 5.3.4. For comparison with [Ric19] we study the Navier–Stokes equation in $\Omega := (-L, L)$ for fixed $L > 0$, i.e.

$$\partial_s v_\pi + (v_\pi \cdot \nabla) v_\pi - \nu \Delta v_\pi + \nabla p_\pi = f, \quad \operatorname{div} v_\pi = 0 \quad \text{in } (0,1) \times \Omega$$

with $v_\pi = 0$ on $(0,1) \times \partial\Omega$, $v_\pi(0) = v_\pi(1)$ in Ω and 1-periodic right-hand side

$$f(x, y, s) := \frac{1}{L} \tanh(y) \sin(2\pi s) \begin{pmatrix} 1 \\ 0 \end{pmatrix}.$$

In contrast to [Ric19] we only use a period of length 1. The domain Ω is discretized for all L with a uniform triangular mesh with a total number of 91 003 degrees of freedom, 80 802 for the velocity and 10 201 for the pressure. This differs from [Ric19] where a quadrilateral mesh is employed. ◇

The amount of parameters and the peculiar scaling of f with L in Test Case 5.3.4 obfuscates the behavior of the periodic solver, motivating the use of the following non-dimensional test case.

Test Case 5.3.5. Proceeding just as for the model by Yang et. al. in Section 2.3 the non-dimensional version of Test Case 5.3.4 is

$$St\, \partial_s v_\pi + (v_\pi \cdot \nabla) v_\pi - Re^{-1} \Delta v_\pi + \nabla p_\pi = f, \quad \operatorname{div} v_\pi = 0 \quad \text{in } (0,1) \times \Omega$$

where $\Omega := (-\frac{1}{2}, \frac{1}{2})^2$, with $v_\pi(0) = v_\pi(1)$ in Ω, $v_\pi = 0$ on $(0,1) \times \partial\Omega$ and 1-periodic right-hand side

$$f(x, y, s) := \tanh(2y) \sin(2\pi s) \begin{pmatrix} 1 \\ 0 \end{pmatrix}$$

which has been scaled to 1. The spatial discretization is the same as in Test Case 5.3.4. ◇

Both Test Case 5.3.4 and Test Case 5.3.5 are of the type for which we formulated the algorithms, with homogeneous Dirichlet boundary conditions and time-periodic right-hand side. The final test case is the periodic problem which arises in the limit system of the problem described in the beginning of this chapter. Here we wish to investigate how the algorithms depend on the domain and test convergence for the actual quantities of interest as they appear in the right hand side of g_0 in the limit system.

Test Case 5.3.6. We study the Navier–Stokes problem as it appears in the limit system in the beginning of this chapter, i.e. eqs. (5.3c) to (5.3f). This system differs from the previous test cases due to the time-periodic pressure boundary conditions and the dependence on the (fixed) geometry Ω_q. The spatial discretization is just as in the fast-slow system. ◇

Mean Correction for the Stokes Equation

In [Ric19] the use of a θ-scheme for $\theta \in [\frac{1}{2}, 1]$ is proposed, which we also primarily discuss here and only briefly sketch some results for the BDF2 scheme below. We remind of the notation $s^m := km$ with $m = 0, \dots, M$ for the $M \in \mathbb{N}$ time steps of the temporal discretization of the periodic problem, with $k := 1/M$.

The θ-scheme discretization of the periodic Stokes problem from eq. (5.11) is to find $(v_\pi^m, p_\pi^m) \in V_h \times Q_h$ for $m = 1, \dots, M$ such that

$$\begin{aligned}(v_\pi^m - v_\pi^{m-1}, \varphi) + k(\nabla(\theta v_\pi^m + (1-\theta)v_\pi^{m-1}), \nabla\varphi) - k(p_\pi^m, \operatorname{div}\varphi) \\ + (\operatorname{div} v_\pi^m, \xi) = k(\theta f^m + (1-\theta)f^{m-1}, \varphi)\end{aligned} \tag{5.26}$$

with $v_\pi^0 = v_\pi^M$. The discretization of the initial value problem is the solution $(v^m, p^m) \in V_h \times Q_h$ for $m = 1, \dots, M$ of

$$\begin{aligned}(v^m - v^{m-1}, \varphi) + k(\nabla(\theta v^m + (1-\theta)v^{m-1}), \nabla\varphi) - k(p^m, \operatorname{div}\varphi) \\ + (\operatorname{div} v^m, \xi) = k(\theta f^m + (1-\theta)f^{m-1}, \varphi)\end{aligned} \tag{5.27}$$

for all $(\varphi, \xi) \in V_h \times Q_h$, where $f^m := f(s^m)$ and $v^0 \in V_h$ is a given space-discrete initial value. As in the continuous case we also write $v^m(v^0)$ to emphasize the dependence on the initial value. Note that $\theta = \frac{1}{2}$ corresponds to the Crank-Nicolson and $\theta = 1$ to the implicit Euler discretization, while $\theta = \frac{1}{2} + \mathcal{O}(k)$ is known as shifted Crank-Nicolson scheme. Shifted Crank-Nicolson schemes are still second-order accurate but are, in contrast to the Crank-Nicolson scheme, strongly A-stable and have thus superior stability properties [Ric17], e.g. don't require a step size condition such as $k \lesssim h^2$ which is, at least theoretically, required for the Crank-Nicolson scheme [LR82].

To carry over the continuous ideas into the discrete setting, we need to define an appropriate decomposition of the discrete solution into mean and oscillatory components such that the mean value of v_π can be computed without knowledge of v_π^0. The identity

$$\sum_{m=1}^{M} v_\pi^m - v_\pi^{m-1} = v_\pi^M - v_\pi^0 = 0 \tag{5.28}$$

motivates the definition of the discrete θ-mean for some discrete function $w^0, \dots, w^M$ as

$$\overline{w^m}^{\theta,k} := \sum_{m=1}^{M} k(\theta w^m + (1-\theta)w^{m-1}) \tag{5.29}$$

since then

$$(\nabla \overline{v_\pi}^{\theta,k}, \nabla\varphi) - (\overline{p_\pi}^{1,k}, \operatorname{div}\varphi) + (\operatorname{div}\overline{v_\pi}^{\theta,k}, \xi) = (\overline{f}^{\theta,k}, \varphi) \tag{5.30}$$

for all $(\varphi, \xi) \in V_h \times Q_h$. We implicitly used that the divergence condition $(\operatorname{div} v_\pi^m, \xi) = 0$ holds for $m = 1, \dots, M$ but also for $m = 0$ due to periodicity, which implies that we can can choose any discrete $\tilde{\theta}$-mean for the corresponding condition in eq. (5.30), in particular $\tilde{\theta} = \theta$ such that only $\overline{v_\pi}^{\theta,k}$ and $\overline{p_\pi}^{1,k}$ are unknowns of the problem.

With this definition of the discrete θ-mean, which allows the computation of $\overline{v_\pi}^{\theta,k}$ without knowledge of v_π^0, we can formulate a discrete version of the Picard iteration from eq. (5.16):

$$v_i^0 = v^M(v_{i-1}^0) + \gamma\,\delta_i, \quad \delta_i := \overline{v_\pi}^{\theta,k} - \overline{v^m(v_{i-1}^0)}^{\theta,k}. \tag{5.31}$$

Input:
- discrete initial guess $v_0^0 \in V_h$ with $(\operatorname{div} v_0^0, \xi) = 0$ for all $\xi \in Q_h$,
- maximum number of iterations $n_i \in \mathbb{N}$,
- absolute tolerance $TOL_a > 0$,
- relative tolerance $TOL_r > 0$

Output: Approximation of v_π^0

1: Compute $\overline{v_\pi}^{\theta,k}$ by solving eq. (5.30)
2: **for** $i = 1, \dots, n_i$ **do**
3: Compute $v^m(v_{i-1}^0)$ for $m = 1, \dots, M$ by solving eq. (5.27)
4: $\tilde{v}_i^0 \leftarrow v^M(v_{i-1}^0)$
5: **if** $\|\tilde{v}_i^0 - v_{i-1}^0\| \le TOL_a$ or $\|\tilde{v}_i^0 - v_{i-1}^0\| \le TOL_r \|\tilde{v}_i^0\|$ **then**
6: **return** $\tilde{v}_i^0$
7: **end if**
8: Compute $\overline{v^m(v_{i-1}^0)}^{\theta,k}$ using eq. (5.29)
9: $v_i^0 \leftarrow \tilde{v}_i^0 + \gamma(\overline{v_\pi}^{\theta,k} - \overline{v^m(v_{i-1}^0)}^{\theta,k})$
10: **end for**
11: **raise error:** tolerance not reached in n_i iterations

Algorithm 5.12: Algorithmic realization of the mean value correction iteration for the Stokes equation discretized with the θ-scheme.

An algorithmic realization of the mean correction iteration from eq. (5.31) requires an evaluable stopping criterion. The theoretical results estimate the distance to the true periodic solution, but this is of course unknown in practise. Instead we examine the $L^2(\Omega)$ periodicity error E_i given by

$$E_i := \|\tilde{v}_i^0 - v_{i-1}^0\|, \quad \text{with } \tilde{v}_i^0 := v^M(v_0^{i-1})$$

where $v^M(v_0^{i-1})$ is the final value of the discrete initial value problem from eq. (5.27). Here and in the following we will measure the periodicity error with respect to the $L^2(\Omega)$ norm, for Test Case 5.3.6 it is later checked that this is not detrimental, see Figure 5.21. Note that the periodicity error is measured prior to correction. The error $\|v_i^0 - v_{i-1}^0\|$ between iterates of the fixed-point iteration is of course also valid but requires the calculation of an additional correction if the iteration is stopped afterwards.

With this evaluable error we can formulate Algorithm 5.12 for the discrete mean correction iteration, where a solution is accepted if either absolute or relative periodicity error is below a tolerance threshold. The focus of the algorithmic description is not efficiency, for which e.g. the θ-mean should already be computed during the initial value solution to avoid the storage of the solution for averaging.

As for convergence of the mean correction iteration, we only cite the following result from [Ric19] where the case $\gamma = 1$ is investigated.

Lemma 5.3.7 (from [Ric19, Lemma 6])**.** *Let Ω be a convex polygonal domain, $f \in L^2(0,1;L^2(\Omega))$. Let $V_h \times Q_h \subset H_0^1(\Omega) \times L^2(\Omega)$ be an inf-sup stable finite element space and $v_0^0 \in V_h$ with $(\operatorname{div} v_0^0, \xi) = 0$ for all $\xi \in Q_h$. Let the time discretization be equidistant with parameter θ depending on the step size by*

$$\theta_k = \frac{1}{2} + \frac{k}{2}.$$

Then, the discrete mean correction iteration from eq. (5.31) with $\gamma = 1$ applied to the Stokes equations converges like

$$\|v_i^0 - v_\pi^0\| \leq 0.42 \|v_{i-1}^0 - v_\pi^0\|. \tag{5.32}$$

Proof. See [Ric19, Lemma 6]. □

Remark 5.3.8. It is remarked in [Ric19] that numerical results indicate no problem if $\theta = \frac{1}{2}$ is chosen. Furthermore, the estimate of the reduction factor in eq. (5.32) appears to be not sharp and a reduction factor similar the continuous case is observed numerically, see Figure 5.15(a) below. That such a result holds, at least asymptotically as $k \to 0$, can be already seen from the proof of Lemma 5.3.7 from [Ric19], where it is observed that the discrete reduction rate, in dependence on the eigenvalues of the discrete operator, converges to the same expression from the continuous case as $k \to \infty$. ◇

Mean Correction for the Navier–Stokes Equation

The discrete Navier–Stokes problem as studied here is to find $(v_\pi^m, p_\pi^m) \in V_h \times Q_h$ for $m = 1, \dots, M$ such that

$$\begin{aligned} &(v_\pi^m - v_\pi^{m-1}, \varphi) + k(\theta(v_\pi^m \cdot \nabla) v_\pi^m + (1-\theta)(v_\pi^{m-1} \cdot \nabla) v_\pi^{m-1}, \varphi) \\ &\quad + k(\nabla(\theta v_\pi^m + (1-\theta) v_\pi^{m-1}), \nabla\varphi) - k(p_\pi^m, \operatorname{div}\varphi) + (\operatorname{div} v_\pi^m, \xi) \\ &\quad = k(\theta f^m + (1-\theta) f^{m-1}, \varphi) \end{aligned} \tag{5.33}$$

for all $(\varphi, \xi) \in V_h \times Q_h$ with $v_\pi^0 = v_\pi^M$. While different time-discretizations for the nonlinearity are possible, the choice made here is naturally compatible with averaging as will be seen later. Following [Ric19] we proceed just as in the continuous case. For a time-discrete function w^m with $m = 0, \dots, M$ there holds by algebraic manipulations that

$$\begin{aligned} &\sum_{m=1}^{M} k(\theta(w^m \cdot \nabla) w^m + (1-\theta)(w^{m-1} \cdot \nabla) w^{m-1}) \\ &\quad = (\overline{w^m}^{\theta,k} \cdot \nabla) \overline{w^m}^{\theta,k} \\ &\qquad + \sum_{m=1}^{M} k(\theta(\widetilde{w^m}^{\theta,k} \cdot \nabla) \widetilde{w^m}^{\theta,k} + (1-\theta)(\widetilde{w^{m-1}}^{\theta,k} \cdot \nabla) \widetilde{w^{m-1}}^{\theta,k}) \end{aligned}$$

where the oscillatory part of the discrete solution is defined analogous to the continuous setting

$$\widetilde{w^m}^{\theta,k} = w^m - \overline{w^m}^{\theta,k}.$$

Application of this identity to $w^m = v_\pi^m$ and $w^m = v^m := v^m(v^0) \in V_h$, being the solution to

$$\begin{aligned}(v^m - v^{m-1}, \varphi) + k(\theta(v^m \cdot \nabla)v^m + (1-\theta)(v^{m-1} \cdot \nabla)v^{m-1}, \varphi) \\ + k(\nabla(\theta v^m + (1-\theta)v^{m-1}), \nabla\varphi) - k(p^m, \operatorname{div}\varphi) + (\operatorname{div} v^m, \xi) \\ = k(\theta f^m + (1-\theta)f^{m-1}, \varphi)\end{aligned} \tag{5.34}$$

for $m = 1, \dots, M$ and $(\varphi, \xi) \in V_h \times Q_h$ with associated discrete pressure $p^m \in Q_h$, yields the following equation for the update $\delta_i := \overline{v_\pi^m}^{\theta,k} - \overline{v_i^m}^{\theta,k}$ where $v_i^m := v^m(v_{i-1}^0)$:

$$\begin{aligned}((\overline{v_\pi^m}^{\theta,k} \cdot \nabla)\overline{v_\pi^m}^{\theta,k} - (\overline{v^m}^{\theta,k} \cdot \nabla)\overline{v^m}^{\theta,k}, \varphi) \\ + (\nabla\delta_i, \nabla\varphi) - (q_i, \operatorname{div}\varphi) + (\operatorname{div}\delta_i, \xi) = (R_i, \varphi) + (v_i^M - v_i^0, \varphi)\end{aligned}$$

for all $(\varphi, \xi) \in V_h \times Q_h$, with associated pressure q_i and remainder

$$\begin{aligned}R_i := \sum_{m=1}^{M} k_m \big((\widetilde{v_i^m}^{\theta,k} \cdot \nabla)\widetilde{v_i^m}^{\theta,k} + (1-\theta)(\widetilde{v_i^{m-1}}^{\theta,k} \cdot \nabla)\widetilde{v_i^{m-1}}^{\theta,k} \\ - (\widetilde{v_\pi^m}^{\theta,k} \cdot \nabla)\widetilde{v_\pi^m}^{\theta,k} - (1-\theta)(\widetilde{v_\pi^{m-1}}^{\theta,k} \cdot \nabla)\widetilde{v_\pi^{m-1}}^{\theta,k}\big)\end{aligned}$$

which corresponds to $\int_0^1 (\widetilde{v_i} \cdot \nabla)\widetilde{v_i} - (\widetilde{v_\pi} \cdot \nabla)\widetilde{v_\pi}\,\mathrm{d}s$ from the continuous setting. With the same heuristic that the remainder is small if v_i is close to v_π we assume that the uncomputable $R_i \approx 0$. This yields the update equation

$$\begin{aligned}((\overline{v_\pi^m}^{\theta,k} \cdot \nabla)\overline{v_\pi^m}^{\theta,k} - (\overline{v^m}^{\theta,k} \cdot \nabla)\overline{v^m}^{\theta,k}, \varphi) + (\nabla\delta_i, \nabla\varphi) - (q_i, \operatorname{div}\varphi) + (\operatorname{div}\delta_i, \xi) \\ = (v_i^M - v_i^0, \varphi).\end{aligned}$$

Just as in the continuous case we rewrite the difference of the averages and drop the quadratic nonlinearity to arrive at

$$\begin{aligned}((\delta_i \cdot \nabla)\overline{v_i^m}^{\theta,k} + (\overline{v_i^m}^{\theta,k} \cdot \nabla)\delta_i, \varphi) + (\nabla\delta_i, \nabla\varphi) - (q_i, \operatorname{div}\varphi) + (\operatorname{div}\delta_i, \xi) \\ = (v_i^M - v_i^0, \varphi).\end{aligned} \tag{5.35}$$

With an evaluable stopping criterion just as in the linear case, this leads to Algorithm 5.13.

Numerical Results for Test Cases 5.3.4 and 5.3.5

The improvements due to the use of the correction scheme can be seen in Figure 5.14 for Test Case 5.3.4 with $L = 4$ and $\nu = 2.5 \times 10^{-3}$. For these parameters, the solver without correction does not converge in 50 iterations, whereas all corrected schemes converge. The best convergence properties for the selected set of γ can be seen for $\gamma = 0.79$, which in particular converges faster than $\gamma = 1$. Here and in the following, unless specified otherwise, the temporal discretization consists of $M = 40$ time steps per period and the simulation was stopped after an absolute tolerance of 10^{-8} was reached. In the error analysis we will see that such a tolerance is far lower than required.

Input:
- discrete initial guess $v_0^0 \in V_h$ with $(\operatorname{div} v_0^0, \xi) = 0$ for all $\xi \in Q_h$,
- maximum number of iterations $n_i \in \mathbb{N}$,
- absolute tolerance $TOL_a > 0$,
- relative tolerance $TOL_r > 0$

Output: Approximation v_i^0 of v_π^0

1: **for** $i = 1, \dots, n_i$ **do**
2: Compute $v^m(v_{i-1}^0)$ for $m = 1, \dots, M$ by solving eq. (5.34)
3: $\tilde{v}_i^0 \leftarrow v^M(v_{i-1}^0)$
4: **if** $\|\tilde{v}_i^0 - v_{i-1}^0\| \leq TOL_a$ or $\|\tilde{v}_i^0 - v_{i-1}^0\| \leq TOL_r \|\tilde{v}_i^0\|$ **then**
5: **return** $\tilde{v}_i^0$
6: **end if**
7: Compute $\overline{v^m(v_{i-1}^0)}^{\theta,k}$ using eq. (5.29)
8: Compute δ_i by solving eq. (5.25)
9: $v_i^0 \leftarrow \tilde{v}_i^0 + \gamma\, \delta_i$
10: **end for**
11: **raise error:** tolerance not reached in n_i iterations

Algorithm 5.13: Algorithmic realization of the mean value correction iteration for the Navier–Stokes equation discretized with the θ-scheme.

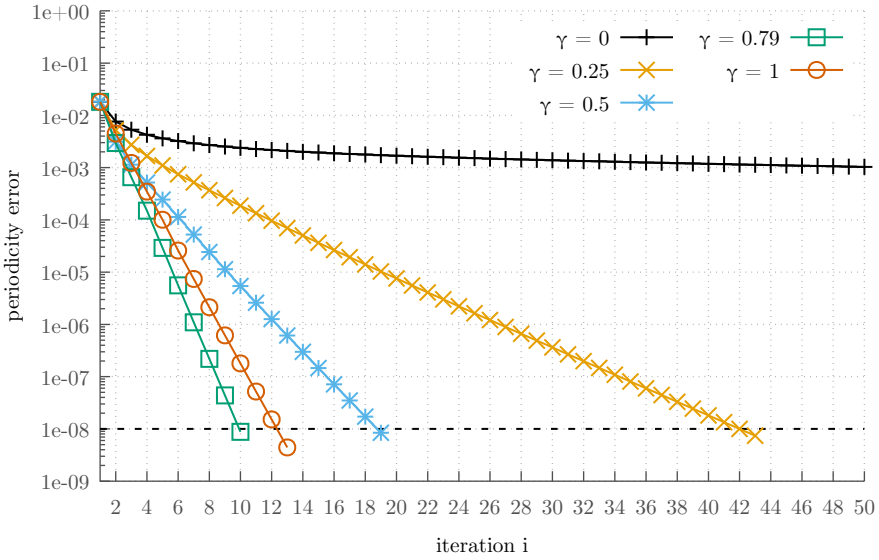

Figure 5.14: Periodicity error for Test Case 5.3.4 with $\nu = 2.5 \times 10^{-3}$ and $L = 4$ for different relaxation parameters γ. The horizontal line indicates the tolerance threshold.

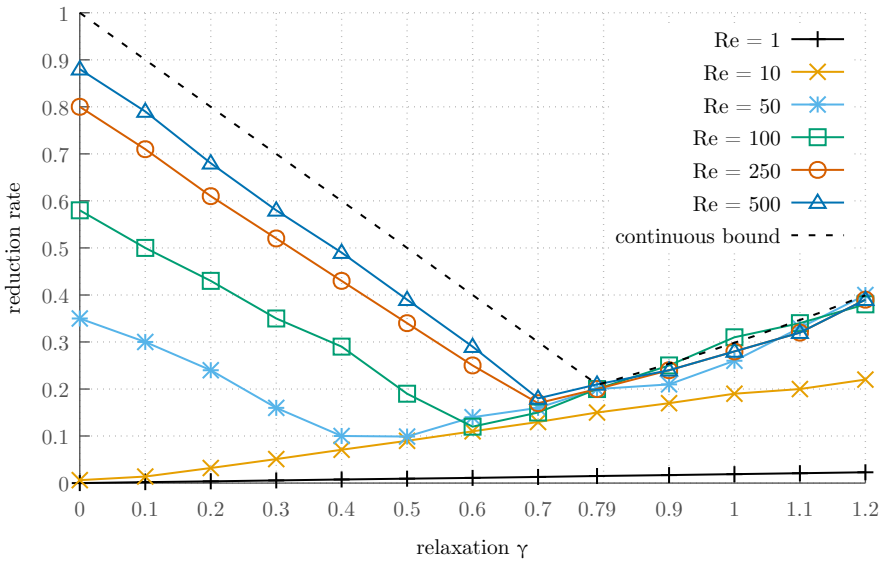

(a) Navier–Stokes equation.

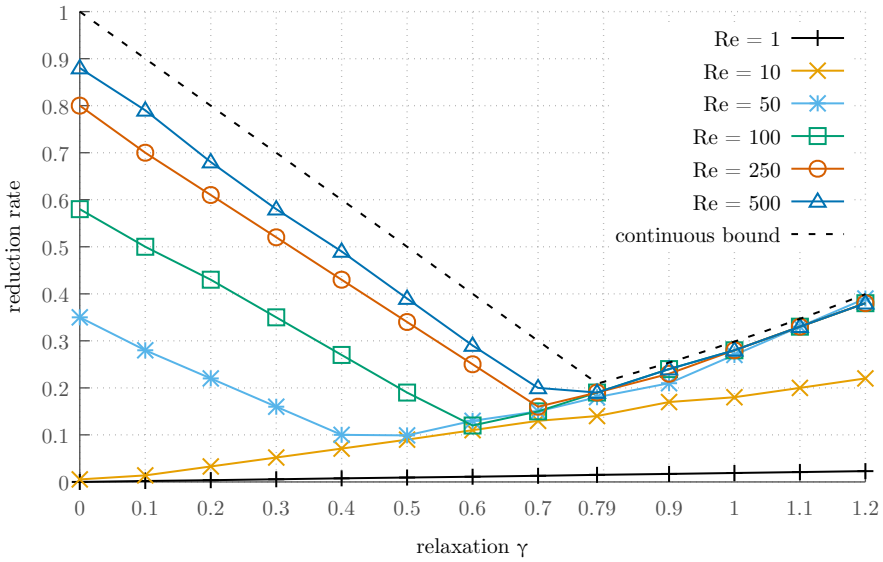

(b) Stokes equation.

Figure 5.15: Averaged numerical reduction rate for Test Case 5.3.5 for different values of Re depending on relaxation factor γ with fixed $St = 1$. The theoretical upper bound for the continuous algorithm for the linear problem from Figure 5.11 is also plotted.

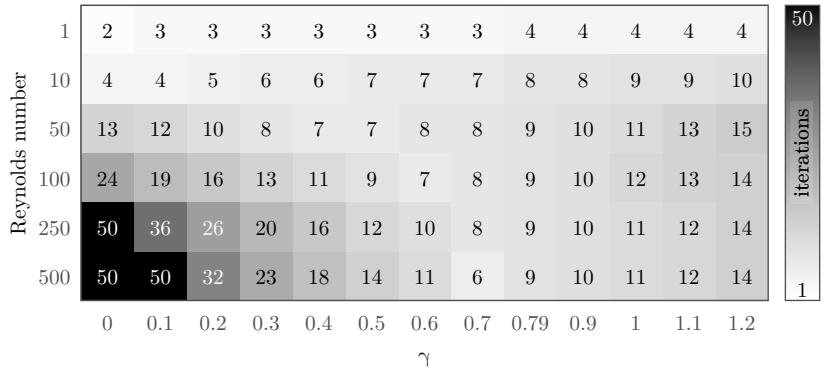

(a) Navier–Stokes equation.

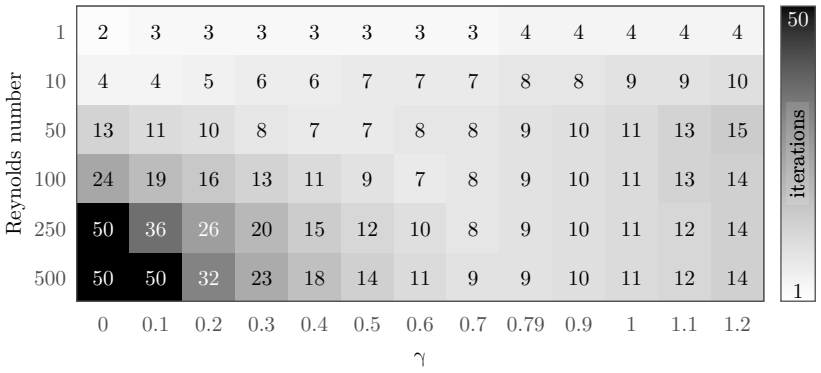

(b) Stokes equation.

Figure 5.16: Number of iterations until the tolerance is reached for Test Case 5.3.5 in the same setting as Figure 5.15.

To examine the relation between the different parameters, we will focus exclusively on the non-dimensional Test Case 5.3.5 from now on. The influence of the Reynolds number on the (numerical) reduction rate, given by

$$\rho_i = \frac{\|v_i^0 - v_{i-1}^0\|}{\|v_{i-1}^0 - v_{i-2}^0\|} \quad \text{for } i \geq 2 \tag{5.36}$$

with fixed $St = 1$ can be seen in Figure 5.15, where the reduction rate is averaged over all iterations. The first observation is that the reduction rate is very similar when comparing Navier–Stokes and Stokes equation, Figures 5.15(a) and 5.15(b), with slightly less consistent behavior for the nonlinear equation. For the Stokes equation the rate of convergence is bound from above by the theoretical upper bound from the continuous setting from Lemma 5.3.2 and is an increasingly good fit for increasing Reynolds number. With some minor

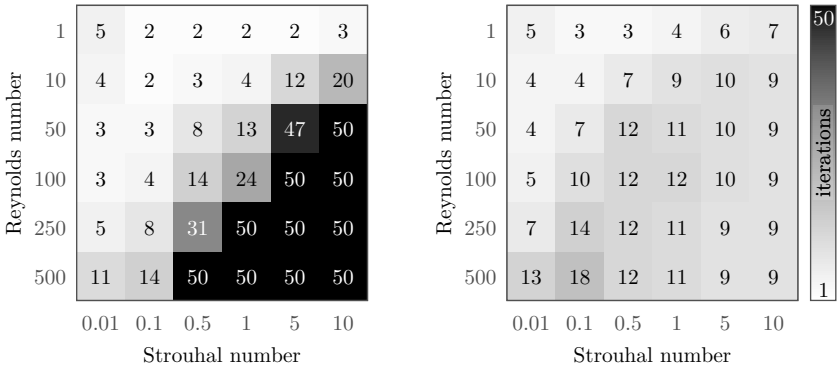

(a) Navier–Stokes eq. with $\gamma = 0$.

(b) Navier–Stokes eq. with $\gamma = 1$.

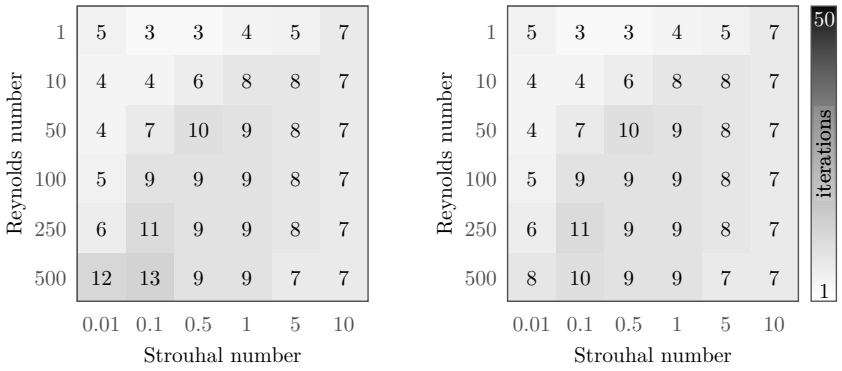

(c) Navier–Stokes eq. with $\gamma = 0.79$.

(d) Stokes eq. with $\gamma = 0.79$.

Figure 5.17: Number of iterations until the tolerance is reached for different Strouhal and Reynolds numbers for Test Case 5.3.5. The Navier–Stokes equation is investigated for $\gamma = 0$, $\gamma = 1$ and $\gamma = 0.79$. The iteration number for the Stokes equation for $\gamma = 0.79$ is shown as comparison.

exception this is also true for the Navier–Stokes equation. The optimality of $\gamma = 0.79$ was with respect to bounds independent of the operator spectrum, i.e. independent of Re. Figure 5.15 shows that for many cases other choices of γ perform better for the specific operator spectrum. No mean correction ($\gamma = 0$) is best for $Re = 10$ and $Re = 50$, but with increasing Reynolds number the quality of mean corrections with small γ deteriorate quickly. While $\gamma = 0.79$ is not be optimal for most specific settings, it is nevertheless a good general choice with consistent performance when no prior knowledge is available. This is corroborated by Figure 5.16, where the number of iterations for the same set of simulations is plotted, which is of course linked to the convergence rate.

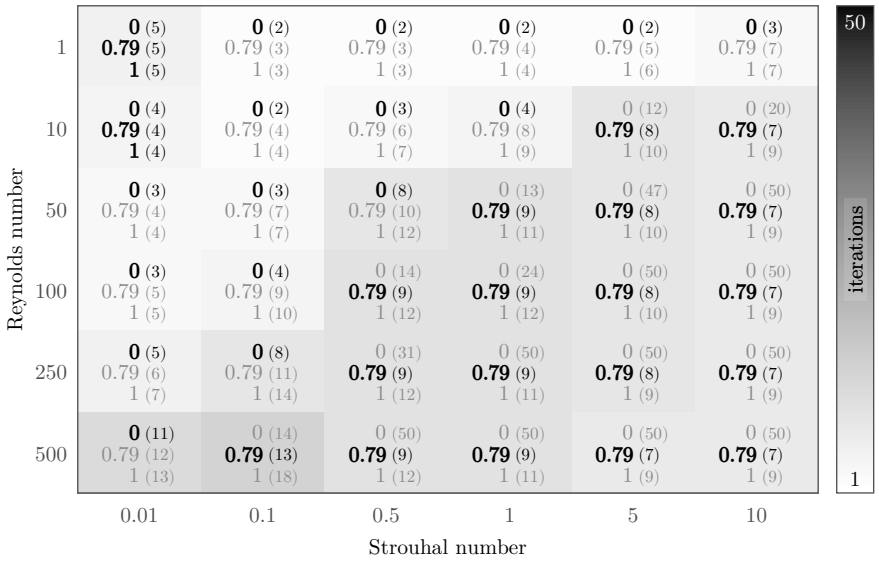

Figure 5.18: Summary of Figure 5.17. Each cell contains the best choice of $\gamma \in \{0, 0.79, 1\}$ in bold for that combination of Reynolds and Strouhal numbers, with the number of iterations in parenthesis. Background color according to the iteration number for the best γ.

The influence of Re and St on the iteration number until convergence has been tested only for the special values of $\gamma \in \{0, 0.79, 1\}$, the results of which can be found in Figure 5.17. For large Reynolds and Strouhal numbers the forward iteration without correction ($\gamma = 0$) does not converge within 50 iterations as can be seen in Figure 5.17(a). For $\gamma = 0.79$ and $\gamma = 1$ convergence is reached for all tested parameter combinations in at most 18 iterations, see Figures 5.17(a) to 5.17(c). It can be observed that the correction schemes needed the largest number of iterations for high Reynolds and low Strouhal numbers, although this pattern is not always consistent, e.g. for $Re = 500$ the Strouhal number $St = 0.1$ required more iterations than $St = 0.01$ for all studied γ. The set of parameters for which the mean correction iteration, respectively the forward iteration, performed well, differed. For $\gamma = 0.79$ the iteration numbers for the Stokes variant of the problem are plotted in Figure 5.17(d). Only for $Re = 500$ and $St \in \{0.1, 0.01\}$ differences to the Navier–Stokes problem from Figure 5.17(c) can be seen, where the determination of a periodic solution to the Stokes equation required, as expected, fewer iterations.

A direct comparison of the results for $\gamma = 0$, $\gamma = 0.79$ and $\gamma = 1$ is given in Figure 5.18. Ignoring the cases $Re = 1$ and $Re = 10$ for $St = 0.01$, where all methods perform equally well, it can be observed that the parameters for which $\gamma = 0$ performs best satisfy $Re \cdot St \leq 25$, whereas $\gamma = 0.79$ performs best for $Re \cdot St \geq 50$. In other words, the product of Reynolds and Strouhal numbers characterize the optimal choice of γ in this example.

The convergence behavior of the periodicity error for the case $Re = 500$

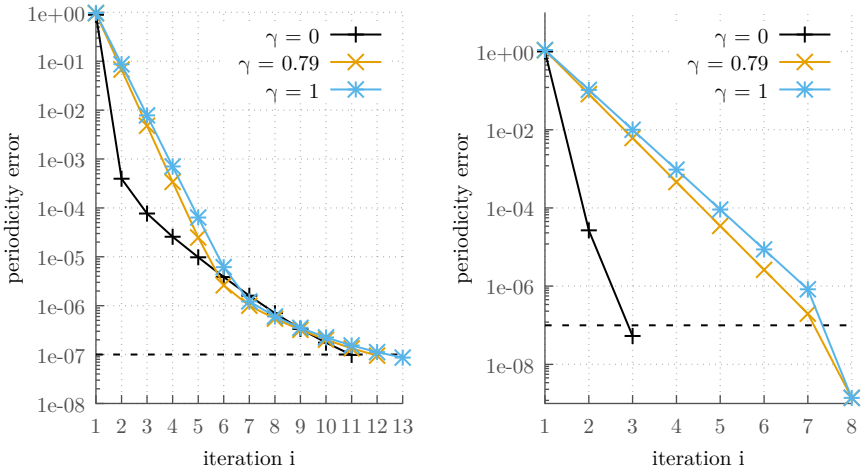

(a) Navier–Stokes equation.

(b) Stokes equation.

Figure 5.19: Periodicity error for different values of γ for the Navier–Stokes and Stokes equation for Test Case 5.3.5 with $Re = 500$ and $St = 0.01$ from Figure 5.17.

and $St = 0.01$ can be seen in Figure 5.19. The first observation is that the initial periodicity error is equal to the L^2 norm of the first iterate since $v_0^0 = 0$. The reduction rate for the Stokes equation stays, approximately, constant for all methods with slightly better convergence in the last iteration. For the Navier–Stokes equation the error is greatly reduced in the second iteration for $\gamma = 0$, but then slows down significantly. A similar behavior can be observed for $\gamma = 0.79$ and $\gamma = 1$, where the slowdown occurs at a point where the periodicity error is smaller. For these schemes the slowdown is more severe, with a smaller error than $\gamma = 0$ after the 7th iteration but more total iterations, indicating that the correction may be detrimental in this scenario. These results show a fundamental difference in the convergence behavior for the Navier–Stokes compared to the Stokes equation for these parameters and further investigations could be carried out to improve the mean correction iteration for the Navier–Stokes problem.

Numerical Results for Test Case 5.3.6

Test Case 5.3.6 is the problem occurring in the limit system, where the Reynolds and Strouhal numbers are fixed. We will instead focus on the dependence of the periodic solver on the domain through the parameter $q \in Q$ and the periodicity error for the wall shear stress dependent quantities used in the limit system. All simulations were carried out with $M = 40$ time steps per period until an absolute tolerance of 10^{-7} is reached for the L^2 periodicity error. The calculations for the limit problem use variable temporal discretizations and periodicity tolerances to balance the overall error, see Theorem 5.4.1 at the end of this chapter. For the finest macro discretization of the limit system

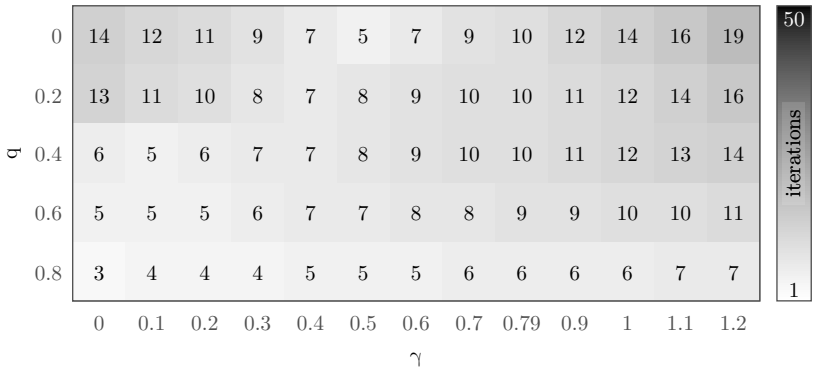

Figure 5.20: Number of iterations until the tolerance is reached for Test Case 5.3.6 for a number of different channel geometries, described by q, and different relaxation parameters.

$M = 60$ steps were performed per period with a tolerance of 10^{-4}, meaning that the tolerance of 10^{-7} we consider here is far lower than the tolerances used for the solution of the limit system.

The number of iterations necessary for convergence is shown in Figure 5.20 for different stages of the stenosis q in dependence on γ. The lowest number of iterations, averaged over all examined domains, is achieved for $\gamma = 0.4$ and $\gamma = 0.5$. The theoretical $\gamma = 0.79$ required on average 2–3 iterations more, showing once again that the convergence can improved by tuning γ to the problem parameters. Another observation which can be made from Figure 5.20 is that the domain corresponding to $q = 0.8$ requires the fewest iterations. An explanation for this behavior is that the narrowing of the channel reduces the velocity field induced by the pressure drop, such that the Reynolds number is effectively decreasing as q increases.

Based on the observations from Figure 5.20 the relaxation $\gamma = 0.5$ was chosen for the limit system to minimize the number of iterations until periodic convergence. The comparison of the periodic solver for different q and γ carried out here is already a significant investment of resources and thus unlikely to be performed a priori for more complex problems. Note however, that the adaptive discretizations and tolerances employed for the limit system, together with other strategies discussed below, lower the required number of iterations significantly, as evident by comparing Figure 5.20 to Figure 5.9.

Another question which naturally arises for our application is the choice of control criteria for the periodic solver since the actual quantity of interest is g_0. Figure 5.21 displays the error of various functionals between periods for $\gamma = 0.5$ and $q = 0$, where $\sigma^0_{\mathrm{WS}} := 0.04$ was chosen for the last functional, as for the limit system from above. It can be observed that the absolute and relative errors for the quantities involving the wall shear stress are very similar to or smaller than the measured $L^2(\Omega)$ error. Similar behavior was observed for other values of γ and q.

While unlikely in practise, it is possible that the wall shear stress dependent functionals do not change between iterations even if the solution has not reached the periodic orbit, since only changes of the velocity field near the wall

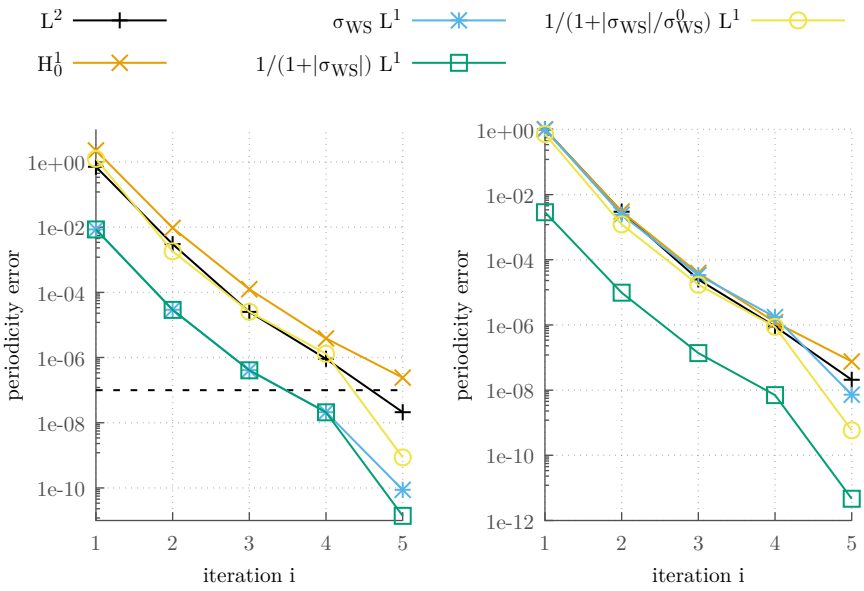

(a) Absolute periodicity error. The dashed line indicates the convergence tolerance for the L^2 error.

(b) Relative periodicity error.

Figure 5.21: Periodicity error for Test Case 5.3.6 with $\gamma = 0.5$ and $q = 0$ using different functionals. The functionals involving the wall shear stress were integrated over the permeable part of the wall.

are taken into account. We chose the L^2 periodicity error as a more accurate measurement of reaching the periodic orbit for this reason, with Figure 5.21 indicating that this does not under-estimate the true error made in the evaluation of g_0.

Extending the Mean Correction Scheme to BDF2

The translation of the mean correction scheme to other time discretizations is non-trivial, as will be discussed here for example of the two-step backward differentiation formula (BDF2). This is not of interest in itself but also allows us to reflect on the construction of the algorithm for the θ-schemes. BDF2 is a second order method where the time derivative is approximated by

$$\partial_s v(s^m) \approx d_s v^m := \tfrac{1}{k}\left(\tfrac{3}{2}v^m - 2v^{m-1} + \tfrac{1}{2}v^{m-2}\right)$$

which is the derivative of the quadratic Lagrange polynomial through the points (s^j, v^j) for $j = m-2, \dots, m$. Restricting ourselves for simplicity to the Stokes equation, the BDF2 discretization for the periodic problem then reads

$$(kd_s v_\pi^m, \varphi) + k(\nabla v_\pi^m, \nabla\varphi) - k(p_\pi^m, \operatorname{div}\varphi) + (\operatorname{div} v_\pi^m, \xi) = k(f^m, \varphi) \qquad (5.37)$$

for all $(\varphi, \xi) \in V_h \times Q_h$ and $m = 1, \dots, M$. Note that the BDF2 scheme can also be used for $m = 1$ in this problem by setting $v_\pi^{-1} := v_\pi^{M-1}$.

The discrete average from eq. (5.29) for the θ-scheme was motivated by eq. (5.28), where a summation cancelled out the time derivative due to the periodicity of the discrete periodic solution. Since

$$\sum_{m=1}^{M} k d_s v_\pi^m = \tfrac{3}{2}\sum_{m=1}^{M} v_\pi^m - 2\sum_{m=0}^{M-1} v_\pi^m + \tfrac{1}{2}\sum_{m=-1}^{M-2} v_\pi^m = \left(\tfrac{3}{2} - 2 + \tfrac{1}{2}\right)\sum_{m=1}^{M} v_\pi^m = 0$$

we can similarly sum over $m = 1, \dots, M$ in eq. (5.37) to arrive at

$$(\nabla \overline{v_\pi^m}^{1,k}, \nabla\varphi) - (\overline{p_\pi^m}^{1,k}, \operatorname{div}\varphi) + (\operatorname{div}\overline{v_\pi^m}^{1,k}, \xi) = (\overline{f^m}^{1,k}, \varphi)$$

for all $(\varphi, \xi) \in V_h \times Q_h$ using the notation for the $(\theta = 1)$-mean from eq. (5.29).

For the iterates v_i^m the discretization of the time derivative in the first step of eq. (5.37) must be modified since v_i^{-1} is undefined for an initial value problem. An implicit Euler step is typically employed, leading to

$$(k\tilde{d}_s v_i^m, \varphi) + k(\nabla v_i^m, \nabla\varphi) - k(p_i^m, \operatorname{div}\varphi) + (\operatorname{div} v_i^m, \xi) = k(f^m, \varphi)$$

for $m = 1, \dots, M$ and all $(\varphi, \xi) \in V_h \times Q_h$ with modified time derivative

$$\tilde{d}_s v_i^1 := \tfrac{1}{k}(v_i^1 - v_i^0), \quad \tilde{d}_s v_i^m := d_s v_i^m \quad \text{for } m = 2, \dots, M.$$

The mismatching time derivatives used for the iterates and periodic solution is problematic. This can be seen by studying the equation for the corrector, using the $(\theta = 1)$-mean for both iterate and periodic solution, i.e.

$$\delta_i := \overline{v_\pi^m}^{1,k} - \overline{v_i^m}^{1,k}.$$

Then the corrector satisfies, with associated pressure q_i,

$$(\nabla\delta_i, \nabla\varphi) - (q_i, \operatorname{div}\varphi) + (\operatorname{div}\delta_i, \xi) = \sum_{m=1}^{M} k(\tilde{d}_s v_i^m, \varphi)$$

for all $(\varphi, \xi) \in V_h \times Q_h$ and there holds

$$\begin{aligned}\sum_{m=1}^{M} k\tilde{d}_s v_i^m &= v_i^1 - v_i^0 + \tfrac{3}{2}\sum_{m=2}^{M} v_i^m - 2\sum_{m=1}^{M-1} v_i^m + \tfrac{1}{2}\sum_{m=0}^{M-2} v_i^m \\ &= (-1 + \tfrac{1}{2})v_i^0 + (1 - 2 + \tfrac{1}{2})v_i^1 + (\tfrac{3}{2} - 2)v_i^{M-1} + \tfrac{3}{2}v_i^M \\ &= -\tfrac{1}{2}v_i^0 - \tfrac{1}{2}v_i^1 - \tfrac{1}{2}v_i^{M-1} + \tfrac{3}{2}v_i^M.\end{aligned}$$

Since $\delta_i \to 0$ is necessary for the convergence of the fixed-point iteration, this implies that the iteration cannot converge to the periodic solution for which there holds

$$\sum_{m=1}^{M} k\tilde{d}_s v_\pi^m = v_\pi^0 - \tfrac{1}{2}v_\pi^1 - \tfrac{1}{2}v_\pi^{M-1} \neq 0 \tag{5.38}$$

and this expression only vanishes as $k \to 0$. This reveals that the correction using the $(\theta = 1)$-mean is incompatible with the modified time derivative.

As a remedy one could try to find a more suitable averaging scheme for the modified time derivative $\tilde{d}_s$ and use the same scheme for the periodic solution. One approach could be to find $\alpha \in \mathbb{R}^M$ such that

$$\sum_{m=1}^{M} \alpha^m \tilde{d}_s v^m = 0$$

for any $v^m \in V_h^{M+1}$ for $m = 0, \dots, M$ which is periodic, $v^0 = v^M$. It can be verified that the solution space for α is one-dimensional. It remains open however, for which α, if any, the use of the average

$$\overline{v^m}^{\alpha,k} := \sum_{m=1}^{M} k\alpha^m v^m,$$

leads to a convergent fixed-point iteration.

To circumvent the necessity to solve for α and scale it correctly, we will pursue another approach which keeps the $(\theta = 1)$-mean. Since we already use the (mean-corrected) last time step from the previous iteration as initial value for the next iteration, it is natural that we also use the (mean-corrected) second-last time step from the previous iteration as approximation to v_i^{-1}. This allows us to use the BDF2 time discretization for all steps except for the very first step of the first iteration. This is computationally beneficial since the matrices containing the time derivative won't change after the first step. Mathematically, the mean correction would then be a fixed-point iteration for the tuple (v_π^0, v_π^{-1}), but we won't go into details here. Using this approach, the equation for the corrector δ_i for $i > 1$ is then

$$(\nabla\delta_i, \nabla\varphi) - (q_i, \operatorname{div}\varphi) + (\operatorname{div}\delta_i, \xi) = \tfrac{3}{2}(v_i^M - v_i^0) - \tfrac{1}{2}(v_i^{M-1} - v_i^{-1}) \quad (5.39)$$

for all $(\varphi, \xi) \in V_h \times Q_h$ with associated pressure q_i. Similar to the θ-schemes, the right-hand side now converges to 0 as $i \to \infty$ if the fixed-point is the periodic solution, since

$$\lim_{i\to\infty} v_i^{-1} = \lim_{i\to\infty} (v_{i-1}^{M-1} + \gamma\delta_i) = v_\pi^{M-1}.$$

We tested two approaches for the first iteration $i = 1$, either applying the (incorrect) correction from eq. (5.39) or no correction at all, i.e. as in the forward iteration. No error analysis for this correction scheme is carried out here, but the numerical results from Figure 5.22 show that the initial corrections disturbs the convergence at the beginning but has no influence on the total number of iterations. In both cases, the use of a correction improves the convergence to the periodic solution significantly compared to BDF2 without mean correction. The periodicity error behaves identically to the Crank–Nicolson scheme.

Nonlinear Terms in the Correction Scheme

In the derivation of Algorithm 5.13 for the Navier–Stokes equation the identity

$$\begin{aligned}(\overline{v_\pi^m}^{\theta,k} \cdot \nabla)\overline{v_\pi^m}^{\theta,k} - (\overline{v_i^m}^{\theta,k} \cdot \nabla)\overline{v_i^m}^{\theta,k} \\ = \underbrace{(\delta_i \cdot \nabla)\delta_i}_{\text{“N”}} + \underbrace{(\delta_i \cdot \nabla)\overline{v_i^m}^{\theta,k}}_{\text{“R”}} + \underbrace{(\overline{v_i^m}^{\theta,k} \cdot \nabla)\delta_i}_{\text{“A”}}\end{aligned} \quad (5.40)$$

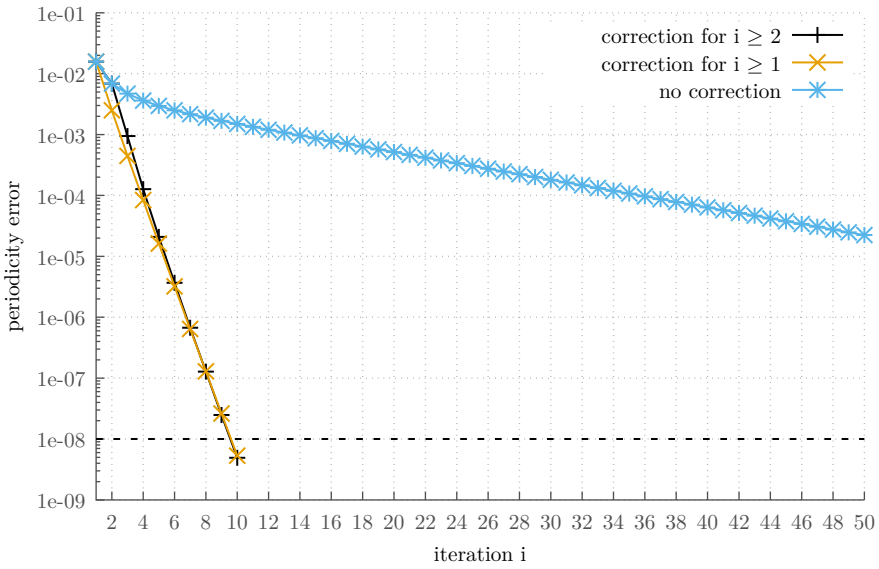

Figure 5.22: Periodicity error for Test Case 5.3.5 with $Re = 500$ and $St = 1$ for the BDF2 time discretization. Depicted are three mean correction strategies using the update δ_i from eq. (5.39): Correction only for periods $i \geq 2$, correction for all periods $i \geq 1$ and no correction at all, i.e. as in the forward iteration.

was used and the nonlinear term "N" dropped. The effect of using a correction with different combinations of terms from eq. (5.40) is graphed in Figure 5.23 for the Test Case 5.3.5 with $St = 0.01$ and $Re = 500$. These results indicate that dropping the nonlinear term, which circumvents the need to solve a nonlinear equation, does not affect the convergence negatively if both "A" and "R" are included, which is the choice used in Algorithm 5.13.

Anderson Acceleration

We finally discuss another, independent method to improve the convergence of the periodic solver by employing an Anderson acceleration strategy. This is a general method to improve the convergence of a fixed-point iteration and is related to the GMRES method for linear systems and to a quasi-Newton method for nonlinear problems, among others. We refer to [WN11] for an overview of the Anderson acceleration and [Eva+20] for a proof of improved convergence.

We will of course apply the Anderson acceleration to the fixed-point problem $v_\pi^0 = \mathcal{S}_\gamma(v_\pi^0)$ with $\mathcal{S}_\gamma$ as in eq. (5.14). The Anderson acceleration contains an optimization problem which takes the previous $l \in \mathbb{N}$ iterates into account, where we set $l = 10$ in our calculations. For this optimization problem we identify the iterates v_i^0 as basis coefficient vectors with respect to the standard nodal basis, i.e. $v_i^0 \in \mathbb{R}^D$ where $D \in \mathbb{N}$ is the nodal dimension, and optimize with respect to the ℓ^2 norm. This is a simplification and more appropriate

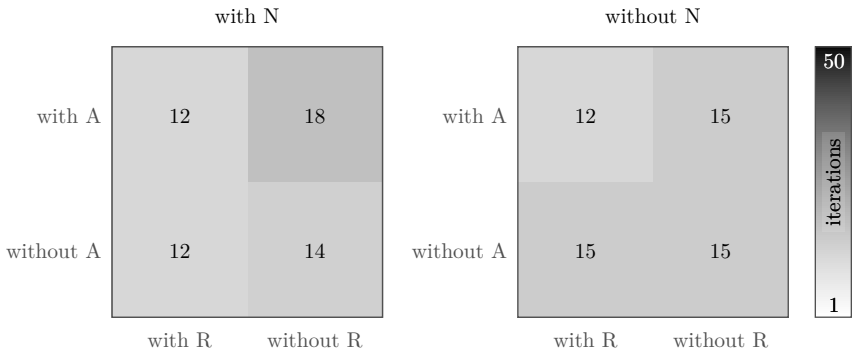

Figure 5.23: Number of iterations until the tolerance is reached for Test Case 5.3.5 with $St = 0.01$ and $Re = 500$ if the correction step uses a combination of the terms from eq. (5.40).

would be an optimization with respect to the $L^2(\Omega)$ norm.

For $i \in \mathbb{N}$ we set $l_i := \min\{l, i-1\}$ and define

$$\alpha_i := \underset{\alpha=(\alpha^0,\dots,\alpha^{l_i-1})^\mathsf{T}}{\arg\min} \|r_i - R_i\alpha\|_{\ell^2}$$

where

$$R_i := (\delta r_{i-l_i}, \cdots, \delta r_{i-1}), \quad \delta r_i := r_i - r_{i-1}, \quad r_i := \mathcal{S}_\gamma(v_i^0) - v_i^0 \tag{5.41}$$

and r_0 is defined analogously. The next iterate is then given by

$$v_i^0 = \mathcal{S}_\gamma(v_{i-1}^0) - \sum_{j=0}^{l_i-1} \alpha_i^j \left(\mathcal{S}_\gamma(v_{i-l_i+j}^0) - \mathcal{S}_\gamma(v_{i-l_i+j-1}^0)\right).$$

Other formulations of the Anderson acceleration can be found in [WN11].

We remind that evaluating $\mathcal{S}_\gamma$ requires the solution of one period of the Navier–Stokes initial value problem. By storing the last l values of v_i^0 and $\mathcal{S}_\gamma(v_i^0)$ only one initial value problem must be solved per iteration, i.e. the same as without acceleration. The main additional computational expense is solving the optimization problem for α_i, for which `linalg.lstsq` from the NumPy library [Oli06], is employed. The cost for this is negligible compared the solution of the initial value problem.

The improvements due to the use of the Anderson acceleration are pictured in Figure 5.24. The number of iterations is reduced for all tested values of γ for the Navier–Stokes equation and for all values except $\gamma = 0$ for the Stokes equation, where the iteration number is the same. The number of periods is reduced between 0% and 50% with $\approx 16\%$ mean reduction rate between all test cases. The periodicity error between periods is depicted in Figure 5.25 showing the effect of the acceleration compared to Figure 5.19. These results are very promising and further tests should be carried out to assess the performance and robustness of this method. The Anderson acceleration was not used for the discretization of the limit system, where only a few iterations were required anyway due to the higher employed tolerances.

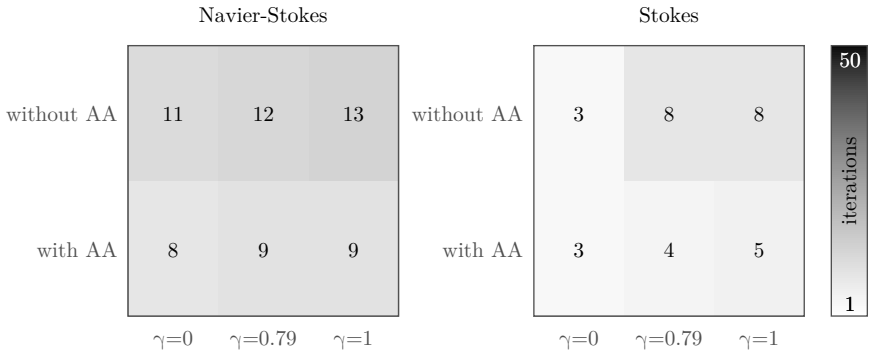

Figure 5.24: Number of iterations until the tolerance is reached for Test Case 5.3.5 for $St = 0.01$ and $Re = 500$ with and without Anderson acceleration (AA).

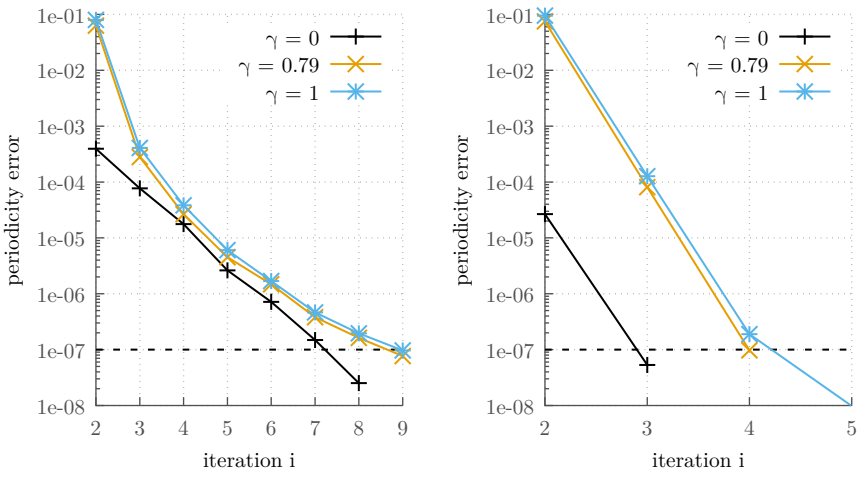

(a) Navier–Stokes equation

(b) Stokes equation

Figure 5.25: Periodicity error for different values of γ for the Navier–Stokes and Stokes equation in the same scenario as Figure 5.19 with the Anderson acceleration.

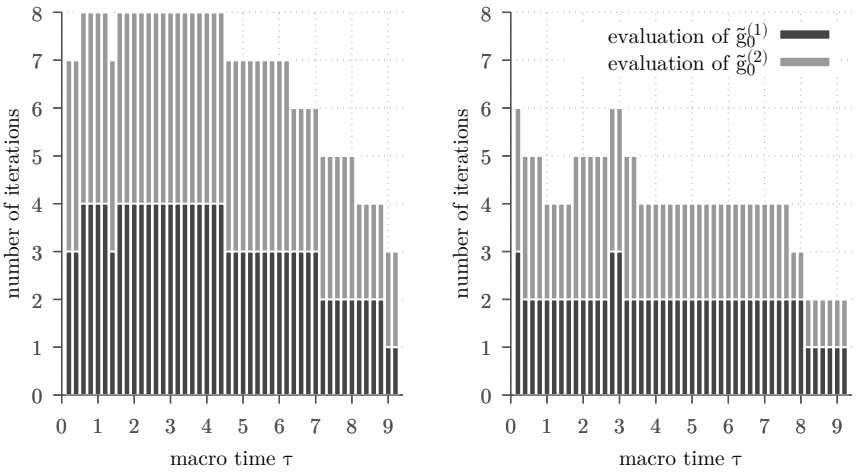

(a) Initial guess zero.

(b) Initial guess from previous periodic solution.

Figure 5.26: Number of iterations until an approximately periodic solution was found in each macro step of the limit system for the RK2 discretization with step size $\kappa = 0.2$. The initial guess for the periodic solver is zero in each evaluation of $\tilde{g}_0^{(i)}$ for (a) and uses the last periodic solution in (b), which is a replication of Figure 5.9.

Integration into the Limit System Solver

This section discusses the integration of the mean correction iteration into the solution process of the limit system, where in each macro step one (for the explicit Euler) or two (for the RK2 scheme) periodic Navier–Stokes problems must be solved. A previously determined periodic solution can be used as initial guess for a periodic solution in a new geometry as follows. Starting with the second evaluation of g_0, the initial guess for the periodic solution, denoted as v_0^0 above, is taken as the final solution of the previous evaluation of g_0, pushed forward to the mesh of the new geometry. For the first evaluation $v_0^0 := 0$ is used for simplicity. The positive effect of technique can be observed by comparing Figure 5.26(a), which uses an initial guess of zero for all evaluations, with Figure 5.26(b), which uses the previously described technique of reusing periodic solutions. The total number of iterations is reduced by 40% from 307 to 186. Note that the evaluation of $\tilde{g}_0^{(1)}$ uses the periodic solution from the evaluation of $\tilde{g}_0^{(2)}$ from the previous macro step and the evaluation of $\tilde{g}_0^{(2)}$ uses the periodic solution from the evaluation of $\tilde{g}_0^{(1)}$ from the current macro step, which is easily possible since both problems employ the same spatial discretization.

In the algorithmic description of the limit system solver an approximatively periodic solution is first determined and then used to compute the discrete average g_0 according to e.g. eq. (5.6). The computation of g_0 would then either

require the storage of the solution for all time steps of the previous iteration or another forward iteration after periodicity is determined. In our computations we used the alternative approach of computing g_0 within the time stepping of each iteration and discarding the result if the threshold has not been reached. While g_0 requires the evaluation of a boundary integral, it can be assumed that the cost of computing the discarded g_0 is lower than performing a forward iteration of the full problem if memory requirements or performance considerations prohibit the storage of all time steps of an iteration.

5.4 Temporal Error Analysis for the Limit System

In this section we sketch an error analysis for the limit system. In line with our general focus on the temporal aspects of the problem we only discuss a temporal semi-discretization of the limit equation with a space-continuous fluid problem. For the equation for q_0 on the macro scale we will use the Runge–Kutta 2 (RK2) method from eq. (5.5), for the periodic fluid problem on the micro scale the Crank–Nicolson scheme is employed.

The error analysis is non-standard due to the coupling of micro and macro scales and the discretization of the time-periodic fluid equation. While the presented analysis is new, the basic principles of micro and macro coupling are also discussed e.g. in the context of the heterogeneous multiscale method [E+07]. To focus on the non-standard aspects of the error analysis, we will simplify the micro problem to a Stokes equation and make assumptions on the regularity of the solution and limit right-hand side g_0 which are expected for the error analysis, likely to hold, but are not verified. This is the sense in which this is merely a sketch of the error analysis. Constants occurring in the rest of this section, either explicitly or implicitly in the $\lesssim$-notation, will be independent of the discretization parameters but may depend on the limit solution and the data.

Simplified Limit System and Discretization

For simplicity we only study a Stokes equation with time-periodic right-hand side, Strouhal and Reynolds numbers equal to 1, just as in the discussion of the mean correction iterations, cf. eq. (5.11). Specifically, we denote by $v_\pi(\cdot;\hat{q})$ for $\hat{q} \in Q$ in this section the solution to

$$\left.\begin{aligned} \partial_s v_\pi(s;\hat{q}) - P\Delta v_\pi(s;\hat{q}) &= Pf(s;\hat{q}), \\ \operatorname{div} v_\pi(s;\hat{q}) &= 0 \end{aligned}\right\} \quad \text{in } (0,1)\times\Omega_{\hat{q}} \tag{5.42a}$$

with Helmholtz projection P and 1-periodic right-hand side $f(\cdot;\hat{q})$. The solution $v_\pi(\cdot;\hat{q})$ must be 1-periodic,

$$v_\pi(0;\hat{q}) = v_\pi(1;\hat{q}) \quad \text{in } \Omega_{\hat{q}} \tag{5.42b}$$

and satisfy the homogeneous Dirichlet boundary values

$$v_\pi(s) = 0 \quad \text{on } (0,1)\times\partial\Omega_{\hat{q}}. \tag{5.42c}$$

The calculations carried out in the following will work the same way with pressure boundary conditions. We make various regularity assumptions in the

following which require regularity of $\partial\Omega_{\hat{q}}$, f and g_0 greater than those previously assumed, e.g. differentiability of g_0. Such assumptions are natural for an error analysis but are not verified here.

The limit equation for q_0 is assumed to be just as eq. (5.3a), i.e.

$$q_0'(\tau) = g_0(q_0(\tau)) \tag{5.43a}$$

with initial value $q_0(0) := 0$ and right-hand side

$$g_0(\hat{q}) := \gamma(1-\hat{q}) \int_0^1 \int_{\Gamma_{\hat{q}}} \left(1 + \frac{|\sigma_{\mathrm{WS},\pi}(s;\hat{q})|}{\sigma_{\mathrm{WS}}^0}\right)^{-1} \mathrm{d}o\,\mathrm{d}s \tag{5.43b}$$

where $\sigma_{\mathrm{WS},\pi}(\cdot;\hat{q})$ is the wall shear stress of the simplified Stokes equation and $\Gamma_{\hat{q}} \subset \partial\Omega_{\hat{q}}$ has positive measure and is sufficiently regular.

An approximation of the right-hand side g_0 is evaluated twice per macro step in the RK2 discretization of the limit equation, we denote these approximations by $\tilde{g}_0^{(i)}$ for $i \in \{1,2\}$. The analysis will show that the use of different micro discretizations is more efficient and we denote by $M^{(i)} \in \mathbb{N}$ the number of micro time steps per period with step size $k^{(i)} := 1/M^{(i)}$ and by $TOL^{(i)} > 0$ a periodicity tolerance parameter, see ineq. (5.46) below. For notational simplicity will however often omit the index i and just write M, k and TOL.

The temporal discretization of the simplified Stokes equation is a Crank–Nicolson scheme analogous to the one used for the computations, where $v_\pi^m(\hat{q})$ for $m = 1,\dots,M$ is a solution to

$$\left.\begin{aligned} v_\pi^m(\hat{q}) - v_\pi^{m-1}(\hat{q}) - \tfrac{k}{2}P\Delta(v_\pi^m(\hat{q}) + v_\pi^{m-1}(\hat{q})) \\ = \tfrac{k}{2}(Pf^m(\hat{q}) + Pf^{m-1}(\hat{q})), \\ \operatorname{div} v_\pi^m(\hat{q}) = 0, \end{aligned}\right\} \quad \text{in } \Omega_{\hat{q}} \tag{5.44a}$$

with periodicity condition

$$v_\pi^0(\hat{q}) = v_\pi^M(\hat{q}) \quad \text{in } \Omega_{\hat{q}} \tag{5.44b}$$

and boundary condition

$$v_\pi^m(\hat{q}) = 0 \quad \text{on } \partial\Omega_{\hat{q}}. \tag{5.44c}$$

The solution v_π^m of course depends on the parameters $M = M^{(i)}$ and $k = k^{(i)}$ for $i \in \{1,2\}$, such that formally $v_\pi^m = v_\pi^{m,(i)}$.

For the RK2 discretization of the limit equation there must hold for $n = 1,\dots,\mathcal{N}$ that

$$q_0^n = q_0^{n-1} + \kappa\tilde{g}_0^{(2)}(q_0^{n-1} + \tfrac{\kappa}{2}\tilde{g}_0^{(1)}(q_0^{n-1})) \tag{5.45a}$$

with $q_0^0 = 0$. The numbers 1 and 2 here refer to the order of evaluation. We will mainly investigate the discretization of g_0 from eq. (5.7),

$$\tilde{g}_0^{(i)}(\hat{q}) := \gamma(1-\hat{q}) \sum_{m=1}^{M} k \int_{\Gamma_{\hat{q}}} \left(1 + \frac{|\frac{1}{2}(\tilde{\sigma}_{\mathrm{WS},\pi}^m(\hat{q}) + \tilde{\sigma}_{\mathrm{WS},\pi}^{m-1}(\hat{q}))|}{\sigma_{\mathrm{WS}}^0}\right)^{-1} \mathrm{d}o \tag{5.45b}$$

where $\tilde{\sigma}_{\mathrm{WS},\pi}^m$ is the wall shear stress of the time-discrete, but only approximatively periodic solution $\tilde{v}_\pi^m(\hat{q})$. This discretization of g_0 will be beneficial since

the resulting velocity error can be easily estimated for the Crank–Nicolson scheme, we will later also discuss the corresponding estimates for other discretizations of g_0.

We assume that there is a periodicity tolerance $TOL = TOL^{(i)} > 0$ which guarantees that

$$\|\tilde{v}_\pi^m(\hat{q}) - v_\pi^m(\hat{q})\|_{H^2(\Omega_{\hat{q}})} \leq TOL \tag{5.46}$$

for $m = 1, \dots, M$ and $\hat{q} \in Q$. For the analysis such a criterion is reasonable, but the periodic solver will not guarantee such a bound, in particular since the periodic solution is unknown.

Macro Scale Error

The error is split into the errors due to this inexact approximation of the right-hand side g_0 and the normal error analysis for the RK2 scheme. Subtracting eqs. (5.43a) and (5.45a) for $q_0(\tau)$ and q_0^n, the error $e^n := q_0(\tau^n) - q_0^n$ satisfies the recursion

$$e^n = e^{n-1} + \int_{\tau^{n-1}}^{\tau^n} g_0(q_0(\tau))\,\mathrm{d}\tau - \kappa \tilde{g}_0^{(2)}(q_0^{n-1} + \tfrac{\kappa}{2}\tilde{g}_0^{(1)}(q_0^{n-1}))$$

and we split the right-hand side as follows

$$\begin{aligned} e^n = e^{n-1} &+ \int_{\tau^{n-1}}^{\tau^n} g_0(q_0(\tau))\,\mathrm{d}\tau - \kappa g_0(q_0(\tau^{n-1}) + \tfrac{\kappa}{2} g_0(q_0(\tau^{n-1}))) \\ &+ \kappa g_0(q_0(\tau^{n-1}) + \tfrac{\kappa}{2} g_0(q_0(\tau^{n-1}))) - \kappa g_0(q_0^{n-1} + \tfrac{\kappa}{2} g_0(q_0^{n-1})) \\ &+ \kappa g_0(q_0^{n-1} + \tfrac{\kappa}{2} g_0(q_0^{n-1})) - \kappa \tilde{g}_0^{(2)}(q_0^{n-1} + \tfrac{\kappa}{2}\tilde{g}_0^{(1)}(q_0^{n-1})). \end{aligned} \tag{5.47}$$

The second and third terms on the right of eq. (5.47) are the standard local truncation error for the RK2 method and of order $\mathcal{O}(\kappa^3)$, verified e.g. using Taylor polynomials, assuming that q_0 is sufficiently regular. The term on the second line of eq. (5.47) is estimated by

$$\begin{aligned} &\kappa |g_0(q_0(\tau^{n-1}) + \tfrac{\kappa}{2} g_0(q_0(\tau^{n-1}))) - g_0(q_0^{n-1} + \tfrac{\kappa}{2} g_0(q_0^{n-1}))| \\ &\quad \lesssim \kappa |e^{n-1} + \tfrac{\kappa}{2} g_0(q_0(\tau^{n-1})) - \tfrac{\kappa}{2} g_0(q_0^{n-1})| \\ &\quad \lesssim \kappa |e^{n-1}| + \kappa^2 |e^{n-1}|. \end{aligned}$$

The final line of eq. (5.47) measures the inexact solution of the micro problem and is split up as

$$\begin{aligned} &\kappa |g_0(q_0^{n-1} + \tfrac{\kappa}{2} g_0(q_0^{n-1})) - \tilde{g}_0^{(2)}(q_0^{n-1} + \tfrac{\kappa}{2}\tilde{g}_0^{(1)}(q_0^{n-1}))| \\ &\quad \leq \kappa |g_0(q_0^{n-1} + \tfrac{\kappa}{2} g_0(q_0^{n-1})) - g_0(q_0^{n-1} + \tfrac{\kappa}{2}\tilde{g}_0^{(1)}(q_0^{n-1}))| \\ &\qquad + \kappa |g_0(q_0^{n-1} + \tfrac{\kappa}{2}\tilde{g}_0^{(1)}(q_0^{n-1})) - \tilde{g}_0^{(2)}(q_0^{n-1} + \tfrac{\kappa}{2}\tilde{g}_0^{(1)}(q_0^{n-1}))| \\ &\quad \lesssim \kappa \|g_0 - \tilde{g}_0^{(2)}\|_{C^0(Q)} + \kappa^2 |g_0(q_0^{n-1}) - \tilde{g}_0^{(1)}(q_0^{n-1})|, \end{aligned}$$

using the Lipschitz continuity of g_0, and consequently

$$\begin{aligned} &\kappa |g_0(q_0^{n-1} + \tfrac{\kappa}{2} g_0(q_0^{n-1})) - \tilde{g}_0^{(2)}(q_0^{n-1} + \tfrac{\kappa}{2}\tilde{g}_0^{(1)}(q_0^{n-1}))| \\ &\quad \lesssim \kappa \|g_0 - \tilde{g}_0^{(2)}\|_{C^0(Q)} + \kappa^2 \|g_0 - \tilde{g}_0^{(1)}\|_{C^0(Q)}. \end{aligned}$$

Combining these estimates for eq. (5.47) leads to

$$|e^n| \lesssim (1+\kappa+\kappa^2)|e^{n-1}| + \kappa^3 + \kappa\|g_0 - \tilde{g}_0^{(2)}\|_{C^0(Q)} + \kappa^2\|g_0 - \tilde{g}_0^{(1)}\|_{C^0(Q)}$$

and Gronwall's inequality hence implies that

$$|e^n| \lesssim \kappa^2 + \kappa\|g_0 - \tilde{g}_0^{(1)}\|_{C^0(Q)} + \|g_0 - \tilde{g}_0^{(2)}\|_{C^0(Q)} \tag{5.48}$$

with constant depending on the solution, properties of g_0 and the slow time $\mathcal{T}$. Inequality (5.48) shows that the (micro) error in the evaluation of $\tilde{g}_0^{(2)}$ must be of order $\mathcal{O}(\kappa^2)$, while the evaluation of $\tilde{g}_0^{(1)}$ must be only of order $\mathcal{O}(\kappa)$ for an overall balance of errors.

Micro Scale Error

To complete the estimate of e^n from ineq. (5.48) we must bound $\|g_0 - \tilde{g}_0^{(i)}\|_{C^0(Q)}$ for $i \in \{1,2\}$. By definition of g_0 from eq. (5.43b) and for the specific form of $\tilde{g}_0^{(i)}$ from eq. (5.45b) we can rewrite both functions using g from the fast-slow system, given by

$$g(\hat{q}, v) := \gamma(1-\hat{q}) \int_{\Gamma_{\hat{q}}} \left(1 + \frac{|\sigma_{\mathrm{WS}}(v)|}{\sigma_{\mathrm{WS}}^0}\right)^{-1} \mathrm{d}o.$$

for sufficiently regular velocity field $v\colon \hat{\Omega}_q \to \mathbb{R}^d$ with associated wall shear stress $\sigma_{\mathrm{WS}}(v)$. The micro discretization error can then be expressed as

$$g_0(\hat{q}) - \tilde{g}_0^{(i)}(\hat{q}) = \int_0^1 g(\hat{q}, v_\pi(s;\hat{q}))\,\mathrm{d}s - \sum_{m=1}^{M} k g(\hat{q}, \tfrac{1}{2}(\tilde{v}_\pi^m(\hat{q}) + \tilde{v}_\pi^{m-1}(\hat{q}))).$$

We split this expression into integration error, discretization error and periodicity error:

$$\begin{aligned} &|g_0(\hat{q}) - \tilde{g}_0^{(i)}(\hat{q})| \\ &\quad\le \Big| \int_0^1 g(\hat{q}, v_\pi(s;\hat{q}))\,\mathrm{d}s - \sum_{m=1}^{M} k g(\hat{q}, \tfrac{1}{2}(v_\pi(s^m;\hat{q}) + v_\pi(s^{m-1};\hat{q})))\Big| \\ &\qquad + \sum_{m=1}^{M} k\big|g(\hat{q}, \tfrac{1}{2}(v_\pi(s^m;\hat{q}) + v_\pi(s^{m-1};\hat{q}))) - g(\hat{q}, \tfrac{1}{2}(v_\pi^m(\hat{q}) + v_\pi^{m-1}(\hat{q})))\big| \\ &\qquad + \sum_{m=1}^{M} k\big|g(\hat{q}, \tfrac{1}{2}(v_\pi^m(\hat{q}) + v_\pi^{m-1}(\hat{q}))) - g(\hat{q}, \tfrac{1}{2}(\tilde{v}_\pi^m(\hat{q}) + \tilde{v}_\pi^{m-1}(\hat{q})))\big|. \end{aligned} \tag{5.49}$$

The second line of ineq. (5.49) describes the error for the midpoint integration rule, which is of second order. Thus for sufficiently regular $v_\pi(\cdot;\hat{q})$ there holds

$$\Big| \int_0^1 g(\hat{q}, v_\pi(s;\hat{q}))\,\mathrm{d}s - \sum_{m=1}^{M} k g(\hat{q}, \tfrac{1}{2}(v_\pi(s^m;\hat{q}) + v_\pi(s^{m-1};\hat{q})))\Big| \lesssim k^2.$$

The third line of ineq. (5.49) is, by Lipschitz continuity of g and the H^2-dependence on the velocity, estimated by

$$\begin{aligned}\sum_{m=1}^{M} k|g(\hat{q}, \tfrac{1}{2}(v_\pi(s^m;\hat{q}) + v_\pi(s^{m-1};\hat{q}))) - g(\hat{q}, \tfrac{1}{2}(v_\pi^m(\hat{q}) + v_\pi^{m-1}(\hat{q})))| \\ \lesssim \sum_{m=1}^{M} k\|\tfrac{1}{2}(w_\pi^m(\hat{q}) + w_\pi^{m-1}(\hat{q}))\|_{H^2(\Omega_{\hat{q}})}\end{aligned}$$

where we write $w_\pi^m(\hat{q}) := v_\pi(s^m;\hat{q}) - v_\pi^m(\hat{q})$ for the error between continuous and time-discrete periodic solutions. Before investigating this velocity error, we estimate the last line of ineq. (5.49) using our periodicity tolerance condition from ineq. (5.46), which yields

$$\begin{aligned}&\sum_{m=1}^{M} k|g(\hat{q}, \tfrac{1}{2}(v_\pi^m(\hat{q}) + v_\pi^{m-1}(\hat{q}))) - g(\hat{q}, \tfrac{1}{2}(\tilde{v}_\pi^m(\hat{q}) + \tilde{v}_\pi^{m-1}(\hat{q})))| \\ &\quad\lesssim \sum_{m=1}^{M} k\left(\|v_\pi^m(\hat{q}) - \tilde{v}_\pi^m(\hat{q})\|_{H^2(\Omega_{\hat{q}})} + \|v_\pi^{m-1}(\hat{q}) - \tilde{v}_\pi^{m-1}(\hat{q})\|_{H^2(\Omega_{\hat{q}})}\right) \\ &\quad\lesssim TOL.\end{aligned}$$

Combining these estimates for the right-hand side of ineq. (5.49) we get

$$|g_0(\hat{q}) - \tilde{g}_0^{(i)}(\hat{q})| \lesssim k^2 + TOL + \sum_{m=1}^{M} k\|\tfrac{1}{2}(w_\pi^m(\hat{q}) + w_\pi^{m-1}(\hat{q}))\|_{H^2(\Omega_{\hat{q}})}. \tag{5.50}$$

The final part of the error analysis will be the estimate for the velocity error $w_\pi^m(\hat{q})$. Subtracting eq. (5.44) from eq. (5.42) we arrive at the error equation

$$\left.\begin{aligned} w_\pi^m(\hat{q}) - w_\pi^{m-1}(\hat{q}) - \tfrac{k}{2}P\Delta(w_\pi^m(\hat{q}) + w_\pi^{m-1}(\hat{q})) &= r^m(\hat{q}), \\ \operatorname{div} w_\pi^m(\hat{q}) &= 0, \end{aligned}\right\} \quad \text{in } \Omega_{\hat{q}}$$

for $m = 1, \ldots, M$ with residual

$$r^m(\hat{q}) := \int_{s^{m-1}}^{s^m} \partial_s v_\pi(s;\hat{q})\,\mathrm{d}s - \tfrac{k}{2}(\partial_s v_\pi(s^m;\hat{q}) + \partial_s v_\pi(s^{m-1};\hat{q})).$$

The error is 1-periodic, $w_\pi^0(\hat{q}) = w_\pi^M(\hat{q})$, and $w_\pi^m = 0$ on $\partial\Omega_{\hat{q}}$.

Testing the momentum equation with $-P\Delta\frac{1}{2}(w_\pi^m(\hat{q}) + w_\pi^{m-1}(\hat{q}))$ and integrating in space yields, with some standard estimates, that

$$\begin{aligned}&\|w_\pi^m(\hat{q})\|_{H^1(\Omega_{\hat{q}})}^2 - \|w_\pi^{m-1}(q)\|_{H^1(\Omega_{\hat{q}})}^2 + k\|P\Delta\tfrac{1}{2}(w_\pi^m(\hat{q}) + w_\pi^{m-1}(\hat{q}))\|_{L^2(\Omega_{\hat{q}})}^2 \\ &\quad\lesssim k^4\|\partial_{tt}v_\pi\|_{L^2(s^{m-1},s^m;L^2(\Omega_{\hat{q}}))}^2\end{aligned}$$

using that the residual corresponds to the local error for the trapezoidal integration scheme. Summing over $m = 1, \ldots, M$, the estimate $\|\cdot\|_{H^2(\Omega_{\hat{q}})} \lesssim \|P\Delta\cdot\|_{L^2(\Omega_{\hat{q}})}$ under our domain regularity assumptions and the periodicity of $w_\pi^m(\hat{q})$ yields that

$$\sum_{m=1}^{M} k\|\tfrac{1}{2}(w_\pi^m(\hat{q}) + w_\pi^{m-1}(\hat{q}))\|_{H^2(\Omega_{\hat{q}})}^2 \lesssim k^4. \tag{5.51}$$

Just as in the continuous theory a temporal L^∞ estimate is not directly available with periodic boundary conditions in time. This finishes the estimate for the micro error since

$$\sum_{m=1}^{M} k\|\tfrac{1}{2}(w_\pi^m(\hat{q}) + w_\pi^{m-1}(\hat{q}))\|_{H^2(\Omega_{\hat{q}})} \leq \left(\sum_{m=1}^{M} k\|\tfrac{1}{2}(w_\pi^m(\hat{q}) + w_\pi^{m-1}(\hat{q})\|^2_{H^2(\Omega_{\hat{q}})}\right)^{\frac{1}{2}}$$

and thus we can conclude in eq. (5.50) that

$$|g_0(\hat{q}) - \tilde{g}_0^{(i)}(\hat{q})| \lesssim k^2 + TOL. \tag{5.52}$$

The error estimate from ineq. (5.51) as a time-discrete L^2 integral of averages is somewhat natural for the Crank–Nicolson scheme, see [SR20]. The discretization of g_0 from eq. (5.7) was chosen for this analysis since it naturally leads to such averages in the velocity error. We briefly discuss the estimates for the discretization scheme of g_0 from eq. (5.6), which is used in the computations, for the remainder of this section. Such discretization leads to the micro error estimate

$$|g_0(\hat{q}) - \tilde{g}_0^{(i)}(\hat{q})| \lesssim k^2 + TOL + \sum_{m=1}^{M} k\|w_\pi^m(\hat{q})\|_{H^2(\Omega_{\hat{q}})}$$

and a velocity error estimate in this form is not readily available for the Crank–Nicolson scheme. One strategy to derive such a result is using a time-discrete version of the (temporal) Poincaré inequality

$$\|v_\pi(\hat{q}) - \overline{v}_\pi(\hat{q})\|_{L^2(0,1;H^2(\Omega_{\hat{q}}))} \lesssim \|\partial_s v_\pi(\hat{q})\|_{L^2(0,1;H^2(\Omega_{\hat{q}}))}$$

where $\overline{v}_\pi(\hat{q})$ is the temporal average of the periodic solution $v_\pi(\cdot;\hat{q})$. By testing the error momentum equation by $\frac{1}{k}(w_\pi^m(\hat{q}) - w_\pi^{m-1}(\hat{q}))$ one can derive an $\mathcal{O}(k^2)$-estimate for the discrete time-derivative. By summing the error momentum equation over $m = 1, \dots, M$ one can derive an $\mathcal{O}(k^2)$-estimate for the time-discrete average. Together with the Poincaré inequality this yields the desired estimate for the velocity error. We note that this approach requires much more regularity for the continuous solution to compensate for the mismatch between the spatial regularity of the time-derivative and the solution itself.

Overall Error Estimate

To finish the error estimate we must combine the macro error estimate from ineq. (5.48),

$$|e^n| \lesssim \kappa^2 + \kappa\|g_0 - \tilde{g}_0^{(1)}\|_{C^0(Q)} + \|g_0 - \tilde{g}_0^{(2)}\|_{C^0(Q)},$$

and the micro error estimate from ineq. (5.52),

$$|g_0(\hat{q}) - \tilde{g}_0^{(i)}(\hat{q})| \lesssim k^2 + TOL.$$

Distinguishing now between the micro parameters for the two evaluations $\tilde{g}_0^{(i)}$, $i \in \{1, 2\}$, this yields the following result.

Theorem 5.4.1. *Under suitable regularity assumptions the error between the solution q_0 of eq. (5.43) and its temporal semi-discretization q_0^n using the RK2 method on the macro scale, eq. (5.45), and the Crank–Nicolson scheme for the fluid problem on the micro scale, eq. (5.44), using in particular the approximations of g_0 from eq. (5.45b), satisfies the error estimate*

$$\max_{n=1,\dots,\mathcal{N}} |q_0(\tau^n) - q_0^n| \lesssim \kappa^2 + \kappa \left(\left(k^{(1)} \right)^2 + TOL^{(1)} \right) + \left(k^{(2)} \right)^2 + TOL^{(2)}.$$

Here $k^{(1)}$ and $k^{(2)}$ are the step sizes of the two micro discretizations corresponding to the two evaluations of the right-hand side g_0 in the RK2 scheme. Similarly, $TOL^{(1)}$ and $TOL^{(2)}$ are the assumed tolerances for the approximatively periodic solution, as specified in ineq. (5.46).

The choice of parameters for the micro discretization as

$$k^{(1)} \approx \sqrt{\kappa}, \quad TOL^{(1)} \approx \kappa, \quad k^{(2)} \approx \kappa, \quad TOL^{(2)} \approx \kappa^2, \tag{5.53}$$

to be understood asymptotically in κ, hence yields the overall balanced error

$$\max_{n=1,\dots,N} |q_0(\tau^n) - q_0^n| \lesssim \kappa^2. \tag{5.54}$$

Application to the Limit System

The computations for RK2 in the limit system presented at the beginning of this chapter were carried out with a balanced error according to Theorem 5.4.1. The balancing from eq. (5.53) is valid only asymptotically as $\kappa \to 0$ and no constants are known. For the computations presented in e.g. Figure 5.6 the following relations were employed

$$M^{(1)} = 6\lceil \kappa^{-1/2} \rceil,\ TOL^{(1)} = 10^{-2}\kappa,\ M^{(2)} = 6\lceil \kappa^{-1} \rceil,\ TOL^{(2)} = 10^{-2}\kappa^2. \tag{5.55}$$

These factors were chosen experimentally such that the solutions for the balanced parameters are of similar quality as the "RK2 (unbalanced)" solutions depicted in Figure 5.6 with $TOL^{(1)} = TOL^{(2)} = 10^{-7}$ and $M^{(1)} = M^{(2)} = 40$.

The benefit of choosing a lower tolerance and larger step size for $\tilde{g}_0^{(1)}$ can be estimated using the numbers provided for the RK2 discretization of the limit system with $\kappa = 0.2$ from Figure 5.9. For this problem a total of 1602 time steps were used for the evaluation of $\tilde{g}_0^{(1)}$ and 2910 time steps for $\tilde{g}_0^{(2)}$. Assuming that $\tilde{g}_0^{(1)}$ requires as many steps as $\tilde{g}_0^{(2)}$ without adaptivity, the total number of time steps required for the limit system would increase by $\approx 29\%$ from 4512 to 5820.

Chapter 6

Multiscale Analysis of a Permeable Membrane Model

Departing from the previous three chapters we now discuss another aspect of the model by Yang et. al. from Section 2.3 by investigating the equations for monocytes in the fluid (lumen) and macrophages in the structure (wall), coupled through the permeable endothelium. These equations also feature processes on differing scales, with fast advection compared to diffusion and reaction, as visible from the magnitude of the nondimensional parameters from Table 2.4 and reflected in the scaling by ε in eqs. (6.1) below.

This chapter is organized as follows. After introduction of the problem and review of the existing literature we investigate the singular limit convergence for a series of simplified problems. Starting with a stationary equation we show qualitative convergence to the limit equation, then quantify this convergence under further assumptions on the velocity field, first in the case of non-vanishing advection velocities, then for Poiseuille-flow like fields which vanish on the boundary of the domain. These results are then carried over to the instationary case. The final part of this chapter discusses a numerical realization of the equations and the agreement between theoretical and numerical results.

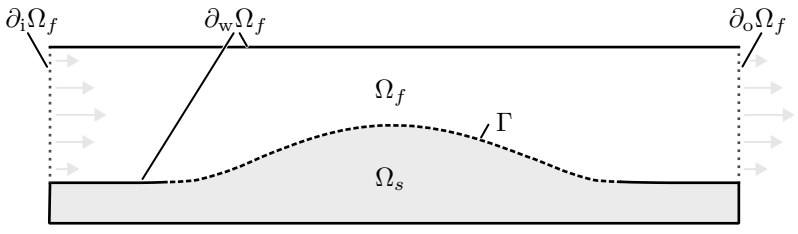

Figure 6.1: Example geometry for the concentration equations in two dimensions. The boundary of Ω_s is only divided into Γ and $\partial\Omega_s \setminus \overline{\Gamma}$. Even though $(\partial\Omega_s \setminus \overline{\Gamma}) \cap \partial_{\mathrm{w}}\Omega_f \neq \varnothing$ in this example, we use $\partial_{\mathrm{w}}\Omega_f$ only in the context of the fluid problem.

6.1 Problem Description

We begin with a description of the geometry, an example of which is sketched in Figure 6.1. We assume that Ω_f, $\Omega_s \subset \mathbb{R}^d$ with $d \in \{2, 3\}$ are disjoint domains with Lipschitz boundaries and $\partial\Omega_f \cap \partial\Omega_s \neq \varnothing$. As in Chapter 4 the fluid domain's boundary is disjointly subdivided into inflow boundary $\partial_{\mathrm{i}}\Omega_f$, outflow boundary $\partial_{\mathrm{o}}\Omega_f$, the wall $\partial_{\mathrm{w}}\Omega_f$ and the permeable interface $\Gamma \subset \partial\Omega_f \cap \partial\Omega_s$. In contrast to the previous chapters Γ is not assumed to be part of $\partial_{\mathrm{w}}\Omega_f$, leading to the decomposition

$$\partial\Omega_f = \overline{\partial_{\mathrm{i}}\Omega_f} \cup \overline{\partial_{\mathrm{w}}\Omega_f} \cup \overline{\partial_{\mathrm{o}}\Omega_f} \cup \overline{\Gamma}.$$

We assume that only $\partial_{\mathrm{w}}\Omega_f$ and Γ are on the shared boundary with Ω_s, such that $(\partial_{\mathrm{i}}\Omega_f \cup \partial_{\mathrm{o}}\Omega_f) \cap \partial\Omega_s = \varnothing$, and that Γ, $\partial_{\mathrm{i}}\Omega_f$ and $\partial_{\mathrm{o}}\Omega_f$ have non-zero Lebesgue surface measure. On the structure domain we only distinguish between the permeable interface Γ and the remainder

$$\partial\Omega_s = \overline{\Gamma} \cup (\partial\Omega_s \setminus \overline{\Gamma}).$$

Even though $\partial_{\mathrm{w}}\Omega_f \cap \partial\Omega_s$ may be non-empty we will not use $\partial_{\mathrm{w}}\Omega_f$ in the context of the structure problem.

We study the following simplified version of the non-dimensional equations from eqs. (2.21a) and (2.21b) for the monocytes $c_{\varepsilon,f}$ inside the fluid and macrophages $c_{\varepsilon,s}$ in the structure, formulated on the slow timescale. Let

$$\partial_\tau c_{\varepsilon,f} - \Delta c_{\varepsilon,f} + \tfrac{1}{\varepsilon} v_f \cdot \nabla c_{\varepsilon,f} = 0 \qquad \text{in } \mathcal{I} \times \Omega_f, \tag{6.1a}$$

$$\partial_\tau c_{\varepsilon,s} - \Delta c_{\varepsilon,s} + c_{\varepsilon,s} = 0 \qquad \text{in } \mathcal{I} \times \Omega_s, \tag{6.1b}$$

with initial values $c_{\varepsilon,f}(0) = c^0_{\varepsilon,f}$ and $c_{\varepsilon,s}(0) = c^0_{\varepsilon,s}$ whose possible dependence on ε is specified below, with exterior boundary conditions

$$c_{\varepsilon,f} = c_f^{\mathrm{in}} \quad \text{on } \mathcal{I} \times \partial_{\mathrm{i}}\Omega_f, \tag{6.1c}$$

$$\partial_{\mathfrak{n}_f} c_{\varepsilon,f} = 0 \quad \text{on } \mathcal{I} \times (\partial_{\mathrm{o}}\Omega_f \cup \partial_{\mathrm{w}}\Omega_f), \tag{6.1d}$$

$$\partial_{\mathfrak{n}_s} c_{\varepsilon,s} = 0 \quad \text{on } \mathcal{I} \times (\partial\Omega_s \setminus \overline{\Gamma}) \tag{6.1e}$$

and interface coupling conditions

$$\partial_{\mathfrak{n}_f} c_{\varepsilon,f} + \xi(c_{\varepsilon,f} - c_{\varepsilon,s}) = 0 \quad \text{on } \mathcal{I} \times \Gamma, \tag{6.1f}$$

$$\partial_{\mathfrak{n}_s} c_{\varepsilon,s} + \xi(c_{\varepsilon,s} - c_{\varepsilon,f}) = 0 \quad \text{on } \mathcal{I} \times \Gamma. \tag{6.1g}$$

We assume that $\xi \geq 0$ is a bounded, measurable permeability function on Γ with $\xi > 0$ on a set of non-zero Lebesgue surface measure. Furthermore, the transport velocity v_f inside the lumen is assumed to satisfy $\operatorname{div} v_f = 0$ in Ω_f, $v_f \cdot \mathfrak{n}_f = 0$ on $\Gamma \cup \partial_{\mathrm{w}}\Omega_f$ and $v_f \cdot \mathfrak{n}_f < 0$ on $\partial_{\mathrm{i}}\Omega_f$.

The scaling of eqs. (6.1) agrees with that of the model of Yang et. al., cf. Table 2.4, in such that diffusion, reaction and permeation are slow processes, whereas advection is fast. All ε-independent parameters were set to 1 for simplicity. In contrast to the model by Young et. al. the blood velocity in the lumen is assumed to be a given stationary field and any effects of fluid-structure interaction or growth are omitted. There is in particular no domain movement and thus no advection of macrophages inside the wall. Future research is

necessary to extend the present analysis to more accurate models, to include e.g. periodic velocities and a coupling to growth.

Equations (6.1) is a singularly perturbed system of partial differential equations, since for $\varepsilon \to 0$ the equation in the fluid domain becomes hyperbolic. The equation in the wall is regular, but coupled to the fluid equation through the interface, which makes this problem non-standard.

For fixed $\varepsilon = 1$ a linear problem similar to eqs. (6.1) was analyzed in [QVZ02b]. An analysis with nonlinear coupling conditions is discussed in [CZ06] although for the case that one domain is contained in the other. None of these models study the limit as $\varepsilon \to 0$.

There is a vast literature for singularly perturbed problems on a single domain $\Omega \subset \mathbb{R}^d$ of the form

$$\partial_\tau c_\varepsilon - \Delta c_\varepsilon + \tfrac{1}{\varepsilon} v \cdot \nabla c_\varepsilon = 0 \quad \text{in } \mathcal{I} \times \Omega$$

and its stationary variant

$$-\Delta c_\varepsilon + \tfrac{1}{\varepsilon} v \cdot \nabla c_\varepsilon = 0 \quad \text{in } \Omega$$

with corresponding boundary and initial conditions, see e.g. the monographs [Lio73; Eck79; Goe+83] for an overview. The limit behavior depends fundamentally on the velocity field v, specifically on the solution to the pure advection problem, which in the stationary case is given by

$$v \cdot \nabla c_0 = 0 \quad \text{in } \Omega.$$

We assume that the velocity field is such that monocytes are transported out of the domain in finite time. We only investigate stationary velocity fields here, where such a condition prevents flow reversal, which is an important phenomenon in atherosclerosis. Nevertheless, we consider this as an artifact of the assumption that the flow is stationary, whereas finite exit times are physiologically essential. Under the assumption of finite exit times, formulated as Assumption 6.2.8 below, [Eck79] gives integral norm estimates for the advection-diffusion problem similar to those we will employ for the permeable interface problem. [DEF74] uses a similar condition to estimate the smallest eigenvalue of the operator associated with the singularly perturbed advection-diffusion problem, although the velocity field is allowed to vanish at a point.

Since it has links to the averaging theory from the previous chapters, we briefly also discuss the setting where v is a periodic velocity field with trajectories which do not leave the domain. After a coordinate transformation along the characteristics of the unperturbed advection problem [Kro91; HKV95] could show that the solutions of such problems converge to an averaging-type limit with order $\mathcal{O}(\varepsilon)$ on a slow timescale of order $\mathcal{O}(1)$ [Kro91] or for all time [HKV95]. [Spi16] formally extends this method to more general scenarios using multiscale expansions. In [SPV09; Ded+15] similar problems to [Kro91] are investigated using Lie averaging techniques, focusing in particular on the spectral properties of the averaging limit to check for advection-enhanced dissipation, where the rate of decay of initial values is nonlinear in ε, in contrast to the linear rate of decay expected from the diffusive term alone.

6.2 Analysis of the Stationary Problem

We first examine the stationary variant of eqs. (6.1), i.e. the problem of finding $c_{\varepsilon,f}\colon \overline{\Omega}_f \to \mathbb{R}$ and $c_{\varepsilon,s}\colon \overline{\Omega}_s \to \mathbb{R}$ such that

$$-\Delta c_{\varepsilon,f} + \tfrac{1}{\varepsilon} v_f \cdot \nabla c_{\varepsilon,f} = 0 \quad \text{in } \Omega_f, \tag{6.2a}$$
$$-\Delta c_{\varepsilon,s} + c_{\varepsilon,s} = 0 \quad \text{in } \Omega_s, \tag{6.2b}$$

with exterior boundary conditions

$$c_{\varepsilon,f} = c_f^{\text{in}} \quad \text{on } \partial_{\text{i}}\Omega_f, \tag{6.2c}$$
$$\partial_{\mathfrak{n}} c_{\varepsilon,f} = 0 \quad \text{on } \partial_{\text{o}}\Omega_f \cup \partial_{\text{w}}\Omega_f, \tag{6.2d}$$
$$\partial_{\mathfrak{n}} c_{\varepsilon,s} = 0 \quad \text{on } \partial\Omega_s \setminus \overline{\Gamma} \tag{6.2e}$$

and interface coupling conditions

$$\partial_{\mathfrak{n}_f} c_{\varepsilon,f} + \xi(c_{\varepsilon,f} - c_{\varepsilon,s}) = 0 \quad \text{on } \Gamma, \tag{6.2f}$$
$$\partial_{\mathfrak{n}_s} c_{\varepsilon,s} + \xi(c_{\varepsilon,s} - c_{\varepsilon,f}) = 0 \quad \text{on } \Gamma. \tag{6.2g}$$

where $\xi \in L^\infty(\Gamma)$ with $\xi > 0$ a.e. and $v_f \in L^\infty(\Omega_f)$ with $\operatorname{div} v_f = 0$. The regularity of c_f^{in} and further assumptions on v_f are expressed below in terms of regularity of solutions to the pure advection problem. For the weak formulation of eqs. (6.2) we define the spaces

$$\mathcal{C}_f := \{\varphi_f \in H^1(\Omega_f) \mid \varphi_f|_{\partial_{\text{i}}\Omega_f} = 0\}, \quad \bar{\mathcal{C}}_f := H^1(\Omega_f), \quad \mathcal{C}_s := H^1(\Omega_s).$$

and, reminding of the notation $(\,\cdot\,,\,\cdot\,)_i$ for the scalar product on $L^2(\Omega_i)$ for $i \in \{f, s\}$, the bilinear forms

$$a_{\varepsilon,f}(c_f, \varphi_f) := (\nabla c_f, \nabla \varphi_f)_f + \tfrac{1}{\varepsilon}(v_f \cdot \nabla c_f, \varphi_f)_f \quad \forall c_f \in \bar{\mathcal{C}}_f, \varphi_f \in \bar{\mathcal{C}}_f,$$
$$a_s(c_s, \varphi_s) := (\nabla c_s, \nabla \varphi_s)_s + (c_s, \varphi_s)_s \quad \forall c_s, \varphi_s \in \mathcal{C}_s.$$

In practise only the restriction of $a_{\varepsilon,f}$ to $\mathcal{C}_f \times \mathcal{C}_f$ will be of interest, requiring the typical reduction of the problem to homogeneous boundary values. We equip $L^2(\Gamma)$ with the ξ-weighted scalar product

$$(\,\cdot\,,\,\cdot\,)_\xi := (\xi^{\frac{1}{2}}\,\cdot\,, \xi^{\frac{1}{2}}\,\cdot\,)_\Gamma, \quad \|\,\cdot\,\|_\xi := (\,\cdot\,,\,\cdot\,)_\xi^{\frac{1}{2}}.$$

With these definitions, eqs. (6.2) can be rewritten in weak form as:

Problem 6.2.1. *Find $c_{\varepsilon,f} \in \bar{\mathcal{C}}_f$ and $c_{\varepsilon,s} \in \mathcal{C}_s$ such that*

$$a_{\varepsilon,f}(c_{\varepsilon,f}, \varphi_f) + (c_{\varepsilon,f} - c_{\varepsilon,s}, \varphi_f)_\xi = 0 \quad \forall \varphi_f \in \mathcal{C}_f, \tag{6.3a}$$
$$a_s(c_{\varepsilon,s}, \varphi_s) + (c_{\varepsilon,s} - c_{\varepsilon,f}, \varphi_s)_\xi = 0 \quad \forall \varphi_s \in \mathcal{C}_s \tag{6.3b}$$

with $c_{\varepsilon,f} = c_f^{in}$ on $\partial_i\Omega_f$.

That strong solutions to eqs. (6.2) are weak solutions in the sense of Problem 6.2.1 and vice versa (under additional regularity assumptions) can be easily seen and uses that the interface condition is satisfied due to the boundary terms occurring while partially integrating $\Delta c_{\varepsilon,f}$ on Ω_f and $\Delta c_{\varepsilon,s}$ on Ω_s.

We make the following assumption on the regularity of the pure advection problem.

Assumption 6.2.2. There is exactly one $c_{0,f} \in \bar{\mathcal{C}}_f$ such that

$$(v_f \cdot \nabla c_{0,f}, \varphi_f)_f = 0 \quad \forall \varphi_f \in L^2(\Omega_f)$$

with $c_{0,f}|_{\partial_{\mathrm{i}}\Omega_f} = c_f^{\mathrm{in}}$. ◇

The notation $c_{0,f}$ anticipates our later proof that $c_{0,f}$ is the zeroth order approximation of $c_{\varepsilon,f}$ as $\varepsilon \to 0$, see Theorem 6.2.11. Assumption 6.2.2 is restrictive in the sense that $c_{0,f} \in H^1(\Omega_f)$ requires regularity perpendicular to the advection velocity, a requirement which is not easily satisfied given that $c_{0,f}$ is determined by the value of c_f^{in} along the characteristics of v_f. This assumption is nevertheless central for the subsequent analysis, not least because a trace of $c_{0,f}$ is required for the well-posedness of the presented limit equation for $c_{\varepsilon,s}$. In the model by Yang et. al. there holds $c_f^{\mathrm{in}} \equiv 1$ and Assumption 6.2.2 is trivially satisfied with $c_{0,f} \equiv 1$. This even greater regularity of $c_{0,f}$ is exploited in some of the results below.

Existence and uniqueness of solutions for a similar, instationary model was proven in [QVZ02b], but the arguments are repeated here to show the (in-) dependence of the constants on ε.

Lemma 6.2.3. *For every $\varepsilon > 0$ Problem 6.2.1 has a unique solution with*

$$\|c_{\varepsilon,f}\|_{H^1(\Omega_f)} + \|c_{\varepsilon,s}\|_{H^1(\Omega_s)} \lesssim 1 \tag{6.4}$$

where the constant depends on the data, e.g. $\|c_{0,f}\|_{H^1(\Omega_f)}$, but not on ε.

Proof. Define the bilinear form

$$a_\varepsilon((c_f, c_s), (\varphi_f, \varphi_s)) := a_{\varepsilon,f}(c_f, \varphi_f) + a_s(c_s, \varphi_s) + (c_f - c_s, \varphi_f - \varphi_s)_\xi$$

for $c_f, \varphi_f \in \bar{\mathcal{C}}_f$ and $c_s, \varphi_s \in \mathcal{C}_s$. Then the solution of Problem 6.2.1 satisfies

$$a_\varepsilon((c_{\varepsilon,f} - c_{0,f}, c_{\varepsilon,s}), (\varphi_f, \varphi_s)) = -(\nabla c_{0,f}, \nabla \varphi_f)_f - (c_{0,f}, \varphi_f - \varphi_s)_\xi \tag{6.5}$$

for all $(\varphi_f, \varphi_s) \in \mathcal{C}_f \times \mathcal{C}_s$. We claim that a_ε is coercive on $(\mathcal{C}_f \times \mathcal{C}_s) \times (\mathcal{C}_f \times \mathcal{C}_s)$ with constant independent of ε. This follows by $\xi > 0$ and using that

$$\begin{aligned}\int_{\Omega_f} v_f \cdot \nabla \varphi_f \varphi_f \,\mathrm{d}x &= \int_{\Omega_f} \operatorname{div}(v_f \varphi_f) \varphi_f \,\mathrm{d}x \\ &= -\int_{\Omega_f} (v_f \varphi_f) \cdot \nabla \varphi_f \,\mathrm{d}x + \int_{\partial\Omega_f} v_f \cdot \mathfrak{n}_f |\varphi_f|^2 \,\mathrm{d}o\end{aligned}$$

for $\varphi_f \in \mathcal{C}_f$, which implies

$$\int_{\Omega_f} v_f \cdot \nabla \varphi_f \varphi_f \,\mathrm{d}x = \frac{1}{2} \int_{\partial\Omega_f} v_f \cdot \mathfrak{n}_f |\varphi_f|^2 \,\mathrm{d}o \geq 0$$

using for the last inequality that $v_f \cdot \mathfrak{n}_f \geq 0$ on $\partial\Omega_f \setminus \partial_{\mathrm{i}}\Omega_f$ and $\varphi_f = 0$ on $\partial_{\mathrm{i}}\Omega_f$. Since $(c_{\varepsilon,f} - c_{0,f}, c_{\varepsilon,s}) \in \mathcal{C}_f \times \mathcal{C}_s$ the existence and uniqueness of solutions to eq. (6.5), and thus to Problem 6.2.1, is guaranteed by the Riesz representation theorem. Inequality (6.4) follows by coercivity of a_ε and that the right-hand side of eq. (6.5) is independent of ε. □

Remark 6.2.4. We emphasize that the ε-independence in ineq. (6.4) depends fundamentally on Assumption 6.2.2. For an arbitrary extension of c_f^{in} in $H^1(\Omega_f)$, as typically employed for non-homogeneous boundary values, the right-hand side of eq. (6.5) in the proof of Lemma 6.2.3 would contain an advection term of order $\mathcal{O}(\varepsilon^{-1})$. ◇

In the limit, $c_{\varepsilon,f}$ and $c_{\varepsilon,s}$ will converge in some appropriate sense to solutions of (repeating the definition of $c_{0,f}$ for convenience):

Problem 6.2.5 (Stationary limit)**.** *Find $c_{0,f} \in \bar{\mathcal{C}}_f$ and $c_{0,s} \in \mathcal{C}_s$ such that*

$$\begin{aligned} (v_f \cdot \nabla c_{0,f}, \varphi_f)_f &= 0 \quad \forall \varphi_f \in L^2(\Omega_f), \\ a_s(c_{0,s}, \varphi_s) + (c_{0,s} - c_{0,f}, \varphi_s)_\xi &= 0 \quad \forall \varphi_s \in \mathcal{C}_s \end{aligned}$$

with $c_{0,f} = c_f^{in}$ on $\partial_i \Omega_f$.

Lemma 6.2.6. *The solution $c_{0,s}$ to Problem 6.2.5 exists, is unique and satisfies*

$$\|c_{0,s}\|_{H^1(\Omega_s)} \lesssim 1$$

with constant depending on the data. The existence of $c_{0,f}$ is guaranteed by Assumption 6.2.2

Proof. Moving $c_{0,f}$ in the equation for $c_{0,s}$ to the right-hand side, the left-hand side is a coercive, continuous and symmetric bilinear form, hence existence, uniqueness and the claimed estimate follows by the Riesz representation theorem. □

The estimate from ineq. (6.4) is sufficient to prove qualitative results about the convergence of $c_{\varepsilon,f}$ and $c_{\varepsilon,s}$ as $\varepsilon \to 0$ without any further assumptions.

Lemma 6.2.7. *As $\varepsilon \to 0$ there holds*

$$\begin{aligned} c_{\varepsilon,f} &\rightharpoonup c_{0,f} \quad \text{in } H^1(\Omega_f), \\ c_{\varepsilon,s} &\to c_{0,s} \quad \text{in } H^1(\Omega_s). \end{aligned}$$

Proof. The estimate from ineq. (6.4) implies that there are $c_{0,f}^* \in H^1(\Omega_f)$ and $c_{0,s}^* \in H^1(\Omega_s)$ such that for subsequences of $c_{\varepsilon,f}$ and $c_{\varepsilon,s}$ there holds

$$\begin{aligned} c_{\varepsilon,f} &\rightharpoonup c_{0,f}^* \quad \text{in } H^1(\Omega_f), \\ c_{\varepsilon,s} &\rightharpoonup c_{0,s}^* \quad \text{in } H^1(\Omega_s) \end{aligned}$$

as $\varepsilon \to 0$. We do not distinguish between sequence and subsequence in notation here. To see that $c_{0,f}^* = c_{0,f}$ we multiply eq. (6.3a) by ε and take the limit as $\varepsilon \to 0$. The claim follows for this subsequence using the weak convergence and the ε-independent bounds from Lemma 6.2.3. Due to the uniqueness of the limit the claim then follows for the whole sequence $c_{\varepsilon,f}$, an argument which is also implicitly used for $c_{\varepsilon,s}$ in the following.

In eq. (6.3b) we directly pass to the limit, establishing $c_{0,s}^* = c_{0,s}$. For strong convergence of $c_{\varepsilon,s}$ we use the standard Sobolev embedding

$$H^{\frac{1}{2}}(\Gamma) \hookrightarrow\!\!\!\!\!\rightarrow L^2(\Gamma)$$

which implies $c_{\varepsilon,f} \to c_{0,f}$ in $L^2(\Gamma)$. The error $e_{\varepsilon,s} := c_{\varepsilon,s} - c_{0,s}$ satisfies

$$a_s(e_{\varepsilon,s}, \varphi_s) + (e_{\varepsilon,s}, \varphi_s)_\xi = (c_{\varepsilon,f} - c_{0,f}, \varphi_s)_\xi$$

for $\varphi_s \in \mathcal{C}_s$ and testing with $\varphi_s = e_{\varepsilon,s}$ yields

$$\|e_{\varepsilon,s}\|_s^2 + \|\nabla e_{\varepsilon,s}\|_s^2 \lesssim \|c_{\varepsilon,f} - c_{0,f}\|_\xi \to 0 \tag{6.6}$$

which concludes the proof. □

We use the following additional assumption on the advection velocity field, following [Eck79, Chapter 6], to establish quantitative convergence results.

Assumption 6.2.8. There exists $\psi \in C^2(\overline{\Omega}_f)$ such that

$$-v_f \cdot \nabla\psi \geq \nu > 0$$

where $\nu \in \mathbb{R}$. ◇

Assumption 6.2.8 implies that any trajectory of the pure advection problem leaves Ω after finite time, in fact Assumption 6.2.8 holds if v_f has no closed curves and $v_f \neq 0$ in Ω_f [DEF74]. The required regularity of ψ can be reduced to $\psi \in W^{2,\infty}(\Omega_f)$, for which a similar characterization was proven in [AM09]. Note that the condition $\nu > 0$ cannot be satisfied if $v_f = 0$ along the boundary of the artery, preventing the application to the plaque problem. We will nevertheless treat this, simpler, case first to demonstrate the main techniques, before extending the analysis under more permissive conditions.

Example 6.2.9. In [Eck79, Chapter 6] the function $\psi(x) = \alpha \cdot x$ for $\alpha \in \mathbb{R}^d$ was investigated. In our numerical examples we consider $\Omega_f = (-\frac{L}{2}, \frac{L}{2}) \times (0, 1)$ with $L > 0$ and $v_f(x, y) = (1, 0)^\intercal$, where the assumption is satisfied for $\alpha := (-1, 0)^\intercal$ and $\nu := 1$. ◇

To handle the interface term we will employ the following interpolation-type trace estimate.

Lemma 6.2.10. *For any $c_f \in \mathcal{C}_f$ there holds*

$$\|c_f\|_{L^2(\partial\Omega_f)} \lesssim \|c_f\|_f^{\frac{1}{2}} \|\nabla c_f\|_f^{\frac{1}{2}}. \tag{6.7}$$

Proof. According to [Gri11, Lemma 1.5.1.9] there exists $\delta > 0$ and $\nu_f \in C^\infty(\overline{\Omega}_f)$ such that $\nu_f \cdot \mathfrak{n}_f \geq \delta$ on $\partial\Omega_f$, making ν_f in this sense a smooth approximation of $\mathfrak{n}_f$. Then, following the proof of Theorem 1.5.1.10 in [Gri11], there holds by Green's theorem that

$$\begin{aligned}\int_{\partial\Omega_f} c_f^2 \, \nu_f \cdot \mathfrak{n}_f \, \mathrm{d}o &= \int_{\Omega_f} \nabla(c_f^2) \cdot \nu_f \, \mathrm{d}x + \int_{\Omega_f} c_f^2 \operatorname{div}(\nu_f) \, \mathrm{d}x \\ &= 2 \int_{\Omega_f} c_f \nabla c_f \cdot \nu_f \, \mathrm{d}x + \int_{\Omega_f} c_f^2 \operatorname{div}(\nu_f) \, \mathrm{d}x\end{aligned}$$

Using $\nu_f \cdot \mathfrak{n}_f \geq \delta$, bounding the terms involving ν_f by $\|\nu_f\|_{C^1(\overline{\Omega}_f)}$ and applying Hölder's inequality, it follows that

$$\|c_f\|_{L^2(\partial\Omega_f)}^2 \lesssim \|c_f\|_f \|\nabla c_f\|_f + \|c_f\|_f^2.$$

The claimed ineq. (6.7) is then a consequence of applying Poincaré's inequality to one factor $\|c_f\|_f$ of the last term on the right. □

Theorem 6.2.11. *Let $c_{\varepsilon,f}$ and $c_{\varepsilon,s}$ solve Problem 6.2.1, $c_{0,f}$ and $c_{0,s}$ solve Problem 6.2.5. Let Assumption 6.2.8 hold. Then for ε small enough we have*

$$\|c_{\varepsilon,f} - c_{0,f}\|_f \lesssim \varepsilon^{\frac{1}{2}}, \tag{6.8a}$$
$$\|\nabla(c_{\varepsilon,f} - c_{0,f})\|_f \lesssim 1, \tag{6.8b}$$
$$\|c_{\varepsilon,s} - c_{0,s}\|_{H^1(\Omega_s)} \lesssim \varepsilon^{\frac{1}{4}}. \tag{6.8c}$$

If additionally $c_{0,f} \in H^2(\Omega_f)$ then

$$\|c_{\varepsilon,f} - c_{0,f}\|_f \lesssim \varepsilon^{\frac{3}{4}}, \tag{6.9a}$$
$$\|\nabla(c_{\varepsilon,f} - c_{0,f})\|_f \lesssim \varepsilon^{\frac{1}{4}}, \tag{6.9b}$$
$$\|c_{\varepsilon,s} - c_{0,s}\|_{H^1(\Omega_s)} \lesssim \varepsilon^{\frac{1}{2}}, \tag{6.9c}$$

i.e. the order is increased by $\frac{1}{4}$ compared to ineqs. (6.8).

Proof. Set $e_{\varepsilon,f} := c_{\varepsilon,f} - c_{0,f}$ and $e_{\varepsilon,s} := c_{\varepsilon,s} - c_{0,s}$. By stability of $c_{\varepsilon,f}$ and $c_{0,f}$ from ineq. (6.4), respectively Assumption 6.2.2, ineq. (6.8b) is trivial. Let us outline the derivation of the other estimates in ineqs. (6.8): We use Assumption 6.2.8 to establish the estimate for $\|e_{\varepsilon,f}\|_f$ and with Lemma 6.2.10 we estimate $\|e_{\varepsilon,f}\|_\xi$ in ineq. (6.6) using ineq. (6.8a) and ineq. (6.8b) to establish the bound for $e_{\varepsilon,s}$.

We modify a techniques from [Eck79, Chapter 6] to establish the estimate for $e_{\varepsilon,f}$. We have

$$a_{\varepsilon,f}(e_{\varepsilon,f}, \varphi_f) = -(\nabla c_{0,f}, \nabla\varphi_f)_f - (c_{\varepsilon,f} - c_{\varepsilon,s}, \varphi_f)_\xi \tag{6.10}$$

for $\varphi_f \in \mathcal{C}_f$. By Assumption 6.2.2 on $c_{0,f}$ and ineq. (6.4), the right-hand side is bounded:

$$-(\nabla c_{0,f}, \nabla\varphi_f)_f - (c_{\varepsilon,f} - c_{\varepsilon,s}, \varphi_f)_\xi \lesssim \|\nabla\varphi_f\|_f \tag{6.11}$$

with constant depending on the data. We choose as test function $\varphi_f := \mathrm{e}^{\psi} e_{\varepsilon,f}$. For the left-hand side of eq. (6.10) we must estimate $a_{\varepsilon,f}(e_{\varepsilon,f}, \varphi_f)$ from below. For the Laplace term there holds

$$(\nabla e_{\varepsilon,f}, \nabla(\mathrm{e}^{\psi} e_{\varepsilon,f}))_f = (\nabla e_{\varepsilon,f}, \mathrm{e}^{\psi}\nabla e_{\varepsilon,f})_f + (\nabla e_{\varepsilon,f}, (\nabla \mathrm{e}^{\psi}) e_{\varepsilon,f})_f$$

and for the second term, partial integration yields

$$2(\nabla e_{\varepsilon,f}, (\nabla \mathrm{e}^{\psi}) e_{\varepsilon,f})_f = -(e_{\varepsilon,f}, (\Delta \mathrm{e}^{\psi}) e_{\varepsilon,f})_f + \int_{\partial\Omega_f} \nabla \mathrm{e}^{\psi} \cdot \mathfrak{n}_f |e_{\varepsilon,f}|^2 \,\mathrm{d}o.$$

Writing min for $\min_{x\in\overline{\Omega}_f}$ and max for $\max_{x\in\overline{\Omega}_f}$, this implies

$$\begin{aligned}(\nabla e_{\varepsilon,f}, \nabla(\mathrm{e}^{\psi} e_{\varepsilon,f}))_f \geq \min \mathrm{e}^{\psi} \|\nabla e_{\varepsilon,f}\|_f^2 - \tfrac{1}{2} \max |\Delta \mathrm{e}^{\psi}| \|e_{\varepsilon,f}\|_f^2 \\ + \tfrac{1}{2} \int_{\partial\Omega_f} \nabla \mathrm{e}^{\psi} \cdot \mathfrak{n}_f |e_{\varepsilon,f}|^2 \,\mathrm{d}o.\end{aligned} \tag{6.12}$$

The boundary term needs special care, since the sign of $\nabla \mathrm{e}^{\psi} \cdot \mathfrak{n}_f$ can be negative on $\partial\Omega_f \setminus \partial_{\mathrm{i}}\Omega_f$, in contrast to the similar integral with $v_f \cdot \mathfrak{n}_f$ which occurred in the proof of Lemma 6.2.3. Let us assume that this situation occurs, i.e.

$$\operatorname*{ess\,inf}_{\partial\Omega_f \setminus \partial_{\mathrm{i}}\Omega_f} \nabla \mathrm{e}^{\psi} \cdot \mathfrak{n}_f < 0,$$

otherwise we directly estimate this term in ineq. (6.12). Using $|\mathfrak{n}_f| = 1$ we get

$$\begin{aligned}\frac{1}{2}\int_{\partial\Omega_f} \nabla \mathrm{e}^{\psi} \cdot \mathfrak{n}_f |e_{\varepsilon,f}|^2 \,\mathrm{d}o &\geq -\tfrac{1}{2}\max|\nabla \mathrm{e}^{\psi}| \int_{\partial\Omega_f} |e_{\varepsilon,f}|^2 \,\mathrm{d}o \\ &\geq -\tfrac{C}{2}\max|\nabla \mathrm{e}^{\psi}| \|\nabla e_{\varepsilon,f}\|_f^2\end{aligned}$$

where $C > 0$ is independent of ψ. Employing this in ineq. (6.12), we conclude

$$\begin{aligned}(\nabla e_{\varepsilon,f}, \nabla(\mathrm{e}^{\psi} e_{\varepsilon,f}))_f \geq \big(\min \mathrm{e}^{\psi} - \tfrac{C}{2}\max|\nabla \mathrm{e}^{\psi}|\big) \|\nabla e_{\varepsilon,f}\|_f^2 \\ - \tfrac{1}{2}\max|\Delta \mathrm{e}^{\psi}| \|e_{\varepsilon,f}\|_f^2.\end{aligned}$$

If we rescale $\psi \mapsto \psi_0^{-1}\psi$ with some scalar $\psi_0 > 0$, we see that the validity of Assumption 6.2.8 is unaffected apart from the value of ν. Since

$$\min \mathrm{e}^{\psi_0 \psi} - \tfrac{C}{2}\psi_0 \max|\nabla \psi \mathrm{e}^{\psi_0 \psi}| \to 1 \quad \text{for } \psi_0 \to 0$$

we may assume that, after rescaling, ψ is such that there holds

$$(\nabla e_{\varepsilon,f}, \nabla(\mathrm{e}^{\psi} e_{\varepsilon,f}))_f \geq \tfrac{1}{2}\|\nabla e_{\varepsilon,f}\|_f^2 - \tfrac{1}{2}\max|\Delta \mathrm{e}^{\psi}| \|e_{\varepsilon,f}\|_f^2. \tag{6.13}$$

For the transport term in $a_{\varepsilon,f}$ we have by a similar partial integration argument that the boundary integral vanishes by our assumptions on v_f

$$\begin{aligned}2(v_f \cdot \nabla e_{\varepsilon,f}, \mathrm{e}^{\psi} e_{\varepsilon,f})_f &= -(e_{\varepsilon,f}, v_f \cdot \nabla \psi \, \mathrm{e}^{\psi} e_{\varepsilon,f})_f + \int_{\partial\Omega_f} v_f \cdot \mathfrak{n}_f \, \mathrm{e}^{\psi} |e_{\varepsilon,f}|^2 \,\mathrm{d}o \\ &\geq -(e_{\varepsilon,f}, v_f \cdot \nabla \psi \, \mathrm{e}^{\psi} e_{\varepsilon,f})_f \geq \nu \min \mathrm{e}^{\psi} \|e_{\varepsilon,f}\|_f^2 \end{aligned} \tag{6.14}$$

using Assumption 6.2.8. Combining this estimate with ineq. (6.13), we get

$$a_{\varepsilon,f}(e_{\varepsilon,f}, \mathrm{e}^{\psi} e_{\varepsilon,f}) \geq \tfrac{1}{2}\|\nabla e_{\varepsilon,f}\|_f^2 + (\tfrac{\nu}{2\varepsilon}\min \mathrm{e}^{\psi} - \tfrac{1}{2}\max|\Delta \mathrm{e}^{\psi}|)\|e_{\varepsilon,f}\|_f^2. \tag{6.15}$$

Applying ineqs. (6.11) and (6.15) to eq. (6.10) we conclude

$$\|\nabla e_{\varepsilon,f}\|_f^2 + (\tfrac{1}{\varepsilon} - C_0)\|e_{\varepsilon,f}\|_f^2 \lesssim \|\nabla(\mathrm{e}^{\psi} e_{\varepsilon,f})\|_f^2 \tag{6.16}$$

with $C_0 > 0$ independent of ε. For ε small enough, $\frac{1}{\varepsilon} - C_0 \geq \frac{1}{2\varepsilon}$. Using the stability of $e_{\varepsilon,f}$ and similar estimates as before imply $\|\nabla(\mathrm{e}^{\psi} e_{\varepsilon,f})\|_f^2 \lesssim 1$ and hence ineq. (6.8a) follows from ineq. (6.16). For the structure error, ineq. (6.8c), the arguments leading to ineq. (6.6) in the proof of Lemma 6.2.7 imply

$$\|e_{\varepsilon,s}\|_{H^1(\Omega_s)} \lesssim \|e_{\varepsilon,f}\|_{L^2(\Gamma)}.$$

Using the interpolation-type trace ineq. (6.7) from Lemma 6.2.10 we can conclude ineq. (6.8c), since

$$\|e_{\varepsilon,s}\|_{H^1(\Omega_s)} \lesssim \|e_{\varepsilon,f}\|_f^{\frac{1}{2}} \|\nabla e_{\varepsilon,f}\|_f^{\frac{1}{2}} \lesssim \varepsilon^{\frac{1}{4}} \tag{6.17}$$

as $\|e_{\varepsilon,f}\|_f \lesssim \varepsilon^{\frac{1}{2}}$ and $\|\nabla e_{\varepsilon,f}\|_f \lesssim 1$. This finishes the proof if $c_{0,f} \in H^1(\Omega_f)$.

If additionally $c_{0,f} \in H^2(\Omega_f)$ we proceed as above and mainly improve the estimate of the right-hand side of eq. (6.10). For the first term on the right of eq. (6.10) we have

$$\begin{aligned}-(\nabla c_{0,f}, \nabla \varphi_f)_f &= (\Delta c_{0,f}, \varphi_f)_f - (\nabla c_{0,f} \cdot \mathfrak{n}, \varphi_f)_{\partial\Omega_f \setminus \partial_{\mathrm{i}}\Omega_f} \\ &\lesssim \|c_{0,f}\|_{H^2(\Omega_f)} (\|\varphi_f\|_f + \|\varphi_f\|_{L^2(\partial\Omega_f \setminus \partial_{\mathrm{i}}\Omega_f)}).\end{aligned}$$

Estimating the second term on the right of eq. (6.10) as

$$-(c_{\varepsilon,f} - c_{\varepsilon,s}, \varphi_f)_\xi \lesssim \|\xi\|_{L^\infty(\Gamma)}(\|c_{\varepsilon,f}\|_{H^1(\Omega_f)} + \|c_{\varepsilon,s}\|_{H^1(\Omega_s)})\|\varphi_f\|_{L^2(\Gamma)}$$

we can hence conclude, using stability of $c_{\varepsilon,f}$ and $c_{\varepsilon,s}$, and moving estimates for the data into the constant, that

$$-(\nabla c_{0,f}, \nabla\varphi_f)_f - (c_{\varepsilon,f} - c_{\varepsilon,s}, \varphi_f)_\xi \lesssim \|\varphi_f\|_f + \|\varphi_f\|_{L^2(\partial\Omega_f\setminus\partial_{\mathrm{i}}\Omega_f)}.$$

With $\varphi_f = \mathrm{e}^{\psi} e_{\varepsilon,f}$, as above, this leads to

$$-(\nabla c_{0,f}, \nabla\varphi_f)_f - (c_{\varepsilon,f} - c_{\varepsilon,s}, \varphi_f)_\xi \lesssim \|e_{\varepsilon,f}\|_f + \|e_{\varepsilon,f}\|_{L^2(\partial\Omega_f\setminus\partial_{\mathrm{i}}\Omega_f)}. \tag{6.18}$$

Using the coercivity bound for $a_{\varepsilon,f}$ from ineq. (6.15) we can hence conclude from eq. (6.10), using arguments as in the derivation of ineq. (6.16), that

$$\|\nabla e_{\varepsilon,f}\|_f^2 + \tfrac{1}{\varepsilon}\|e_{\varepsilon,f}\|_f^2 \lesssim \|e_{\varepsilon,f}\|_f + \|e_{\varepsilon,f}\|_{L^2(\partial\Omega_f\setminus\partial_{\mathrm{i}}\Omega_f)}. \tag{6.19}$$

For the second term on the right of ineq. (6.19) we use the trace ineq. (6.7) as in the $e_{\varepsilon,s}$-estimate so that there holds

$$\|e_{\varepsilon,f}\|_{L^2(\partial\Omega_f\setminus\partial_{\mathrm{i}}\Omega_f)} \lesssim \|e_{\varepsilon,f}\|_f^{\frac{1}{2}}\|\nabla e_{\varepsilon,f}\|_f^{\frac{1}{2}}.$$

Inserting this estimate into ineq. (6.19) and rewriting the terms in preparation for the next step, we conclude

$$\|\nabla e_{\varepsilon,f}\|_f^2 + \tfrac{1}{\varepsilon}\|e_{\varepsilon,f}\|_f^2 \leq (C\varepsilon^{\frac{1}{2}})(\tfrac{1}{\varepsilon}\|e_{\varepsilon,f}\|_f^2)^{\frac{1}{2}} + (C\varepsilon^{\frac{1}{4}})(\tfrac{1}{\varepsilon}\|e_{\varepsilon,f}\|_f^2)^{\frac{1}{4}}(\|\nabla e_{\varepsilon,f}\|_f^2)^{\frac{1}{4}}.$$

Using the suggestive grouping of the terms on the right, we apply Young's inequality with $\frac{1}{2}+\frac{1}{2}=1$ for the first summand and with $\frac{1}{2}+\frac{1}{4}+\frac{1}{4}=1$ for the second summand, rescaling such that

$$\|\nabla e_{\varepsilon,f}\|_f^2 + \tfrac{1}{\varepsilon}\|e_{\varepsilon,f}\|_f^2 \leq C\varepsilon + \tfrac{1}{4\varepsilon}\|e_{\varepsilon,f}\|_f^2 + C\varepsilon^{\frac{1}{2}} + \tfrac{1}{4\varepsilon}\|e_{\varepsilon,f}\|_f^2 + \tfrac{1}{2}\|\nabla e_{\varepsilon,f}\|_f^2 \tag{6.20}$$

which implies ineq. (6.9a) and ineq. (6.9b) since

$$\|\nabla e_{\varepsilon,f}\|_f^2 + \tfrac{1}{\varepsilon}\|e_{\varepsilon,f}\|_f^2 \lesssim \varepsilon + \varepsilon^{\frac{1}{2}} \lesssim \varepsilon^{\frac{1}{2}}.$$

For ineq. (6.9c) we proceed as in the derivation of ineq. (6.17) in the low regularity case. With our improved estimates for $e_{\varepsilon,f}$ this yields ineq. (6.9c) since

$$\|e_{\varepsilon,s}\|_{H^1(\Omega_s)} \lesssim \|e_{\varepsilon,f}\|_f^{\frac{1}{2}}\|\nabla e_{\varepsilon,f}\|_f^{\frac{1}{2}} \lesssim \varepsilon^{\frac{1}{2}(\frac{3}{4}+\frac{1}{4})} = \varepsilon^{\frac{1}{2}}. \qquad \square$$

We now investigate the case $-v_f\cdot\nabla\psi \geq \nu \geq 0$ with some function ν being zero in a small set. To outline the arguments: Proceeding as in Theorem 6.2.11 one gets $\|e_{\varepsilon,f}\|_{f,\nu}^2 \lesssim \varepsilon$ where $\|\cdot\|_{f,\nu}$ is the ν-weighted $L^2(\Omega_f)$-norm. Assuming that $\{\nu = 0\}$ is small and ν well-behaved in a neighborhood, we can recover estimates without weight but with worse rate of convergence.

Assumption 6.2.12. Let ψ be of the regularity as in Assumption 6.2.8 with

$$-v_f\cdot\nabla\psi \geq \nu \geq 0$$

but now $\nu \in C(\overline{\Omega}_f)$ is allowed to be zero at some points in $\overline{\Omega}_f$. Assume that for any $0 < \delta < \delta_0$ there are subdomains $\Omega_f^\delta \subset \Omega_f$ such that for any $0 < \mu < 1$ there holds for all $f \in H^1(\Omega_f)$

$$\|f\|^2_{L^2(\Omega_f \setminus \Omega_f^\delta)} \leq \mu \|f\|^2_{L^2(\Omega_f)} + C(\mu)\delta^2 \|f\|^2_{H^1(\Omega_f)} \tag{6.21}$$

with constant $C(\mu) > 0$ depending on μ but not on δ. Furthermore,

$$\nu_0(\delta) := \operatorname*{ess\,inf}_{x \in \Omega_f^\delta} \nu(x)$$

is assumed to satisfy for some $\kappa \in \mathbb{N}$ the estimate

$$\frac{\delta^\kappa}{\nu_0(\delta)} \lesssim 1 \tag{6.22}$$

with constant independent of δ. ◇

One can think of Ω_f^δ as a "nice" subset of Ω_f with distance δ from $\{\nu = 0\}$. The constant κ measures the order at which ν vanishes as $\delta \to 0$. To construct Ω_f^δ with the property from ineq. (6.21) the following lemma can be used.

Lemma 6.2.13. *Let ψ and ν be as in Assumption 6.2.12. Furthermore, assume*

$$N := \{x \in \overline{\Omega}_f \mid \nu(x) = 0\} \subset \partial\Omega_f$$

and $N \neq \varnothing$. If there is $\delta_0 > 0$ such that

$$\Lambda \colon N \times [0, \delta_0) \to \overline{\Omega}_f, \quad (x_N, d) \mapsto x_N - d\mathfrak{n}_f(x_N)$$

is a C^1-diffeomorphism onto its image, we can choose

$$\Omega_f^\delta := \Omega_f \setminus \Lambda(N \times [0, \delta))$$

with $0 < \delta < \delta_0$ for the sets in Assumption 6.2.12 such that ineq. (6.21) is satisfied.

Proof. Let $f \in H^1(\Omega_f)$. Transformation into normal coordinates by Λ yields

$$\begin{aligned}
\int_{\Omega_f \setminus \Omega_f^\delta} |f|^2 \,\mathrm{d}x &= \int_N \int_0^\delta |f(x_N - \mathfrak{n}_f(x_N)r)|^2 |\det \nabla \Lambda(x_N, r)| \,\mathrm{d}r \,\mathrm{d}x_N \\
&\lesssim \int_N \int_0^\delta \left(|f(x_N)| + \int_0^r |\nabla f(x_N - s\mathfrak{n}_f(x_N))\mathfrak{n}_f(x_N)| \,\mathrm{d}s \right)^2 \mathrm{d}r \,\mathrm{d}x_N \\
&\lesssim \delta \int_N |f(x_N)|^2 \,\mathrm{d}x_N + \delta^2 \int_N \int_0^\delta |\nabla f(x_N - r\mathfrak{n}_f(x_N))|^2 \,\mathrm{d}r \,\mathrm{d}x_N \\
&\lesssim \delta \|f\|^2_{L^2(N)} + \delta^2 \|\nabla f\|^2_{L^2(\Omega_f \setminus \Omega_f^\delta)}
\end{aligned}$$

with constants independent of δ. Proceeding as in the proof of ineq. (6.7) from Lemma 6.2.10 we get

$$\|f\|^2_{L^2(N)} \leq \|f\|_{L^2(\partial\Omega_f)} \lesssim \|f\|^{\frac{1}{2}}_f \|f\|^{\frac{1}{2}}_{H^1(\Omega_f)}.$$

We can hence conclude that ineq. (6.21) holds since

$$\begin{aligned}\|f\|^2_{L^2(\Omega_f\setminus\Omega_f^\delta)} &\lesssim \|f\|_f(\delta^2\|f\|^2_{H^1(\Omega_f)})^{\frac{1}{2}} + \delta^2\|f\|^2_{H^1(\Omega_f)}\\ &\leq \mu\|f\|^2_f + C(\mu)\delta^2\|f\|^2_{H^1(\Omega_f)}\end{aligned}$$

with $C(\mu) > 0$ independent of δ. □

Example 6.2.14. In $\Omega_f := (-\frac{L}{2}, \frac{L}{2})\times(0,1)$ with $L > 0$ consider the Poiseuille-type flow

$$v(x,y) = v_0(y^\mu(1-y)^\mu, 0)^\intercal$$

for $v_0 > 0$ and $\mu \in \mathbb{N}$. Then Assumption 6.2.12 is satisfied with

$$\psi(x) = (-1,0)^\intercal \cdot x$$

and $\kappa = \mu$, supporting the interpretation that κ measures the rate at which the flow vanishes. ◇

Proof. The conditions of Lemma 6.2.13 are satisfied with

$$\nu(x,y) = v_0 y^\mu(1-y)^\mu \geq 0.$$

There holds $N = (0,L)\times\{0,1\}$ and Λ is a diffeomorphism for $0 < \delta_0 \leq \frac{1}{2}$, with

$$\Omega_f^\delta = (0,L)\times(\delta, 1-\delta).$$

Finally

$$\nu_0(\delta) = \operatorname*{ess\,inf}_{(x,y)\in\Omega_f^\delta} \nu(x) = v_0 \operatorname*{ess\,inf}_{y\in(\delta,1-\delta)} y^\mu(1-y)^\mu = v_0\delta^\mu(1-\delta)^\mu$$

which implies that the optimal choice for κ is $\kappa = \mu$ since

$$\frac{\delta^\kappa}{\nu_0(\delta)} = \delta^{\kappa-\mu}\frac{1}{v_0(1-\delta)} \lesssim 1$$

with constant independent of δ if and only if $\kappa \geq \mu$. □

Definition 6.2.15. For ν from Assumption 6.2.12, $(\,\cdot\,,\,\cdot\,)_{f,\nu} := (\nu^{\frac{1}{2}}\,\cdot\,, \nu^{\frac{1}{2}}\,\cdot\,)_f$ defines the weighted $L^2_\nu(\Omega_f)$-space with norm $\|\,\cdot\,\|_{L^2_\nu(\Omega_f)} = \|\,\cdot\,\|_{f,\nu}$. ◇

Before proceeding to the convergence proof under Assumption 6.2.12, we investigate how a ν-weighted $L^2(\Omega_f)$ estimate and stability in $H^1(\Omega_f)$ with respect to ε yields non-weighted error estimates in $L^2(\Omega_f)$.

Lemma 6.2.16. *Let Assumption 6.2.12 be satisfied for some $\kappa \in \mathbb{N}$. Then for any $f \in H^1(\Omega_f)$ there holds*

$$\|f\|^2_f \lesssim \delta^{-\kappa}\|f\|^2_{f,\nu} + \delta^2\|f\|^2_{H^1(\Omega_f)}$$

for any $0 < \delta < \delta_0$ with constant independent of δ.

Proof. For any $0 < \delta < \delta_0$ split

$$\|f\|_f^2 = \int_{\Omega_f^\delta} |f|^2 \,\mathrm{d}x + \int_{\Omega_f \setminus \Omega_f^\delta} |f|^2 \,\mathrm{d}x. \tag{6.23}$$

For the first term we use ineq. (6.22) such that

$$\int_{\Omega_f^\delta} |f|^2 \,\mathrm{d}x \leq \frac{1}{\nu_0(\delta)} \int_{\Omega_f^\delta} \nu |f|^2 \,\mathrm{d}x \lesssim \delta^{-\kappa} \int_{\Omega_f^\delta} \nu |f|^2 \,\mathrm{d}x.$$

For the second term on the right of eq. (6.23) we use ineq. (6.21) with $\mu = \frac{1}{2}$:

$$\|f\|^2_{L^2(\Omega_f \setminus \Omega_f^\delta)} \leq \tfrac{1}{2}\|f\|_f^2 + C\delta^2 \|f\|^2_{H^1(\Omega_f)}.$$

Moving the first term on the right to the left-hand side in eq. (6.23) we conclude

$$\|f\|_f^2 \lesssim \delta^{-\kappa} \|f\|^2_{f,\nu} + \delta^2 \|f\|^2_{H^1(\Omega_f)}. \qquad \square$$

Theorem 6.2.17. *Let $c_{\varepsilon,f}$ and $c_{\varepsilon,s}$ solve Problem 6.2.1, $c_{0,f}$ and $c_{0,s}$ solve Problem 6.2.5. Let assumption Assumption 6.2.12 hold. Then for ε small enough we have*

$$\|c_{\varepsilon,f} - c_{0,f}\|_f \lesssim \varepsilon^{\frac{1}{2+\kappa}}, \tag{6.24a}$$
$$\|\nabla(c_{\varepsilon,f} - c_{0,f})\|_f \lesssim 1, \tag{6.24b}$$
$$\|c_{\varepsilon,s} - c_{0,s}\|_{H^1(\Omega_s)} \lesssim \varepsilon^{\frac{1}{4+2\kappa}} \tag{6.24c}$$

with $\kappa \in \mathbb{N}$ as given by Assumption 6.2.12. If additionally $c_{0,f} \in H^2(\Omega_f)$ then

$$\|c_{\varepsilon,f} - c_{0,f}\|_f \lesssim \varepsilon^{\frac{3}{4+2\kappa}}, \tag{6.25a}$$
$$\|\nabla(c_{\varepsilon,f} - c_{0,f})\|_f \lesssim \varepsilon^{\frac{1}{4+2\kappa}}, \tag{6.25b}$$
$$\|c_{\varepsilon,s} - c_{0,s}\|_{H^1(\Omega_s)} \lesssim \varepsilon^{\frac{1}{2+\kappa}}. \tag{6.25c}$$

Proof. Inequality (6.24b) follows from stability of $c_{\varepsilon,f}$ and $c_{0,f}$ in $H^1(\Omega_f)$. For ineq. (6.24a) we repeat the main steps of the proof of Theorem 6.2.11. Inequality (6.11) for the right-hand side of eq. (6.10) implies

$$a_{\varepsilon,f}(e_{\varepsilon,f}, \varphi_f) = -(\nabla c_{0,f}, \nabla \varphi_f)_f - (c_{\varepsilon,f} - c_{\varepsilon,s}, \varphi_f)_\xi \lesssim \|\nabla \varphi_f\|_f \tag{6.26}$$

and for $\varphi_f := \mathrm{e}^{\psi} e_{\varepsilon,f}$ there holds $\|\nabla \varphi_f\|_f \lesssim 1$. For the Laplace term in $a_{\varepsilon,f}$ the arguments leading to ineq. (6.13) can be repeated verbatim, i.e.

$$(\nabla e_{\varepsilon,f}, \nabla(\mathrm{e}^{\psi} e_{\varepsilon,f}))_f \geq \tfrac{1}{2}\|\nabla e_{\varepsilon,f}\|_f^2 - \tfrac{1}{2}\max|\Delta \mathrm{e}^{\psi}| \|e_{\varepsilon,f}\|_f^2. \tag{6.27}$$

Using the new assumptions, we can modify the arguments for the advection term from ineq. (6.14) to arrive at

$$2(v_f \cdot \nabla e_{\varepsilon,f}, \mathrm{e}^{\psi} e_{\varepsilon,f})_f \geq \min \mathrm{e}^{\psi} \|e_{\varepsilon,f}\|^2_{f,\nu}. \tag{6.28}$$

Combining ineq. (6.27) and ineq. (6.28) we have

$$a_{\varepsilon,f}(e_{\varepsilon,f}, \mathrm{e}^{\psi} e_{\varepsilon,f}) \geq \tfrac{1}{2}\|\nabla e_{\varepsilon,f}\|_f^2 - \tfrac{1}{2}\max|\Delta \mathrm{e}^{\psi}| \|e_{\varepsilon,f}\|_f^2 + \tfrac{1}{2\varepsilon}\min \mathrm{e}^{\psi} \|e_{\varepsilon,f}\|^2_{f,\nu}. \tag{6.29}$$

In the current scenario we could move the $|\Delta \mathrm{e}^{\psi}|$-term to the right-hand side of eq. (6.26). In preparation for the case $c_{0,f} \in H^2(\Omega_f)$ we instead use Lemma 6.2.16 to absorb this term into the other two terms of ineq. (6.29). By Lemma 6.2.16 there exists $C_0 > 0$ such that

$$\max |\Delta \mathrm{e}^{\psi}| \|e_{\varepsilon,f}\|_f^2 \leq C_0 \delta^{-\kappa} \|e_{\varepsilon,f}\|_{f,\nu}^2 + C_0 \delta^2 \|\nabla e_{\varepsilon,f}\|_f^2$$

holds for any $0 < \delta < \delta_0$. This implies

$$a_{\varepsilon,f}(e_{\varepsilon,f}, \mathrm{e}^{\psi} e_{\varepsilon,f}) \geq \tfrac{1}{2}(1 - C_0\delta^2)\|\nabla e_{\varepsilon,f}\|_f^2 + \tfrac{1}{2}(\tfrac{1}{\varepsilon} \min \mathrm{e}^{\psi} - C_0 \delta^{-\kappa})\|e_{\varepsilon,f}\|_{f,\nu}^2.$$

and for $\delta := (2C_0\varepsilon)^{\frac{1}{\kappa}} (\min \mathrm{e}^{\psi})^{-\frac{1}{\kappa}}$ and ε small enough such that $\delta < \delta_0$ and $C_0\delta^2 < \frac{1}{2}$ we conclude

$$a_{\varepsilon,f}(e_{\varepsilon,f}, \mathrm{e}^{\psi} e_{\varepsilon,f}) \geq \tfrac{1}{4}(\|\nabla e_{\varepsilon,f}\|_f^2 + \tfrac{1}{\varepsilon} \min \mathrm{e}^{\psi} \|e_{\varepsilon,f}\|_{f,\nu}^2). \tag{6.30}$$

Using this coercivity-type estimate in eq. (6.26) yields by $\|\nabla \varphi_f\|_f \lesssim 1$ that

$$\|\nabla e_{\varepsilon,f}\|_f^2 + \tfrac{1}{\varepsilon}\|e_{\varepsilon,f}\|_{f,\nu}^2 \lesssim \|\nabla \varphi_f\|_f \lesssim 1 \tag{6.31}$$

which implies in particular

$$\|e_{\varepsilon,f}\|_{f,\nu}^2 \lesssim \varepsilon.$$

We use Lemma 6.2.16 to pass to the non-weighted L^2-norm of $e_{\varepsilon,f}$. Combining the previous estimate with the stability of $e_{\varepsilon,f}$ in $H^1(\Omega_f)$, we get

$$\|e_{\varepsilon,f}\|_f^2 \lesssim \delta^{-\kappa}\|e_{\varepsilon,f}\|_{f,\nu}^2 + \delta^2 \|e_{\varepsilon,f}\|_{H^1(\Omega_f)}^2 \lesssim \delta^{-\kappa}\varepsilon + \delta^2$$

for arbitrary $0 < \delta < \delta_0$. With the Ansatz $\delta = \varepsilon^{\alpha}$ for $\alpha > 0$ the right-hand side is balanced if $\alpha = \frac{1}{2+\kappa}$, which yields ineq. (6.24a). Inequality (6.24c) follows as in the proof of Theorem 6.2.11.

In case of enhanced regularity, $c_{0,f} \in H^2(\Omega_f)$, we use the improved estimate from ineq. (6.18) from the proof of Theorem 6.2.11 for the right-hand side of eq. (6.26). Combined with the coercivity-type estimate from ineq. (6.30) for $a_{\varepsilon,f}$ this implies

$$\|\nabla e_{\varepsilon,f}\|_f^2 + \tfrac{1}{\varepsilon}\|e_{\varepsilon,f}\|_{f,\nu}^2 \lesssim \|e_{\varepsilon,f}\|_f + \|e_{\varepsilon,f}\|_{L^2(\partial\Omega_f \setminus \partial_{\mathrm{i}}\Omega_f)}. \tag{6.32}$$

For the first term on the right of ineq. (6.32) we have

$$\begin{aligned}
\|e_{\varepsilon,f}\|_f &\lesssim \varepsilon^{-\frac{\kappa\alpha}{2}} \|e_{\varepsilon,f}\|_{f,\nu} + \varepsilon^{\alpha} \|\nabla e_{\varepsilon,f}\|_f \\
&\lesssim \varepsilon^{\frac{1-\kappa\alpha}{2}} (\tfrac{1}{\varepsilon}\|e_{\varepsilon,f}\|_{f,\nu}^2)^{\frac{1}{2}} + \varepsilon^{\alpha}\|\nabla e_{\varepsilon,f}\|_f \\
&\leq C\varepsilon^{1-\kappa\alpha} + \tfrac{1}{4\varepsilon}\|e_{\varepsilon,f}\|_{f,\nu}^2 + C\varepsilon^{2\alpha} + \tfrac{1}{6}\|\nabla e_{\varepsilon,f}\|_f^2
\end{aligned}$$

for any $\alpha > 0$ by Lemma 6.2.16 with $\delta = \varepsilon^{\alpha}$ and Young's inequality. With the choice $\alpha = \frac{1}{2+\kappa}$ the ε-powers are balanced, implying

$$\|e_{\varepsilon,f}\|_f \leq C\varepsilon^{\frac{2}{2+\kappa}} + \tfrac{1}{4\varepsilon}\|e_{\varepsilon,f}\|_{f,\nu}^2 + \tfrac{1}{6}\|\nabla e_{\varepsilon,f}\|_f^2. \tag{6.33}$$

For the second term on the right of ineq. (6.32) we again use the interpolation-type trace estimate from ineq. (6.7). With α as above then

$$\|e_{\varepsilon,f}\|_{L^2(\partial\Omega_f \setminus \partial_{\mathrm{i}}\Omega_f)} \lesssim \|e_{\varepsilon,f}\|_f^{\frac{1}{2}} \|\nabla e_{\varepsilon,f}\|_f^{\frac{1}{2}} \lesssim \varepsilon^{\frac{\alpha}{2}} \left(\varepsilon^{-\alpha}\|e_{\varepsilon,f}\|_f\right)^{\frac{1}{2}} \|\nabla e_{\varepsilon,f}\|_f^{\frac{1}{2}}.$$

Using Young's inequality with $\frac{1}{2}+\frac{1}{4}+\frac{1}{4}=1$ we arrive at

$$\|e_{\varepsilon,f}\|_{L^2(\partial\Omega_f\setminus\partial_i\Omega_f)} \leq C\varepsilon^{\alpha} + \mu\varepsilon^{-2\alpha}\|e_{\varepsilon,f}\|_f^2 + \tfrac{1}{6}\|\nabla e_{\varepsilon,f}\|_f^2 \tag{6.34}$$

with free parameter $\mu > 0$. This parameter is chosen such that application of Lemma 6.2.16 with $\delta = \varepsilon^{\alpha}$ yields

$$\mu\|e_{\varepsilon,f}\|_f^2 \leq \varepsilon^{1-\kappa\alpha}\tfrac{1}{4\varepsilon}\|e_{\varepsilon,f}\|_{f,\nu}^2 + \varepsilon^{2\alpha}\tfrac{1}{6}\|\nabla e_{\varepsilon,f}\|_f^2.$$

Since $\alpha = \frac{1}{2+\kappa}$ the exponents for ε on the right are equal and

$$\mu\varepsilon^{-2\alpha}\|e_{\varepsilon,f}\|_f^2 \leq \tfrac{1}{4\varepsilon}\|e_{\varepsilon,f}\|_{f,\nu}^2 + \tfrac{1}{6}\|\nabla e_{\varepsilon,f}\|_f^2.$$

Inserting this estimate in ineq. (6.34) we arrive at

$$\|e_{\varepsilon,f}\|_{L^2(\partial\Omega_f\setminus\partial_i\Omega_f)} \leq C\varepsilon^{\frac{1}{2+\kappa}} + \tfrac{1}{4\varepsilon}\|e_{\varepsilon,f}\|_{f,\nu}^2 + \tfrac{1}{3}\|\nabla e_{\varepsilon,f}\|_f^2. \tag{6.35}$$

Combining ineqs. (6.33) and (6.35) in the right-hand side of ineq. (6.32) we get

$$\|\nabla e_{\varepsilon,f}\|_f^2 + \tfrac{1}{\varepsilon}\|e_{\varepsilon,f}\|_{f,\nu}^2 \leq C\varepsilon^{\frac{2}{2+\kappa}} + C\varepsilon^{\frac{1}{2+\kappa}} + \tfrac{1}{2\varepsilon}\|e_{\varepsilon,f}\|_{f,\nu}^2 + \tfrac{1}{2}\|\nabla e_{\varepsilon,f}\|_f^2$$

and hence, estimating the higher order ε term, we arrive at ineq. (6.25b), since

$$\|\nabla e_{\varepsilon,f}\|_f^2 + \tfrac{1}{\varepsilon}\|e_{\varepsilon,f}\|_{f,\nu}^2 \lesssim \varepsilon^{\frac{1}{2+\kappa}}. \tag{6.36}$$

The unweighted $L^2(\Omega_f)$ estimate from ineq. (6.25a) follows as above using Lemma 6.2.16 with $\delta = \varepsilon^{\alpha}$ for $\alpha = \frac{1}{2+\kappa}$. The final ineq. (6.25c) for $e_{\varepsilon,s}$ again follows as in the proof of Theorem 6.2.11. □

Remark 6.2.18. Setting formally $\kappa = 0$ in Theorem 6.2.17 we recover the estimates from Theorem 6.2.11. ◇

6.3 Analysis of the Instationary Problem

We now go back to the instationary problem from eqs. (6.1), but still making the simplifying assumption that v_f, ξ and c_f^{in} are independent of time. Our goal is primarily to investigate how the results from the previous section carry over, in particular the influence of the initial values on the convergence behavior. We only study quantitative convergence in this section and either make Assumption 6.2.8 or Assumption 6.2.12.

We use the notation from the stationary problem, e.g. denote the involved function spaces by $\mathcal{C}_f$, $\bar{\mathcal{C}}_f$ and $\mathcal{C}_s$, use the bilinear forms $a_{\varepsilon,f}$ and a_s and write $(\cdot,\cdot)_\xi$ for the ξ-weighted $L^2(\Gamma)$ scalar product. Furthermore, we write $\langle\cdot,\cdot\rangle_f$ and $\langle\cdot,\cdot\rangle_s$ for the dual products on $\mathcal{C}_f$, respectively $\mathcal{C}_s$. With these definitions, eqs. (6.1) can be rewritten in weak form as follows.

Problem 6.3.1. *For $\mathcal{I} = (0,\mathcal{T})$, with $\mathcal{T} > 0$ independent of ε, find $c_{\varepsilon,f} \in L^2(\mathcal{I},\bar{\mathcal{C}}_f) \cap H^1(\mathcal{I},\mathcal{C}_f^*)$ and $c_{\varepsilon,s} \in L^2(\mathcal{I},\mathcal{C}_s) \cap H^1(\mathcal{I},\mathcal{C}_s^*)$ such that*

$$\langle\partial_\tau c_{\varepsilon,f},\varphi_f\rangle_f + a_{\varepsilon,f}(c_{\varepsilon,f},\varphi_f) + (c_{\varepsilon,f}-c_{\varepsilon,s},\varphi_f)_\xi = 0 \quad \forall\varphi_f \in \mathcal{C}_f, \tag{6.37a}$$

$$\langle\partial_\tau c_{\varepsilon,s},\varphi_s\rangle_s + a_s(c_{\varepsilon,s},\varphi_s) + (c_{\varepsilon,s}-c_{\varepsilon,f},\varphi_s)_\xi = 0 \quad \forall\varphi_s \in \mathcal{C}_s \tag{6.37b}$$

holds pointwise in $\mathcal{I}$ a.e. with $c_{\varepsilon,f} = c_f^{in}$ on $\mathcal{I}\times\partial_i\Omega_f$ and initial values $c_{\varepsilon,f}(0) = c_{\varepsilon,f}^0 \in L^2(\Omega_f)$ and $c_{\varepsilon,s}(0) = c_{\varepsilon,s}^0 \in L^2(\Omega_s)$.

Just as in the stationary case we assume that $\xi \in L^\infty(\Gamma)$ and $v_f \in L^\infty(\Omega_f)$ with $\operatorname{div} v_f = 0$. We still make Assumption 6.2.2 about the existence of a $H^1(\Omega_f)$-regular, stationary solution $c_{0,f}$ to the pure advection problem.

Lemma 6.3.2. *For every $\varepsilon > 0$ Problem 6.3.1 has a unique solution. Assuming that $\|c^0_{\varepsilon,f}\|_f \lesssim 1$ and $\|c^0_{\varepsilon,s}\|_s \lesssim 1$, with constants independent of ε, there holds*

$$\|c_{\varepsilon,f}\|_{L^\infty(\mathcal{I},L^2(\Omega_f))} + \|c_{\varepsilon,f}\|_{L^2(\mathcal{I},H^1_0(\Omega_f))} \lesssim 1$$

and

$$\|c_{\varepsilon,s}\|_{L^\infty(\mathcal{I},L^2(\Omega_s))} + \|c_{\varepsilon,s}\|_{L^2(\mathcal{I},H^1(\Omega_s))} \lesssim 1$$

with constants independent of ε.

Proof. Testing eq. (6.37a) and eq. (6.37b) with $c_{\varepsilon,f}$, respectively $c_{\varepsilon,s}$, and integrating in time leads to the stability estimates (and uniqueness), using the coercivity estimates and techniques from the proof of the corresponding result from the stationary case, Lemma 6.2.3. The existence of solutions follows by standard procedures for parabolic equations by construction of approximating Galerkin sequences. □

The requirements on $c^0_{\varepsilon,f}$ and $c^0_{\varepsilon,s}$ must be strengthened for the multiscale convergence results below. We will prove below that the limit equation takes the following (weak) form.

Problem 6.3.3 (Instationary limit)**.** *Find $c_{0,f} \in \bar{\mathcal{C}}_f$ and $c_{0,s} \in L^2(\mathcal{I},\mathcal{C}_s) \cap H^1(\mathcal{I},\mathcal{C}_s^*)$ such that*

$$\begin{aligned} (v_f \cdot \nabla c_{0,f}, \varphi_f)_f &= 0 \quad \forall \varphi_f \in \mathcal{C}_f, \\ \langle \partial_\tau c_{0,s}, \varphi_s \rangle_s + a_s(c_{0,s}, \varphi_s) + (c_{0,s} - c_{0,f}, \varphi_s)_\xi &= 0 \quad \forall \varphi_s \in \mathcal{C}_s \end{aligned}$$

where the second equation holds pointwise in $\mathcal{I}$ a.e., with $c_{0,f} = c_f^{in}$ on $\partial_i\Omega_f$ and initial value $c_{0,s}(0) = c_s^0 \in L^2(\Omega_s)$.

Note that the limit equation in the fluid domain has no initial value, which will result in the occurrence of boundary layers for the fluid solution near $\tau = 0$ if the initial value $c^0_{\varepsilon,f}$ is not already close to $c_{0,f}$.

Lemma 6.3.4. *The solution $c_{0,s}$ to Problem 6.3.3 exists, is unique and satisfies*

$$\|c_{0,s}\|_{L^\infty(\mathcal{I},L^2(\Omega_s))} + \|c_{0,s}\|_{L^2(\mathcal{I},H^1(\Omega_s))} \lesssim 1$$

with constant depending on the data. The existence of $c_{0,f}$ is guaranteed by Assumption 6.2.2.

Proof. We rewrite the equation for $c_{0,s}$ as

$$\langle \partial_\tau c_{0,s}, \varphi_s \rangle_s + a_s(c_{0,s}, \varphi_s) + (c_{0,s}, \varphi_s)_\xi = (c_{0,f}, \varphi_s)_\xi.$$

Testing with $\varphi_s = c_{0,s} \in H^1(\Omega_f)$ and integrating in time, the stability estimate (and thus uniqueness) follows, using in particular the coercivity of $a_s(\cdot,\cdot)$. Existence follows from the stability estimate using standard techniques for parabolic equations through the construction of a sequence of Galerkin solutions. □

We now prove the results corresponding to Theorems 6.2.11 and 6.2.17 for the stationary problem, i.e. quantitative convergence to the limit solution where the velocity field may vanish in the sense of Assumption 6.2.12. The influence of the initial values on the quality of the approximation is the major difference to the stationary theory.

Theorem 6.3.5. *Let $\mathcal{I} = (0, \mathcal{T})$ with $\mathcal{T} > 0$ independent of ε. Let $c_{\varepsilon,f}$ and $c_{\varepsilon,s}$ solve Problem 6.3.1, $c_{0,f}$ and $c_{0,s}$ solve Problem 6.3.3. Let either Assumption 6.2.8 or Assumption 6.2.12 hold. If the initial values satisfy*

$$\|c^0_{\varepsilon,f}\|_f \lesssim 1 \quad \text{and} \quad \|c^0_{\varepsilon,s} - c^0_s\|_s \lesssim \varepsilon^{\frac{1}{4+2\kappa}} \tag{6.38}$$

then there holds for ε small enough that

$$\|c_{\varepsilon,f} - c_{0,f}\|_{L^2(\mathcal{I},L^2(\Omega_f))} \lesssim \varepsilon^{\frac{1}{2+\kappa}}, \tag{6.39a}$$

$$\|c_{\varepsilon,f} - c_{0,f}\|_{L^\infty(\mathcal{I},L^2(\Omega_f))} + \|\nabla(c_{\varepsilon,f} - c_{0,f})\|_{L^2(\mathcal{I},L^2(\Omega_f))} \lesssim 1, \tag{6.39b}$$

$$\|c_{\varepsilon,s} - c_{0,s}\|_{L^\infty(\mathcal{I},L^2(\Omega_s))} + \|c_{\varepsilon,s} - c_{0,s}\|_{L^2(\mathcal{I},H^1(\Omega_s))} \lesssim \varepsilon^{\frac{1}{4+2\kappa}} \tag{6.39c}$$

where we set $\kappa = 0$ if Assumption 6.2.8 holds. If additionally $c_{0,f} \in H^2(\Omega_f)$ and the initial value bounds are strengthened to

$$\|c^0_{\varepsilon,f}\|_f \lesssim 1 \quad \text{and} \quad \|c^0_{\varepsilon,s} - c^0_s\|_s \lesssim \varepsilon^{\frac{1}{2+\kappa}} \tag{6.40}$$

then the previous estimates can be improved to

$$\|c_{\varepsilon,f} - c_{0,f}\|_{L^2(\mathcal{I}_0,L^2(\Omega_f))} \lesssim \varepsilon^{\frac{3}{4+2\kappa}}, \tag{6.41a}$$

$$\|c_{\varepsilon,f} - c_{0,f}\|_{L^\infty(\mathcal{I}_0,L^2(\Omega_f))} + \|\nabla(c_{\varepsilon,f} - c_{0,f})\|_{L^2(\mathcal{I}_0,L^2(\Omega_f))} \lesssim \varepsilon^{\frac{1}{4+2\kappa}}, \tag{6.41b}$$

$$\|c_{\varepsilon,s} - c_{0,s}\|_{L^\infty(\mathcal{I},L^2(\Omega_s))} + \|c_{\varepsilon,s} - c_{0,s}\|_{L^2(\mathcal{I},H^1(\Omega_s))} \lesssim \varepsilon^{\frac{1}{2+\kappa}-\eta}, \tag{6.41c}$$

where $0 < \eta \ll 1$ in ineq. (6.41c) is arbitrary but influences the constant and $\mathcal{I}_0 := (\tau_0, \mathcal{T})$ excludes the boundary layer at $\tau = 0$ with τ_0 given by

$$\tau_0 = -\tfrac{1}{2\mu_0}\varepsilon^{\frac{2}{2+\kappa}}\tfrac{\ln\varepsilon}{2+\kappa}, \tag{6.42}$$

where $\mu_0 > 0$ is a constant from the proof. We clearly assume that ε is small enough such that $\tau_0 < \mathcal{T}$. If the condition on $c^0_{\varepsilon,f}$ in ineq. (6.40) is replaced by

$$\|c^0_{\varepsilon,f} - c_{0,f}\|_f \lesssim \varepsilon^{\frac{1}{4+2\kappa}} \tag{6.43}$$

we may set $\tau_0 = 0$, i.e. all estimates from ineqs. (6.41) hold on $\mathcal{I}$, and $\eta = 0$.

Remark 6.3.6. We emphasize that ineq. (6.41c) for $c_{\varepsilon,s}$ holds on the whole interval $\mathcal{I}$, whereas ineqs. (6.41a) and (6.41b) exclude the boundary layer. ◇

Remark 6.3.7. If the limit system is solved as an approximation to the ε-system for some specific $0 < \hat{\varepsilon} \ll 1$ only condition ineq. (6.40) can be satisfied in general by setting $c^0_s := c^0_{\hat{\varepsilon},s}$. Inequality (6.43) on the other hand requires the closeness of two fixed quantities, $c^0_{\hat{\varepsilon},f}$ and c^0_f. This motivates the more technical proof if only ineq. (6.40) is assumed. ◇

Proof of Theorem 6.3.5. Inequality (6.39b) follows by stability of $c_{\varepsilon,f}$ and $c_{0,f}$. We write $e_{\varepsilon,f} = c_{\varepsilon,f} - c_{0,f}$ and $e_{\varepsilon,s} = c_{\varepsilon,s} - c_{0,s}$. Then

$$\langle \partial_\tau e_{\varepsilon,f}, \varphi_f \rangle_f + a_{\varepsilon,f}(e_{\varepsilon,f}, \varphi_f) = -(c_{\varepsilon,f} - c_{\varepsilon,s}, \varphi_f)_\xi - (\nabla c_{0,f}, \nabla \varphi_f)_f \tag{6.44}$$

holds for all $\varphi_f \in \mathcal{C}_f$ in $\mathcal{I}$ almost everywhere and $e_{\varepsilon,f}(0) = c^0_{\varepsilon,f} - c_{0,f}$. We again use the trick to test with $\varphi_f = \mathrm{e}^{\psi} e_{\varepsilon,f}$. Since ψ is independent of time we have

$$\langle \partial_\tau e_{\varepsilon,f}, \mathrm{e}^{\psi} e_{\varepsilon,f} \rangle_f = \frac{1}{2} \frac{\mathrm{d}}{\mathrm{d}\tau} \int_{\Omega_f} \mathrm{e}^{\psi} |e_{\varepsilon,f}|^2 \,\mathrm{d}x.$$

For $a_{\varepsilon,f}$ we use the coercivity estimate ineq. (6.30), which is valid under both Assumption 6.2.8 and Assumption 6.2.12. This implies

$$\begin{aligned} &\frac{\mathrm{d}}{\mathrm{d}\tau} \int_{\Omega_f} \mathrm{e}^{\psi} |e_{\varepsilon,f}|^2 \,\mathrm{d}x + \|\nabla e_{\varepsilon,f}\|_f^2 + \tfrac{1}{\varepsilon} \|e_{\varepsilon,f}\|_{f,\nu}^2 \\ &\qquad \lesssim \|c_{\varepsilon,f}\|_{H^1(\Omega_f)}^2 + \|c_{\varepsilon,s}\|_{H^1(\Omega_s)}^2 + \|c_{0,f}\|_{H^1(\Omega_f)}^2. \end{aligned}$$

Integrating over $(0,\tau)$ for $\tau \in \mathcal{I}$, this implies

$$\begin{aligned} &\int_{\Omega_f} \mathrm{e}^{\psi} |e_{\varepsilon,f}(\tau)|^2 \,\mathrm{d}x + \|\nabla e_{\varepsilon,f}\|_{L^2(0,\tau;L^2(\Omega_f))}^2 + \tfrac{1}{\varepsilon} \|e_{\varepsilon,f}\|_{L^2(0,\tau;L^2_\nu(\Omega_f))}^2 \\ &\qquad \lesssim \int_{\Omega_f} \mathrm{e}^{\psi} |e_{\varepsilon,f}(0)|^2 \,\mathrm{d}x + \|c_{\varepsilon,f}\|_{L^2(0,\tau;H^1(\Omega_f))}^2 + \|c_{\varepsilon,s}\|_{L^2(0,\tau;H^1(\Omega_s))}^2 \\ &\qquad\quad + \tau \|c_{0,f}\|_{H^1(\Omega_f)}^2. \end{aligned}$$

Using that $\tau \lesssim \mathcal{T}$ with $\mathcal{T}$ independent of ε and for $\sigma \in \{0,\tau\}$ the estimates

$$\min \mathrm{e}^{\psi} \, \|e_{\varepsilon,f}(\sigma)\|_f^2 \le \int_{\Omega_f} \mathrm{e}^{\psi} |e_{\varepsilon,f}(\sigma)|^2 \,\mathrm{d}x \le \max \mathrm{e}^{\psi} \, \|e_{\varepsilon,f}(\sigma)\|_f^2$$

we arrive at

$$\begin{aligned} &\|e_{\varepsilon,f}\|_{L^\infty(\mathcal{I},L^2(\Omega_f))}^2 + \|\nabla e_{\varepsilon,f}\|_{L^2(\mathcal{I},L^2(\Omega_f))}^2 + \tfrac{1}{\varepsilon} \|e_{\varepsilon,f}\|_{L^2(\mathcal{I},L^2_\nu(\Omega_f))}^2 \\ &\qquad \lesssim \|e_{\varepsilon,f}(0)\|_f^2 + \|c_{\varepsilon,f}\|_{L^2(\mathcal{I},H^1(\Omega_f))}^2 + \|c_{\varepsilon,s}\|_{L^2(\mathcal{I},H^1(\Omega_s))}^2 + \|c_{0,f}\|_{H^1(\Omega_f)}^2. \end{aligned} \tag{6.45}$$

If Assumption 6.2.8 holds, we use that $\|\cdot\|_{f,\nu}$ is equivalent to $\|\cdot\|_f$ and ineq. (6.39a) for $e_{\varepsilon,f}$ follows using in particular the estimate ineq. (6.38) for $c^0_{\varepsilon,f}$ and the stability estimates for $c_{\varepsilon,f}$ and $c_{\varepsilon,s}$ from Lemma 6.3.2. Under Assumption 6.2.12, ineq. (6.39a) follows by Lemma 6.2.16 applied pointwise in time with $\delta = \varepsilon^{\frac{1}{2+\kappa}}$, just as in the stationary case. To derive ineq. (6.39c) for $e_{\varepsilon,s}$ we use the identity

$$\langle \partial_\tau e_{\varepsilon,s}, \varphi_s \rangle_s + a_s(e_{\varepsilon,s}, \varphi_s) + (e_{\varepsilon,s}, \varphi_s)_\xi = (e_{\varepsilon,f}, \varphi_s)_\xi \tag{6.46}$$

which holds for all $\varphi_s \in \mathcal{C}_s$ and in $\mathcal{I}$ almost everywhere. Using standard techniques we arrive at

$$\|e_{\varepsilon,s}\|_{L^\infty(\mathcal{I},L^2(\Omega_s))}^2 + \|e_{\varepsilon,s}\|_{L^2(\mathcal{I},H^1(\Omega_s))}^2 \lesssim \|e_{\varepsilon,s}(0)\|_s^2 + \int_{\mathcal{I}} (e_{\varepsilon,f}, e_{\varepsilon,s})_\xi \,\mathrm{d}\tau.$$

Since $\xi \in L^\infty(\Gamma)$, standard trace estimates for $H^1(\Omega_s)$ yield

$$\|e_{\varepsilon,s}\|^2_{L^\infty(\mathcal{I},L^2(\Omega_s))} + \|e_{\varepsilon,s}\|^2_{L^2(\mathcal{I},H^1(\Omega_s))} \lesssim \|e_{\varepsilon,s}(0)\|_s^2 + \|e_{\varepsilon,f}\|^2_{L^2(\mathcal{I},L^2(\Gamma))}. \tag{6.47}$$

Using the interpolation-type trace ineq. (6.7) pointwise-in-time, we have

$$\|e_{\varepsilon,f}\|_{L^2(\mathcal{I},L^2(\Gamma))} \lesssim \|e_{\varepsilon,f}\|^{\frac{1}{2}}_{L^2(\mathcal{I},L^2(\Omega_f))}\|e_{\varepsilon,f}\|^{\frac{1}{2}}_{L^2(\mathcal{I},H^1(\Omega_f))}.$$

The already proven estimates for $e_{\varepsilon,f}$ from ineqs. (6.39a) and (6.39b) imply

$$\|e_{\varepsilon,f}\|_{L^2(\mathcal{I},L^2(\Gamma))} \lesssim \varepsilon^{\frac{1}{4+2\kappa}}. \tag{6.48}$$

Together with ineq. (6.38) for $e_{\varepsilon,s}(0)$ this yields for ineq. (6.47) that

$$\|e_{\varepsilon,s}\|^2_{L^\infty(\mathcal{I},L^2(\Omega_s))} + \|e_{\varepsilon,s}\|^2_{L^2(\mathcal{I},H^1(\Omega_s))} \lesssim \varepsilon^{\frac{1}{2+\kappa}}$$

such that ineq. (6.39c) is satisfied.

For ineqs. (6.41) let us for simplicity first assume that $c^0_{\varepsilon,f}$ is close to $c_{0,f}$ in the sense of ineq. (6.43). Repeating the arguments leading to ineq. (6.18) in the proof of Theorem 6.2.11 pointwise in time leads to

$$(-\nabla c_{0,f}, \nabla\varphi_f)_f - (c_{\varepsilon,f} - c_{\varepsilon,s}, \varphi_f)_\xi \lesssim \|e_{\varepsilon,f}\|_f + \|e_{\varepsilon,f}\|_{L^2(\partial\Omega_f\setminus\partial_{\mathrm{i}}\Omega_f)}$$

where $\varphi_f = \mathrm{e}^\psi e_{\varepsilon,f}$ as above. Repeating the arguments leading to ineqs. (6.33) and (6.35) from the proof of Theorem 6.2.17 we get

$$(-\nabla c_{0,f}, \nabla\varphi_f)_f - (c_{\varepsilon,f} - c_{\varepsilon,s}, \varphi_f)_\xi \le C\varepsilon^{\frac{2}{2+\kappa}} + \tfrac{1}{2\varepsilon}\|e_{\varepsilon,f}\|^2_{f,\nu} + \tfrac{1}{2}\|\nabla e_{\varepsilon,f}\|_f^2.$$

The corresponding estimate under Assumption 6.2.8 is of the same form with $\kappa = 0$, see ineq. (6.20). Modifying the arguments leading to ineq. (6.45) with this improved estimate of the right-hand side in eq. (6.44), we conclude

$$\begin{aligned}\|e_{\varepsilon,f}\|^2_{L^\infty(\mathcal{I},L^2(\Omega_f))} + \|\nabla e_{\varepsilon,f}\|^2_{L^2(\mathcal{I},L^2(\Omega_f))} + \tfrac{1}{\varepsilon}\|e_{\varepsilon,f}\|^2_{L^2(\mathcal{I},L^2_\nu(\Omega_f))} \\ \lesssim \|e_{\varepsilon,f}(0)\|_f^2 + \varepsilon^{\frac{1}{2+\kappa}} \lesssim \varepsilon^{\frac{1}{2+\kappa}}\end{aligned} \tag{6.49}$$

where we used our assumption on the initial error, ineq. (6.43), in the last step. Proceeding just as in the case of low regularity we arrive at ineqs. (6.41) with $\tau_0 = 0$, using in particular the improved ineq. (6.40) for $e_{\varepsilon,s}(0)$.

If ineq. (6.43) does not hold, the previous argument shows that the finer estimates for the right-hand side of eq. (6.44) alone are insufficient for improved convergence. To control the initial error let $c^*_{\varepsilon,f} \in L^2(\mathcal{I},\bar{\mathcal{C}}_f) \cap H^1(\mathcal{I},\mathcal{C}^*_f)$ solve the same equation as $c_{\varepsilon,f}$ but with initial value $c_{0,f}$, i.e. let there hold

$$\langle\partial_\tau c^*_{\varepsilon,f}, \varphi_f\rangle_f + a_{\varepsilon,f}(c^*_{\varepsilon,f}, \varphi_f) + (c^*_{\varepsilon,f} - c_{\varepsilon,s}, \varphi_f)_\xi = 0$$

for all $\varphi_f \in \mathcal{C}_f$ in $\mathcal{I}$ almost everywhere with $c^*_{\varepsilon,f}(0) = c_{0,f}$. Moving $(c_{\varepsilon,s},\varphi_f)_\xi$ to the right-hand side, the existence and uniqueness of $c^*_{\varepsilon,f}$ follows by standard arguments since $a_{\varepsilon,f} + (\cdot,\cdot)_\xi$ is coercive. Define $e^*_{\varepsilon,f} := c_{\varepsilon,f} - c^*_{\varepsilon,f}$, then

$$\langle\partial_\tau e^*_{\varepsilon,f}, \varphi_f\rangle_f + a_{\varepsilon,f}(e^*_{\varepsilon,f}, \varphi_f) + (e^*_{\varepsilon,f}, \varphi_f)_\xi = 0$$

for all $\varphi_f \in \mathcal{C}_f$ in $\mathcal{I}$ almost everywhere. Testing with $\varphi_f = \mathrm{e}^{\psi} e^*_{\varepsilon,f}$ and using the coercivity of $a_{\varepsilon,f}$ from ineq. (6.30) we conclude that

$$\frac{\mathrm{d}}{\mathrm{d}\tau} \int_{\Omega_f} \mathrm{e}^{\psi} |e^*_{\varepsilon,f}(\tau)|^2 \,\mathrm{d}x + (\|\nabla e^*_{\varepsilon,f}(\tau)\|_f^2 + \tfrac{1}{\varepsilon} \min \mathrm{e}^{\psi} \|e^*_{\varepsilon,f}(\tau)\|_{f,\nu}^2) \leq 0 \tag{6.50}$$

holds for $\tau \in \mathcal{I}$. We multiply ineq. (6.50) by $\mathrm{e}^{2\mu\tau}$ with $\mu > 0$ arbitrary. Since

$$\frac{\mathrm{d}}{\mathrm{d}\tau} \left(\mathrm{e}^{2\mu\tau} |e^*_{\varepsilon,f}(\tau)|^2\right) = \mathrm{e}^{2\mu\tau} \frac{\mathrm{d}}{\mathrm{d}\tau} |e^*_{\varepsilon,f}(\tau)|^2 + 2\mu \mathrm{e}^{2\mu\tau} |e^*_{\varepsilon,f}(\tau)|^2$$

we conclude for ineq. (6.50) that

$$\begin{aligned} &\frac{\mathrm{d}}{\mathrm{d}\tau} \int_{\Omega_f} \mathrm{e}^{\psi} \mathrm{e}^{2\mu\tau} |e^*_{\varepsilon,f}(\tau)|^2 \,\mathrm{d}x \\ &\quad + \mathrm{e}^{2\mu\tau} (-2\mu \max \mathrm{e}^{\psi} \|e^*_{\varepsilon,f}(\tau)\|_f^2 + \|\nabla e^*_{\varepsilon,f}(\tau)\|_f^2 + \tfrac{1}{\varepsilon} \min \mathrm{e}^{\psi} \|e^*_{\varepsilon,f}(\tau)\|_{f,\nu}^2) \leq 0. \end{aligned} \tag{6.51}$$

By Lemma 6.2.16 there exists $C_0 > 0$ such that for all $0 < \delta < \delta_0$ there holds

$$2 \max \mathrm{e}^{\psi} \|e^*_{\varepsilon,f}(\tau)\|_f^2 \leq C_0 \delta^{-\kappa} \|e^*_{\varepsilon,f}(\tau)\|_{f,\nu}^2 + C_0 \delta^2 \|\nabla e^*_{\varepsilon,f}(\tau)\|_f^2.$$

Applying this to ineq. (6.51) implies

$$\begin{aligned} &\frac{\mathrm{d}}{\mathrm{d}\tau} \int_{\Omega_f} \mathrm{e}^{\psi} \mathrm{e}^{2\mu\tau} |e^*_{\varepsilon,f}(\tau)|^2 \,\mathrm{d}x \\ &\quad + \mathrm{e}^{2\mu\tau} ((1 - C_0\mu\delta^2) \|\nabla e^*_{\varepsilon,f}(\tau)\|_f^2 + (\tfrac{1}{\varepsilon} \min \mathrm{e}^{\psi} - C_0\mu\delta^{-\kappa}) \|e^*_{\varepsilon,f}(\tau)\|_{f,\nu}^2) \leq 0. \end{aligned} \tag{6.52}$$

With the Ansatz $\mu = \mu_0 \varepsilon^{-\hat{\mu}}$ and $\delta = \varepsilon^{\hat{\delta}}$ for $\mu_0, \hat{\mu}, \hat{\delta} > 0$ we see that

$$1 - C_0\mu\delta^2 \geq \tfrac{1}{2}, \quad \tfrac{1}{\varepsilon} \min \mathrm{e}^{\psi} - C_0\mu\delta^{-\kappa} \geq \tfrac{1}{2\varepsilon} \min \mathrm{e}^{\psi}$$

if $\hat{\mu} = \frac{2}{2+\kappa}$, $\hat{\delta} = \frac{1}{2+\kappa}$ and μ_0 is sufficiently small. This implies for ineq. (6.52):

$$\frac{\mathrm{d}}{\mathrm{d}\tau} \int_{\Omega_f} \mathrm{e}^{\psi} \mathrm{e}^{2\mu\tau} |e^*_{\varepsilon,f}(\tau)|^2 \,\mathrm{d}x + \mathrm{e}^{2\mu\tau} (\|\nabla e^*_{\varepsilon,f}(\tau)\|_f^2 + \tfrac{1}{\varepsilon} \|e^*_{\varepsilon,f}(\tau)\|_{f,\nu}^2) \leq 0.$$

Renaming τ as $\tilde{\tau}$ and integrating over $\tilde{\tau} \in (0, \tau)$, we conclude that

$$\mathrm{e}^{2\mu\tau} \|e^*_{\varepsilon,f}(\tau)\|_f^2 + \int_0^{\tau} \mathrm{e}^{2\mu\tilde{\tau}} (\|\nabla e^*_{\varepsilon,f}(\tilde{\tau})\|_f^2 + \tfrac{1}{\varepsilon} \|e^*_{\varepsilon,f}(\tilde{\tau})\|_{f,\nu}^2) \,\mathrm{d}\tilde{\tau} \lesssim \|e^*_{\varepsilon,f}(0)\|_f^2. \tag{6.53}$$

From ineq. (6.53) we can immediately read off

$$\|e^*_{\varepsilon,f}(\tau)\|_f^2 \lesssim \mathrm{e}^{-2\mu\tau} \|e^*_{\varepsilon,f}(0)\|_f^2 \lesssim \mathrm{e}^{-2\mu\tau_0}.$$

for all $\tau \in (\tau_0, \mathcal{T})$, but also conclude that for $\tau_0 > 0$ we have

$$\begin{aligned} &\|\nabla e^*_{\varepsilon,f}\|^2_{L^2(\tau_0,\mathcal{T};L^2(\Omega_f))} + \tfrac{1}{\varepsilon} \|e^*_{\varepsilon,f}\|^2_{L^2(\tau_0,\mathcal{T};L^2_\nu(\Omega_f))} \\ &\quad \leq \mathrm{e}^{-2\mu\tau_0} \int_{\tau_0}^{\mathcal{T}} \mathrm{e}^{2\mu\tilde{\tau}} (\|\nabla e^*_{\varepsilon,f}(\tilde{\tau})\|_f^2 + \tfrac{1}{\varepsilon} \|e^*_{\varepsilon,f}(\tilde{\tau})\|_{f,\nu}^2) \,\mathrm{d}\tilde{\tau} \\ &\quad \lesssim \mathrm{e}^{-2\mu\tau_0} \|e^*_{\varepsilon,f}(0)\|_f^2 \lesssim \mathrm{e}^{-2\mu\tau_0}. \end{aligned}$$

Since $\mu = \mu_0 \varepsilon^{-\frac{2}{2+\kappa}}$, eq. (6.42) for τ_0 implies $\mathrm{e}^{-2\mu\tau_0} = \varepsilon^{\frac{1}{2+\kappa}}$, thus

$$\begin{aligned}&\|e^*_{\varepsilon,f}\|^2_{L^\infty(\tau_0,\mathcal{T},L^2(\Omega_f))} + \|\nabla e^*_{\varepsilon,f}\|^2_{L^2(\tau_0,\mathcal{T},L^2(\Omega_f))} + \tfrac{1}{\varepsilon}\|e^*_{\varepsilon,f}\|^2_{L^2(\tau_0,\mathcal{T};L^2_\nu(\Omega_f))} \\ &\quad\lesssim \varepsilon^{\frac{1}{2+\kappa}}. \end{aligned} \tag{6.54}$$

This concludes our estimate of $e^*_{\varepsilon,f}$. We split $e_{\varepsilon,f}$ as

$$e_{\varepsilon,f} = c_{\varepsilon,f} - c_{0,f} = (c_{\varepsilon,f} - c^*_{\varepsilon,f}) + (c^*_{\varepsilon,f} - c_{0,f}) = e^*_{\varepsilon,f} + e^\diamond_{\varepsilon,f}$$

with $e^\diamond_{\varepsilon,f} := c^*_{\varepsilon,f} - c_{0,f}$. By construction of $c^*_{\varepsilon,f}$, the error $e^\diamond_{\varepsilon,f}$ satisfies

$$\langle \partial_\tau e^\diamond_{\varepsilon,f}, \varphi_f\rangle_f + a_{\varepsilon,f}(e^\diamond_{\varepsilon,f}, \varphi_f) = -(c^*_{\varepsilon,f} - c_{\varepsilon,s}, \varphi_f)_\xi - (\nabla c_{0,f}, \nabla\varphi_f)_f \tag{6.55}$$

for all $\varphi_f \in \mathcal{C}_f$ in $\mathcal{I}$ almost everywhere with $e^\diamond_{\varepsilon,f}(0) = 0$. Since eq. (6.55) has the same form as the error identity for $e_{\varepsilon,f}$, eq. (6.44), and $c^*_{\varepsilon,f}$ has the same stability properties as $c_{\varepsilon,f}$, we can repeat the arguments leading to ineq. (6.49) for $e^\diamond_{\varepsilon,f}$, implying that

$$\begin{aligned}&\|e^\diamond_{\varepsilon,f}\|^2_{L^\infty(\mathcal{I},L^2(\Omega_f))} + \|\nabla e^\diamond_{\varepsilon,f}\|^2_{L^2(\mathcal{I},L^2(\Omega_f))} + \tfrac{1}{\varepsilon}\|e^\diamond_{\varepsilon,f}\|^2_{L^2(\mathcal{I},L^2_\nu(\Omega_f))} \\ &\quad\lesssim \|e^\diamond_{\varepsilon,f}(0)\|^2_f + \varepsilon^{\frac{1}{2+\kappa}} \lesssim \varepsilon^{\frac{1}{2+\kappa}} \end{aligned} \tag{6.56}$$

where now we used that $e^\diamond_{\varepsilon,f}(0) = 0$. Since $e_{\varepsilon,f} = e^*_{\varepsilon,f} + e^\diamond_{\varepsilon,f}$ we can combine the estimates ineq. (6.54) for $e^*_{\varepsilon,f}$ and ineq. (6.56) for $e^\diamond_{\varepsilon,f}$ to arrive at ineq. (6.41a) and ineq. (6.41b).

To prove ineq. (6.41c) we first investigate the error equation eq. (6.46) for $e_{\varepsilon,s}$ at some $\tau \in (0,\tau_0)$. Proceeding just as for ineq. (6.47) we conclude that

$$\tfrac{1}{2}\|e_{\varepsilon,s}(\tau)\|^2_s + \|e_{\varepsilon,s}\|^2_{L^2(0,\tau;H^1(\Omega_s))} \le \int_0^\tau (e_{\varepsilon,f}, e_{\varepsilon,s})_\xi \,\mathrm{d}\tilde\tau. \tag{6.57}$$

Using the interpolation-type trace ineq. (6.7), we have

$$\|e_{\varepsilon,f}\|_{L^2(\Gamma)} \lesssim \|e_{\varepsilon,f}\|_f^{\frac{1}{2}} \|\nabla e_{\varepsilon,f}\|_f^{\frac{1}{2}}, \quad \|e_{\varepsilon,s}\|_{L^2(\Gamma)} \lesssim \|e_{\varepsilon,s}\|_s^{\frac{1}{2}} \|e_{\varepsilon,s}\|_{H^1(\Omega_s)}^{\frac{1}{2}}$$

and thus pointwise in time for $\tilde\tau \in (0,\tau)$

$$(e_{\varepsilon,f}, e_{\varepsilon,s})_\xi \lesssim \|e_{\varepsilon,f}\|_f^{\frac{1}{2}} \big(\tau^{\frac{1}{4}} \|\nabla e_{\varepsilon,f}\|_f^{\frac{1}{2}}\big) \big(\tau^{-\frac{1}{4}} \|e_{\varepsilon,s}\|_s^{\frac{1}{2}}\big) \|e_{\varepsilon,s}\|_{H^1(\Omega_s)}^{\frac{1}{2}}.$$

Applying Young's inequality to this estimate with $\frac{1}{4}+\frac{1}{4}+\frac{1}{4}+\frac{1}{4} = 1$ to the indicated grouping of the terms, we have for ineq. (6.57) that

$$\begin{aligned}&\tfrac{1}{2}\|e_{\varepsilon,s}(\tau)\|^2_s + \|e_{\varepsilon,s}\|^2_{L^2(0,\tau;H^1(\Omega_s))} \\ &\quad\le C\int_0^\tau \|e_{\varepsilon,f}\|_f^2 \,\mathrm{d}\tilde\tau + C\tau \int_0^\tau \|\nabla e_{\varepsilon,f}\|_f^2 \,\mathrm{d}\tilde\tau + \tfrac{1}{4}\tau^{-1}\int_0^\tau \|e_{\varepsilon,s}\|_s^2 \,\mathrm{d}\tilde\tau \\ &\qquad + \tfrac{1}{2}\int_0^\tau \|e_{\varepsilon,s}\|^2_{H^1(\Omega_s)} \,\mathrm{d}\tilde\tau. \end{aligned}$$

For the first and second term on the right we use the established ineqs. (6.39a) and (6.39b) from the low regularity case. The third term is estimated with the

L^∞-in-time norm, while the fourth and final term on the right is moved to the left. This yields

$$\tfrac{1}{2}\|e_{\varepsilon,s}(\tau)\|_s^2 + \tfrac{1}{2}\|e_{\varepsilon,s}\|^2_{L^2(0,\tau;H^1(\Omega_s))} \leq C\varepsilon^{\frac{2}{2+\kappa}} + C\tau + \tfrac{1}{4}\|e_{\varepsilon,s}\|^2_{L^\infty(0,\tau;L^2(\Omega_f))}.$$

Taking the essential supremum over $\tau \in (0,\tau_0)$ leads to

$$\|e_{\varepsilon,s}\|^2_{L^\infty(0,\tau_0;L^2(\Omega_f))} + \|e_{\varepsilon,s}\|^2_{L^2(0,\tau_0;H^1(\Omega_s))} \lesssim \varepsilon^{\frac{2}{2+\kappa}} + \tau_0. \tag{6.58}$$

By definition of τ_0 from eq. (6.42) there holds

$$\tau_0 \lesssim \varepsilon^{\frac{2}{2+\kappa}}(-\ln\varepsilon) \lesssim \varepsilon^{\frac{2}{2+\kappa}-2\eta}$$

for arbitrary $0 < \eta \ll 1$, with constant depending on η. Thus we can conclude for ineq. (6.58) that

$$\|e_{\varepsilon,s}\|^2_{L^\infty(0,\tau_0;L^2(\Omega_f))} + \|e_{\varepsilon,s}\|^2_{L^2(0,\tau_0;H^1(\Omega_s))} \lesssim \varepsilon^{\frac{2}{2+\kappa}-2\eta}. \tag{6.59}$$

This is ineq. (6.41b) on $(0,\tau_0)$. Now if $\tau \in (\tau_0,\mathcal{T})$ we again start with ineq. (6.57) and split the integral on the right-hand side into $(0,\tau_0)$ and (τ_0,τ), yielding

$$\begin{aligned}&\tfrac{1}{2}\|e_{\varepsilon,s}(\tau)\|_s^2 + \|e_{\varepsilon,s}\|^2_{L^2(0,\tau;H^1(\Omega_s))}\\ &\qquad\leq \int_0^{\tau_0}(e_{\varepsilon,f},e_{\varepsilon,s})_\xi \,\mathrm{d}\tilde\tau + \int_{\tau_0}^{\tau}(e_{\varepsilon,f},e_{\varepsilon,s})_\xi \,\mathrm{d}\tilde\tau.\end{aligned} \tag{6.60}$$

For the first term on the right we repeat the arguments from the case $\tau \in (0,\tau_0)$, but use the now established estimate for $e_{\varepsilon,s}$ in L^∞ from ineq. (6.59), yielding

$$\int_0^{\tau_0}(e_{\varepsilon,f},e_{\varepsilon,s})_\xi \,\mathrm{d}\tilde\tau \leq C\varepsilon^{\frac{2}{2+\kappa}-2\eta} + \tfrac{1}{2}\int_0^{\tau_0}\|e_{\varepsilon,s}\|^2_{H^1(\Omega_s)}\,\mathrm{d}\tilde\tau.$$

For the second term on the right of ineq. (6.60) we use the improved estimates for $e_{\varepsilon,f}$ from ineq. (6.41a) and ineq. (6.41b) just as in the proof of ineq. (6.39c), implying that

$$\begin{aligned}&\int_{\tau_0}^{\tau}(e_{\varepsilon,f},e_{\varepsilon,s})_\xi \,\mathrm{d}\tilde\tau\\ &\qquad\leq C\|e_{\varepsilon,f}\|^{\frac{1}{2}}_{L^2(\tau_0,\tau;L^2(\Omega_f))}\|\nabla e_{\varepsilon,f}\|^{\frac{1}{2}}_{L^2(\tau_0,\tau;L^2(\Omega_f))} + \tfrac{1}{2}\int_{\tau_0}^{\tau}\|e_{\varepsilon,s}\|^2_{H^1(\Omega_s)}\,\mathrm{d}\tilde\tau\\ &\qquad\leq C\varepsilon^{\frac{2}{2+\kappa}} + \tfrac{1}{2}\int_{\tau_0}^{\tau}\|e_{\varepsilon,s}\|^2_{H^1(\Omega_s)}\,\mathrm{d}\tilde\tau.\end{aligned}$$

Combining the two estimates for the right-hand side of ineq. (6.60) we conclude

$$\|e_{\varepsilon,s}(\tau)\|_s^2 + \|e_{\varepsilon,s}\|^2_{L^2(0,\tau;H^1(\Omega_s))} \leq C\varepsilon^{\frac{2}{2+\kappa}-2\eta} + \tfrac{1}{2}\int_0^{\tau}\|e_{\varepsilon,s}\|^2_{H^1(\Omega_s)}\,\mathrm{d}\tilde\tau.$$

Taking the essential supremum over $\tau \in (\tau_0,\mathcal{T})$ the claimed ineq. (6.41c) follows on $(\tau_0,\mathcal{T})$, and hence due to ineq. (6.59) on all of $\mathcal{I}$. □

Theorem 6.3.5 is only a first step in the analysis of problem occurring in the model of Yang et. al. and further work is required to investigate the multiscale behavior under assumptions of periodic advection velocities and permeabilities.

6.4 Numerics

Discretization

We use a discontinuous Galerkin (dG) discretization in space. This is motivated by the stability of this scheme for the advection dominated equation in the fluid domain as $\varepsilon \to 0$, but the use of discontinuous elements also allows the use a single dG function to represent both lumen and wall concentrations. Furthermore, the interface condition can be easily formulated in the framework of dG jumps and averages, allowing a simple implementation in existing dG code. We refer to [DE12] for an exhaustive introduction into discontinuous Galerkin methods. A similar dG discretization is analyzed in [CGJ13; CGJ16] with nonlinear coupling conditions. A conforming finite element discretization of a similar equation is analyzed in [QVZ02b] using domain decomposition methods to solve fluid and structure problems separately.

For simplicity we assume that Ω_f and Ω_s are polygonal domains using a linear interpolation of the continuous deformation field for the interface, even though e.g. isoparametric approaches would be better suited for the curved geometry [BS08]. Let $\Omega_{h,f}$ be a triangulation of Ω_f in the sense that $\Omega_{h,f}$ consists of disjoint, open, non-degenerate simplices $K \in \Omega_{h,f}$ with $\bigcup_{K\in\Omega_{h,f}} \overline{K} = \overline{\Omega_f}$ and no vertex of any simplex lies in the interior of an edge of another simplex. Similarly $\Omega_{h,s}$ denotes a triangulation of Ω_s and $\Omega_h := \Omega_{h,f} \cup \Omega_{h,s}$. The triangulations are assumed to match at the permeable interface Γ.

We denote the set of all edges $e \subset \partial K$ of all $K \in \Omega_{h,f}$ by $E_{h,f}$ and define analogously $E_{h,s}$ and write E_h for the set of edges in both $E_{h,f}$ and $E_{h,s}$. Edges shared by both $E_{h,f}$ and $E_{h,s}$ but not lying on the permeable part of the interface are assumed to be distinct in the sense of a disjoint union. We assume that any edge on the domain boundaries $\partial\Omega_f$ and $\partial\Omega_s$ lies entirely in $\partial_\mathrm{i}\Omega_f$, $\partial_\mathrm{o}\Omega_f$, $\partial_\mathrm{w}\Omega_f$, $\partial\Omega_s \setminus \Gamma$ or Γ. We write E_h^int for the set of interior edges which excludes, by convention, interface edges which we denote by E_h^Γ. The exterior edges are denoted by $E_h^\mathrm{ext} := E_h \setminus (E_h^\mathrm{int} \cup E_h^\Gamma)$ and subdivided into inflow edges $E_{h,f}^\mathrm{in} := \{e \in E_{h,f} \mid e \subset \partial_\mathrm{i}\Omega_f\}$ and Neumann-type boundary edges $E_{h,f}^\mathrm{N} := \{e \in E_{h,f} \mid e \subset \partial_\mathrm{o}\Omega_f \cup \partial_\mathrm{w}\Omega_f\}$. The set of exterior boundary edges of $E_{h,s}$ is denoted by $E_{h,s}^\mathrm{N} := \{e \in E_{h,s} \mid e \subset \partial\Omega_s \setminus \Gamma\}$. We write $E_h^\mathrm{N} := E_{h,f}^\mathrm{N} \cup E_{h,s}^\mathrm{N}$ for the set of all Neumann-type boundary edges. Exterior edges may lie on $(\partial\Omega_f \cap \partial\Omega_s) \setminus \Gamma$ but are, by the disjoint union construction mentioned above, assumed to be adjacent only to one element. For every interior or interface edge $e \in E_h^\mathrm{int} \cup E_h^\Gamma$ we choose an orientation by denoting the two elements sharing that edge by K^+ and $K^- \in \Omega_h$ with outward normal unit vectors $\mathfrak{n} := \mathfrak{n}^+$ and $\mathfrak{n}^-$, respectively. For exterior edges, $\mathfrak{n}^+$ is the outward normal unit vector.

We write

$$\mathcal{C}_h := \{c_h \colon \Omega_h \to \mathbb{R} \mid c_h|_K \in \mathcal{P}^1(K) \quad \forall K \in \Omega_h\}$$

for the space of dG functions of first order. As common for discontinuous Galerkin methods we define average and jump of a dG function $c_h \in \mathcal{C}_h$ over edges. We write c_h^+ and c_h^- for the continuous extension of $c_h|_{K^+}$, respectively $c_h|_{K^-}$, to e. Jump and average of c_h over e are then defined by

$$[\![c_h]\!] := c_h^+\mathfrak{n}^+ + c_h^-\mathfrak{n}^-, \quad \{c_h\} := \frac{1}{2}\left(c_h^+ + c_h^-\right) \quad \text{on } e \in E_h^\mathrm{int} \cup E_h^\Gamma$$

for interior and interface edges. For exterior edges we define

$$[\![c_h]\!] := c_h \mathfrak{n}^+, \quad \{c_h\} := c_h \quad \text{on } e \in E_h^{\text{ext}}.$$

The gradient of a dG function is not defined over the whole domain, but we use the notation $\nabla_h c_h$ for the broken gradient defined as the L^2 function satisfying $\nabla_h c_h|_K := \nabla(c_h|_K)$ for each $K \in \Omega_h$. For vector-valued dG functions, such as $\nabla_h c_h$, the definition of jump and average are analogous, using the scalar product with the normal vector for the definition of the jump.

With the notation for jumps and averages the condition on the permeable interface can be formulated as

$$[\![\varepsilon \nabla c_\varepsilon]\!] = 0, \quad \{\varepsilon \nabla c_\varepsilon\} + \varepsilon \xi [\![c_\varepsilon]\!] = 0 \quad \text{on } \Gamma. \tag{6.61}$$

The discretization of the advection-diffusion equation in Ω_f is standard with a symmetric interior penalty Galerkin method and upwinding for the advective term, see [DE12] for an introduction to these methods. A symmetric interior penalty method is also employed for the diffusion-reaction equation in Ω_s. Using the representation from eqs. (6.61) of the interface condition it can be checked by a lengthy but elementary calculation that the following equation for the discrete solution $c_{h,\varepsilon} \in \mathcal{C}_h$ is consistent:

$$\begin{aligned}
&\int_\Omega \varepsilon \nabla_h c_{h,\varepsilon} \cdot \nabla_h \varphi_h \,\mathrm{d}x - \int_{\Omega_f} c_{h,\varepsilon}\, v_f \cdot \nabla_h \varphi_h \,\mathrm{d}x + \int_{\Omega_s} \varepsilon\, c_{h,\varepsilon}\, \varphi_h \,\mathrm{d}x \\
&\quad - \sum_{e \in E_h^{\text{int}} \cup E_{h,f}^{\text{in}}} \int_e \{\varepsilon \nabla_h c_{h,\varepsilon}\} [\![\varphi_h]\!] + [\![c_{h,\varepsilon}]\!] \cdot \{\varepsilon \nabla_h \varphi_h\} - \frac{\varepsilon \eta}{h_e} [\![c_{h,\varepsilon}]\!] \cdot [\![\varphi_h]\!] \,\mathrm{d}o \\
&\quad + \sum_{e \in E_{h,f} \setminus (E_h^\Gamma \cup E_{h,f}^{\text{in}})} \int_e \{c_{h,\varepsilon}\}\, v_f \cdot [\![\varphi_h]\!] + \tfrac{1}{2} |v_f \cdot \mathfrak{n}^+| [\![c_{h,\varepsilon}]\!] \cdot [\![\varphi_h]\!] \,\mathrm{d}o \\
&\quad + \sum_{e \in E_h^\Gamma} \int_e \varepsilon \xi [\![c_{h,\varepsilon}]\!] \cdot [\![\varphi_h]\!] \,\mathrm{d}o \\
&\quad = \sum_{e \in E_{h,f}^{\text{in}}} \int_e -c_f^{\text{in}} \varepsilon \nabla \varphi \cdot \mathfrak{n}^+ - v_f \cdot \mathfrak{n}^+ c_f^{\text{in}} \varphi + \frac{\eta_\varepsilon}{h_e} c_f^{\text{in}} \varphi \,\mathrm{d}o
\end{aligned}$$

for all $\varphi_h \in \mathcal{C}_h$ where $\eta > 0$ is a penalty parameter and $h_e := \operatorname{diam}(e)$. The inflow boundary condition is only enforced weakly. We refer to [CGJ13; CGJ16] for theoretical results for a dG discretization of a similar nonlinear problem.

The discretization for the limit system is very similar, given as solution

$c_{h,0} \in \mathcal{C}_h$ to

$$
\begin{aligned}
&- \int_{\Omega_f} c_{h,0}\, v_f \cdot \nabla_h \varphi_h \,\mathrm{d}x + \int_{\Omega_s} \nabla_h c_{h,0} \cdot \nabla_h \varphi_h + c_{h,0}\, \varphi_h \,\mathrm{d}x \\
&\quad - \sum_{e \in E_h^{\mathrm{int}} \setminus E_{h,f}} \int_e \{\nabla_h c_{h,0}\} [\![\varphi_h]\!] + [\![c_{h,0}]\!] \cdot \{\nabla_h \varphi_h\} - \frac{\eta}{h_e} [\![c_{h,0}]\!] \cdot [\![\varphi_h]\!] \,\mathrm{d}o \\
&\quad + \sum_{e \in E_{h,f} \setminus (E_h^\Gamma \cup E_{h,f}^{\mathrm{in}})} \int_e \{c_{h,0}\}\, v_f \cdot [\![\varphi_h]\!] + \tfrac{1}{2} |v_f \cdot \mathfrak{n}^+| [\![c_{h,0}]\!] \cdot [\![\varphi_h]\!] \,\mathrm{d}o \\
&\quad + \sum_{e \in E_h^\Gamma} \int_e \xi [\![c_{h,0}]\!] \cdot \mathfrak{n}_s \varphi_{h,s} \,\mathrm{d}o \\
&\quad = \sum_{e \in E_{h,f}^{\mathrm{in}}} \int_e -v_f \cdot \mathfrak{n}^+ c_f^{\mathrm{in}} \varphi \,\mathrm{d}o
\end{aligned}
$$

for all $\varphi_h \in \mathcal{C}_h$. Apart from the obvious changes due to the missing diffusion in Ω_f in the limit problem, note that the interface term only contains the test function $\varphi_{h,s}$ from the structure domain. The solution on $\Omega_{h,f}$ is in particular decoupled from $\Omega_{h,s}$, allowing a more efficient numerical solution.

For the instationary problem an implicit Euler discretization was chosen for both the ε and limit system for simplicity. An adaptive step size control as discussed in [HV03] with fixed minimal step size was implemented to reduce the cost after the transient initial phase. We remark that while κ denoted the macro step size in Chapter 5 we will keep our notation from the previous theoretical results and refer to the macro step size by name.

The following numerical calculations were carried out using EniCS v2018.1 [Aln+15; LWH12; Log+12; Aln+14; Kir04; ALM12].

Numerical Test Case

To observe the effect of increasing stenosis on the quality of the approximation of c_ε by c_0 we will use a family of 2D fluid domains as defined in Chapter 5, with complementary structure domains, with a growth parameter $q \in Q := [0, 1)$. No growth actually occurs, so q is a fixed parameter.

For $q = 0$ both fluid and structure domains are rectangular and given by

$$\Omega_{0,f} := (-\tfrac{L}{2}, \tfrac{L}{2}) \times (0, 1), \quad \Omega_{0,s} := (-\tfrac{L}{2}, \tfrac{L}{2}) \times (-0.3, 0)$$

with $L := 5$. For $q \in Q$ we define $\Omega_{q,f}$ and $\Omega_{q,s}$ through a transformation of those rectangular domains, just as in Chapter 4 and Chapter 5. Let η be a bump function as in Example 4.1.2, i.e.

$$\eta(s) := \begin{cases} \mathrm{e}^{\frac{s^2}{s^2-1}} & \text{if } |s| < 1, \\ 0 & \text{else} \end{cases}$$

Then we defined the transformation

$$\Phi_q(x, y) := \begin{cases} \big(x, y + q\eta(\frac{2x}{L_0})(1 - y)\big)^\intercal & \text{if } y \in (0, 1), \\ \big(x, y + q\eta(\frac{2x}{L_0})(1 + \frac{y}{0.3})\big)^\intercal & \text{if } y \in (-0.3, 0) \end{cases}$$

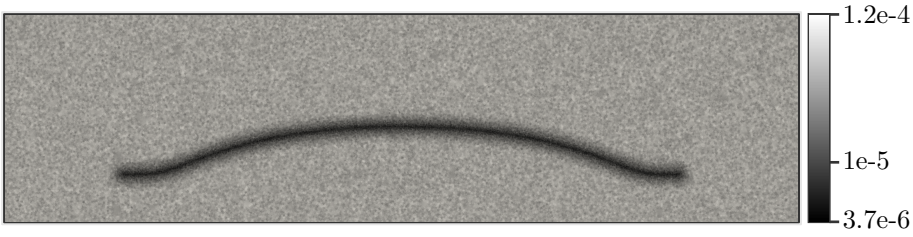

Figure 6.2: Area of triangles for a discretization of $\Omega_{q,f} \cup \Omega_{q,s}$ for $q = 0.3$. Logarithmic color scale.

with plaque length $L_0 := 3.5$. Φ_q is a linear interpolation in y between the fixed boundary $y = 1$ in $\Omega_{0,f}$, respectively $y = -0.3$ in $\Omega_{0,s}$, and the graph of a bump-shaped function at the interface $y = 0$. Then define fluid and structure domains by

$$\Omega_{q,f} := \Phi_q(\Omega_{0,f}), \quad \Omega_{q,s} := \Phi_q(\Omega_{0,s}).$$

Note that $\Omega_{f,q}$ corresponds to Ω_q as defined in Chapter 5. In the following there will always hold $\Omega_f = \Omega_{q,f}$ and $\Omega_s = \Omega_{q,s}$ for some $q \in Q$. The boundaries are just as shown in Figure 6.1 at the beginning of this section with permeable interface $\Gamma_0 := (-\frac{L_0}{2}, \frac{L_0}{2}) \times \{0\}$ spanning the whole section which gets deformed and $\Gamma_q := \Phi_q(\Gamma_0)$.

For $q = 0$ we will use the Poiseuille-like flow fields

$$v_0(x, y) = v_0(y^\kappa(1 - y)^\kappa, 0)^\intercal \quad \text{in } \Omega_{0,f}$$

with $\kappa \in \mathbb{N}_0$ as advection velocity, $v = v_0$. Such velocity fields were found in Example 6.2.14 to satisfy Assumption 6.2.12 such that our theory with vanishing velocities is applicable. The advection field for $q \in Q$ is $v = v_q$ where v_q is the inverse Piola transformation of v_0 from eq. (4.5), preserving the vector field's solenoidality and vanishing behavior near the interface, i.e.

$$v_q(x, y) := (\mathcal{P}_q^{-1} v_0)(x, y) \quad \text{in } \Omega_{q,f}.$$

Following the model by Yang et. al. we assume that $c_f^{\text{in}} \equiv 1$. As a consequence the fluid concentration in the limit solution is known a priori, $c_{0,f} \equiv 1$, such that only the structure concentration $c_{0,s}$ must be determined.

For the instationary problem we set $c_{\varepsilon,s}^0 := c_s^0 := 0$. On the fluid domain we set either $c_{\varepsilon,f}^0 := 0$ or $c_{\varepsilon,f}^0 := 1$ to investigate the occurrence of boundary layers if the initial value and $c_{0,f}$ disagrees, as predicted in Theorem 6.3.5.

The computational meshes were generated by triangulating the fluid and structure domains, delimited by the exterior boundaries and $\partial\Omega_{q,f} \cap \partial\Omega_{q,s}$ using `Gmsh` [GR09]. The triangulation was manually refined around the interface to better resolve the boundary layer. This meshing approach guarantees an even triangulation in both subdomains, in contrast to the method from Chapter 5 where a (structured) reference mesh for $q = 0$ was deformed by Φ_q. We present results for $q \in \{0, 0.3, 0.6\}$ with similar observed behavior for other values of q. The size of mesh elements for $q = 0.3$ is displayed in Figure 6.2. This mesh consisted of 438 390 degrees of freedom, 280 566 in the fluid and 157 824 in the structure domain, the other meshes had a similar total number of degrees of freedom with decomposition in fluid and structure nodes depending on q.

Results for the Stationary Problem

Figure 6.3 shows the solution c_ε of the stationary problem for $q = 0$ and $\kappa = 0$. For $\kappa \in \{0, \dots, 3\}$ the error between c_ε and c_0 is in good agreement with the theoretical results from Theorem 6.2.11 for $\kappa = 0$ and Theorem 6.2.17 for $\kappa > 0$ as evident from Figure 6.4, noting that since $c_{0,f} \equiv 1$ the improved estimates from ineqs. (6.9), respectively ineqs. (6.25), hold. In Figure 6.4 and in the following $\|\cdot\|^2_{H^1_0(\Omega_f)} = \|\nabla \cdot\|^2_{L^2(\Omega_f)}$. The numerical order of convergence is directly compared to the theoretical predictions in Figure 6.4(b), showing only slight under-estimation of the predicted order of convergence for the $L^2(\Omega_f)$ error for large κ.

For stenosed domains with $q > 0$ similar good agreement with the theoretical results was found, cf. Figure 6.6. Only for $\kappa = 0$ the $H^1_0(\Omega_f)$ errors deviate from the predicted results, presumably due to numerical errors tangential to the permeable interface, most pronounced at the beginning and end of the bump as shown in Figure 6.7. For $\kappa = 0$ the simulation was in general most sensitive to the mesh refinement and quality near the interface, which is unsurprising given that the advection is affecting the fluid concentration near the interface with full force for $\kappa = 0$, an unrealistic configuration. Note that it is not apparent that the discrete solution possesses the same $H^1_0(\Omega_f)$ stability as the continuous solution, which rested on Assumption 6.2.2.

Results for the Instationary Problem

As mentioned above we use an implicit Euler discretization for the temporal discretization of both ε and limit system on a time interval of $\mathcal{I} = (0, \mathcal{T})$ with $\mathcal{T} = 1$. A step size control is employed to reduce the cost after the initial transient phase, with a minimal macro step size of $0.1 \cdot \varepsilon$. For simplicity of implementation the step size control is only employed for the ε system and the solution of the limit equation which is compared to this solution employs the same temporal discretization. This is not considered a problem since the step size for the pure diffusion problem on Ω_s in the limit equation is not a bottleneck for the accuracy. Figure 6.8 shows the step sizes used for our computation. The spatial discretization, including the underlying mesh, is identical to the stationary problem but only the domain with $q = 0$ is investigated.

In Figure 6.9 the error for the instationary problem with $\kappa = 0$ and $c^0_{\varepsilon,f} = 0$, i.e. an initial value not satisfying the stronger condition from ineq. (6.43), is plotted in various space-time norms to test the results from Theorem 6.3.5. These numerical results for the fully discrete equation mostly agree with the predictions from Theorem 6.3.5, with the exception that the $L^2(\mathcal{I}, H^1_0(\Omega_f))$ error is of order $\varepsilon^{1/4}$ even though the boundary layer is included, instead of ε^0 as predicted. Furthermore, the order of convergence for the norms in Ω_s is with approximately $\varepsilon^{0.58}$ slightly better than the predicted $\varepsilon^{1/2}$.

The boundary layer estimates require knowledge of τ_0 which by eq. (6.42) depends on an unknown constant μ_0. The boundary layer behavior for the $L^2(\Omega_f)$ norm for $\kappa = 0$ and $c^0_{\varepsilon,f} \equiv 1$ is depicted in Figure 6.10, making it apparent that for $\varepsilon = 0.1$ the boundary layer with transient behavior spans across the whole time interval. We set $\mu_0 = 1/8$ such that $\tau_0 \approx -2\varepsilon \ln \varepsilon$, omitting η, lies behind the transient phase for $\varepsilon < 0.1$.

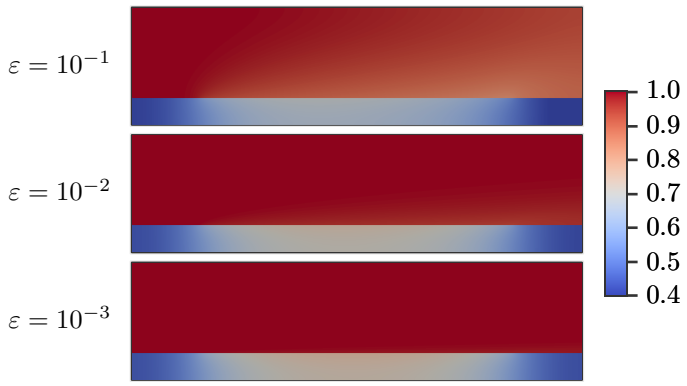

(a) Solution c_ε for $q = 0$.

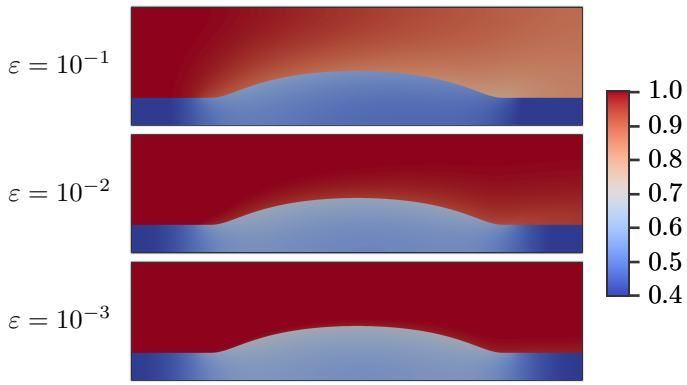

(b) Solution c_ε for $q = 0.3$.

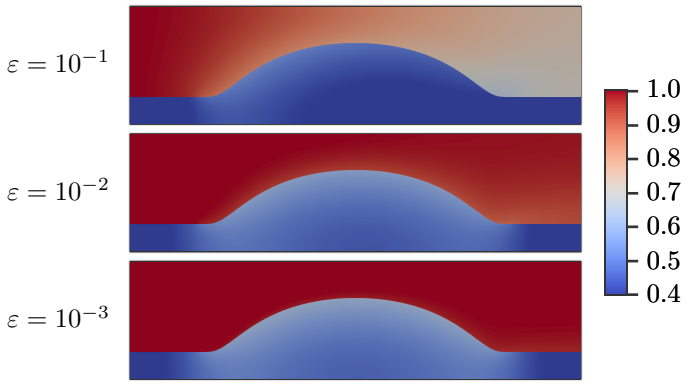

(c) Solution c_ε for $q = 0.6$.

Figure 6.3: Solution c_ε of the stationary problem for $\kappa = 0$ and multiple values of q and ε.

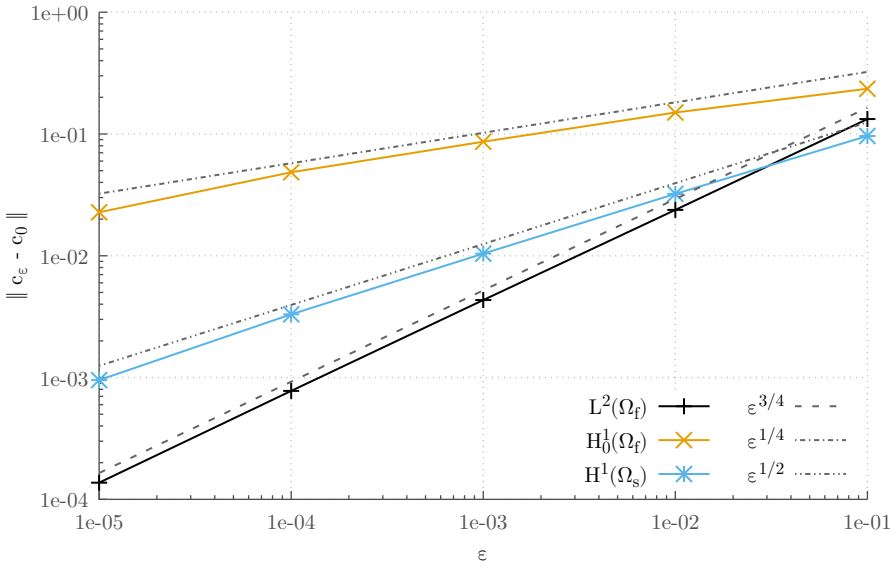

(a) Errors for $\kappa = 0$.

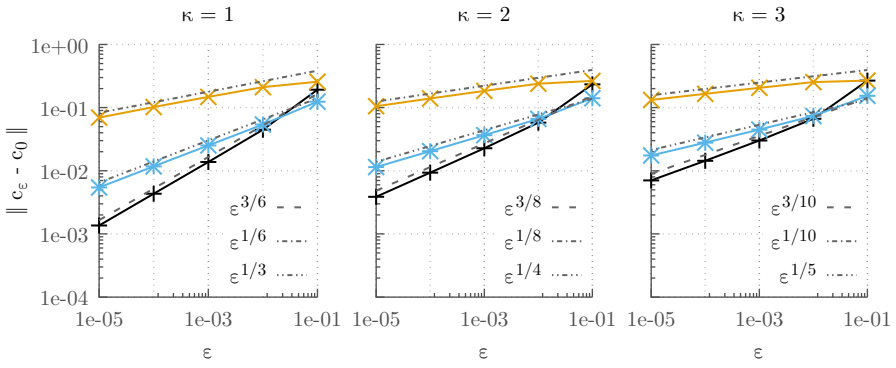

(b) Errors for $\kappa \in \{1, 2, 3\}$. Solid lines with the same meaning as in (a).

Figure 6.4: Error between the numerical approximations of c_ε and c_0 for the stationary problem on Ω_q for $q = 0$ for different norms with $\kappa = 0, \ldots, 3$. The dashed lines show the predicted convergence rates from ineqs. (6.9) in Theorem 6.2.11.

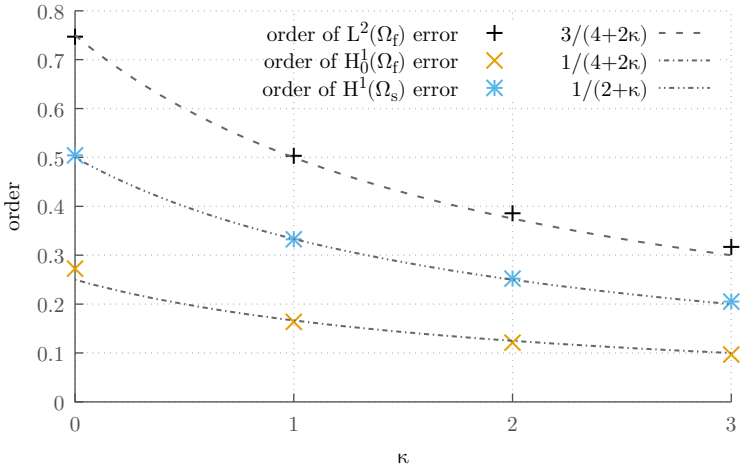

Figure 6.5: Numerically determined order of convergence in ε from Figure 6.4 for $q = 0$ and different values of κ in comparison with the predicted orders from Theorem 6.2.17.

Figure 6.11 complements Figure 6.9 by showing the errors from Theorem 6.3.5 which exclude the boundary layer, with τ_0 as specified above. In contrast to the theoretical predictions the $L^\infty(\mathcal{I}_0, L^2(\Omega_f))$ error is of the same order $\varepsilon^{3/4}$ as the $L^2(\mathcal{I}_0, L^2(\Omega_f))$ error, which itself is improved compared to $\varepsilon^{1/2}$ for $L^2(\mathcal{I}, L^2(\Omega_f))$, cf. Figure 6.9, as predicted by the theory. The exclusion of the boundary layer does not change the convergence for the $H_0^1(\Omega_f)$ error, which was already better than expected in Figure 6.9, as remarked above, but has the predicted order if the boundary layer is excluded. As mentioned in the discussion of Figure 6.10 the behavior of the error at $\varepsilon = 0.1$ should be ignored. Another choice of μ_0 did not improve the convergence but the results deteriorate as $\mu_0 \to \infty$ to those on the whole interval $\mathcal{I}$, as expected.

For the initial value $c^0_{\varepsilon,f} \equiv 1$, which is a plausible choice in the model by Yang et. al., no boundary layer appears as predicted by the theory, cf. Figure 6.12. The convergence behavior is as predicted in Theorem 6.3.5 with the exception of the error in $L^\infty(\mathcal{I}, L^2(\Omega_f))$ which is of order $\varepsilon^{3/4}$ just as observed for $c^0_{\varepsilon,f} \equiv 0$. As expected the exclusion of a boundary layer in the error norms does not improve the convergence in this case (not pictured).

For $\kappa = 1$ the discrepancies between numerical and theoretical results increase. As Figure 6.13(a) shows the error in $L^2(\mathcal{I}, L^2(\Omega_f))$ converges with rate $\varepsilon^{0.47}$ instead of $\varepsilon^{1/3}$ as predicted in Theorem 6.3.5, which is close to the order of convergence $\varepsilon^{3/6} = \varepsilon^{1/2}$ predicted if the boundary layer is excluded, while the error in $L^2(\mathcal{I}, H_0^1(\Omega_f))$ again behaves as predicted by our theory if the boundary layer is excluded. The convergence for the errors in Ω_s is again slightly better than predicted with $\varepsilon^{0.41}$ compared to $\varepsilon^{1/3}$. If the boundary layer is excluded, Figure 6.13(b), the behavior is very similar to $\kappa = 0$, with good agreement with the theoretical results except for the $L^\infty(\mathcal{I}_0, L^2(\Omega_f))$ error which converges with the same rate as the temporal L^2 error. Similar mixed agreement with the theoretical results was observed for $\kappa > 1$.

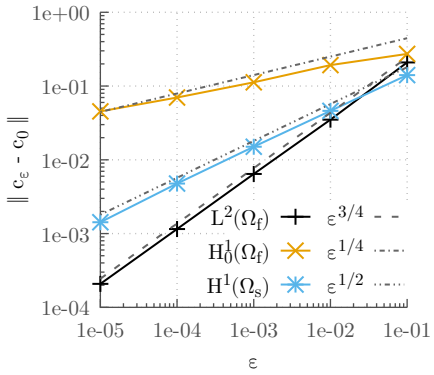

(a) Errors for $q = 0.3$ and $\kappa = 0$.

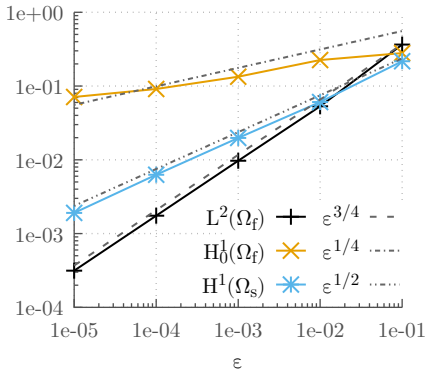

(b) Errors for $q = 0.6$ and $\kappa = 0$.

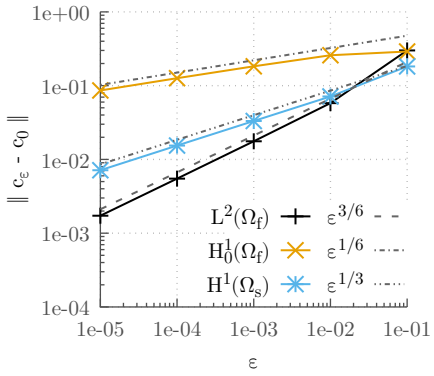

(c) Errors for $q = 0.3$ and $\kappa = 1$.

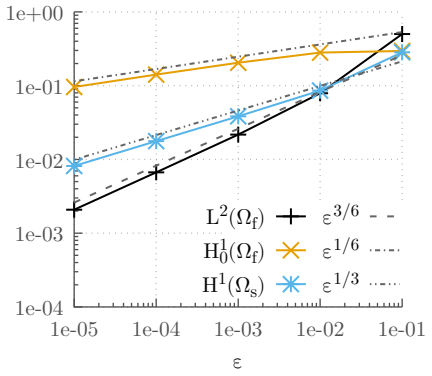

(d) Errors for $q = 0.6$ and $\kappa = 1$.

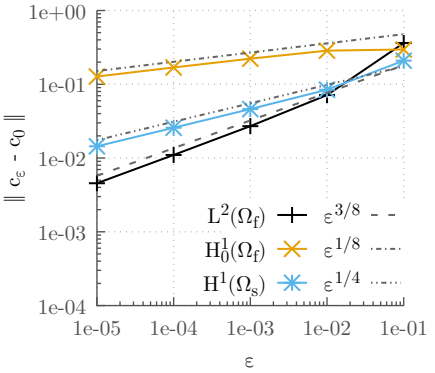

(e) Errors for $q = 0.3$ and $\kappa = 2$.

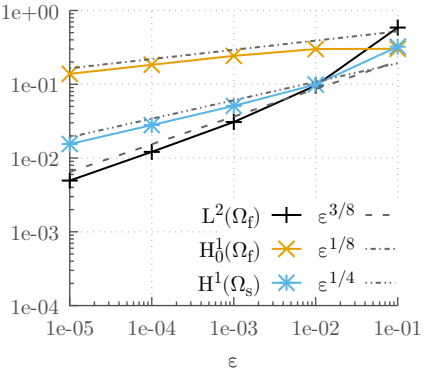

(f) Errors for $q = 0.6$ and $\kappa = 2$.

Figure 6.6: Error between c_ε and c_0 for the stationary problem for $q \in \{0.3, 0.6\}$ and $\kappa \in \{0, 1, 2\}$. Compare with Figure 6.4 for $q = 0$.

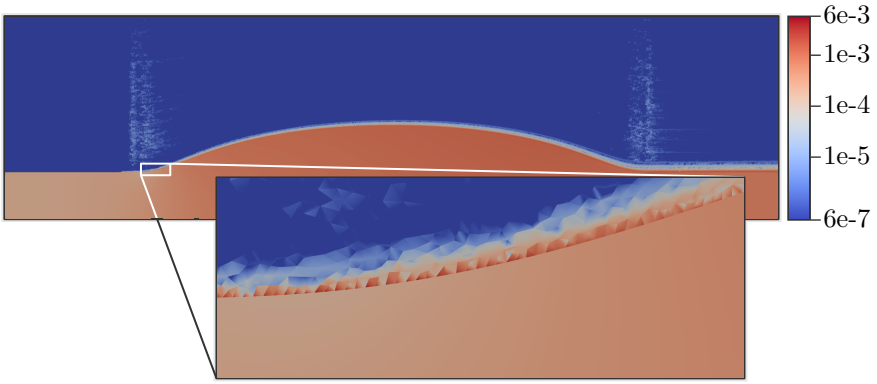

Figure 6.7: Plot of $|c_\varepsilon - c_0|$ for $q = 0.3$, $\kappa = 0$ and $\varepsilon = 10^{-5}$ with magnification of the error near the permeable interface. Colored by error magnitude in logarithmic scale.

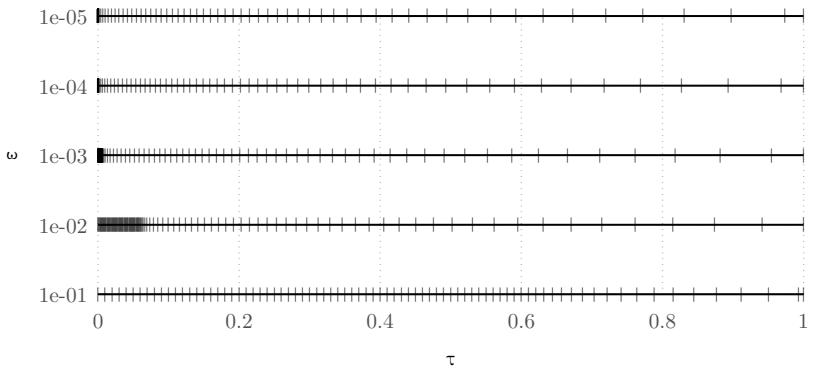

Figure 6.8: Macro step size used for our multiscale convergence computations, as determined from the step size control.

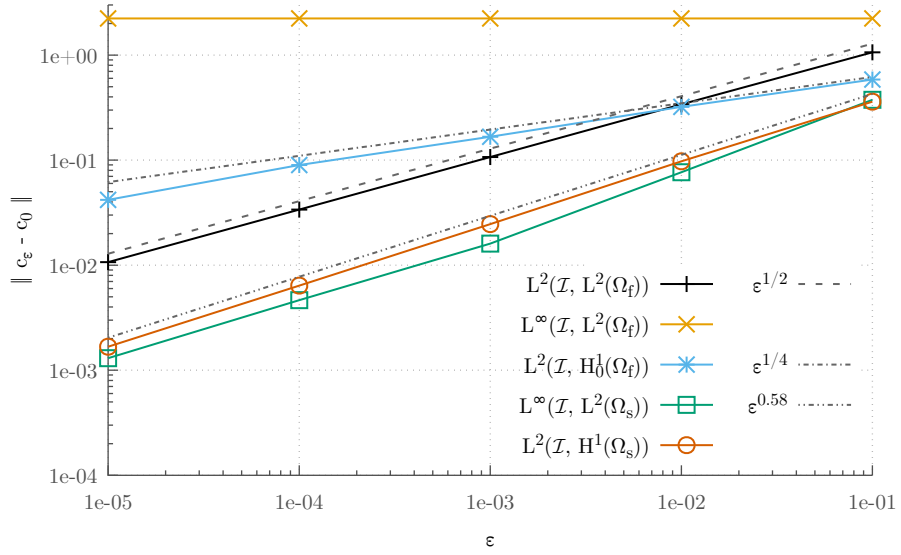

Figure 6.9: Error between c_ε and c_0 for the instationary problem with $\kappa = 0$ and $c^0_{\varepsilon,f} \equiv 0$ for various norms including the boundary layer, together with some convergence orders.

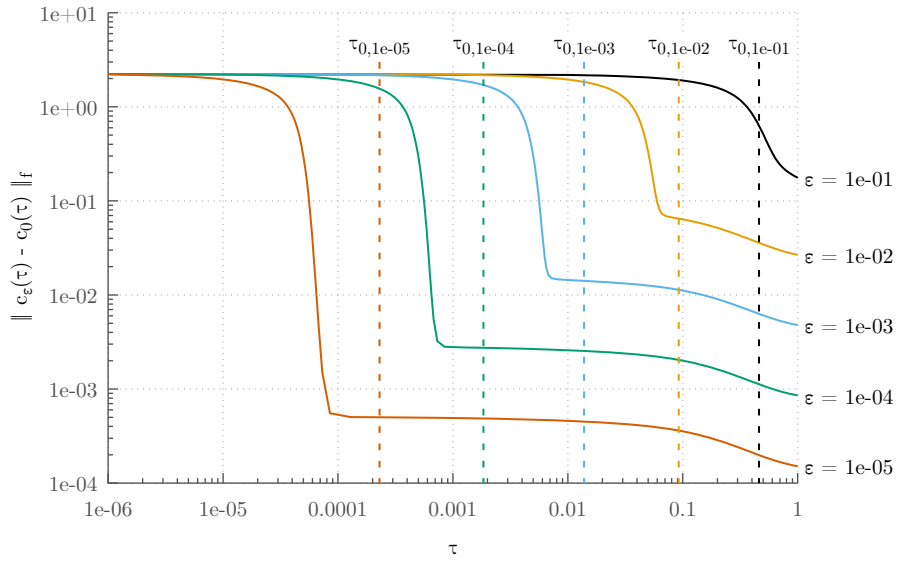

Figure 6.10: Pointwise-in-time error between c_ε and c_0 for the instationary problem with $\kappa = 0$ and $c^0_{\varepsilon,f} \equiv 0$ for the $L^2(\Omega_f)$ norm. The boundary layer time τ_0 with $\mu_0 := 1/8$ for each ε is also plotted (dashed lines).

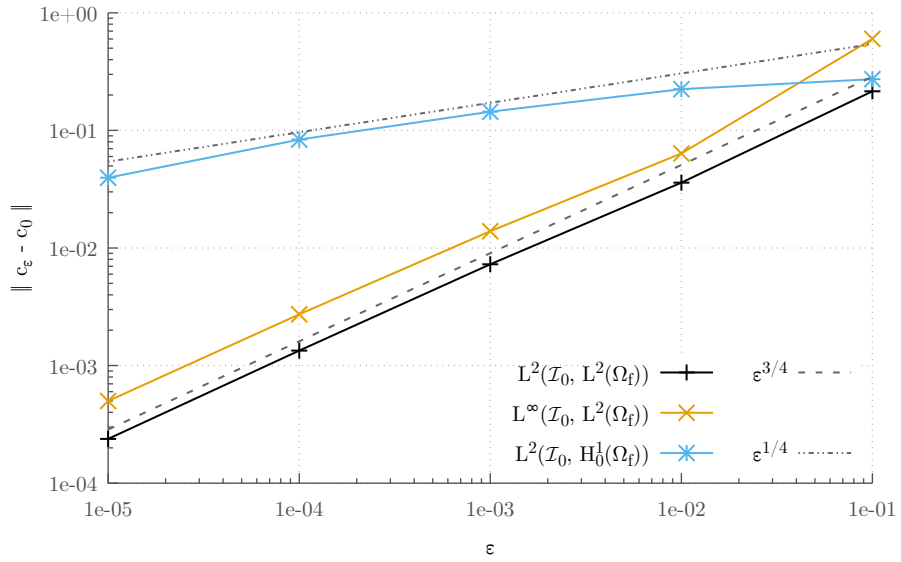

Figure 6.11: Error between c_ε and c_0 for the instationary problem with $\kappa = 0$ and $c^0_{\varepsilon,f} \equiv 0$ for various norms excluding the boundary layer for τ_0 as depicted in Figure 6.10, together with some convergence orders.

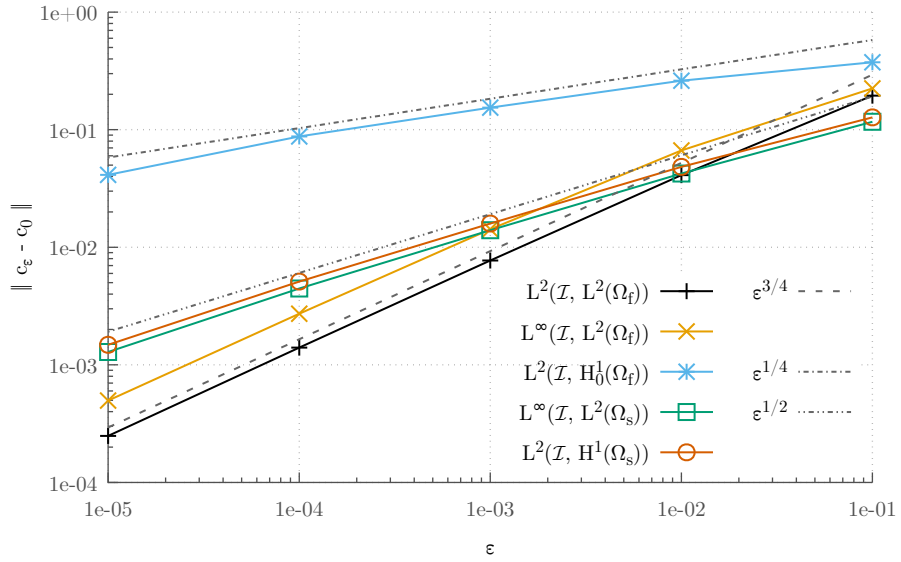

Figure 6.12: Error between c_ε and c_0 for the instationary problem with $\kappa = 0$ and $c^0_{\varepsilon,f} \equiv 1$ for various norms, together with some convergence orders.

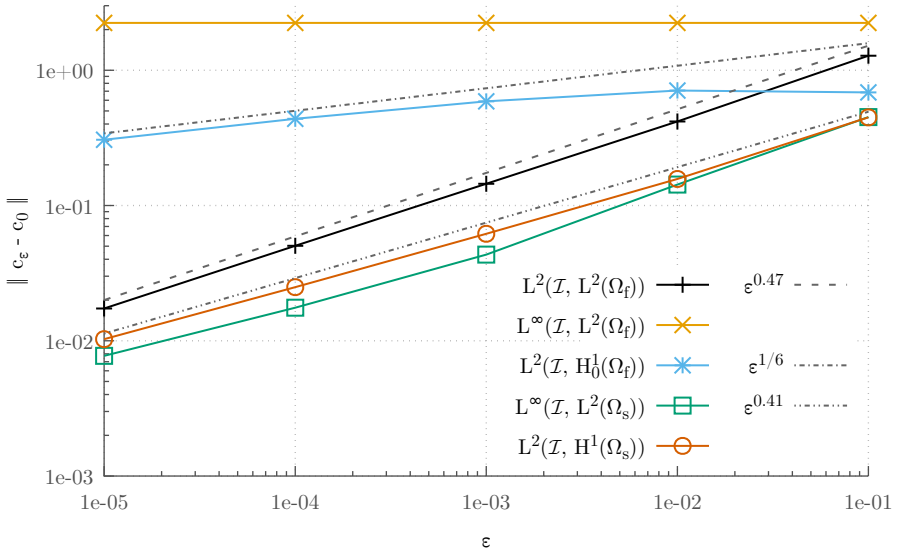

(a) Errors including the boundary layer.

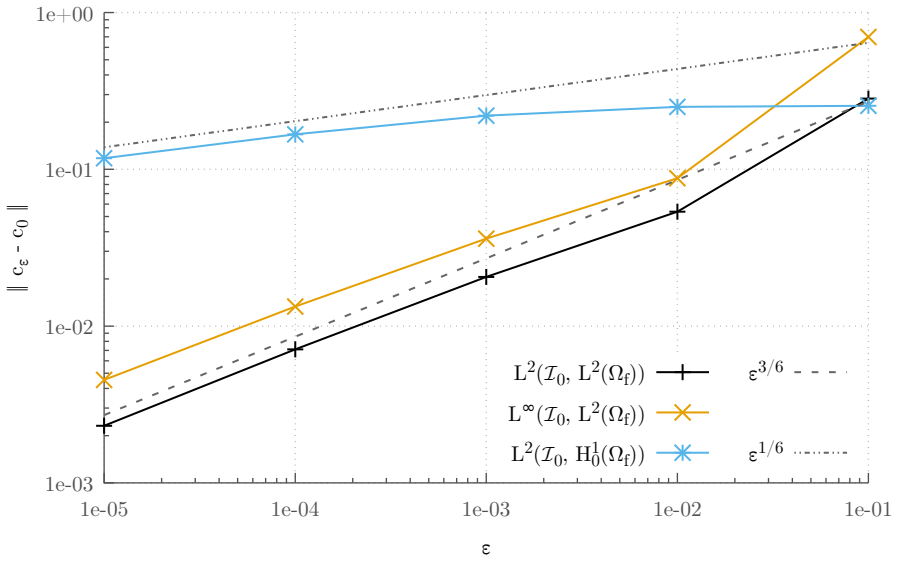

(b) Errors excluding the boundary layer.

Figure 6.13: Error between c_ε and c_0 for the instationary problem with $q = 0$, $\kappa = 1$ and $c^0_{\varepsilon,f} \equiv 0$ for various norms, together with some convergence orders.

Bibliography

[AV05] L. Ai and K. Vafai. "An Investigation of Stokes' Second Problem for Non-Newtonian Fluids". In: *Numerical Heat Transfer; Part A: Applications* 47.10 (2005), pp. 955–980. DOI: 10.1080/10407780590926390.

[AV06] L. Ai and K. Vafai. "A coupling model for macromolecule transport in a stenosed arterial wall". In: *International Journal of Heat and Mass Transfer* 49.9-10 (2006), pp. 1568–1591. DOI: 10.1016/j.ijheatmasstransfer.2005.10.041.

[Aln+15] M. S. Alnæs, J. Blechta, J. Hake, A. Johansson, B. Kehlet, A. Logg, C. Richardson, J. Ring, M. E. Rognes, and G. N. Wells. "The FEniCS Project Version 1.5". In: *Archive of Numerical Software* 3.100 (2015). DOI: 10.11588/ans.2015.100.20553.

[ALM12] M. S. Alnæs, A. Logg, and K.-A. Mardal. "UFC: a Finite Element Code Generation Interface". In: *Automated Solution of Differential Equations by the Finite Element Method*. Ed. by A. Logg, K.-A. Mardal, and G. N. Wells. Berlin, Heidelberg: Springer, 2012. Chap. 16. DOI: 10.1007/978-3-642-23099-8_16.

[Aln+14] M. S. Alnæs, A. Logg, K. B. Ølgaard, M. E. Rognes, and G. N. Wells. "Unified Form Language: A domain-specific language for weak formulations of partial differential equations". In: *ACM Transactions on Mathematical Software* 40.2 (2014). DOI: 10.1145/2566630.

[Alz+18] G. Alzetta, D. Arndt, W. Bangerth, V. Boddu, B. Brands, D. Davydov, R. Gassmöller, T. Heister, L. Heltai, K. Kormann, M. Kronbichler, M. Maier, J.-P. Pelteret, B. Turcksin, and D. Wells. "The deal.II library, Version 9.0". In: *Journal of Numerical Mathematics* 26.4 (2018), pp. 173–183. DOI: 10.1515/jnma-2018-0054.

[AW12] D. M. Ambrose and J. Wilkening. "Computing Time-periodic Solutions of Nonlinear Systems of Partial Differential Equations". In: *Proceedings of Hyperbolic Problems: Theory, Numerics, and Applications. Beijing, China, 2010*. Ed. by T. Li and S. Jiang. Singapore: World Scientific / Higher Education Press, 2012, pp. 273–280. DOI: 10.1142/9789814417099_0022.

[AM02] D. Ambrosi and F. Mollica. "On the mechanics of a growing tumor". In: *International Journal of Engineering Science* 40.12 (2002), pp. 1297–1316. DOI: 10.1016/S0020-7225(02)00014-9.

[Arb+16] G. Arbia, I. E. Vignon-Clementel, T. Y. Hsia, and J. F. Gerbeau. "Modified Navier–Stokes equations for the outflow boundary conditions in hemodynamics". In: *European Journal of Mechanics, B/Fluids* 60 (2016), pp. 175–188. DOI: 10.1016/j.euromechflu.2016.06.001.

[ADF17] W. Arendt, D. Dier, and S. Fackler. "J. L. Lions' problem on maximal regularity". In: *Archiv der Mathematik* 109.1 (2017), pp. 59–72. DOI: 10.1007/s00013-017-1031-6.

[Art07] Z. Artstein. "Averaging of time-varying differential equations revisited". In: *Journal of Differential Equations* 243.2 (2007), pp. 146–167. DOI: 10.1016/j.jde.2007.01.022.

[AH13] P. Assemat and K. Hourigan. "Evolution and rupture of vulnerable plaques: a review of mechanical effects". In: *ChronoPhysiology and Therapy* 3 (2013), pp. 23–40. DOI: 10.2147/CPT.S32050.

[AFM17] L. Athanasiou, D. Fotiadis, and L. Michalis. *Atherosclerotic Plaque Characterization Methods Based on Coronary Imaging*. London: Academic Press, 2017, p. 234.

[AN19] N. A. Avgerinos and P. Neofytou. "Mathematical Modelling and Simulation of Atherosclerosis Formation and Progress: A Review". In: *Annals of Biomedical Engineering* 47.8 (2019), pp. 1764–1785. DOI: 10.1007/s10439-019-02268-3.

[AM09] B. Ayuso and L. D. Marini. "Discontinuous Galerkin Methods for Advection-Diffusion-Reaction Problems". In: *SIAM Journal on Numerical Analysis* 47.2 (2009), pp. 1391–1420. DOI: 10.1137/080719583.

[BV92] A. V. Babin and M. I. Vishik. *Attractors of Evolution Equations*. Vol. 25. Studies in Mathematics and Its Applications. Amsterdam: North-Holland, 1992, p. 531.

[BQQ09] S. Badia, A. Quaini, and A. Quarteroni. "Coupling Biot and Navier-Stokes equations for modelling fluid-poroelastic media interaction". In: *Journal of Computational Physics* 228.21 (2009), pp. 7986–8014. DOI: 10.1016/j.jcp.2009.07.019.

[Bal+] S. Balay, S. Abhyankar, M. Adams, J. Brown, P. Brune, K. Buschelman, L. Dalcin, A. Dener, V. Eijkhout, W. Gropp, D. Karpeyev, D. Kaushik, M. Knepley, D. May, L. C. McInnes, R. T. Mills, T. Munson, K. Rupp, P. Sanan, B. Smith, S. Zampini, H. Zhang, and H. Zhang. *PETSc Web page*. URL: https://www.mcs.anl.gov/petsc.

[Bel+09] J. Bell, C. Breward, T. Chou, P. W. Fok, J. M. Haugh, Q. Li, M. Nowwar, L. Rossi, A. Walter, X. Yang, A. Zemlyanova, and N. Zhang. *Mathematical models for vulnerable plaques : MPI Workshop Delaware 2009*. Tech. rep. 2009, pp. 1–9.

[Ben14] M. Beneš. "A note on regularity and uniqueness of natural convection with effects of viscous dissipation in 3D open channels". In: *Zeitschrift fur Angewandte Mathematik und Physik* 65.5 (2014), pp. 961–975. DOI: 10.1007/s00033-013-0373-6.

[BK16] M. Beneš and P. Kučera. "Solutions to the Navier-Stokes equations with mixed boundary conditions in two-dimensional bounded domains". In: *Mathematische Nachrichten* 289.2-3 (2016), pp. 194–212. DOI: 10.1002/mana.201400046.

[Ben+14] J. F. Bentzon, F. Otsuka, R. Virmani, and E. Falk. "Mechanisms of plaque formation and rupture". In: *Circulation Research* 114.12 (2014), pp. 1852–1866. DOI: 10.1161/CIRCRESAHA.114.302721.

[Ber+18] C. Bertoglio, A. Caiazzo, Y. Bazilevs, M. Braack, M. Esmaily, V. Gravemeier, A. L. Marsden, O. Pironneau, I. E. Vignon-Clementel, and W. A. Wall. "Benchmark problems for numerical treatment of backflow at open boundaries". In: *International Journal for Numerical Methods in Biomedical Engineering* 34.2 (2018). DOI: 10.1002/cnm.2918.

[Blu+08] D. Bluestein, Y. Alemu, I. Avrahami, M. Gharib, K. Dumont, J. J. Ricotta, and S. Einav. "Influence of microcalcifications on vulnerable plaque mechanics using FSI modeling". In: *Journal of Biomechanics* 41.5 (2008), pp. 1111–1118. DOI: 10.1016/j.jbiomech.2007.11.029.

[BM14] M. Braack and P. B. Mucha. "Directional Do-Nothing Condition for the Navier-Stokes Equations". In: *Journal of Computational Mathematics* 32.5 (2014), pp. 507–521. DOI: 10.4208/jcm.1405-m4347.

[BS08] S. C. Brenner and L. R. Scott. *The Mathematical Theory of Finite Element Methods*. 3rd ed. Vol. 15. Texts in Applied Mathematics. New York: Springer, 2008, p. 398. DOI: 10.1007/978-0-387-75934-0.

[Buk+15] M. Bukac, I. Yotov, R. Zakerzadeh, and P. Zunino. "Effects of Poroelasticity on Fluid-Structure Interaction in Arteries: a Computational Sensitivity Study". In: *Modeling the Heart and the Circulatory System*. Ed. by A. Quarteroni. Vol. 14. MS&A. Cham: Springer, 2015. Chap. 8, pp. 197–220. DOI: 10.1007/978-3-319-05230-4_8.

[BD12] M. A. K. Bulelzai and J. L. A. Dubbeldam. "Long time evolution of atherosclerotic plaques". In: *Journal of Theoretical Biology* 297 (2012), pp. 1–10. DOI: 10.1016/j.jtbi.2011.11.023.

[CZ06] F. Calabrò and P. Zunino. "Analysis of parabolic problems on partitioned domains with nonlinear conditions at the interface. Application to mass transfer through semi-permeable membranes". In: *Mathematical Models and Methods in Applied Sciences* 16.4 (2006), pp. 479–501. DOI: 10.1142/S0218202506001236.

[Cal+09] V. Calvez, A. Ebde, N. Meunier, and A. Raoult. "Mathematical modelling of the atherosclerotic plaque formation". In: *ESAIM: Proceedings* 28 (2009). Ed. by M. Ismail, B. Maury, and J.-F. Gerbeau, pp. 1–12. DOI: 10.1051/proc/2009036.

[CGJ13] A. Cangiani, E. H. Georgoulis, and M. Jensen. "Discontinuous Galerkin Methods for Mass Transfer through Semipermeable Membranes". In: *SIAM Journal on Numerical Analysis* 51.5 (2013), pp. 2911–2934. DOI: 10.1137/120890429.

[CGJ16] A. Cangiani, E. H. Georgoulis, and M. Jensen. "Discontinuous Galerkin methods for fast reactive mass transfer through semipermeable membranes". In: *Applied Numerical Mathematics* 104 (2016), pp. 3–14. DOI: 10.1016/j.apnum.2014.06.007.

[CW14] L. Cardoso and S. Weinbaum. "Changing Views of the Biomechanics of Vulnerable Plaque Rupture: A Review". In: *Annals of Biomedical Engineering* 42.2 (2014), pp. 415–431. DOI: 10.1007/s10439-013-0855-x.

[CLR13] A. N. Carvalho, J. A. Langa, and J. C. Robinson. *Attractors for infinite-dimensional non-autonomous dynamical systems*. Vol. 182. Applied Mathematical Sciences. New York: Springer, 2013, p. 412. DOI: 10.1007/978-1-4614-4581-4.

[CBM17] A. D. Chalmers, C. A. Bursill, and M. R. Myerscough. "Nonlinear dynamics of early atherosclerotic plaque formation may determine the efficacy of high density lipoproteins (HDL) in plaque regression". In: *PLoS ONE* 12.11 (2017), pp. 1–23. DOI: 10.1371/journal.pone.0187674.

[CV01] V. V. Chepyzhov and M. I. Vishik. "Averaging of Trajectory Attractors of Evolution Equations with Rapidly Oscillating Coefficients". In: *Functional Differential Equations* 8.1-2 (2001), pp. 123–140.

[CPV08] V. V. Chepyzhov, V. Pata, and M. I. Vishik. "Averaging of nonautonomous damped wave equations with singularly oscillating external forces". In: *Journal des Mathematiques Pures et Appliquees* 90.5 (2008), pp. 469–491. DOI: 10.1016/j.matpur.2008.07.001.

[CV12] S. Chung and K. Vafai. "Effect of the fluid-structure interactions on low-density lipoprotein transport within a multi-layered arterial wall". In: *Journal of Biomechanics* 45.2 (2012), pp. 371–381. DOI: 10.1016/j.jbiomech.2011.10.002.

[CV13] S. Chung and K. Vafai. "Low-density lipoprotein transport within a multi-layered arterial wall – Effect of the atherosclerotic plaque / stenosis". In: *Journal of Biomechanics* 46.3 (2013), pp. 574–585. DOI: 10.1016/j.jbiomech.2012.09.022.

[Cia88] P. Ciarlet. *Mathematical Elasticity Volume I: Three-Dimensional Elasticity*. Vol. 20. Amsterdam: North-Holland, 1988, p. 448. DOI: 10.1016/S0168-2024(08)70051-1.

[CPM14] M. Cilla, E. Peña, and M. A. Martínez. "Mathematical modelling of atheroma plaque formation and development in coronary arteries". In: *Journal of the Royal Society Interface* 11.90 (2014). DOI: 10.1098/rsif.2013.0866.

[Cio+08] D. Cioranescu, A. Damlamian, G. Griso, and D. Onofrei. "The periodic unfolding method for perforated domains and Neumann sieve models". In: *Journal des Mathematiques Pures et Appliquees* 89.3 (2008), pp. 248–277. DOI: 10.1016/j.matpur.2007.12.008.

[CSM02] C. A. Cobbold, J. A. Sherratt, and S. R. Maxwell. "Lipoprotein oxidation and its significance for atherosclerosis: A mathematical approach". In: *Bulletin of Mathematical Biology* 64.1 (2002), pp. 65–95. DOI: 10.1006/bulm.2001.0267.

[DTW01] T. David, S. Thomas, and P. G. Walker. "Platelet deposition in stagnation point flow: An analytical and computational simulation". In: *Medical Engineering and Physics* 23.5 (2001), pp. 299–312. DOI: 10.1016/S1350-4533(01)00047-9.

[Dav92] M. J. Davies. "Anatomic features in victims of sudden coronary death. Coronary artery pathology." In: *Circulation* 85.1 Suppl (1992), pp. I19–I24.

[Dav95] P. F. Davies. "Flow-mediated endothelial mechanotransduction." In: *Physiological reviews* 75.3 (1995), pp. 519–60. DOI: 10.1152/physrev.1995.75.3.519.

[Dav04] T. A. Davis. "Algorithm 832: UMFPACK V4.3—an unsymmetric-pattern multifrontal method". In: *ACM Transactions on Mathematical Software (TOMS)* 30.2 (2004), pp. 196–199. DOI: 10.1145/992200.992206.

[Ded+15] E. Dedits, A. C. Poje, T. Schäfer, and J. Vukadinovic. "Averaging and spectral properties for the 2D advection-diffusion equation in the semi-classical limit for vanishing diffusivity". In: *Physica D: Nonlinear Phenomena* 310 (2015), pp. 1–18. DOI: 10.1016/j.physd.2015.07.011.

[DEF74] A. Devinatz, R. Ellis, and A. Friedman. "The Asymptotic Behavior of the First Real Eigenvalue of Second Order Elliptic Operators with a Small Parameter in the Highest Derivatives, II". In: *Indiana University Mathematics Journal* 23.11 (1974), p. 991. DOI: 10.1512/iumj.1974.23.23081.

[DNS15] A. Deyranlou, H. Niazmand, and M. R. Sadeghi. "Low-density lipoprotein accumulation within a carotid artery with multi-layer elastic porous wall: Fluid-structure interaction and non-Newtonian considerations". In: *Journal of Biomechanics* 48.12 (2015), pp. 2948–2959. DOI: 10.1016/j.jbiomech.2015.08.002.

[DE12] D. A. Di Pietro and A. Ern. *Mathematical Aspects of Discontinuous Galerkin Methods*. Vol. 69. Mathématiques et Applications. Berlin, Heidelberg: Springer, 2012, p. 401. DOI: 10.1007/978-3-642-22980-0.

[DDP11] G. Di Tomaso, V. Daz-Zuccarini, and C. Pichardo-Almarza. "A multiscale model of atherosclerotic plaque formation at its early stage". In: *IEEE Transactions on Biomedical Engineering* 58.12 (2011), pp. 3460–3463. DOI: 10.1109/TBME.2011.2165066.

[Di +15] G. Di Tomaso, C. Pichardo-Almarza, O. Agu, and V. Díaz-Zuccarini. "A multiscale and Patient-specific computational framework of atherosclerosis formation and progression: A case study in the aorta and peripheral arteries". In: *Procedia Computer Science* 51.1 (2015), pp. 1118–1127. DOI: 10.1016/j.procs.2015.05.281.

[DQ09] M. Discacciati and A. Quarteroni. "Navier-Stokes/Darcy Coupling: Modeling, Analysis, and Numerical Approximation". In: *Revista Matematica Complutense* 22.2 (2009), pp. 315–426. DOI: 10.5209/rev_rema.2009.v22.n2.16263.

[Doe+20] E. Doedel, A. Champneys, A. Fairgrieve, Y. Kuznetsov, B. Oldman, R. Paffenroth, B. Sandstede, X. Wang, and C. Zhang. *AUTO-07P: Continuation and bifurcation software for ordinary differential equations*. 2020.

[DSB08] W. N. Durán, F. A. Sánchez, and J. W. Breslin. "Microcirculatory Exchange Function". In: *Microcirculation*. Ed. by R. F. Tuma, W. N. Durán, and K. Ley. 2nd ed. Elsevier, 2008, pp. 81–124. DOI: 10.1016/B978-0-12-374530-9.00004-8.

[E+07] W. E, B. Engquist, X. Li, and W. Ren. "The Heterogeneous Multiscale Method: A Review". In: *Communications in Computational Physics* 2.3 (2007), pp. 367–450.

[Eck79] W. Eckhaus. *Asymptotic Analysis of Singular Perturbations*. Amsterdam: North-Holland, 1979, p. 287.

[EGV07] N. El Khatib, S. Génieys, and V. Volpert. "Atherosclerosis initiation modeled as an inflammatory process". In: *Mathematical Modelling of Natural Phenomena* 2.2 (2007), pp. 126–141. DOI: 10.1051/mmnp:2008022.

[Eva+20] C. Evans, S. Pollock, L. G. Rebholz, and M. Xiao. "A Proof That Anderson Acceleration Improves the Convergence Rate in Linearly Converging Fixed-Point Methods (But Not in Those Converging Quadratically)". In: *SIAM Journal on Numerical Analysis* 58.1 (2020), pp. 788–810. DOI: 10.1137/19m1245384.

[Fen79] N. Fenichel. "Geometric singular perturbation theory for ordinary differential equations". In: *Journal of Differential Equations* 31.1 (1979), pp. 53–98. DOI: 10.1016/0022-0396(79)90152-9.

[Fil+13] N. Filipovic, Z. Teng, M. Radovic, I. Saveljic, D. Fotiadis, and O. Parodi. "Computer simulation of three-dimensional plaque formation and progression in the carotid artery". In: *Medical and Biological Engineering and Computing* 51.6 (2013), pp. 607–616. DOI: 10.1007/s11517-012-1031-4.

[FS96] M. C. Fishbein and R. J. Siegel. "How big are coronary atherosclerotic plaques that rupture?" In: *Circulation* 94.10 (1996), pp. 2662–2666. DOI: 10.1161/01.CIR.94.10.2662.

[Foi+01] C. Foias, O. Manley, R. Rosa, and R. Temam. *Navier-Stokes Equations and Turbulence*. Vol. 83. Encyclopedia of Mathematics and its Applications. Cambridge University Press, 2001, p. 347. DOI: 10.1017/cbo9780511546754.

[Fok12a] P. W. Fok. "Growth of necrotic cores in atherosclerotic plaque". In: *Mathematical Medicine and Biology* 29.4 (2012), pp. 301–327. DOI: 10.1093/imammb/dqr012.

[Fok12b] P. W. Fok. "Mathematical model of intimal thickening in atherosclerosis: Vessel stenosis as a free boundary problem". In: *Journal of Theoretical Biology* 314 (2012), pp. 23–33. DOI: 10.1016/j.jtbi.2012.07.029.

[Fok16] P. W. Fok. "Multi-layer mechanical model of Glagov remodeling in coronary arteries: Differences between in-vivo and ex-vivo measurements". In: *PLoS ONE* 11.7 (2016), pp. 1–17. DOI: 10.1371/journal.pone.0159304.

[FQV09] L. Formaggia, A. Quarteroni, and A. Veneziani, eds. *Cardiovascular Mathematics*. Vol. 1. MS&A. Milano: Springer, 2009, p. 522. DOI: 10.1007/978-88-470-1152-6.

[FRW16] S. Frei, T. Richter, and T. Wick. "Long-term simulation of large deformation, mechano-chemical fluid-structure interactions in ALE and fully Eulerian coordinates". In: *Journal of Computational Physics* 321 (2016), pp. 874–891. DOI: 10.1016/j.jcp.2016.06.015.

[FR20] S. Frei and T. Richter. "Efficient Approximation of Flow Problems With Multiple Scales in Time". In: *Multiscale Modeling & Simulation* 18.2 (2020), pp. 942–969. DOI: 10.1137/19M1258396.

[FH15] A. Friedman and W. Hao. "A Mathematical Model of Atherosclerosis with Reverse Cholesterol Transport and Associated Risk Factors". In: *Bulletin of Mathematical Biology* 77.5 (2015), pp. 758–781. DOI: 10.1007/s11538-014-0010-3.

[Gab+14] S. A. Gabriel, Y. Ding, Y. Feng, and J. A. Gear. "Deposition-driven Growth in Atherosclerosis Modelling". In: *Proceedings of the 19th Australasian Fluid Mechanics Conference* (2014), pp. 2–5.

[Gal+08] G. P. Galdi, R. Rannacher, A. M. Roberston, and S. Turek. *Hemodynamical Flows*. Vol. 37. Oberwolfach Seminars. Basel: Birkhäuser, 2008, pp. 1–512. DOI: 10.1007/978-3-7643-7806-6.

[GK16] G. P. Galdi and M. Kyed. "Time-Periodic Solutions to the Navier-Stokes Equations". In: *Handbook of Mathematical Analysis in Mechanics of Viscous Fluids*. Ed. by Y. Giga and A. Novotny. Cham: Springer, 2016, pp. 1–70. DOI: 10.1007/978-3-319-10151-4.

[GBD18] GBD 2017 Causes of Death Collaborators. "Global, regional, and national age-sex-specific mortality for 282 causes of death in 195 countries and territories, 1980–2017: a systematic analysis for the Global Burden of Disease Study 2017". In: *The Lancet* 392.10159 (2018), pp. 1736–1788. DOI: 10.1016/S0140-6736(18)32203-7.

[GJ10] S. J. George and J. Johnson, eds. *Atherosclerosis: Molecular and Cellular Mechanisms*. Weinheim: Wiley, 2010, p. 420. DOI: 10.1002/9783527629589.

[GL15] T. Gerhardt and K. Ley. "Monocyte trafficking across the vessel wall". In: *Cardiovascular Research* 107.3 (2015), pp. 321–330. DOI: 10.1093/cvr/cvv147.

[Ges+11] V. C. Gessaghi, M. A. Raschi, D. Y. Tanoni, C. A. Perazzo, and A. E. Larreteguy. "Growth model for cholesterol accumulation in the wall of a simplified 3D geometry of the carotid bifurcation". In: *Computer Methods in Applied Mechanics and Engineering* 200.23-24 (2011), pp. 2117–2125. DOI: 10.1016/j.cma.2011.03.001.

[GR09] C. Geuzaine and J.-F. Remacle. "Gmsh: A 3-D finite element mesh generator with built-in pre- and post-processing facilities". In: *International Journal for Numerical Methods in Engineering* 79.11 (2009), pp. 1309–1331. DOI: 10.1002/nme.2579.

[Ghi+17] M. Ghim, P. Alpresa, S. Yang, S. T. Braakman, S. G. Gray, S. J. Sherwin, M. van Reeuwijk, and P. D. Weinberg. "Visualisation of three pathways for macromolecule transport across cultured endothelium and their modification by flow". In: *American Journal of Physiology - Heart and Circulatory Physiology* (2017), H959–H973. DOI: 10.1152/ajpheart.00218.2017.

[Gib+93] C. M. Gibson, L. Diaz, K. Kandarpa, F. M. Sacks, R. C. Pasternak, T. Sandor, C. Feldman, and P. H. Stone. "Relation of vessel wall shear stress to atherosclerosis progression in human coronary arteries". In: *Arteriosclerosis and Thrombosis* 13.2 (1993), pp. 310–315. DOI: 10.1161/01.atv.13.2.310.

[GKO14] S. Girke, R. Klöfkorn, and M. Ohlberger. "Efficient Parallel Simulation of Atherosclerotic Plaque Formation Using Higher Order Discontinuous Galerkin Schemes". In: *Finite Volumes for Complex Applications VII-Elliptic, Parabolic and Hyperbolic Problems*. Ed. by J. Fuhrmann, M. Ohlberger, and C. Rohde. Vol. 78. Springer Proceedings in Mathematics & Statistics. Cham: Springer, 2014, pp. 617–625. DOI: 10.1007/978-3-319-05591-6_61.

[Gla+87] S. Glagov, E. Weisenberg, C. K. Zarins, R. Stankunavicius, and G. J. Kolettis. "Compensatory Enlargement of Human Atherosclerotic Coronary Arteries". In: *New England Journal of Medicine* 316.22 (1987), pp. 1371–1375. DOI: 10.1056/NEJM198705283162204.

[Goe+83] H. Goering, A. Felgenhauer, G. Lube, H.-G. Roos, and L. Tobiska. *Singularly perturbed differential equations*. Berlin: Akademie-Verlag, 1983, p. 176. DOI: 10.1142/9789812832443_0003.

[Gri11] P. Grisvard. *Elliptic Problems in Nonsmooth Domains*. Classics in Applied Mathematics. Philadelphia: Society for Industrial and Applied Mathematics, 2011, p. 410. DOI: 10.1137/1.9781611972030.

[HF14] W. Hao and A. Friedman. "The LDL-HDL profile determines the risk of atherosclerosis: A mathematical model". In: *PLoS ONE* 9.3 (2014). DOI: 10.1371/journal.pone.0090497.

[HKV95] J. J. Heijnekamp, M. S. Krol, and F. Verhulst. "Averaging in non-linear advective transport problems". In: *Mathematical Methods in the Applied Sciences* 18.6 (1995), pp. 437–448. DOI: 10.1002/mma.1670180603.

[Hen81] D. Henry. *Geometric Theory of Semilinear Parabolic Equations*. Vol. 840. Lecture Notes in Mathematics. Berlin, Heidelberg: Springer, 1981. DOI: 10.1007/BFb0089647.

[Her+16] W. Herrington, B. Lacey, P. Sherliker, J. Armitage, and S. Lewington. "Epidemiology of Atherosclerosis and the Potential to Reduce the Global Burden of Atherothrombotic Disease". In: *Circulation Research* 118.4 (2016), pp. 535–546. DOI: 10.1161/CIRCRESAHA.115.307611.

[Hey76] J. G. Heywood. "On uniqueness questions in the theory of viscous flow". In: *Acta Mathematica* 136.1 (1976), pp. 61–102. DOI: 10.1007/BF02392043.

[HRT96] J. G. Heywood, R. Rannacher, and S. Turek. "Artificial Boundaries and Flux and Pressure Conditions for the Incompressible Navier-Stokes Equations". In: *International Journal for Numerical Methods in Fluids* 22 (1996), pp. 325–352. DOI: 10.1002/(SICI)1097-0363(19960315)22:5<325::AID-FLD307>3.0.CO;2-Y.

[Him+04] H. A. Himburg, D. M. Grzybowski, A. L. Hazel, J. A. LaMack, X. M. Li, and M. H. Friedman. "Spatial comparison between wall shear stress measures and porcine arterial endothelial permeability". In: *American Journal of Physiology - Heart and Circulatory Physiology* 286.5 55-5 (2004), pp. 1916–1922. DOI: 10.1152/ajpheart.00897.2003.

[Hon+12] J. Hong, C. Fu, H. Lin, and W. Tan. "Non-Newtonian effects on low-density lipoprotein transport in the arterial wall". In: *Journal of Non-Newtonian Fluid Mechanics* 189-190 (2012), pp. 1–7. DOI: 10.1016/j.jnnfm.2012.09.008.

[Hor03] D. Horstmann. "From 1970 until present : the Keller-Segel model in chemotaxis and its consequences". In: *Jahresbericht der Deutschen Mathematiker-Vereinigung* 105.3 (2003), pp. 103–165.

[Hos+09] T. Hoshino, L. A. Chow, J. J. Hsu, A. A. Perlowski, M. Abedin, J. Tobis, Y. Tintut, A. K. Mal, W. S. Klug, and L. L. Demer. "Mechanical stress analysis of a rigid inclusion in distensible material: A model of atherosclerotic calcification and plaque vulnerability". In: *American Journal of Physiology - Heart and Circulatory Physiology* 297.2 (2009), pp. 802–810. DOI: 10.1152/ajpheart.00318.2009.

[HM07] J. Hron and M. Mádlík. "Fluid-structure interaction with applications in biomechanics". In: *Nonlinear Analysis: Real World Applications* 8.5 (2007), pp. 1431–1458. DOI: 10.1016/j.nonrwa.2006.05.007.

[Hua+09] X. Huang, C. Yang, C. Yuan, F. Liu, G. Canton, J. Zheng, P. K. Woodard, G. A. Sicard, and D. Tang. "Patient-specific artery shrinkage and 3D zero-stress state in multi-component 3D FSI models for carotid atherosclerotic plaques based on in vivo MRI data". In: *Molecular and Cellular Biomechanics* 6.2 (2009), pp. 121–134. DOI: 10.3970/mcb.2009.006.121.

[Hüb+08] K. Hübner, T. Schwager, K. Winkler, J. G. Reich, and H. G. Holzhütter. "Computational lipidology: Predicting lipoprotein density profiles in human blood plasma". In: *PLoS Computational Biology* 4.5 (2008). DOI: 10.1371/journal.pcbi.1000079.

[Hum02] J. D. Humphrey. *Cardiovascular Solid Mechanics*. New York: Springer, 2002, p. 757. DOI: 10.1007/978-0-387-21576-1.

[HL10] A. Hundertmark-Zaušková and M. Lukáčová-Medvid'ová. "Numerical study of shear-dependent non-Newtonian fluids in compliant vessels". In: *Computers and Mathematics with Applications* 60.3 (2010), pp. 572–590. DOI: 10.1016/j.camwa.2010.05.004.

[HV03] W. Hundsdorfer and J. Verwer. *Numerical Solution of Time-Dependent Advection-Diffusion-Reaction Equations*. Vol. 33. Springer Series in Computational Mathematics. Berlin, Heidelberg: Springer, 2003, p. 472. DOI: 10.1007/978-3-662-09017-6.

[Ias+16] M. Iasiello, K. Vafai, A. Andreozzi, and N. Bianco. "Analysis of non-Newtonian effects on Low-Density Lipoprotein accumulation in an artery". In: *Journal of Biomechanics* 49.9 (2016), pp. 1437–1446. DOI: 10.1016/j.jbiomech.2016.03.017.

[Ibr+05] A. I. Ibragimov, C. J. McNeal, L. R. Ritter, and J. R. Walton. "A mathematical model of atherogenesis as an inflammatory response". In: *Mathematical Medicine and Biology* 22.4 (2005), pp. 305–333. DOI: 10.1093/imammb/dqi011.

[IW77] A. Inoue and M. Wakimoto. "On existence of solutions of the Navier-Stokes equation in a time dependent domain". In: *Journal of the Faculty of Science. University of Tokyo. Section IA. Mathematics.* 24.2 (1977), pp. 303–319.

[Isl17] M. H. Islam. "Mathematical Modelling of the Inflammatory Response in Coronary Artery Disease". PhD thesis. Griffith University, 2017, p. 136.

[JMS10] J. Janela, A. Moura, and A. Sequeira. "A 3D non-Newtonian fluid-structure interaction model for blood flow in arteries". In: *Journal of Computational and Applied Mathematics* 234.9 (2010), pp. 2783–2791. DOI: 10.1016/j.cam.2010.01.032.

[JBF03] L. Jiang, L. T. Biegler, and V. G. Fox. "Simulation and optimization of pressure-swing adsorption systems for air separation". In: *AIChE Journal* 49.5 (2003), pp. 1140–1157. DOI: 10.1002/aic.690490508.

[Joh+04] B. M. Johnston, P. R. Johnston, S. Corney, and D. Kilpatrick. "Non-Newtonian blood flow in human right coronary arteries: steady state simulations". In: *Journal of Biomechanics* 37.5 (2004), pp. 709–720. DOI: 10.1016/j.jbiomech.2003.09.016.

[JC12] G. W. Jones and S. J. Chapman. "Modeling Growth in Biological Materials". In: *SIAM Review* 54.1 (2012), pp. 52–118. DOI: 10.1137/080731785.

[KPZ01] G. Karner, K. Perktold, and H. P. Zehentner. "Computational Modeling of Macromolecule Transport in the Arterial Wall". In: *Computer Methods in Biomechanics and Biomedical Engineering* 4.6 (2001), pp. 491–504. DOI: 10.1080/10255840108908022.

[KK58] O. Kedem and A. Katchalsky. "Thermodynamic analysis of the permeability of biological membranes to non-electrolytes". In: *Biochimica et Biophysica Acta* 27.2 (1958), pp. 229–246. DOI: 10.1016/0006-3002(58)90330-5.

[Kei+99] F. Keil, W. Mackens, H. Voß, and J. Werther, eds. *Scientific Computing in Chemical Engineering II*. Berlin, Heidelberg: Springer, 1999, pp. 311–318. DOI: 10.1007/978-3-642-60185-9.

[KV08] M. Khakpour and K. Vafai. "Critical assessment of arterial transport models". In: *International Journal of Heat and Mass Transfer* 51.3-4 (2008), pp. 807–822. DOI: 10/bfvd35.

[Kir04] R. C. Kirby. "Algorithm 839: FIAT, a New Paradigm for Computing Finite Element Basis Functions". In: *ACM Transactions on Mathematical Software* 30.4 (2004), pp. 502–516. DOI: 10.1145/1039813.1039820.

[Kro91] M. S. Krol. "On the Averaging Method in Nearly Time-Periodic Advection-Diffusion Problems". In: *SIAM Journal on Applied Mathematics* 51.6 (1991), pp. 1622–1637. DOI: 10.1137/0151083.

[Kue15] C. Kuehn. *Multiple Time Scale Dynamics*. Vol. 191. Applied Mathematical Sciences. Cham: Springer, 2015, p. 814. DOI: 10.1007/978-3-319-12316-5.

[Lea+10] J. R. Leach, V. L. Rayz, B. Soares, M. Wintermark, M. R. Mofrad, and D. Saloner. "Carotid atheroma rupture observed in vivo and FSI-predicted stress distribution based on pre-rupture imaging". In: *Annals of Biomedical Engineering* 38.8 (2010), pp. 2748–2765. DOI: 10.1007/s10439-010-0004-8.

[LAS09] S. W. Lee, L. Antiga, and D. A. Steinman. "Correlations among indicators of disturbed flow at the normal carotid bifurcation". In: *Journal of Biomechanical Engineering* 131.6 (2009), pp. 1–7. DOI: 10.1115/1.3127252.

[Len+91] C. L. Lendon, M. J. Davies, G. V. Born, and P. D. Richardson. "Atherosclerotic plaque caps are locally weakened when macrophages density is increased". In: *Atherosclerosis* 87.1 (1991), pp. 87–90. DOI: 10.1016/0021-9150(91)90235-U.

[LM10] J. R. Levick and C. C. Michel. "Microvascular fluid exchange and the revised Starling principle". In: *Cardiovascular Research* 87.2 (2010), pp. 198–210. DOI: 10.1093/cvr/cvq062.

[LBT16] P. Libby, K. E. Bornfeldt, and A. R. Tall. "Atherosclerosis: Successes, Surprises, and Future Challenges". In: *Circulation Research* 118.4 (2016), pp. 531–534. DOI: 10.1161/CIRCRESAHA.116.308334.

[LRM02] P. Libby, P. M. Ridker, and A. Maseri. "Inflammation and Atherosclerosis". In: *Circulation* 105.9 (2002), pp. 1135–1143. DOI: 10.1161/hc0902.104353.

[Lio73] J. L. Lions. *Perturbations Singulières dans les Problèmes aux Limites et en Contrôle Optimal*. Vol. 323. Lecture Notes in Mathematics. Berlin, Heidelberg: Springer, 1973. DOI: 10.1007/BFb0060528.

[LT10] B. Liu and D. Tang. "Computer simulations of atherosclerotic plaque growth in coronary arteries". In: *Molecular and Cellular Biomechanics* 7.4 (2010), pp. 193–202. DOI: 10.3970/mcb.2010.007.193.

[Log+12] A. Logg, K. B. Ølgaard, M. E. Rognes, and G. N. Wells. "FFC: the FEniCS Form Compiler". In: *Automated Solution of Differential Equations by the Finite Element Method*. Ed. by A. Logg, K.-A. Mardal, and G. N. Wells. Vol. 84. Lecture Notes in Computational Science and Engineering. Berlin, Heidelberg: Springer, 2012. Chap. 11.

[LWH12] A. Logg, G. N. Wells, and J. Hake. "DOLFIN: a C++/Python Finite Element Library". In: *Automated Solution of Differential Equations by the Finite Element Method*. Ed. by A. Logg, K.-A. Mardal, and G. N. Wells. Vol. 84. Lecture Notes in Computational Science and Engineering. Berlin, Heidelberg: Springer, 2012. Chap. 10.

[LST07] R. Lübke, A. Seidel-Morgenstern, and L. Tobiska. "Numerical method for accelerated calculation of cyclic steady state of ModiCon-SMB-processes". In: *Computers and Chemical Engineering* 31.4 (2007), pp. 258–267. DOI: 10.1016/j.compchemeng.2006.06.013.

[LR82] M. Luskin and R. Rannacher. "On the Smoothing Property of the Crank-Nicolson Scheme". In: *Applicable Analysis* 14.2 (1982), pp. 117–135. DOI: 10.1080/00036818208839415.

[McK+05] C. McKay, S. McDee, N. Mottram, T. Mulholland, S. Wilson, S. Kennedy, and R. Wadsworth. *Towards a Model of Atherosclerosis*. Tech. rep. 2005, p. 29.

[MPR03] M. Minceva, L. S. Pais, and A. E. Rodrigues. "Cyclic steady state of simulated moving bed processes for enantiomers separation". In: *Chemical Engineering and Processing* 42.2 (2003), pp. 93–104. DOI: 10.1016/S0255-2701(02)00038-7.

[MMW11] M. Mitrea, S. Monniaux, and M. Wright. "The Stokes operator with Neumann boundary conditions in Lipschitz domains". In: *Journal of Mathematical Sciences* 176.3 (2011), pp. 409–457. DOI: 10.1007/s10958-011-0400-0.

[MT82] T. Miyakawa and Y. Teramoto. "Existence and periodicity of weak solutions of the Navier- Stokes equations in a time dependent domain". In: *Hiroshima Mathematical Journal* 12 (1982), pp. 513–528.

[Moh+13] F. W. Mohr, M. C. Morice, A. P. Kappetein, T. E. Feldman, E. Ståhle, A. Colombo, M. J. MacK, D. R. Holmes, M. A. Morel, N. Van Dyck, V. M. Houle, K. D. Dawkins, and P. W. Serruys. "Coronary artery bypass graft surgery versus percutaneous coronary intervention in patients with three-vessel disease and left main coronary disease: 5-year follow-up of the randomised, clinical SYNTAX trial". In: *The Lancet* 381.9867 (2013), pp. 629–638. DOI: 10.1016/S0140-6736(13)60141-5.

[NWS08] Y. Nakashima, T. N. Wight, and K. Sueishi. "Early atherosclerosis in humans: Role of diffuse intimal thickening and extracellular matrix proteoglycans". In: *Cardiovascular Research* 79.1 (2008), pp. 14–23. DOI: 10.1093/cvr/cvn099.

[Nem+12] A. Nematollahi, E. Shirani, I. Mirzaee, and M. R. Sadeghi. "Numerical simulation of LDL particles mass transport in human carotid artery under steady state conditions". In: *Scientia Iranica* 19.3 (2012), pp. 519–524. DOI: 10.1016/j.scient.2012.03.005.

[Nic+13] G. Niccoli, G. G. Stefanini, D. Capodanno, F. Crea, J. A. Ambrose, and R. Berg. "Are the culprit lesions severely stenotic?" In: *JACC: Cardiovascular Imaging* 6.10 (2013), pp. 1108–1114. DOI: 10.1016/j.jcmg.2013.05.004.

[NP98] S. Nilchan and C. C. Pantelides. "On the Optimisation of Periodic Adsorption Processes". In: *Adsorption* 4.2 (1998), pp. 113–147. DOI: 10.1023/A:1008823102106.

[NLB99] T. L. van Noorden, S. M. V. Lunel, and A. Bliek. "Direct Determination of Cyclic Steady States of Cyclically Operated Packed Bed Reactors". In: *Scientific Computing in Chemical Engineering II*. Berlin, Heidelberg: Springer, 1999, pp. 311–318. DOI: 10.1007/978-3-642-60185-9_36.

[Ogd09] R. W. Ogden. "Anisotropy and Nonlinear Elasticity in Arterial Wall Mechanics". In: *Biomechanical Modelling at the Molecular, Cellular and Tissue Levels*. Ed. by G. A. Holzapfel and R. W. Ogden. Vol. 508. CISM Courses and Lectures. Vienna: Springer, 2009, pp. 179–258.

[Oha+14] J. Ohayon, G. Finet, S. Le Floc'h, G. Cloutier, A. M. Gharib, J. Heroux, and R. I. Pettigrew. "Biomechanics of atherosclerotic coronary plaque: Site, stability and in vivo elasticity modeling". In: *Annals of Biomedical Engineering* 42.2 (2014), pp. 269–279. DOI: 10.1007/s10439-013-0888-1.

[OKP08] U. Olgac, V. Kurtcuoglu, and D. Poulikakos. "Computational modeling of coupled blood-wall mass transport of LDL: Effects of local wall shear stress". In: *American Journal of Physiology - Heart and Circulatory Physiology* 294.2 (2008), H909–H919. DOI: 10.1152/ajpheart.01082.2007.

[Oli06] T. Oliphant. *A guide to NumPy*. Trelgol Publishing USA. 2006.

[OTM10] A. Ougrinovskaia, R. S. Thompson, and M. R. Myerscough. "An ODE model of early stages of atherosclerosis: Mechanisms of the inflammatory response". In: *Bulletin of Mathematical Biology* 72.6 (2010), pp. 1534–1561. DOI: 10.1007/s11538-010-9509-4.

[Pao02] C. V. Pao. "Numerical Methods for Time-Periodic Solutions of Nonlinear Parabolic Boundary Value Problems". In: *SIAM Journal on Numerical Analysis* 39.2 (2002), pp. 647–667.

[Par+19] A. Parton, V. McGilligan, M. Chemaly, M. O'Kane, and S. Watterson. "New models of atherosclerosis and multi-drug therapeutic interventions". In: *Bioinformatics* 35.14 (2019), pp. 2449–2457. DOI: 10.1093/bioinformatics/bty980.

[Par+16] A. Parton, V. McGilligan, M. O'Kane, F. R. Baldrick, and S. Watterson. "Computational modelling of atherosclerosis". In: *Briefings in Bioinformatics* 17.4 (2016), pp. 562–575. DOI: 10.1093/bib/bbv081.

[PGH63] C. S. Patlak, D. A. Goldstein, and J. F. Hoffman. "The flow of solute and solvent across a two-membrane system". In: *Journal of Theoretical Biology* 5.3 (1963), pp. 426–442. DOI: 10.1016/0022-5193(63)90088-2.

[Ped16] T. R. Pedersen. "The Success Story of LDL Cholesterol Lowering". In: *Circulation Research* 118.4 (2016), pp. 721–731. DOI: 10.1161/CIRCRESAHA.115.306297.

[PSW13] V. Peiffer, S. J. Sherwin, and P. D. Weinberg. "Does low and oscillatory wall shear stress correlate spatially with early atherosclerosis? A systematic review". In: *Cardiovascular Research* 99.2 (2013), pp. 242–250. DOI: 10.1093/cvr/cvt044.

[PPZ09] K. Perktold, M. Prosi, and P. Zunino. "Mathematical models of mass transfer in the vascular walls". In: *Cardiovascular Mathematics*. Ed. by L. Formaggia, A. Quarteroni, and A. Veneziani. Vol. 1. MS&A. Milano: Springer, 2009, pp. 243–278.

[Pla+06] M. J. Plank, A. Comerford, T. David, and D. J. Wall. "Concentration of blood-borne agonists at the endothelium". In: *Proceedings of the Royal Society A: Mathematical, Physical and Engineering Sciences* 462.2066 (2006), pp. 671–688. DOI: 10.1098/rspa.2005.1591.

[Pla+07] M. J. Plank, A. Comerford, D. J. N. Wall, and T. David. "Modelling the Early Stages of Atherosclerosis". In: *Mathematical Modeling of Biological Systems*. Ed. by A. Deutsch, L. Brusch, H. Byrne, G. de Vries, and H. Herzel. Boston: Birkhäuser, 2007, pp. 263–274. DOI: 10.1007/s005350300016.

[Pla+05] F. Platte, D. Kuzmin, C. Fredebeul, and S. Turek. "Novel Simulation Approaches for Cyclic Steady-state Fixed-bed Processes Exhibiting Sharp Fronts and Shocks". In: *Trends and Applications in Constructive Approximation* 151 (2005), pp. 207–223. DOI: 10.1007/3-7643-7356-3_15.

[PR60] L. S. Pontryagin and L. V. Rodygin. "Approximate solution of a system of ordinary differential equations involving a small parameter in the derivatives". In: *Soviet Mathematics Doklady* 1 (1960), pp. 237–240.

[Pop00] S. B. Pope. *Turbulent Flows*. Vol. 1. Cambridge University Press, 2000, p. 771.

[Pro+05] M. Prosi, P. Zunino, K. Perktold, and A. Quarteroni. "Mathematical and numerical models for transfer of low-density lipoproteins through the arterial walls: A new methodology for the model set up with applications to the study of disturbed lumenal flow". In: *Journal of Biomechanics* 38.4 (2005), pp. 903–917. DOI: 10.1016/j.jbiomech.2004.04.024.

[PS16] J. Prüss and G. Simonett. *Moving Interfaces and Quasilinear Parabolic Evolution Equations*. Vol. 105. Monographs in Mathematics. Basel: Birkhäuser, 2016, p. 609. DOI: 10.1007/978-3-319-27698-4.

[QF04] A. Quarteroni and L. Formaggia. "Mathematical Modeling and Numerical Simulation of the Cardiovascular System". In: *Computational Models for the Human Body*. Vol. 12. Handbook of Numerical Analysis. Amsterdam: Elsevier, 2004, pp. 3–127.

[QVZ02a] A. Quarteroni, A. Veneziani, and P. Zunino. "A Domain Decomposition Method for Advection-Diffusion Processes with Application to Blood Solutes". In: *SIAM Journal on Scientific Computing* 23.6 (2002), pp. 1959–1980. DOI: 10.1137/S1064827500375722.

[QVZ02b] A. Quarteroni, A. Veneziani, and P. Zunino. "Mathematical and Numerical Modeling of Solute Dynamics in Blood Flow and Arterial Walls". In: *SIAM Journal on Numerical Analysis* 39.5 (2002), pp. 1488–1511. DOI: 10.1137/S0036142900369714.

[RS04] K. R. Rajagopal and A. R. Srinivasa. "On thermomechanical restrictions of continua". In: *Proceedings of the Royal Society A: Mathematical, Physical and Engineering Sciences* 460.2042 (2004), pp. 631–651. DOI: 10.1098/rspa.2002.1111.

[RPP97] G. Rappitsch, K. Perktold, and E. Pernkopf. "Numerical modelling of shear-dependent mass transfer in large arteries". In: *International Journal for Numerical Methods in Fluids* 25.7 (1997), pp. 847–857. DOI: 10.1002/(sici)1097-0363(19971015)25:7<847::aid-fld590>3.3.co;2-t.

[Ric17] T. Richter. *Fluid-structure Interactions*. Vol. 118. Lecture Notes in Computational Science and Engineering. Cham: Springer, 2017. DOI: 10.1007/978-3-319-63970-3.

[Ric19] T. Richter. *An averaging scheme for the efficient approximation of time-periodic flow problems*. Preprint. 2019. arXiv: 1806.00906v2.

[RW18] T. Richter and W. Wollner. "An Optimization Framework for the Computation of Time-Periodic Solutions of Partial Differential Equations". In: *Vietnam Journal of Mathematics* 46.4 (2018), pp. 949–966. DOI: 10.1007/s10013-018-0314-y.

[RL07] E. Ritman and A. Lerman. "The Dynamic Vasa Vasorum". In: *Cardiovascular Research* 75.4 (2007), pp. 649–658. DOI: 10.1016/j.cardiores.2007.06.020.

[RSK08] A. M. Robertson, A. Sequeira, and M. V. Kameneva. "Hemorheology". In: *Hemodynamical Flows*. Ed. by G. P. Galdi, R. Rannacher, A. M. Roberston, and S. Turek. Basel: Birkhauser, 2008, pp. 63–120.

[RHM94] E. K. Rodriguez, A. Hoger, and A. D. McCulloch. "Stress-dependent finite growth in soft elastic tissues". In: *Journal of Biomechanics* 27.4 (1994), pp. 455–467. DOI: 10.1016/0021-9290(94)90021-3.

[Ros99] R. Ross. "Atherosclerosis — An Inflammatory Disease". In: *New England Journal of Medicine* 340.2 (1999), pp. 115–126. DOI: 10.1056/NEJM199901143400207.

[RNF18] M. Roustaei, M. R. Nikmaneshi, and B. Firoozabadi. "Simulation of Low Density Lipoprotein (LDL) permeation into multilayer coronary arterial wall: Interactive effects of wall shear stress and fluid-structure interaction in hypertension". In: *Journal of Biomechanics* 67 (2018), pp. 114–122. DOI: 10.1016/j.jbiomech.2017.11.029.

[Saa06] J. Saal. "Maximal regularity for the Stokes equations in non-cylindrical space-time domains". In: *Journal of the Mathematical Society of Japan* 58.3 (2006), pp. 617–641. DOI: 10.2969/jmsj/1156342030.

[San80] E. Sanchez-Palencia. *Non-Homogeneous Media and Vibration Theory*. Vol. 127. Lecture Notes in Physics. Berlin, Heidelberg: Springer, 1980, p. 398. DOI: 10.1007/3-540-10000-8.

[SVM07] J. A. Sanders, F. Verhulst, and J. Murdock. *Averaging Methods in Nonlinear Dynamical Systems*. 2nd ed. Vol. 59. Applied Mathematical Sciences. New York: Springer, 2007, p. 431. DOI: 10.1007/978-0-387-48918-6.

[SPV09] T. Schäfer, A. C. Poje, and J. Vukadinovic. "Averaged dynamics of time-periodic advection diffusion equations in the limit of small diffusivity". In: *Physica D: Nonlinear Phenomena* 238.3 (2009), pp. 233–240. DOI: 10.1016/j.physd.2008.10.015.

[Sch12] K. Schmüdgen. *Unbounded Self-adjoint Operators on Hilbert Space*. Vol. 265. Graduate Texts in Mathematics. Dordrecht: Springer, 2012, p. 432. DOI: 10.1007/978-94-007-4753-1.

[SC89a] D. C. Schwenke and T. E. Carew. "Initiation of atherosclerotic lesions in cholesterol-fed rabbits. I. Focal increases in arterial LDL concentration precede development of fatty streak lesions." In: *Arteriosclerosis: An Official Journal of the American Heart Association, Inc.* 9.6 (1989), pp. 895–907. DOI: 10.1161/01.ATV.9.6.895.

[SC89b] D. C. Schwenke and T. E. Carew. "Initiation of atherosclerotic lesions in cholesterol-fed rabbits. II. Selective retention of LDL vs. selective increases in LDL permeability in susceptible sites of arteries." In: *Arteriosclerosis: An Official Journal of the American Heart Association, Inc.* 9.6 (1989), pp. 908–918. DOI: 10.1161/01.ATV.9.6.908.

[Sho96] R. Showalter. *Monotone Operators in Banach Space and Nonlinear Partial Differential Equations*. Providence, Rhode Island: American Mathematical Society, 1996, p. 278.

[Sil+13] T. Silva, A. Sequeira, R. F. Santos, and J. Tiago. "Mathematical Modeling of Atherosclerotic Plaque Formation Coupled with a Non-Newtonian Model of Blood Flow". In: *Conference Papers in Mathematics* (2013), pp. 1–14. DOI: 10.1155/2013/405914.

[Sio+11] P. Siogkas, A. Sakellarios, T. P. Exarchos, L. Athanasiou, E. Karvounis, K. Stefanou, E. Fotiou, D. I. Fotiadis, K. K. Naka, L. K. Michalis, N. Filipovic, and O. Parodi. "Multiscale - Patient-specific artery and atherogenesis models". In: *IEEE Transactions on Biomedical Engineering* 58.12 (2011), pp. 3464–3468. DOI: 10.1109/TBME.2011.2164919.

[SNH17] A. Skiadopoulos, P. Neofytou, and C. Housiadas. "Comparison of blood rheological models in patient specific cardiovascular system simulations". In: *Journal of Hydrodynamics* 29.2 (2017), pp. 293–304. DOI: 10.1016/S1001-6058(16)60739-4.

[Soh01] H. Sohr. *The Navier-Stokes Equations*. Birkhäuser Advanced Texts. Basel: Birkhäuser, 2001, p. 367. DOI: 10.1007/978-3-0348-8255-2.

[SR20] F. Sonner and T. Richter. "Second Order Pressure Estimates for the Crank–Nicolson Discretization of the Incompressible Navier–Stokes Equations". In: *SIAM Journal on Numerical Analysis* 58.1 (2020), pp. 375–409. DOI: 10.1137/18M1234813.

[Spi16] N. Spizzirri. "An Averaging Method for Advection-Diffusion Equations". PhD thesis. City University of New York, 2016.

[SE02] D. K. Stangeby and C. R. Ethier. "Coupled Computational Analysis of Arterial LDL Transport - Effects of Hypertension". In: *Computer Methods in Biomechanics and Biomedical Engineering* 5.3 (2002), pp. 233–241. DOI: 10.1080/10255840290010733.

[Sta99] H. C. Stary. *Atlas of Atherosclerosis: Progression and Regression*. New York: The Parthenon Publishing Group Inc., 1999, p. 131.

[Sta00] H. C. Stary. "Natural History and Histological Classification of Atherosclerotic Lesions: An Update". In: *Arteriosclerosis, Thrombosis, and Vascular Biology* 20.5 (2000), pp. 1177–1178. DOI: 10.1161/01.ATV.20.5.1177.

[Sta+92] H. C. Stary, D. H. Blankenhorn, A. B. Chandler, S. Glagov, W. Insull, M. Richardson, M. E. Rosenfeld, S. A. Schaffer, C. J. Schwartz, and W. D. Wagner. "A definition of the intima of human arteries and of its atherosclerosis-prone regions. A report from the Committee on Vascular Lesions of the Council on Arteriosclerosis, American Heart Association." In: *Circulation* 85.1 (1992), pp. 391–405. DOI: 10.1161/01.CIR.85.1.391.

[Sta+94] H. C. Stary, A. B. Chandler, S. Glagov, J. R. Guyton, W. Insull, M. E. Rosenfeld, S. A. Schaffer, C. J. Schwartz, W. D. Wagner, and R. W. Wissler. "A definition of initial, fatty streak, and intermediate lesions of atherosclerosis. A report from the Committee on Vascular Lesions of the Council on Arteriosclerosis, American Heart Association." In: *Circulation* 89.5 (1994), pp. 2462–2478. DOI: 10.1161/01.CIR.89.5.2462.

[Sta+95] H. C. Stary, A. B. Chandler, R. E. Dinsmore, V. Fuster, S. Glagov, W. Insull, M. E. Rosenfeld, C. J. Schwartz, W. D. Wagner, and R. W. Wissler. "A Definition of Advanced Types of Atherosclerotic Lesions and a Histological Classification of Atherosclerosis". In: *Circulation* 92.5 (1995), pp. 1355–1374. DOI: 10.1161/01.CIR.92.5.1355.

[Ste79] M. Steuerwalt. "The Existence, Computation, and Number of Solutions of Periodic Parabolic Problems". In: *SIAM Journal on Numerical Analysis* 16.3 (1979), pp. 402–420. DOI: 10.1137/0716034.

[SK04] R. Stocker and J. F. Keaney. "Role of oxidative modifications in atherosclerosis". In: *Physiological Reviews* 84.4 (2004), pp. 1381–1478. DOI: 10.1152/physrev.00047.2003.

[SB02] J. Stoer and R. Bulirsch. *Introduction to Numerical Analysis*. 3rd ed. New York: Springer, 2002, p. 746. DOI: 10.1007/978-0-387-21738-3.

[Sun+06] N. Sun, N. B. Wood, A. D. Hughes, S. A. Thom, and X. Y. Xu. "Fluid-wall modelling of mass transfer in an axisymmetric Stenosis: Effects of shear-dependent transport properties". In: *Annals of Biomedical Engineering* 34.7 (2006), pp. 1119–1128. DOI: 10.1007/s10439-006-9144-2.

[SN13] F. K. Swirski and M. Nahrendorf. "Leukocyte Behavior in Atherosclerosis, Myocardial Infarction, and Heart Failure". In: *Science* 339.6116 (2013), pp. 161–166. DOI: 10.1126/science.1230719.

[TWB07] I. Tabas, K. J. Williams, and J. Borén. "Subendothelial lipoprotein retention as the initiating process in atherosclerosis: Update and therapeutic implications". In: *Circulation* 116.16 (2007), pp. 1832–1844. DOI: 10.1161/CIRCULATIONAHA.106.676890.

[Tan+09] D. Tang, C. Yang, S. Kobayashi, J. Zheng, P. K. Woodard, Z. Teng, K. Billiar, R. Bach, and D. N. Ku. "3D MRI-based anisotropic FSI models with cyclic bending for human coronary atherosclerotic plaque mechanical analysis". In: *Journal of Biomechanical Engineering* 131.6 (2009). DOI: 10.1115/1.3127253.

[Tan+08] D. Tang, C. Yang, S. Mondal, F. Liu, G. Canton, T. S. Hatsukami, and C. Yuan. "A negative correlation between human carotid atherosclerotic plaque progression and plaque wall stress: In vivo MRI-based 2D/3D FSI models". In: *Journal of Biomechanics* 41.4 (2008), pp. 727–736. DOI: 10.1016/j.jbiomech.2007.11.026.

[Tan+05] D. Tang, C. Yang, J. Zheng, P. K. Woodard, J. E. Saffitz, J. D. Petruccelli, G. A. Sicard, and C. Yuan. "Local maximal stress hypothesis and computational plaque vulnerability index for atherosclerotic plaque assessment." In: *Annals of biomedical engineering* 33.12 (2005), pp. 1789–801. DOI: 10.1007/s10439-005-8267-1.

[Tar03] J. M. Tarbell. "Mass Transport in Arteries and the Localization of Atherosclerosis". In: *Annual Review of Biomedical Engineering* 5.1 (2003), pp. 79–118. DOI: 10.1146/annurev.bioeng.5.040202.121529.

[Tem01] R. Temam. *Navier–Stokes Equations: Theory and Numerical Analysis*. Providence, Rhode Island: AMS Chelsea Publishing, 2001, p. 408.

[Ten+10] Z. Teng, G. Canton, C. Yuan, M. Ferguson, C. Yang, X. Huang, J. Zheng, P. K. Woodard, and D. Tang. "3D critical plaque wall stress is a better predictor of carotid plaque rupture sites than flow shear stress: An in vivo MRI-based 3D FSI study". In: *Journal of Biomechanical Engineering* 132.3 (2010), p. 031007. DOI: 10.1115/1.4001028.

[Tho+18] M. P. Thon, H. Z. Ford, M. W. Gee, and M. R. Myerscough. "A Quantitative Model of Early Atherosclerotic Plaques Parameterized Using In Vitro Experiments". In: *Bulletin of Mathematical Biology* 80.1 (2018), pp. 175–214. DOI: 10.1007/s11538-017-0367-1.

[Tik48] A. Tikhonov. "On the dependence of the solutions of differential equations on a small parameter". In: *Matematicheskii Sbornik* 22.64 (1948), pp. 193–204.

[Tik52] A. Tikhonov. "Systems of differential equations containing small parameters in the derivatives". In: *Matematicheskii Sbornik* 31.73 (1952), pp. 575–586. DOI: 10.18287/0134-2452-2015-39-4-459-461..

[VV07] J. S. VanEpps and D. A. Vorp. "Mechanopathobiology of Atherogenesis: A Review". In: *Journal of Surgical Research* 142.1 (2007), pp. 202–217. DOI: 10.1016/j.jss.2006.11.001.

[VBD06] A. Versluis, A. J. Bank, and W. H. Douglas. "Fatigue and plaque rupture in myocardial infarction". In: *Journal of Biomechanics* 39.2 (2006), pp. 339–347. DOI: 10.1016/j.jbiomech.2004.10.041.

[Vir+00] R. Virmani, F. D. Kolodgie, A. P. Burke, A. Farb, and S. M. Schwartz. "Lessons From Sudden Coronary Death". In: *Arteriosclerosis, Thrombosis, and Vascular Biology* 20.5 (2000), pp. 1262–1275. DOI: 10.1161/01.atv.20.5.1262.

[Vir+05] R. Virmani, F. D. Kolodgie, A. P. Burke, A. V. Finn, H. K. Gold, T. N. Tulenko, S. P. Wrenn, and J. Narula. "Atherosclerotic plaque progression and vulnerability to rupture: Angiogenesis as a source of intraplaque hemorrhage". In: *Arteriosclerosis, Thrombosis, and Vascular Biology* 25.10 (2005), pp. 2054–2061. DOI: 10.1161/01.ATV.0000178991.71605.18.

[VC07] M. I. Vishik and V. V. Chepyzhov. "The Global Attractor of the Nonautonomous 2D Navier–Stokes System with Singularly Oscillating External Force". In: *Doklady Mathematics* 75.2 (2007), pp. 236–239. DOI: 10.1134/S1064562407020160.

[WN11] H. F. Walker and P. Ni. "Anderson Acceleration for Fixed-Point Iterations". In: *SIAM Journal on Numerical Analysis* 49.4 (2011), pp. 1715–1735. DOI: 10.1137/10078356X.

[WH10] H. Wang and Y. Huo. "Adhesion Molecules and Atherosclerosis". In: *Atherosclerosis: Molecular and Cellular Mechanisms*. Ed. by S. J. George and J. Johnson. Weinheim: Wiley, 2010, pp. 43–62. DOI: 10.1002/9783527629589.ch3.

[War+00] M. R. Ward, G. Pasterkamp, A. C. Yeung, and C. Borst. "Arterial Remodeling". In: *Circulation* 102.10 (2000), pp. 1186–1191. DOI: 10.1161/01.CIR.102.10.1186.

[Wat+18] M. G. Watson, H. M. Byrne, C. Macaskill, and M. R. Myerscough. "A two-phase model of early fibrous cap formation in atherosclerosis". In: *Journal of Theoretical Biology* 456 (2018), pp. 123–136. DOI: 10.1016/j.jtbi.2018.08.010.

[Wat+20] M. G. Watson, H. M. Byrne, C. Macaskill, and M. R. Myerscough. "A multiphase model of growth factor-regulated atherosclerotic cap formation". In: *Journal of Mathematical Biology* 81.2 (2020), pp. 725–767. DOI: 10.1007/s00285-020-01526-6.

[Wom55] J. R. Womersley. "Method for the calculation of velocity, rate of flow and viscous drag in arteries when the pressure gradient is known." In: *The Journal of Physiology* 127.3 (1955), pp. 553–563. DOI: 10.1113/jphysiol.1955.sp005276.

[Yan+07] C. Yang, D. Tang, C. Yuan, T. S. Hatsukami, J. Zheng, and P. K. Woodard. "In vivo/ex vivo MRI-based 3D non-newtonian FSI models for human atherosclerotic plaques compared with fluid/wall-only models". In: *Computer Modeling in Engineering and Sciences* 19.3 (2007), pp. 233–245. DOI: 10.1016/j.csda.2008.07.034.Inferences.

[Yan14] Y. Yang. "Mathematical modeling and simulation of the evolution of plaques in blood vessels". PhD thesis. Heidelberg University, 2014, p. 147.

[Yan+15] Y. Yang, W. Jäger, M. Neuss-Radu, and T. Richter. "Mathematical modeling and simulation of the evolution of plaques in blood vessels". In: *Journal of Mathematical Biology* 72.4 (2015), pp. 973–996. DOI: 10.1007/s00285-015-0934-8.

[Yan+17] Y. Yang, T. Richter, W. Jäger, and M. Neuss-Radu. "An ALE approach to mechano-chemical processes in fluid-structure interactions". In: *International Journal for Numerical Methods in Fluids* 84.4 (2017), pp. 199–220. DOI: 10.1002/fld.4345.

[Yok+99] K. Yokoya, H. Takatsu, T. Suzuki, H. Hosokawa, S. Ojio, T. Matsubara, T. Tanaka, S. Watanabe, N. Morita, K. Nishigaki, G. Takemura, T. Noda, S. Minatoguchi, and H. Fujiwara. "Process of progression of coronary artery lesions from mild or moderate stenosis to moderate or severe stenosis: A study based on four serial coronary arteriograms per year". In: *Circulation* 100.9 (1999), pp. 903–909. DOI: 10.1161/01.CIR.100.9.903.

[Zoh05] T. I. Zohdi. "A simple model for shear stress mediated lumen reduction in blood vessels". In: *Biomechanics and Modeling in Mechanobiology* 4.1 (2005), pp. 57–61. DOI: 10.1007/s10237-004-0059-2.

[ZHB04] T. I. Zohdi, G. A. Holzapfel, and S. A. Berger. "A phenomenological model for atherosclerotic plaque growth and rupture". In: *Journal of Theoretical Biology* 227.3 (2004), pp. 437–443. DOI: 10.1016/j.jtbi.2003.11.025.